SUMMER 2024

GEMS & GEMOLOGY

90th ANNIVERSARY

VOLUME LX

GIA Update on Laboratory-Grown Diamonds

Characterization of Chinese Cassiterite

Anorthoclase Feldspar from Vietnam

Tourmaline Inclusions Chart

THE QUARTERLY JOURNAL OF THE GEMOLOGICAL INSTITUTE OF AMERICA

GEMS & GEMOLOGY

Summer 2024
VOLUME 60, No. 2


p. 164


p. 206

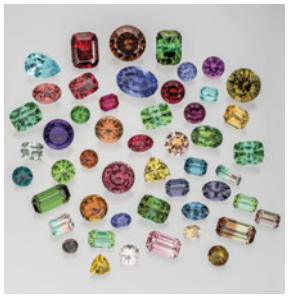
p. 209


p. 220


p. 249


p. 267

GEMS & GEMOLOGY®

gia.edu/gems-gemology

Customer Service
(760) 603-4200
gandg@gia.edu

Subscriptions
Copies of the current issue may be purchased for $29.95 plus shipping. Subscriptions are $79.99 for one year (4 issues) in the U.S. and $99.99 elsewhere. Canadian subscribers should add GST. Discounts are available for renewals, group subscriptions, GIA alumni, and current GIA students. To purchase print subscriptions, visit store.gia.edu or contact Customer Service. For institutional rates, contact Customer Service.

Database Coverage
Gems & Gemology's impact factor is 1.6, according to the 2023 Journal Citation Reports by Clarivate Analytics (issued June 2024). *G&G* is abstracted in Thomson Reuters products (Current Contents: Physical, Chemical & Earth Sciences and Science Citation Index—Expanded, including the Web of Knowledge) and other databases. For a complete list of sources abstracting *G&G*, go to gia.edu/gems-gemology, and click on "Publication Information."

Manuscript Submissions
Gems & Gemology, a peer-reviewed journal, welcomes the submission of articles on all aspects of the field. Please see the Author Guidelines at gia.edu/gems-gemology or contact the Managing Editor. Letters on articles published in *G&G* are also welcome. Please note that Field Reports, Lab Notes, Gem News International, Micro-World, Colored Stones Unearthed, Diamond Reflections, Charts, and In the Spotlight are not peer-reviewed sections but do undergo technical and editorial review.

Gems & Gemology is published quarterly by the Gemological Institute of America, a nonprofit educational organization for the gem and jewelry industry.

Postmaster: Return undeliverable copies of *Gems & Gemology* to GIA, The Robert Mouawad Campus, 5345 Armada Drive, Carlsbad, CA 92008.

Our Canadian goods and service registration number is 126142892RT.

About the Cover

This issue features a chart of tourmaline inclusions. Shown on the cover is a 20 × 16 cm carving by Patrick Dreher and Daniella Becker containing rubellite strawberries and green tourmaline leaves. Jürgen Christmann completed the quartz vase, and Eckhard Cullmann was the goldsmith. The rubellites are from the Himalaya mine in San Diego County, California, and the green tourmalines are Brazilian. Photo by Robert Weldon; courtesy of Pala International.

Printing is by L+L Printers, Carlsbad, CA.

GIA World Headquarters The Robert Mouawad Campus 5345 Armada Drive Carlsbad, CA 92008 USA

ISSN 0016-626X

Gems & Gemology at Ninety: Consistency and Change

In January 1934, GIA published the first installment of a new professional journal for members of the jewelry trade. *Gems & Gemology* editor and GIA founder Robert M. Shipley wrote, "It is our purpose to give our readers accurate and up-to-date information concerning gemstones. We intend to print not only new developments in the field of gems, but also interesting points which will serve the jeweler as sales tools." At the time, there was only one similar publication: *The Gemmologist*, started by the National Association of Goldsmiths in London in 1931. *G&G* quickly made its mark. Initially appearing on a bimonthly basis, the journal adopted a quarterly publication schedule in 1936.

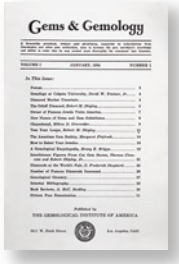

Since the earliest issues, *G&G* has covered a range of gem-related topics, going beyond the standard curriculum of GIA's educational courses. In doing so, it has attracted top contributors and a global readership seeking practical and reliable information on important gemological developments.

The journal underwent a major redesign in 1981, transitioning to a larger format. This included new content sections, superbly detailed maps and illustrations, and the use of color photography, which is crucial to the study of gemstones. Formal peer review and other editorial processes were implemented to promote accuracy and readability. Recent years have seen additional upgrades, including free access to all *G&G* issues since 1934 and an online version of the journal, where print edition content is often supplemented by digital content such as videos of field expeditions and on-site expert interviews. Colorful wall charts on various topics—laboratory-grown diamonds, inclusions, and pearl classification, to name a few—have become a regular feature.

As our longtime readers know, the past two decades have witnessed the transformation of gemology into a far more technical field. Gem testing laboratories now employ a range of advanced scientific techniques. Gem treatment detection and colored stone country-of-origin determination remain the most challenging areas. Other important topics for study include the visual appearance, color stability, and optical phenomena of gems, as well as methods to better analyze and present complex sets of data.

As gemological research relies more heavily on scientific techniques and instrumentation, the need will grow for articles explaining these topics to a broad audience. The use of portable instruments for identifying gems will also continue. Meanwhile, geological field studies of deposits worldwide will provide new insights into the conditions of natural gem formation and the latest techniques for distinguishing them from synthetic and treated gem materials.

Looking beyond our 90th year, *Gems & Gemology* will continue to fulfill its original charter of providing up-to-date information on gemstones. We welcome well-researched contributions on all gemological topics, and we invite readers with a passion for gemology to join us.

James E. Shigley

James E. Shigley | Contributing Editor and Distinguished Research Fellow, GIA

Laboratory-Grown Diamonds: An Update on Identification and Products Evaluated at GIA

Sally Eaton-Magaña, Matthew F. Hardman, and Shoko Odake

Over the past two decades, GIA has documented a rapid evolution of laboratory-grown diamonds; this article provides a comprehensive overview of these developments and summarizes novel laboratory-grown diamonds that may become more common in the future. The industry has seen a significant increase in the quantity, size, and quality of laboratory-grown diamonds, making them viable for commercialization on a larger scale. Nevertheless, there have been relatively few changes in laboratory-grown diamonds during the last five years, indicating that developments have largely stabilized for now. This overview summarizes the two diamond growth processes: high-pressure, high-temperature (HPHT) and chemical vapor deposition (CVD). It explores the major trends observed by GIA since 2007, the year it began issuing synthetic diamond grading reports. CVD products now dominate the supply of laboratory-grown diamonds submitted for grading reports, with the majority of these also undergoing post-growth HPHT treatment to remove their color. This article discusses methods and strategies for identifying laboratory-grown diamonds by providing their distinguishing gemological characteristics as well as results from recent developments in advanced testing approaches.

The introduction of laboratory-grown diamonds to the consumer market has expanded the variety of products available but also increased the complexity of identification for many in the trade. Laboratory-grown diamonds that are colorless to near-colorless share many gemological and physical properties with their natural counterparts (figure 1), which presents a challenge for independent gemologists and appraisers in distinguishing these gems from natural diamonds. Consequently, gemologists have needed to invest in powerful analytical testing equipment or depend on gemological laboratories for accurate identification.

Colorless to near-colorless laboratory-grown diamonds are type II, meaning they have no detectable nitrogen impurities (Breeding and Shigley, 2009). By contrast, only about 1% of natural diamonds are type II (Smith et al., 2016; Eaton-Magaña et al., 2020). Despite the increasing prevalence of laboratory-grown diamonds within the trade, their volume remains small compared to that of natural diamonds submitted for grading. Therefore, only those diamonds that test as type II require extensive analysis to determine whether they are laboratory-grown. These can be produced by high-pressure, high-temperature (HPHT) or chemical vapor deposition (CVD) processes.

In Brief

- HPHT- and CVD-grown diamond size, quantity, and color grades have rapidly improved over the decades.
- A small number of laboratory-grown diamonds show that high concentrations of impurities and post-growth treatments can produce a variety of unusual colors.
- While identification criteria have remained largely the same through time, some laboratory-grown diamonds require experienced gemologists and advanced analytical techniques to confirm laboratory-grown origin.

This study summarizes the wide range of laboratory-grown diamonds submitted to GIA over the years, allowing these stones to tell the story. Over the past 20 years, advances in diamond growth processes have substantially altered the color and size of gem-quality stones submitted to GIA. In addition, this survey emphasizes some new laboratory-grown products that could become more common in the future.

See end of article for About the Authors and Acknowledgments.
Gems & Gemology, Vol. 60, No. 2, pp. 146–167,
http://dx.doi.org/10.5741/GEMS.60.2.146

Figure 1. This 10.02 ct E-color, VS_1-clarity emerald-cut diamond is an example of the great strides made in HPHT growth technology in the past two decades, as laboratory-grown diamonds have become an important sector of the gem diamond market. Photo by Johnny Leung. The as-grown CVD diamond plate (1.24 ct, 8.41 × 8.60 × 1.26 mm) was manufactured by GIA at its New Jersey research facility. Photo by Adrian Chan.

OVERVIEW OF LABORATORY-GROWN DIAMOND MANUFACTURE

Although the mechanisms for laboratory growth of diamonds are well established (e.g., Eaton-Magaña and Shigley, 2016; Eaton-Magaña et al., 2017; D'Haenens-Johansson et al., 2022), this article provides a brief summary of the CVD and HPHT growth processes. For both methods, a diamond substrate (often referred to as a "seed" in HPHT growth) is used to create the crystal blueprint from which the new diamond is created. The quality, size, and preparation of the substrate can have a significant impact on the resulting diamond (D'Haenens-Johansson et al., 2022). Substrate availability—previously a limiting factor for commercial production—has dramatically improved to meet demand.

A report by Bain & Company (Linde et al., 2021) estimated that 6–7 million carats of gem-quality laboratory-grown diamonds were produced globally in 2020. China led the way with approximately 3 million carats (mostly grown using HPHT), followed by India with about 1.5 million carats (mostly CVD) and the United States with about 1 million carats (CVD). Laboratory-grown diamond production has continued to expand as public perceptions of its use in jewelry have evolved. In October 2021, industry analyst Paul Zimnisky estimated that laboratory-grown diamond jewelry accounted for approximately 3.4% of the global diamond jewelry market by value in 2018. He forecast an increase to 7.5% in 2021 and 11.5% by 2025. In January 2024, he revised the 2025 projection to ~20% (Zimnisky, 2021, 2024).

HPHT-grown diamonds are the market leaders in China, including the mass production of small, melee-size goods by both private and government-funded companies such as Zhengzhou Sino-Crystal Diamond Co., Zhongnan Diamond Co., and Henan Huanghe Whirlwind Co. (Linde et al., 2021). HPHT technology has long been used to manufacture diamond grits and powders for the abrasives industry, setting the stage for the rapid development of gem-quality materials. Chinese CVD producers have also demonstrated the ability to grow high-quality gemstones. Shanghai Zhengshi Technology Co. produces large, untreated colorless CVD-grown diamonds (Myagkaya and Johnson, 2021; Wang et al., 2022), while Ningbo Crysdiam Technology Co. creates colorless, pink, and blue CVD products (Lu et al., 2019).

India's output of laboratory-grown diamonds using the CVD method has accelerated dramatically in recent years, supported by an estimated 4,000–6,000 CVD reactors (Rego, 2023). Many of these manufacturers are based in Surat in the state of Gujarat, which is also the world's leading diamond cutting and polishing center. Ethereal Green Diamond produces CVD-grown diamonds in very large sizes, including the largest faceted example to date, a 75.33 ct square emerald cut displayed at the 2024 JCK Las Vegas show. The crystal from which it was fashioned reportedly took nine months to grow (Ord, 2024). Greenlab Diamonds attracted global attention when Indian Prime Minister Narendra Modi presented one of their CVD-grown products to First Lady Jill Biden during a 2023 visit to the White House. This 7.50 ct

F-color, VVS_2-clarity diamond was faceted from a 17 ct crystal that took 40–45 days to synthesize (Fedow, 2023). The 75 ct and 7.50 ct weights for these CVD-grown diamonds were both intended to commemorate the 75th anniversary of India's independence. This high-profile gift demonstrated the dramatic change in attitudes toward laboratory-grown diamonds in recent years.

CVD diamond production in the United States arose as a byproduct of the semiconductor industry, which harnessed them for a range of technological uses. Indeed, diamond's remarkable combination of properties—high hardness, high thermal conductivity, low thermal expansion, wide optical window, biocompatibility, and high resistance to corrosion, acid, and radiation—has sparked a wide range of engineering applications (e.g., De Wit, 2018; Markham and Twitchen, 2020). Some of the players that produce both engineering-related and gem products have included Washington Diamonds, Diamond Foundry, and Plasmability.

CVD Growth. CVD diamond growth is based on a gas-phase chemical process that bears almost no resemblance to natural diamond formation. This technique involves a reactor in which hydrogen and hydrocarbon (typically methane) feed gases flow over one or more diamond seeds. Microwaves are used to activate a plasma, creating a mixture of molecular, radical, and ionic species that are involved in a series of reactions necessary to deposit diamond material on the seeds. Hydrogen, accounting for 90–99% of the gas mixture, suppresses the growth of graphite or non-diamond carbon, which would hinder high-quality diamond formation.

For many decades after the first growth of CVD diamond in 1952, the crystal quality and sizes were not suited for gem applications. Only limited quantities of these diamonds were available in the early 2000s (Wang et al., 2003, 2005, 2007; Martineau et al., 2004; Angus, 2014). Since then, there have been notable improvements to CVD growth techniques (e.g., Butler et al., 2009; Liang et al., 2009; Nad et al., 2015, 2016; Tallaire et al., 2006, 2017), which have yielded substantial amounts of high-quality CVD-grown gem diamonds (e.g., Wang et al., 2010, 2012; Linde et al., 2021; Smith, 2023), including the large specimens mentioned earlier.

HPHT Growth. The HPHT method mimics some of the essential conditions under which natural diamonds form. A solid carbon source, typically graphite powder, is subjected to pressures of 5–6 GPa (equivalent to a depth of 150–190 km within the earth) and temperatures of 1300–1600°C. These temperatures are higher than those for natural diamond formation of ~1040–1250°C (Stachel and Luth, 2015), allowing for rapid growth. HPHT growth takes place inside a capsule that includes the carbon source, a metallic flux for dissolving the carbon to aid in growth, and a diamond seed to initiate the process (Stoupin et al., 2016; Tallaire et al., 2017; D'Haenens-Johansson et al., 2022). The diamond seed is at a lower temperature, so that carbon supersaturates and crystallizes out of the metal solution. An HPHT-grown diamond can usually be grown in a time frame ranging from an hour to a few weeks, depending on the desired size and quality (Sumiya et al., 2015; D'Haenens-Johansson et al., 2015a).

While the CVD method was developed earlier (Angus, 2014), the first gem-quality laboratory-grown diamonds were produced using the HPHT method (Shigley et al., 2002, 2004). Most early HPHT products had saturated fancy colors, often yellow-orange or yellow due to isolated nitrogen impurities or blue due to boron. Over the past 10–15 years, there has been a significant shift toward colorless to near-colorless products (D'Haenens-Johansson et al., 2014; Eaton-Magaña et al., 2017). Additionally, large HPHT-grown diamonds have been created, with Meylor Global reporting crystals surpassing 100 ct in size produced by Alkor-D ("Meylor Global…," 2020; D'Haenens-Johansson et al., 2022). The largest recorded laboratory-grown diamond is a 150.42 ct HPHT-grown crystal (28.55 × 28.25 × 22.53 mm) with good quality, created in November 2021. To date, there are no documented reports of faceted HPHT-grown diamonds larger than 100 ct.

DISTRIBUTION OF QUALITY FACTORS AMONG LABORATORY-GROWN PRODUCTS

GIA maintains a comprehensive database of all types of gemstones submitted to the laboratory, including natural, treated, and laboratory-grown diamonds, both fancy-color and colorless. This resource provides a unique opportunity to review historical data and analyze submission trends over time. The results of GIA's examination of tens of thousands of HPHT-grown and CVD-grown diamonds are documented in figures 2–6 and box A. These include updates to articles that discussed data from years prior (Eaton-Magaña and Shigley, 2016; Eaton-Magaña et al., 2017, 2021b).

GIA has documented the color distribution of CVD-grown diamonds per year (figure 2). Through-

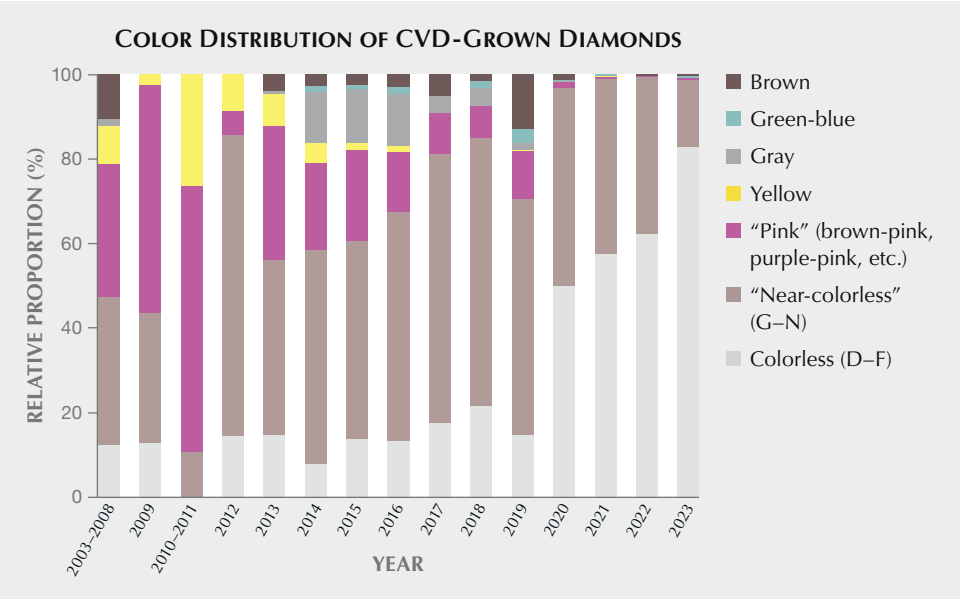

Figure 2. The color distribution of CVD-grown diamonds submitted to GIA, 2003–2023. Several early years with low submission numbers are combined. Updated from Eaton-Magaña and Shigley (2016).

out the first decade of the 2000s, CVD submissions to GIA were relatively low, so the submissions for some years had to be aggregated graphically. For many years, most samples were "near-colorless," with color grades from G to N. Prior to 2020, only a small percentage of CVD submissions had colorless grades (D, E, or F). However, 2020 saw a significant increase in the submission of colorless CVD-grown diamonds, likely due to improvements in growth and treatment procedures by established diamond manufacturers and the emergence of additional growers with new approaches. Moreover, a significant number of CVD-grown diamonds during the mid-2010s were observed to have a gray coloration (e.g., Ardon and Eaton-Magaña, 2014), possibly produced unintentionally through defect contamination during growth—an effect that may be even more evident following the annealing treatments commonly used to decolorize brown-hued CVD-grown diamonds. Gray color in CVD-grown diamonds has been linked to the presence of non-diamond inclusions referred to as "carbon nanoclusters," whose introduction is affected by growth conditions (Zaitsev et al., 2020). The conditions causing gray-colored CVD-grown diamonds have been mostly eliminated, as these stones are no longer being produced and submitted. These trends indicate that manufacturers are constantly—and successfully—refining their growth and treatment procedures to produce large, colorless diamonds in response to consumer tastes.

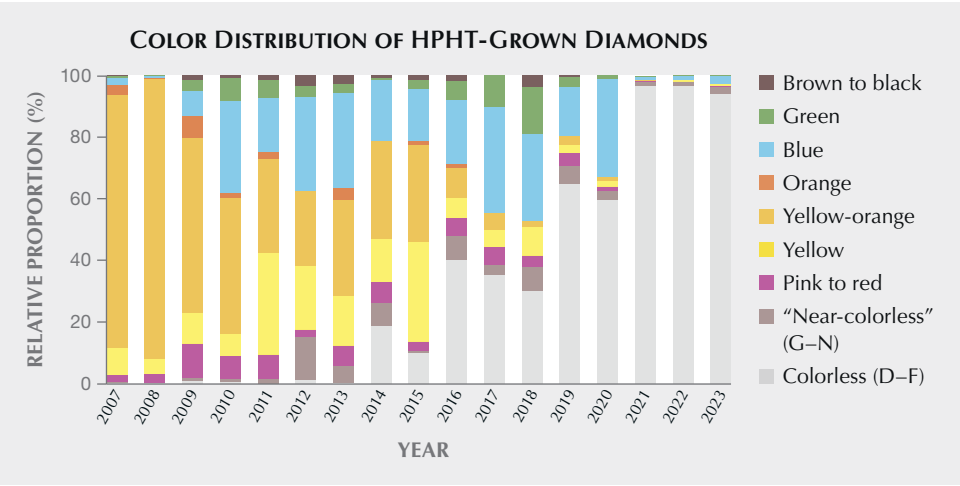

Figure 3. The color distribution of HPHT-grown diamonds submitted to GIA, 2007–2023. Updated from Eaton-Magaña et al. (2017).

Box A: Recent Trends in Laboratory-Grown Diamonds

Type IIb CVD-Grown Diamonds

In recent years, HPHT-grown diamonds have been notable for their lack of bodycolor and low boron content. Fancy-color blue HPHT-grown diamonds deliberately doped with boron were some of the earliest gem laboratory-grown diamonds reported (e.g., Shigley et al., 2002). In colorless HPHT-grown diamonds, boron is usually incorporated accidentally, with concentrations typically <20 ppb (D'Haenens-Johansson et al., 2014, 2015a; Eaton-Magaña et al., 2017). Analysis of HPHT-grown D-to-Z diamonds submitted to GIA since 2020 reveals that more than 80% contain boron concentrations detectable by infrared spectroscopy (uncompensated boron at 2800 cm^{-1}), meaning they are type IIb. Notably, the boron detected by IR is not the total boron present in the diamond, as high amounts of compensating defects can render boron undetectable (Gaillou et al., 2012). Trace amounts of boron are associated with the phosphorescence often observed in these materials (Watanabe et al., 1997).

Meanwhile, colorless to near-colorless CVD-grown diamonds often have had a brownish coloration and were classified as type IIa, without detectable boron impurities. Type IIb CVD-grown diamonds were quite rare until the start of the 2020s, when the number of colorless to near-colorless CVD-grown diamonds with a low concentration of uncompensated boron, evidenced by the 2800 cm^{-1} peak in their IR spectra, began to increase (figure A-1). Since 2020, ~5% of CVD-grown diamonds have shown detectable levels of boron, typically at low concentrations of <10 ppb, which are too low to produce a noticeable difference in diamond color.

The proportion of type IIb CVD-grown diamond submissions increased substantially in 2020–2021. Since then, the percentage of type IIb CVD-grown diamond submissions for many quarters has been greater than 5% (figure A-1A). It is important to note that this chart pertains to GIA laboratory submissions only, and global statistics may differ. Additionally, the increase in type IIb CVD diamonds could be limited to a few producers and might not represent a consistent increase across all manufacturers. The data is further subdivided into type IIb CVD-grown diamonds weighing <4 ct and ≥4 ct, indicating a smaller percentage of type IIb CVD-grown diamonds submitted in 2022–2023, but also a dramatic shift to larger sizes among type IIb material. One notable ex-

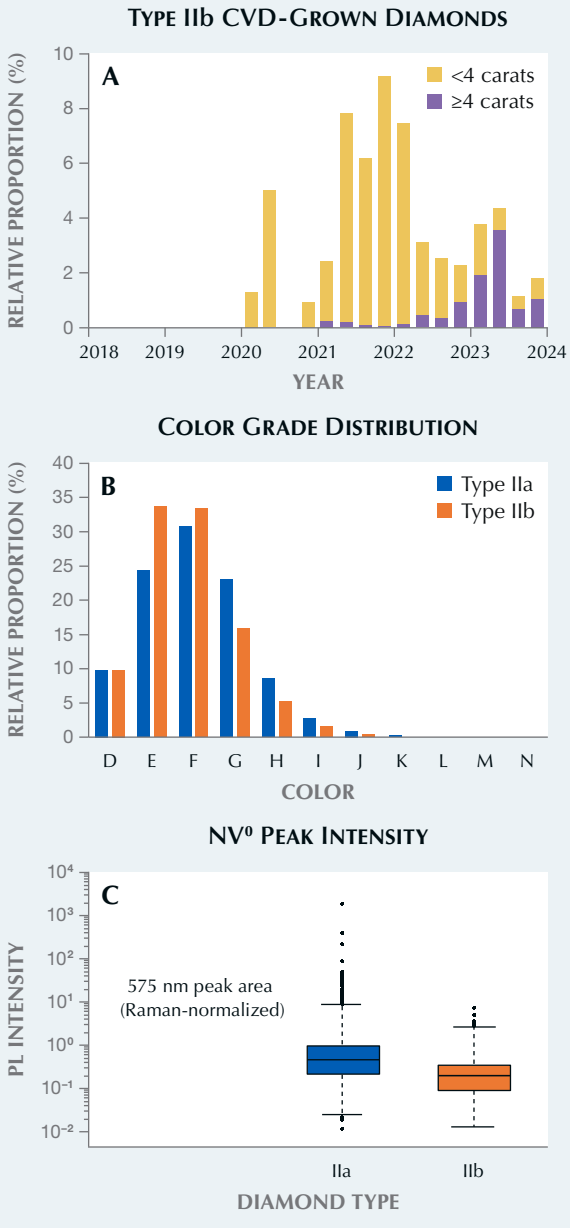

Figure A-1. Statistics for CVD-grown diamond submissions identified as type IIb are illustrated in this series of plots. A: The dataset of all CVD-grown diamonds identified as type IIb from 2018 through 2023 shows a significant increase in type IIb diamonds larger than 4 ct (the percentages across all years in the plot sum to 100%). Before 2018, only 17 type IIb CVD-grown diamonds were submitted. B: Color grade distribution of type IIa and type IIb submissions. The type IIb diamonds are shifted toward higher color grades than their type IIa counterparts. C: A box and whisker plot comparing the photoluminescence (PL) intensity of the NV^0 center between type IIa and type IIb CVD-grown diamonds. The solid horizontal line corresponds to the median value, the boxes correspond to the interquartile range (IQR; 25th–75th percentile), and the dashed "whiskers" extend 1.5× IQR. Samples beyond the whiskers are considered outliers. The NV^0 center is noticeably more intense in many type IIa stones.

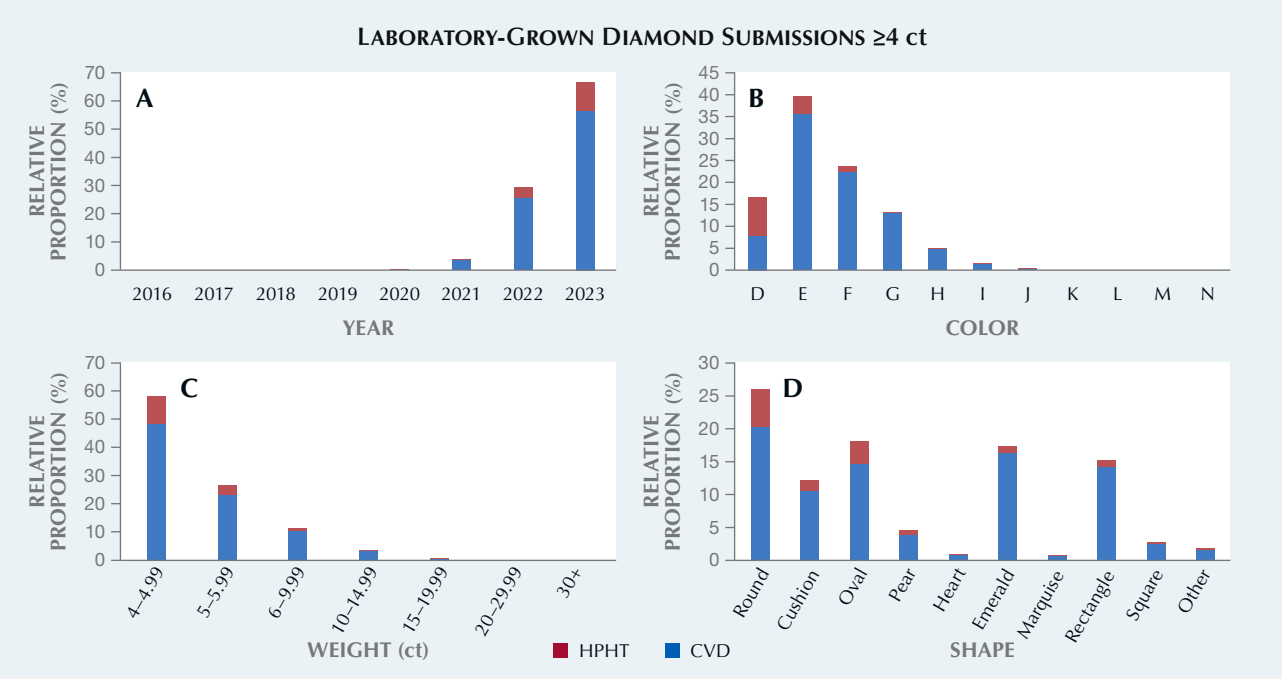

Figure A-2. Statistics of all laboratory-grown diamond submissions 4 ct or larger, the majority of which are CVD-grown. A: The distribution of the dataset plotted by year shows that most have been submitted since 2021. B: The distribution by color grade reveals that most HPHT-grown diamonds are D-color, while most CVD-grown diamonds (and laboratory-grown diamonds overall) are E-color. C: The majority of large laboratory-grown diamonds weighed between 4 and 5 ct. D: Although round diamonds outnumber the other shapes, there is a relatively even distribution of shapes compared with natural diamonds, in which rounds are a heavy majority.

ample of larger type IIb CVD material is a 34.59 ct emerald-cut diamond grown by Ethereal Green with a measured uncompensated boron concentration of ~2 ppb (Tam and Poon, 2023).

Among CVD-grown diamonds submitted to GIA, ~80% have been subjected to post-growth HPHT treatment to improve their color grade (Eaton-Magaña et al., 2021b); among the type IIb CVD-grown diamonds, the percentage of colorless to near-colorless samples that have undergone HPHT treatment is slightly higher (~85%). Additionally, the type IIb submissions tend to have a slightly higher color grade than type IIa CVD-grown diamonds (figure A-1B). Statistical analysis of prominent PL features (NV^0, NV^-, and SiV^-) indicates negligible differences in SiV^- concentrations between type IIa and type IIb CVD-grown diamonds. Conversely, the type IIb population has lower median NV^0 and NV^- concentrations than type IIa (figure A-1C). Although there is significant overlap between the two diamond types, the median of the normalized peak area for NV^0 is noticeably larger in type IIa material than in type IIb. The normalized peak area in NV^- is also greater in type IIa material, but this distinction is less pronounced.

The incorporation of boron into CVD-grown diamonds remains uncertain—it could be incidental during the growth process or limited to doping by a few producers. Additionally, uncompensated boron (i.e., not electrically compensated by other defects or impurities) is the only known boron-related defect that is consistently detectable by IR or PL spectroscopy in CVD-grown diamonds. This means that other boron-related defects may be present, but they cannot be directly detected by these methods. Furthermore, some CVD-grown diamonds may have comparable total boron concentrations but be classified as type IIa due to higher amounts of compensating defects (e.g., nitrogen).

Large (≥4 ct) Laboratory-Grown Diamonds. In recent years, GIA has seen an increase in the quantity of large (defined here as 4 ct or larger) laboratory-grown diamonds produced by both CVD and HPHT processes. Figure A-2 plots some of the parameters for large D-to-Z laboratory-grown diamonds submitted to GIA, illustrating the quantity of submissions and the distribution of color grade, carat weight, and shape. Most of the large laboratory-grown diamonds submitted since 2021 have been CVD (figure A-2A), consistent with the submission trends among laboratory-grown diamonds in general (see figure 7).

The majority of large CVD-grown diamond submissions are colorless, falling in the D–F range (figure A-2B). The highest proportion of CVD-grown submissions (and laboratory-grown diamonds in general) are E-color dia-

monds. Among HPHT-grown submissions, D-color diamonds represent the largest share. Among natural diamonds, the highest proportion fall in the F–G color range (Eaton-Magaña et al., 2020).

As expected, most of the submissions larger than 4 ct are between 4 and 5 ct, with the submissions decreasing at progressively higher weights (figure A-2C). While 70% of D-to-Z natural diamonds are round (Eaton-Magaña et al., 2020), there is a much more even distribution of shapes among laboratory-grown diamonds (figure A-2D). This is likely due to efforts to maximize weight retention from the laboratory-created crystal shape, which is distinctly different from that of natural diamond rough.

The color distribution of HPHT-grown diamonds over the years (figure 3) is much different. Most early HPHT-grown diamond submissions, starting with the introduction of synthetic diamond reports at GIA in 2007, were yellow-orange (e.g., Shigley et al., 2004). With advances in HPHT growth processes, manufacturers successfully eliminated nitrogen from the lattice in growing diamonds—the main cause of their yellow-orange color. There has since been a sharp decline in submissions of yellow-orange HPHT-grown diamonds. Colorless samples now represent the vast majority of submissions, particularly in the years 2021–2023, when >90% of HPHT-grown diamond intake was colorless—a trend that likely reflects consumer preferences.

The size of gem-quality CVD-grown diamonds has seen a dramatic increase over time. There has been a consistent trend toward larger sizes (figure 4). In the first decade of the 2000s, most CVD-grown diamonds submitted to GIA were under half a carat. Today, the majority of them exceed 3 ct. This change in size reflects improvements in CVD methods as well as the availability of large diamond substrates. Figure 5 shows milestones in record size for CVD-grown diamonds, illustrating the rapid evolution in gem-quality CVD growth. Starting from 2003, when GIA received its first faceted CVD-grown diamond for research purposes, specimens remained small (and mainly brown) until about 2010 (Wang et al., 2007, 2010). The years since then have seen a very rapid increase in size. By January 2022, the largest faceted CVD diamond was 16.41 ct (Wang et al., 2022). Since that time, the benchmark has more than quadrupled to 75.33 ct. Now that manufacturers have demonstrated the ability to produce large CVD-grown diamonds, future production will be guided by demand and profitability.

Figure 6 shows the annual weight distribution of faceted HPHT-grown diamonds. The majority of the larger HPHT-grown diamonds were in the less-mar-

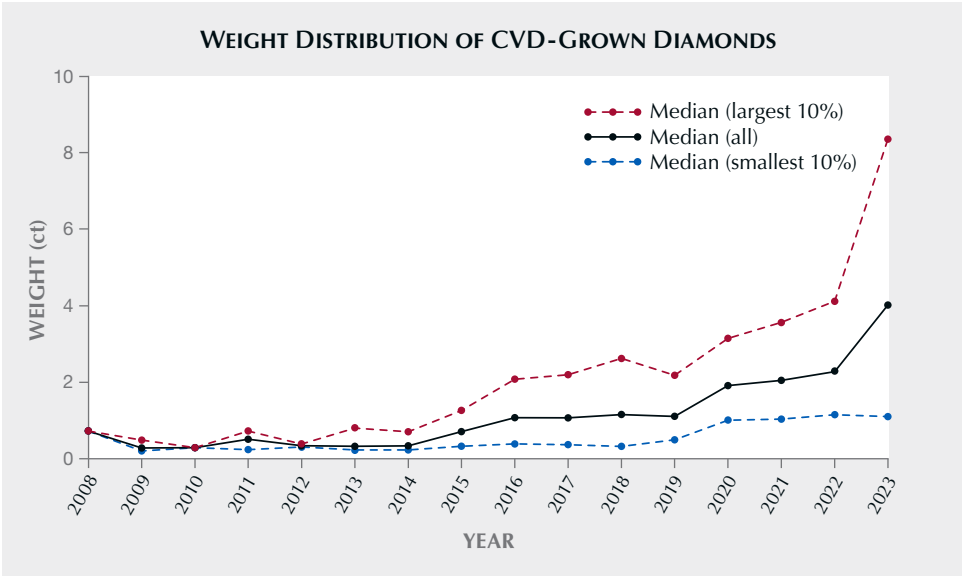

Figure 4. The weight distribution of CVD-grown diamonds submitted to GIA, 2008–2023. The trend lines show an increase in median values for three weight categories: the smallest 10% each year (bottom), all diamonds submitted each year (middle), and the largest 10% each year (top). Updated from Eaton-Magaña and Shigley (2016).

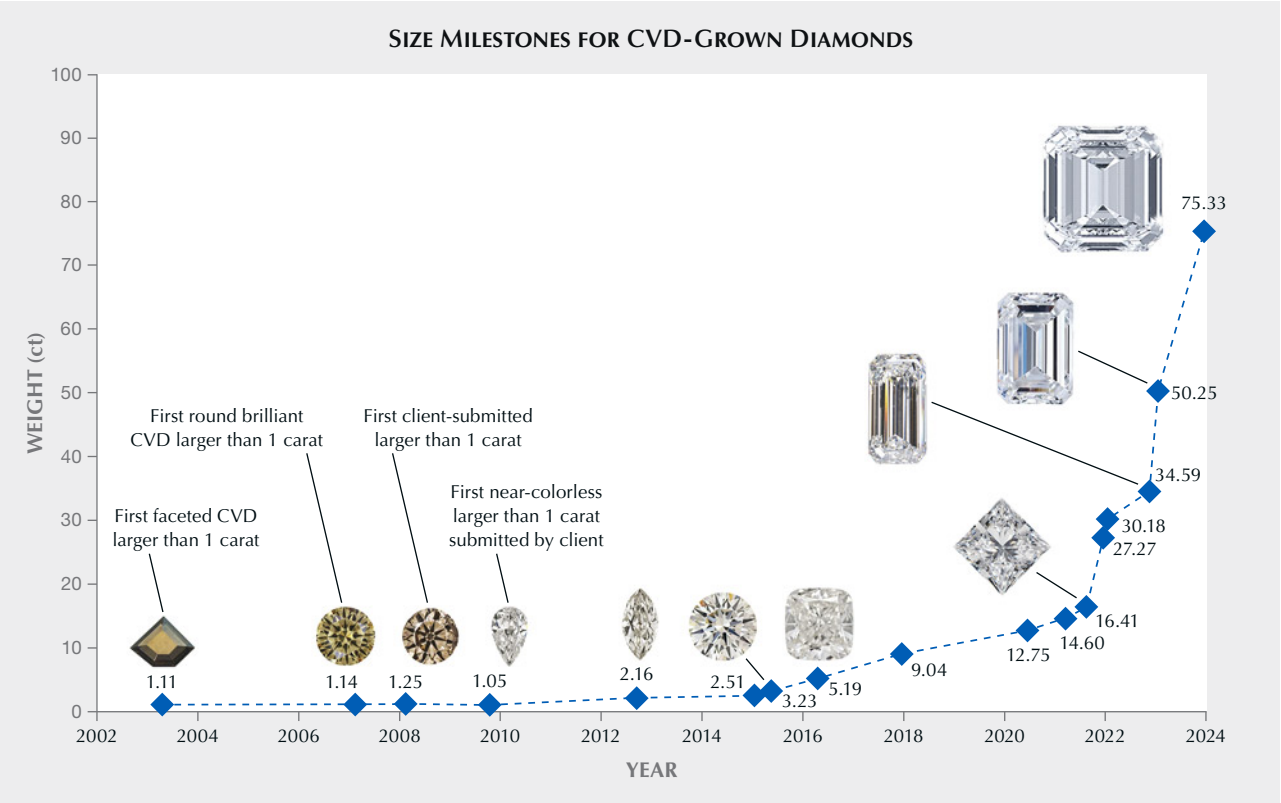

Figure 5. Size milestones over the past two decades for CVD-grown diamonds. The current record holder is a 75.33 ct emerald cut announced in May 2024. Updated from Eaton-Magaña and Shigley (2016).

ketable yellow-orange color range. The growth of large, colorless HPHT-grown diamonds with high purity is particularly challenging, as it requires complex ingredient and recipe development to minimize nitrogen incorporation, as well as the ability to carefully control conditions over extended periods (D'Haenens-Johansson et al., 2022). Nitrogen has a catalytic effect on diamond growth, so its absence re-

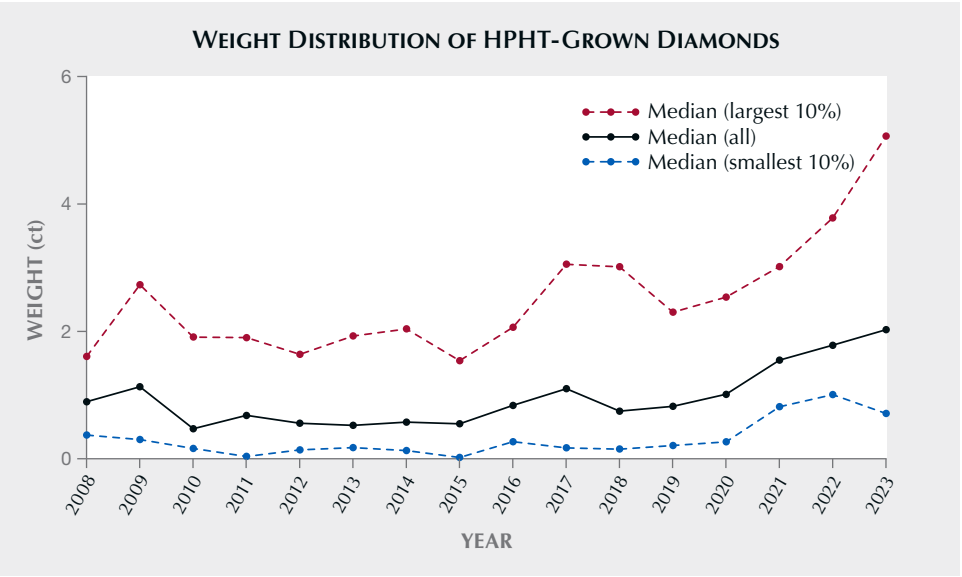

Figure 6. The annual weight distribution of HPHT-grown diamonds submitted to GIA, 2008–2023. The trend lines show the change in median values for three weight categories: the smallest 10% each year (bottom), all diamonds submitted that year (middle), and the largest 10% each year (top). Updated from Eaton-Magaña et al. (2017).

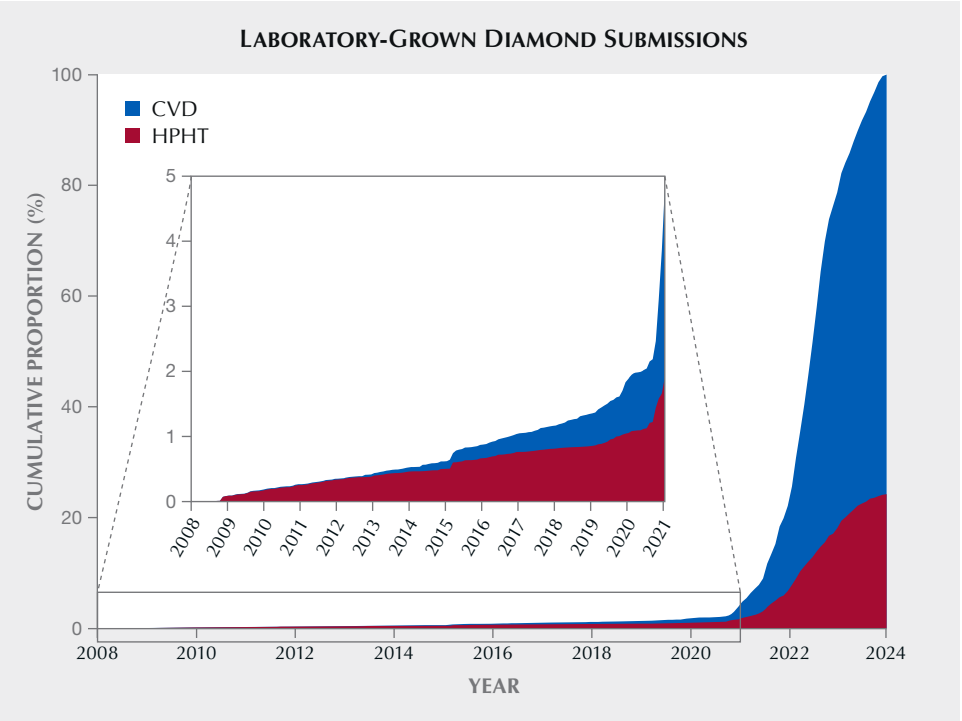

Figure 7. The cumulative increase in laboratory-grown diamond submissions, 2008–2023. Most of the submissions have been in the last few years, marked by a dramatic rise in CVD-grown diamonds. For the years 2008–2021 (inset), the vast majority of submitted stones were HPHT-grown.

duces growth rates. Whereas CVD diamonds can be created over a series of growth steps, alleviating some process control requirements, HPHT-grown diamonds are produced in a single uninterrupted run. Since 2016, there has been a shift toward colorless material (figure 3) and an increase in size, with the majority exceeding 2 ct (figure 6).

Figure 7 shows the cumulative submissions of HPHT- and CVD-grown diamonds to GIA since 2007, when GIA began receiving them. This figure indicates that the vast majority of both HPHT- and CVD-grown diamond submissions have been since 2021. Initially, most of these were created using the HPHT method. Over the ensuing years, however, the CVD population consistently increased and eventually outnumbered HPHT-grown submissions by around 2016. At present, GIA averages more CVD-grown diamond submissions per day than it once did during an entire year.

Some CVD-grown diamonds have a brown coloration after growth, associated with the presence of vacancy clusters and/or nitrogen-related defects (Barnes et al., 2006; Jones et al., 2007; Mäki et al., 2007; Khan et al., 2013; Zaitsev et al., 2020, 2021). As with natural brown diamonds (e.g., Fisher et al., 2009), CVD-grown diamonds can be enhanced using HPHT treatments to reduce or remove the brown coloration (Wang et al., 2003, 2012; Charles et al., 2004; Mäki et al., 2007). Although similar equipment can be used for HPHT treatment and HPHT growth, it is important to note that the underlying methods are distinct. Furthermore, HPHT treatments are conducted at higher temperatures than those used for HPHT growth (>1600°C) and do not result in the synthesis of additional diamond material. Low-pressure, high-temperature (LPHT) treatment, in which samples are annealed at similarly high temperatures under vacuum or an inert gas, can also be used to change the color of CVD-grown diamonds (Meng et al., 2008; Liang et al., 2009; Johnson et al., 2023). Manufacturers of CVD products can thus use recipes that promote rapid growth of diamond layers, even if it results in a brown coloration, and subsequently improve the color grade through post-growth annealing. This approach may be faster, easier, or more cost-effective than directly producing a colorless diamond using CVD. Over time, there has been a consistent increase in the percentage of CVD-grown diamonds exhibiting signs of annealing treatment (Eaton-Magaña et al., 2021b). Since 2020, approximately 80% of the CVD diamonds submitted to GIA have undergone post-growth processing.

IDENTIFICATION AND MELEE DIAMONDS

The gem trade has been facing challenges in identifying laboratory-grown diamonds due to the rapid increase in production as well as mixing (both accidental and intentional) with natural diamonds.

While HPHT and CVD growth processes have been refined, many of the gemological criteria and strategies have remained consistent. Prior publications have documented the detailed gemological characteristics of HPHT- and CVD-grown diamonds (e.g., Eaton-Magaña and Shigley, 2016; Eaton-Magaña et al., 2017; D'Haenens-Johansson et al., 2022), and the reader is referred to those review articles for details on gemological characteristics. The conclusive identification of a laboratory-grown origin typically requires a combination of gemological features, yet simple visual inspection can still be valuable. For instance, a "LABORATORY-GROWN" inscription or manufacturer-specific marking to support transparency and traceability is commonly found on the girdle of commercial-size products.

Although certain gemological features strongly suggest a laboratory-grown origin, there are exceptions due to the wide range of growth recipes and treatments. Phosphorescence—the emission of light from a sample after exposure to UV—is often used as a key indicator for colorless and near-colorless HPHT-grown diamonds, which generally exhibit intense, long-lived blue-green phosphorescence. Only a few natural type IIb diamonds and some CVD-grown diamonds exhibit a comparable reaction. However, low-dose irradiation can reduce or eliminate the phosphorescence response in HPHT-grown diamonds, as initially reported by Robinson (2018) and confirmed by subsequent experiments (e.g., figure 8 and Gao et al., 2021). Relying on a phosphorescence observation or any other single gemological observation in testing colorless HPHT-grown diamonds is not advisable.

Melee Diamonds. Identifying melee-size diamonds as laboratory-grown presents a particular challenge. Due to their small size, they are difficult to handle and not suited for testing using certain laboratory instruments; they also require higher magnification for detailed microscopic inspection and often lack markings from a manufacturer or gemological laboratory (Choi et al., 2020). A tiny melee stone can take two to three times longer to analyze than a half-carat diamond. Most melee-size laboratory-grown diamonds come from manufacturers in China, where the HPHT growth method is preferred for growing small diamonds economically, allowing the simultaneous production of thousands of nearly colorless diamonds using microscopic seed crystals.

Given the small size and abundance of melee, screening instruments are particularly important in analyzing them. But because there are significant dif-

Figure 8. These ~0.4 ct HPHT-grown diamonds remained colorless after low-dose laboratory irradiation. Prior to irradiation, these samples displayed observable phosphorescence to deep UV. Images by Diego Sanchez (top) and Sally Eaton-Magaña (middle and bottom).

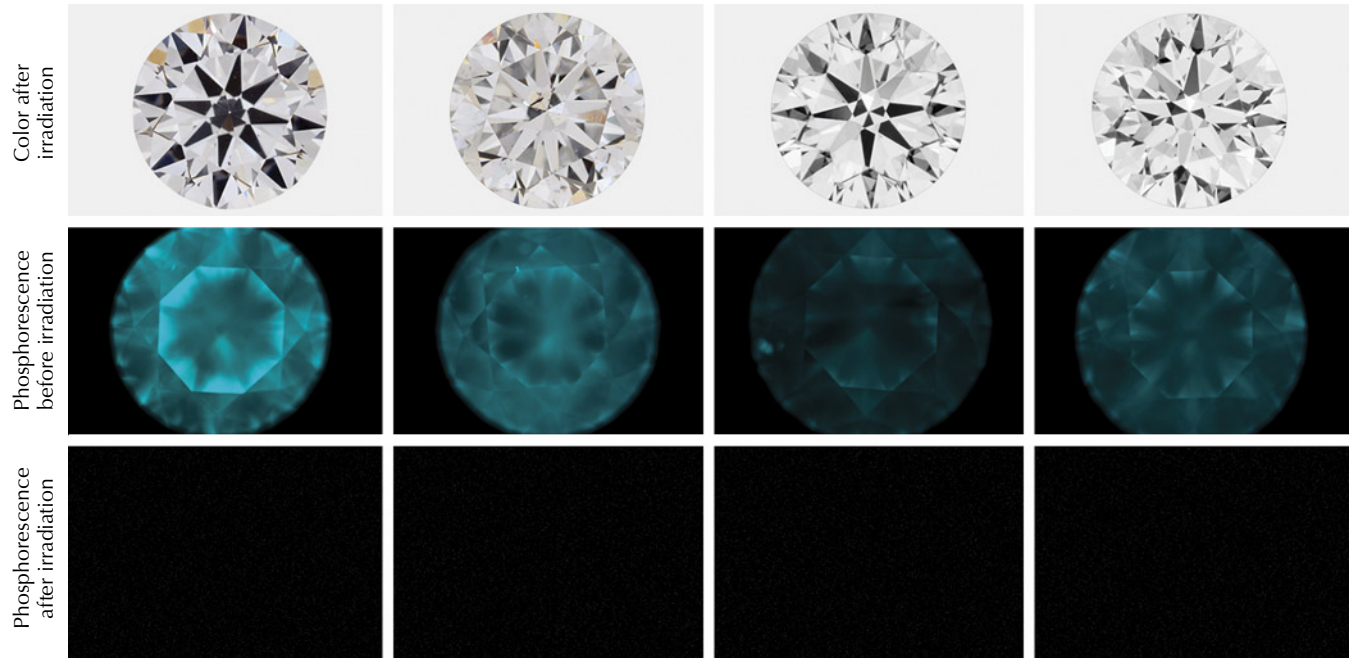

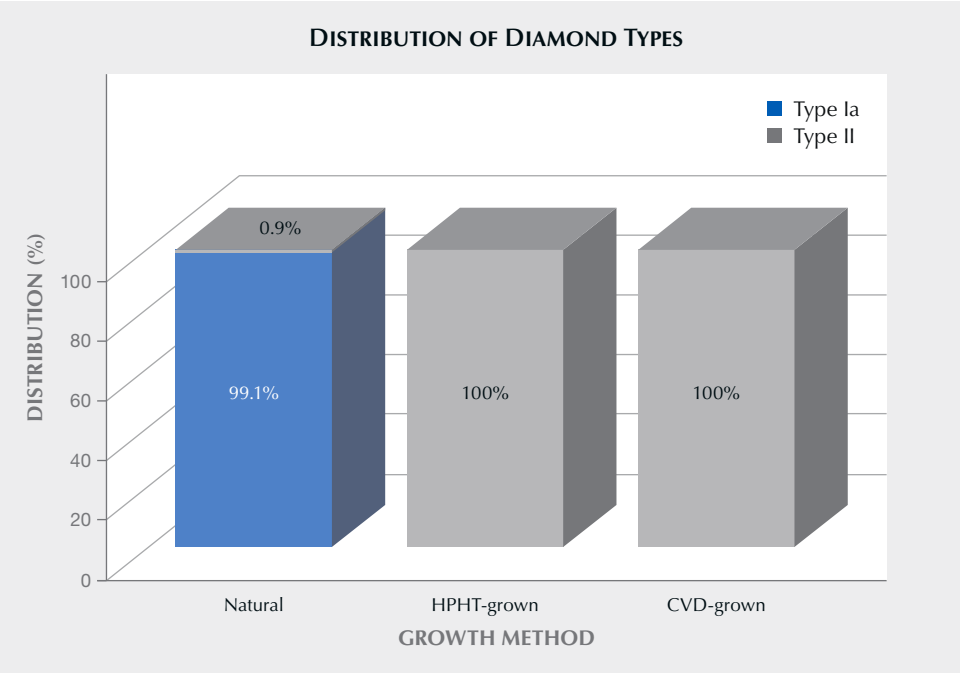

Figure 9. Distribution of diamond types (type Ia and type II) among colorless to near-colorless diamonds. Adapted from Eaton-Magaña et al. (2020).

ferences between HPHT and CVD growth methods, as well as various types of post-growth treatment, there is no cost-effective or rapid screening tool that can definitively identify all laboratory-grown diamonds. Instead, the majority of screening tools available in the consumer market provide a "pass" or "refer" result for colorless to near-colorless diamonds (Tsai and D'Haenens-Johansson, 2019), with "pass" indicating the test sample is natural. Diamonds that produce a "refer" result may be natural or laboratory-grown. These require further testing for conclusive identification, which involves a combination of gemological techniques or examination by a laboratory (e.g., D'Haenens-Johansson et al., 2022). Depending on the method of testing, some screening devices may not be able to refer simulants, incorrectly passing them as natural. Users must understand a screening instrument's scope and limitations (e.g., color range, size, and simulants). The Natural Diamond Council reports on independent testing of popular screening equipment under the ASSURE program (Natural Diamond Council, 2023).

Many screening approaches for colorless or near-colorless diamonds are based on the diamond's type. Diamond type, as described by Breeding and Shigley (2009), is a valuable classification for scientific analysis. To summarize briefly, a type II diamond contains no nitrogen detectable by infrared (IR) spectroscopy, while a type Ia diamond shows the presence of aggregated nitrogen. Figure 9 illustrates the clear differences between natural type Ia and laboratory-grown type II diamond populations. The overwhelming majority of natural diamonds in the D to N range are type Ia, while all colorless laboratory-grown diamonds are type II. This distinction provides a solid basis for various screening approaches and an efficient first step in the identification process. However, there are some caveats to advanced testing, which will be discussed in the next section.

ADVANCED TESTING CHALLENGES AND NEW TECHNIQUES

CVD-grown diamonds often have distinctive gemological and spectroscopic features that make their identification straightforward using the tools available in a gemological laboratory (e.g., Eaton-Magaña and Shigley, 2016; D'Haenens-Johansson et al., 2022). This section will discuss some of the current challenges with advanced testing, as well as additional spectroscopic and imaging instrumentation used.

The spectroscopic characteristics of laboratory-grown diamonds, especially the defects identified through photoluminescence (PL) spectroscopy, have been thoroughly documented (Wang et al., 2012; D'Haenens-Johansson et al., 2014, 2022; Eaton-Magaña and Shigley, 2016).

The silicon vacancy (SiV^-) peak at 736.6/736.9 nm has long been a consistent indicator of CVD-grown diamonds. Silicon incorporation is often caused by

accidental doping due to silicon-containing components such as quartz windows in the reactor chamber. However, silicon-related defects are also detected occasionally in natural diamonds (Breeding and Wang, 2008; Lai et al., 2020). Furthermore, an increasing number of CVD-grown diamonds do not exhibit detectable SiV^- peaks in their PL spectra. In recent years, the GIA laboratory has noticed a higher percentage of CVD-grown diamonds that have only a very weak or undetectable SiV^- feature in the PL spectra. Through the years, there has been a pronounced decrease in SiV^- intensity when detected (figure 10A). In the future, the absence of a detectable SiV^- peak could become more common in CVD-grown diamonds, reducing its value as a diagnostic feature.

Similarly, the fluorescence of CVD-grown diamonds when excited by deep UV using the DiamondView instrument (excitation wavelength <225 nm; Welbourn et al., 1996) is often very distinctive and recognizable. Growth layering, corresponding to defects at growth interfaces, is commonly visible when a diamond is exposed to deep UV (e.g., figure 11, top left). Recently, however, we have seen some examples of CVD-grown diamond that do not exhibit traditional features and patterns (e.g., Eaton-Magaña

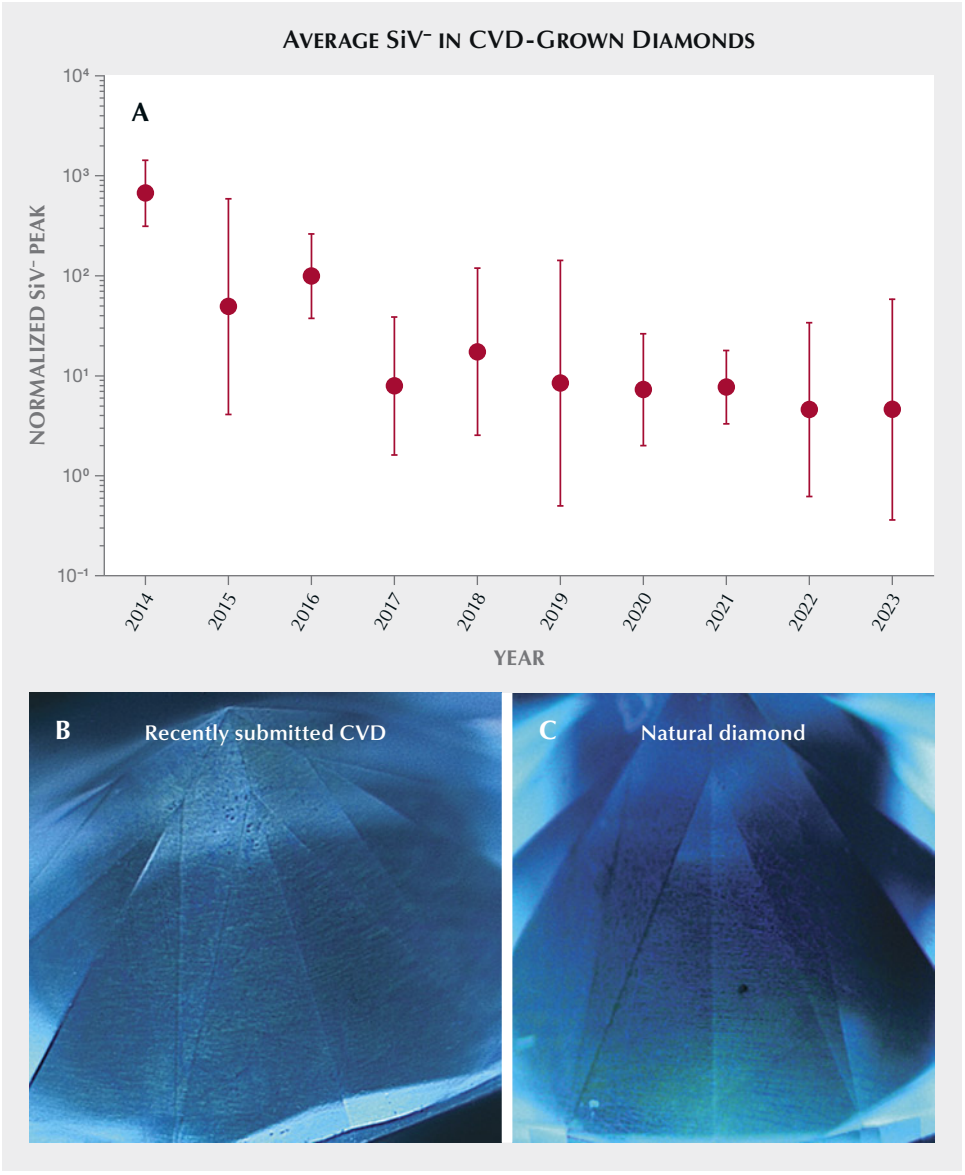

Figure 10. A: This semi-logarithmic plot shows the decrease in SiV^- intensity among available CVD-grown diamonds examined by year using 514 nm excitation; over the ten-year period shown here, the average SiV^- concentration decreased by two orders of magnitude. The peak area of the silicon doublet at 736.6/736.9 nm is normalized to the unsaturated diamond Raman line and then averaged for each year; the error bars correspond to the standard deviation. Although the SiV^- feature is often listed as a reliable indicator of CVD growth, it is not observed in all such stones. B: This 2.22 ct G-color marquise proved to be a CVD-grown diamond with post-growth HPHT treatment, based on spectroscopy and imaging. However, the deep-UV fluorescence image appears nominally similar to deep-UV fluorescence images often seen in natural diamonds (C).

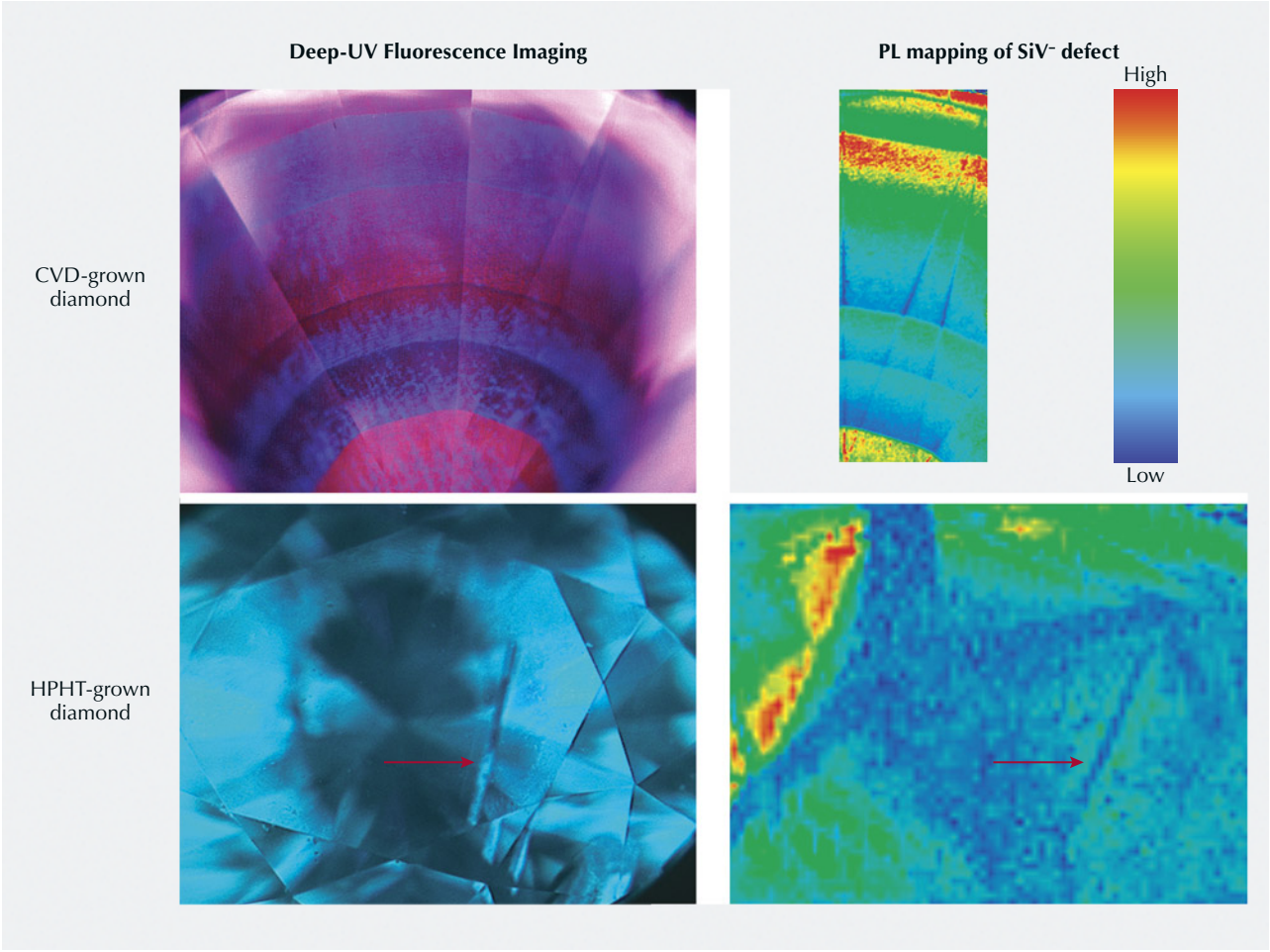

Figure 11. Top: The DiamondView's deep-UV fluorescence imaging of a 2.02 ct near-colorless as-grown CVD diamond is presented along with the results for PL mapping of the pavilion facets using 532 nm excitation and submersion in liquid nitrogen. This sample shows multiple growth layers, with the highest concentrations of SiV^- near the growth interfaces. Bottom: A 0.50 ct D-color HPHT-grown diamond shows different growth sectors through deep-UV fluorescence imaging and PL mapping using 633 nm excitation and liquid nitrogen. The SiV^- concentration is confined to the {111} growth sectors. A metallic rod inclusion is visible in the deep-UV image, and its presence is also displayed in the PL map as an area of lower SiV^- concentration (red arrow in both images).

and Shigley, 2016; D'Haenens-Johansson et al., 2022). Instead, they display a fluorescence that closely resembles what we often see in type II natural diamonds (figure 10, B and C). The ambiguity of deep-UV fluorescence patterns occasionally requires the use of more specialized imaging technologies such as cathodoluminescence (CL) imaging. While CL imaging is not commonly applied even at gemological laboratories, it has successfully revealed growth features diagnostic of CVD growth that were not reliably identified with deep-UV imaging alone (figure 12).

Recently, several new analytical techniques have emerged. Photoluminescence mapping enables the rapid collection of PL spectra across a diamond's surface, generating a map of PL intensities (Eaton-Magaña et al., 2021a). This method can automatically collect thousands of spectra *in situ* for a crystal in less than 10 minutes while the stone is held at liquid nitrogen temperature (–196°C). The size of each pixel in the collected spectrum can be as small as a few microns, enabling the determination of PL spectra and diamond defects at the micron scale.

For example, silicon-related defects are commonly introduced in CVD-grown diamonds by plasma etching of reactor components (Robins et al., 1989; Barjon et al., 2005). The negatively charged SiV^- defects emitting at 737 nm can be easily detected by PL, and their distribution can reveal changes in growth conditions. In a CVD-grown diamond produced using a series of

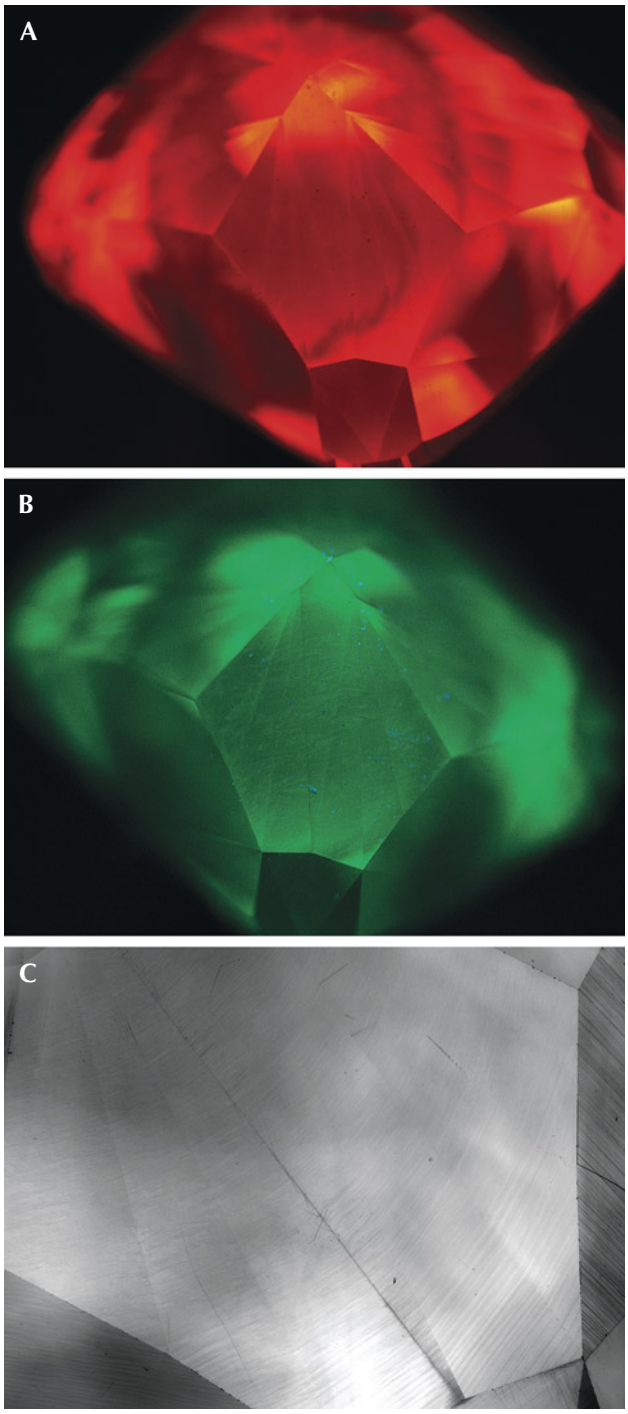

Figure 12. A: A deep-UV fluorescence image of a 1.83 ct treated CVD-grown diamond with a Fancy Intense orangy pink color. The red fluorescence is due to high concentrations of NV centers. B: A deep-UV fluorescence image with a short-pass filter eliminates the red fluorescence so that underlying fluorescence colors, and often additional details, can be revealed. While the very strong NV-related fluorescence is filtered out and glows green due to H3 fluorescence, diagnostic growth features are not distinguishable. C: A CL image shows the striations that were not displayed by fluorescence imaging. Strong fluorescence can sometimes obscure CVD-specific features, and CL is occasionally needed to unambiguously identify the diamond.

growth steps, these interruptions lead to distinct spatial differences in SiV^- concentration (figure 11, top) that reflect the layered growth of CVD diamonds. These variations may be more pronounced than for other commonly observed defects such as nitrogen vacancy (NV) centers.

PL mapping can also reveal the distinctive cuboctahedral growth pattern in HPHT-grown diamonds, in which SiV^- defects are confined to the octahedral {111} growth sectors. PL mapping of various other defects in both CVD- and HPHT-grown diamonds has also been reported (e.g., Loudin, 2017; Eaton-Magaña et al., 2021a). Given the heterogeneity of defects in the diamond lattice for some stones, PL mapping offers advantages over single-point analyses using traditional, non-mapping PL spectroscopy. PL mapping can show the impurity distribution and growth pattern and, with thousands of spectra collected, increases the probability of defect detection compared to a single-point PL spectrum.

Despite the changes in laboratory growth processes and post-growth treatments over time, the combination of distinguishing features can still confirm a diamond's natural or synthetic origin. This reinforces the importance of not relying on only one gemological or spectroscopic feature. Instead, it is essential to evaluate a range of characteristics.

UNCONVENTIONAL LABORATORY-GROWN DIAMONDS

With the influx of laboratory-grown diamonds submitted to gemological laboratories in recent years, we have been able to observe a subset of products that are atypical. Many of these appear to be experimental prototypes created by a combination of novel growth and/or post-growth treatment methods made possible by readily available and inexpensive laboratory-grown material. We have collected several examples of uncommon laboratory-grown diamonds submitted to GIA, some of which may become more prevalent in the future.

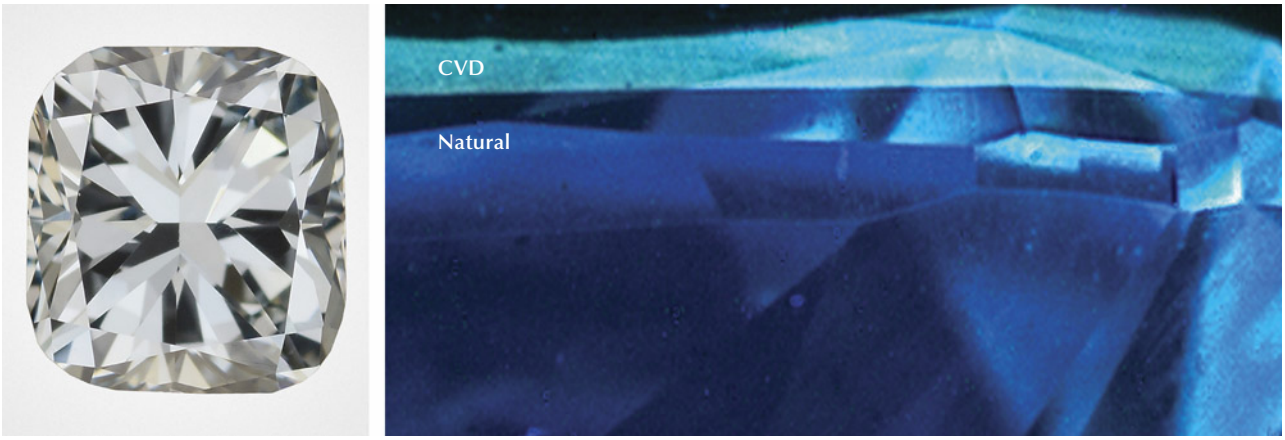

Figure 13. Left: This 0.64 ct Fancy grayish greenish blue stone proved to be a hybrid. Photo by Robison McMurtry. Right: The majority of the sample is natural type Ia diamond, causing a deep blue fluorescence, but boron in the CVD overgrowth layer creates its greenish blue fluorescence.

CVD Overgrowth on Natural Diamonds. In 2017, GIA encountered the first client-submitted CVD overgrowth on a natural faceted gem diamond (also called a "hybrid") (Moe et al., 2017; see figure 13, left). With these hybrids, the manufacturer places a natural diamond in the CVD reactor as the seed plate rather than a CVD-grown or HPHT-grown diamond, which is standard for the CVD process. Both the seed and the overgrowth layer are retained in the faceted gem. CVD overgrowth diamonds are generally designed to add weight or produce a different color. The overgrowth described in Tang et al. (2018) successfully increased the weight of the original diamond such that the 0.11 ct finished gem hybrid diamond was 64% CVD-grown. Other hybrid diamonds reported were generated with the intent to achieve a fancy blue color (Fritsch and Phelps, 1993; Moe et al., 2017; Ardon and McElhenny, 2019).

The CVD overgrowth layer has a limited thickness when deposited on a faceted natural diamond. In order to reduce non-diamond carbon formation during the CVD process, seed plates are often cut within 2° of the cubic {100} direction (Berdermann et al., 2004). The faceted diamond surfaces would deviate significantly from the desired {100} direction, limiting the potential thickness of a deposited CVD layer. Only a small amount of weight can be added, and the table facet is the most likely growth face for these cases of CVD overgrowth (Tang et al., 2018).

To achieve a blue color with a boron-doped CVD diamond overgrowth, only a thin film (<0.1 mm) is needed to significantly influence the stone's color. The deep-UV fluorescence image in figure 13 (right) shows a marked color change at the interface between the natural diamond substrate and the CVD overgrowth layers, resulting in a Fancy grayish greenish blue color (Ardon and McElhenny, 2019). Only a small number of these CVD overgrowth diamonds have been documented by gemological labs. Although their identification is straightforward, it is worth noting that some hybrid diamonds may go undetected by standard screening equipment if the underlying natural diamond is type Ia, as many screening instruments are based (either directly or indirectly) on differences between type Ia and type II diamond (figure 9). Kitawaki et al. (2023) produced hybrid diamonds by growing colorless CVD diamond on top of natural colorless type Ia diamonds. As expected, these hybrid diamonds passed standard screening tests using UV transparency, N3 defect detection, and bulk Fourier-transform infrared (FTIR) measurement. However, deep-UV imaging and PL spectroscopy identified them as natural diamonds with a CVD diamond layer. Growing colorless CVD diamond on natural type Ia diamond substrates requires precise control of the temperature around the natural diamond used as a substrate, and its application currently offers little economic advantage.

Color Changes in CVD-Grown Diamonds. Advances in laboratory growth techniques have enabled manufacturers to produce unique diamond products for which there is no known natural equivalent. In some photochromic diamonds, for example, defect concentrations and thus color can be temporarily modified by exposure to certain lighting conditions. CVD-grown diamonds that have been deliberately doped with high levels of silicon may show an interesting photochromic effect. The doping typically results in a prominent absorption peak at 737 nm caused by the

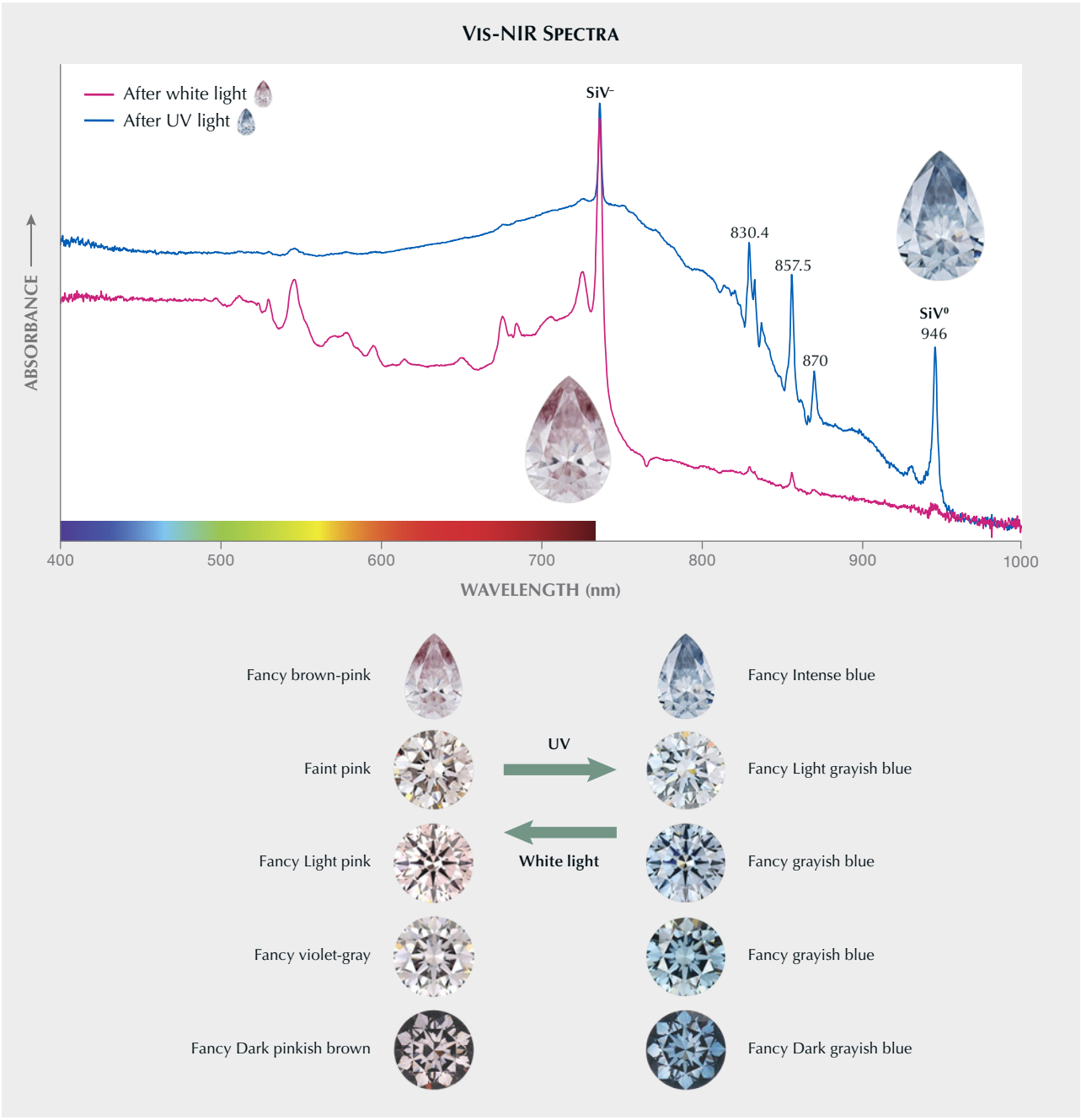

Figure 14. Top: This 0.65 ct CVD-grown diamond has a stable color of Fancy brown-pink but converts to a Fancy Intense blue with deep-UV excitation. The visible/near-infrared (Vis-NIR) absorption spectrum for the stable brown-pink color shows a dramatic but temporary shift with a decrease in the SiV^- centers at 737 nm and an increase in SiV^0 at 946 nm. (D'Haenens-Johansson et al., 2015b). Bottom: Additional examples of photochromism seen in other high-silicon CVD-grown diamonds.

SiV^- defect. These diamonds may have a gray or pinkish brown to pink appearance when observed in ambient lighting conditions. With UV excitation, however, the concentration of the neutrally charged defect counterpart (SiV^0, with absorption at 946 nm) increases due to charge transfer from SiV^- centers, resulting in a more bluish color (figure 14; D'Haenens-Johansson et al., 2015b; Breeze et al., 2020). This color change is temporary, and the diamond will revert to its original stable color when exposed to white light.

Because the unstable blue color in CVD-grown diamonds can potentially revert to a stable pinkish brown or gray color, it is important to confirm the color stability of blue or gray CVD-grown diamonds by exposing them to white light for at least 30 minutes during testing. Such diamonds can also change color when heated (e.g., 550°C for 20 minutes in the dark; Breeze et al., 2020). Heating causes electron donors to convert SiV^- into SiV^{2-}, which does not absorb light (Breeze et al., 2020). The application of heat can cause the pinkish brown or gray diamond to appear colorless—this change is also temporary, and the diamond will revert to its stable color as it cools and is exposed to white light.

An additional form of reversible color change can be produced in CVD-grown diamonds, unrelated to silicon defects. Exposing some CVD-grown diamonds to UV radiation can cause the bodycolor to darken, while heating to temperatures above 450°C can decrease a stone's color saturation (Khan et al., 2010). These color changes are only temporary and fully reversible, though the unstable color can be maintained if the stone is kept in the dark or inside opaque stone papers. Khan et al. (2009) attributed the color change in these diamonds to electron transfer from isolated nitrogen atoms to electron acceptor defects such as NVH^0. NVH^0 is a defect that exhibits IR absorption at 3123 cm^{-1} and can be detected in some as-grown CVD diamonds. Similar to the $SiV^- \leftrightarrow SiV^0$ color change, the original color can be fully restored using white light.

Although there have been some concerns in the trade (Bates, 2019), all photochromic and thermochromic color changes observed in laboratory-grown diamonds submitted to GIA have been temporary and fully reversible, without any permanent or long-term color changes. Furthermore, analysis of CVD-grown diamonds that were submitted multiple times showed no significant or systematic change in color grade, even with stones that were submitted to the GIA laboratory at intervals of several months to a few years.

Unusual Fancy-Color Diamonds. Due to their vastly different growth conditions and chemistries, laboratory-grown diamonds can have unique colors. In HPHT-grown diamond, doping with high amounts of nickel produces an attractive green coloration that is quite distinct from the greenish appearance created by post-growth irradiation. By incorporating large amounts of nickel in the diamond lattice, an absorption band develops in the red portion of the visible spectrum, centered at about 685 nm, thus forming a transmission window in the green portion of the spectrum. To date, only a few HPHT-grown diamonds with saturated green coloration have been submitted to GIA (figure 15, left; Johnson and Myagkaya, 2017), along with a few dozen having Faint to Fancy Light green bodycolor due to high amounts of nickel defects (e.g., Eaton-Magaña, 2019). Some natural diamonds also have a greenish color caused by nickel impurities (Breeding et al., 2018), though generally at far lower concentrations than what is possible in laboratory-created versions, and they often have nitrogen-related defects that create a green-yellow color instead.

In HPHT-grown diamond, distinctive color zoning can occur as a result of growth sectoring (Howell et al., 2019). These growth sectors are detected in most HPHT-grown diamonds under deep-UV imag-

Figure 15. Left: A 0.42 ct Fancy Deep green HPHT-grown diamond that owes its color to high amounts of nickel doping (Johnson and Myagkaya, 2017). Right: A 2.20 ct Fancy Deep brownish orange treated HPHT-grown diamond with different defect concentrations created in the various growth sectors. Photos by Jian Xin (Jae) Liao (left) and Diego Sanchez (right).

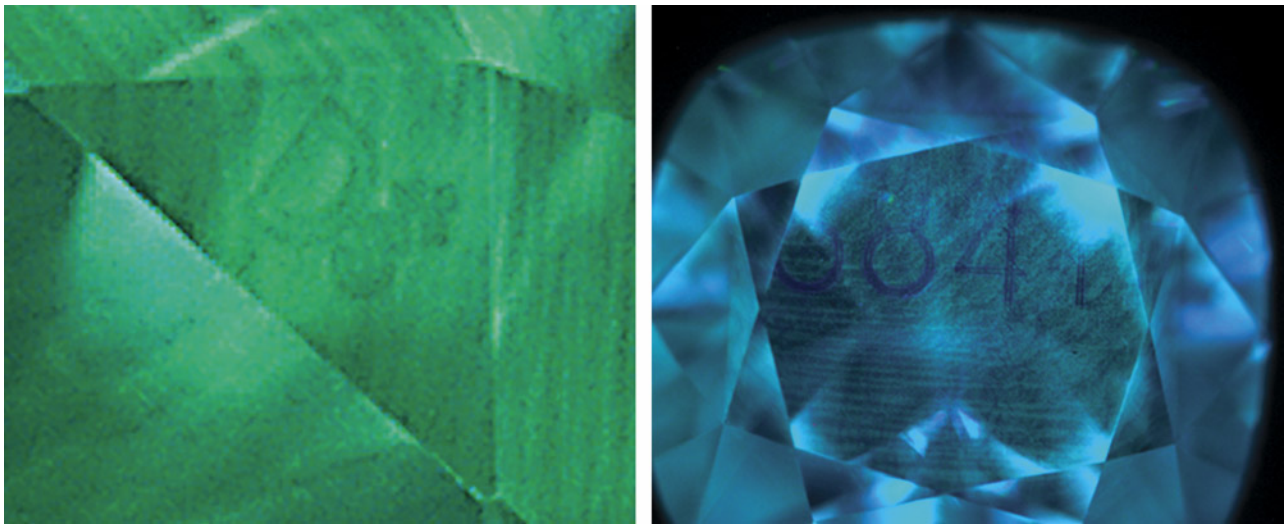

Figure 16. Left: This 0.60 ct I-color CVD-grown diamond shows a logo mark on the star facet that is only visible with fluorescence imaging. Right: The DiamondView image of a 1.93 ct F-color CVD-grown diamond shows numbers on the table facet. Images by Jemini Sawant.

ing due to the various concentrations of defects incorporated into each sector (Shigley et al., 2004). In some HPHT-grown diamonds, the defect concentrations are high enough and distinct enough between the growth sectors to create dramatic color zoning (e.g., figure 15, right; Eaton-Magaña and Linzmeyer, 2023). Another recent example is a 4.32 ct HPHT-grown diamond with pronounced blue and yellow color zones (due to boron and single nitrogen, respectively) that are visible face-up; these colors were intended to evoke the Ukrainian flag (Jeffay, 2023).

CVD-Grown Diamonds with Invisible Markings. A small subset of laboratory-grown diamond submissions have distinctive features that are only revealed using deep-UV excitation. Two CVD-grown diamonds—0.60 ct and 1.93 ct, both enhanced by HPHT treatment—had no identifying patterns when observed visually or with the microscope. When exposed to deep UV, however, logo marks and numbers appeared (figure 16; Odake and Kadam, 2023). These markings were not visible on the 1.93 ct sample when PL mapped with 455, 532, 633, or 830 nm laser. The different font styles and marking positions suggest that these two examples were produced by different methods. Although the method of creating these markings is unknown, they were likely intended as a tracking and security measure.

HPHT-Grown Diamonds with Strain. In general, colorless and near-colorless HPHT-grown diamonds have low impurity concentrations and uniform pressure is applied during growth, resulting in high crystalline perfection and very weak or almost no strain levels, except around inclusions and cracks (D'Haenens-Johansson et al., 2022). Though rare, HPHT-grown diamonds with strain have been previously reported (Ardon and Batin, 2016). Recently, the GIA laboratory received five stones showing two unusual features for HPHT-grown diamonds: a GR1 defect [V^0] detected by PL spectroscopy, as well as the presence of strain (indicated by anomalous birefringence when examining the diamond through crossed polarizers; figure 17). GR1 defects are not usually detected in HPHT-grown colorless diamonds submitted to GIA laboratories. Analysis of the GR1 distribution using PL mapping in these strained HPHT-grown diamonds shows that the defect is limited to the {110} sector (figure 17C), consistent with previous reports (Loudin, 2017). Although this feature is currently rare, it is likely that these stones were distorted during synthesis, introducing the strain, and that GR1 was created by subsequent irradiation treatment.

CONCLUSIONS

With the advancement of CVD and HPHT growth processes, gem-quality laboratory-grown diamonds have become a significant part of the global gem trade. The rapid evolution of both HPHT and CVD diamond growth is driven by manufacturers' efforts to develop innovative new products for both engineering applications and gem purposes. As manufacturers refine their growth methods, they can better tailor these products to satisfy consumer tastes and

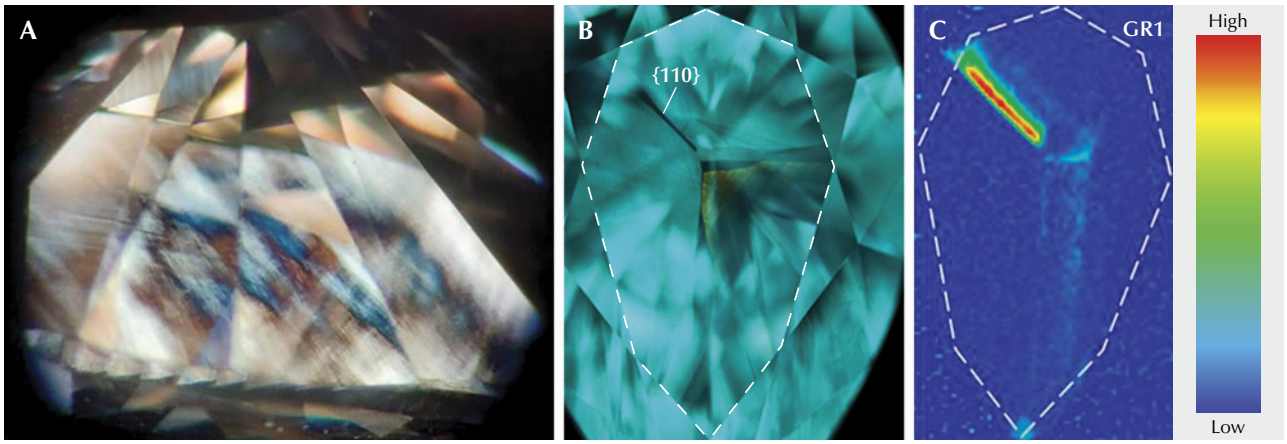

Figure 17. A: Unlike most HPHT-grown diamonds, this 1.60 ct D-color pear shows the presence of strain and anomalous birefringence when viewed through crossed polarizers. B: The deep-UV fluorescence image shows a common fluorescence color for colorless HPHT-grown diamonds. The various growth sectors are indicated. C: PL mapping of the peak area for the GR1 center using 633 nm excitation indicates it is largely limited to the {110} growth sector.

create niche products. In the coming years, we expect that most products will be in the colorless range and increasingly larger (e.g., figure 18). With the additional supply, we will likely see a greater variety of stones with a range of colors.

If the submissions to GIA are an accurate representation of the products on the market (excluding melee diamonds), then the data in this study indicates that the market for laboratory-grown diamonds has shifted dramatically toward colorless and near-colorless products (figures 2 and 3). There are a few exceptions, such as the fancy-color laboratory-grown diamonds treated by some producers (Bates, 2021).

Based on current trends, the quantity of HPHT-grown diamonds is expected to increase most significantly at the extreme ends of the weight scale: both small melee-sized stones and larger samples exceeding 4 ct. CVD-grown diamonds are being submitted at commercial sizes (i.e., non-melee) in far greater quantities than their HPHT-grown counterparts, and this trend is expected to continue.

Many manufacturers worldwide have committed significant capital investment toward their laboratory-grown diamond facilities (Lu et al., 2019; De-

Figure 18. Large laboratory-grown diamonds such as these CVD-grown diamonds have become increasingly common the last few years. From left: a 12.06 ct G-color, VS_2 emerald cut; an 11.36 ct E-color, SI_1 round brilliant; a 10.42 ct G-color, VS_2 heart brilliant; a 10.19 ct F-color, VS_2 emerald cut; and a 9.52 ct E-color, VS_2 oval brilliant. Photos by Gaurav Bera.

Marco, 2020) and developed marketing efforts promoting these stones as a readily available or environmentally friendly commodity (e.g., Lu et al., 2019; Bates, 2021). Although beyond the scope of this article, there are indications that in recent years laboratory-grown diamonds have begun to complement and, in some cases, replace sectors of the natural diamond market (Bates, 2023), especially as their prices have fallen. The long-term impact of laboratory-grown diamonds on the industry will continue to be assessed in the coming years.

This article has summarized many of the developments in laboratory-grown diamond production, based on submissions to GIA over the last two decades. Beyond providing a snapshot of the current range of products seen at GIA, this also allows us to project trends into the future as technological advances enable the controlled production of stones with specific sizes and colors. Even with the rapid progress of the past decade and ongoing developments, GIA's advanced analytical techniques, backed by decades of research, can easily identify and characterize laboratory-grown diamonds.

ABOUT THE AUTHORS

Dr. Sally Eaton-Magaña is senior manager of diamond identification, and Dr. Matthew F. Hardman is a research scientist, at GIA in Carlsbad, California. Dr. Shoko Odake is senior manager of diamond identification at GIA in Tokyo.

ACKNOWLEDGMENTS

We thank Dr. Ulrika D'Haenens-Johansson for her excellent feedback and proofreading and the peer reviewers for suggestions and comments that improved the content of this article. We also thank Elina Myagkaya for collecting the cathodoluminescence image in figure 12, Adrian Chan for his assistance with photography of CVD diamond plates, and the analytic technicians who collect the spectroscopic data and fluorescence images daily at all of GIA's global laboratories, whose consistency, reliability, and vigilance make such studies of our GIA database possible.

REFERENCES

Angus J.C. (2014) Diamond synthesis by chemical vapor deposition: The early years. *Diamond and Related Materials*, Vol. 49, pp. 77–86, http://dx.doi.org/10.1016/j.diamond.2014.08.004

Ardon T., Batin R. (2016) Lab Notes: HPHT-grown synthetic diamond with strain. *G&G*, Vol. 52, No. 4, pp. 417–418.

Ardon T., Eaton-Magaña S. (2014) Lab Notes: Two Fancy Dark gray CVD synthetic diamonds. *G&G*, Vol. 50, No. 3, pp. 239–240.

Ardon T., McElhenny G. (2019) Lab Notes: CVD layer grown on natural diamond. *G&G*, Vol. 55, No. 1, pp. 97–99.

Barjon J., Rzepka E., Jomard F., Laroche J.-M., Ballutaud D., Kociniewski T., Chevallier J. (2005) Silicon incorporation in CVD diamond layers. *Physica Status Solidi (a)*, Vol. 202, No. 11, pp. 2177–2181, http://dx.doi.org/10.1002/pssa.200561920

Barnes R., Bangert U., Martineau P. (2006) HR-TEM imaging and image simulation of vacancy clusters in brown diamond. *Physica Status Solidi (a)*, Vol. 203, No. 12, pp. 3081–3087, http://dx.doi.org/10.1002/pssa.200671111

Bates R. (2019) Why a few lab-grown diamonds temporarily change color. *JCK Online*, December 13, https://www.jckonline.com/editorial-article/lab-grown-diamonds-change-color

——— (2021) Lightbox to offer bigger, better diamonds. *JCK Online*, August 19, https://www.jckonline.com/editorial-article/lightbox-bigger-better-diamonds

——— (2023) Lightbox now selling lab-grown diamond engagement rings. *JCK Online*, June 16, https://www.jckonline.com/editorial-article/lightbox-lab-grown-engagement

Berdermann E., Ciobanu M., Hartmann W., Martemiyanov A., Moritz P., Pomorski M., Rebisz M., Voss B., Darmstadt G. (2004) Characterisation of single-crystal CVD-diamond detectors. https://www.researchgate.net/profile/Mircea-Ciobanu/publication/264999244_Characterisation_of_Single-Crystal_CVD-Diamond_Detectors/links/53fdf1550cf2364ccc09329f/Characterisation-of-Single-Crystal-CVD-Diamond-Detectors.pdf

Breeding C.M., Wang W. (2008) Occurrence of the Si-V defect center in natural colorless gem diamonds. *Diamond and Related Materials*, Vol. 17, No. 7-10, pp. 1335–1344, http://dx.doi.org/10.1016/j.diamond.2008.01.075

Breeding C.M., Shigley J.E. (2009) The "type" classification system of diamonds and its importance in gemology. *G&G*, Vol. 45, No. 2, pp. 96–111, http://dx.doi.org/10.5741/GEMS.45.2.96

Breeding C.M., Eaton-Magaña S.C., Shigley J.E. (2018) Natural-color green diamonds: A beautiful conundrum. *G&G*, Vol. 54, No. 1, pp. 2–27, http://dx.doi.org/10.5741/GEMS.54.1.2

Breeze B.G., Meara C.J., Wu X.X., Michaels C.P., Gupta R., Diggle P.L., Dale M.W., Cann B.L., Ardon T., D'Haenens-Johansson U.F.S., et al. (2020) Doubly charged silicon vacancy center, Si-N complexes, and photochromism in N and Si codoped diamond. *Physical Review B*, Vol. 101, No. 18, article no. 184115, http://dx.doi.org/10.1103/PhysRevB.101.184115

Butler J.E., Mankelevich Y.A., Cheesman A., Ma J., Ashfold M.N.R. (2009) Understanding the chemical vapor deposition of diamond: Recent progress. *Journal of Physics: Condensed Matter*, Vol. 21, No. 36, article no. 364201, http://dx.doi.org/10.1088/0953-8984/21/36/364201

Charles S.J., Butler J.E., Feygelson B.N., Newton M.E., Carroll D.L., Steeds J.W., Darwish H., Yan C.-S., Mao H.K., Hemley R.J. (2004) Characterization of nitrogen doped chemical vapor deposited single crystal diamond before and after high pressure, high temperature annealing. *Physica Status Solidi (a)*, Vol. 201, No. 11, pp. 2473–2485, http://dx.doi.org/10.1002/pssa.200405175

Choi H., Kim Y., Lee M., Seok J. (2020) Spectroscopic analysis of near colorless/pink/blue synthetic diamonds from Lightbox. *Journal of the Korean Crystal Growth and Crystal Technology*, Vol. 30, No. 1, pp. 21–26, http://dx.doi.org/10.6111/JKCGCT.2020.30.1.021

De Wit H. (2018) Understanding diamond and its relationship with optics. *Photonics Online*, September 17, https://www.photonicsonline.com/doc/understanding-diamond-and-its-relationship-with-optics-0001

DeMarco A. (2020) De Beers' Lightbox opens $94 million lab-grown diamond facility, partners with Blue Nile. *Forbes*, October 29, https://www.forbes.com/sites/anthonydemarco/2020/10/29/

de-beers-lightbox-opens-94-million-lab-grown-diamond-facility-partners-with-blue-nile/?sh=936f54270851
D'Haenens-Johansson U.F.S., Moe K.S., Johnson P., Wong S.Y., Lu R., Wang W. (2014) Near-colorless HPHT synthetic diamonds from AOTC Group. *G&G*, Vol. 50, No. 1, pp. 30–45, http://dx.doi.org/10.5741/GEMS.50.1.30
D'Haenens-Johansson U.F.S., Katrusha A., Moe K.S., Johnson P., Wang W. (2015a) Large colorless HPHT-grown synthetic gem diamonds from New Diamond Technology, Russia. *G&G*, Vol. 51, No. 3, pp. 260–279, http://dx.doi.org/10.5741/GEMS.51.3.260
D'Haenens-Johansson U.F.S., Ardon T., Wang W. (2015b) CVD synthetic gem diamonds with high silicon-vacancy concentrations. *Conference on New Diamond and Nano Carbons*, May 2015, Shizuoka, Japan.
D'Haenens-Johansson U.F.S., Butler J.E., Katrusha A.N. (2022) Synthesis of diamonds and their identification. *Reviews in Mineralogy and Geochemistry*, Vol. 88, No. 1, pp. 689–753, http://dx.doi.org/10.2138/rmg.2022.88.13
Eaton-Magaña S. (2019) Lab Notes: Faint green HPHT synthetic diamonds. *G&G*, Vol. 55, No. 1, pp. 99–101.
Eaton-Magaña S., Breeding C.M. (2018) Features of synthetic diamonds. *G&G*, Vol. 54, No. 2, pp. 202–204, http://dx.doi.org/10.5741/GEMS.54.2.202
Eaton-Magaña S., Linzmeyer T. (2023) Lab Notes: Treated HPHT-grown diamond with dramatic color zoning. *G&G*, Vol. 59, No. 4, pp. 489–490.
Eaton-Magaña S., Shigley J.E. (2016) Observations on CVD-grown synthetic diamonds: A review. *G&G*, Vol. 52, No. 3, pp. 222–245, http://dx.doi.org/10.5741/GEMS.52.3.222
Eaton-Magaña S., Shigley J.E., Breeding C.M. (2017) Observations on HPHT-grown synthetic diamonds: A review. *G&G*, Vol. 53, No. 3, pp. 262–284, http://dx.doi.org/10.5741/GEMS.53.3.262
Eaton-Magaña S., Ardon T., Breeding C.M., Shigley J.E. (2020) Natural-color D-to-Z diamonds: A crystal-clear perspective. *G&G*, Vol. 56, No. 3, pp. 318–335, http://dx.doi.org/10.5741/GEMS.56.3.335
Eaton-Magaña S., Breeding C.M., Palke A.C., Homkrajae A., Sun Z., McElhenny G. (2021a) Raman and photoluminescence mapping of gem materials. *Minerals*, Vol. 11, No. 2, article no. 177, http://dx.doi.org/10.3390/min11020177
Eaton-Magaña S., Ardon T., Breeding C.M. (2021b) Laboratory-grown diamond: A gemological laboratory perspective. *Journal of Gems & Gemmology*, Vol. 23, No. 6, pp. 25–39.
Fedow L. (2023) Here are the details on the lab-grown diamond given to Jill Biden. *National Jeweler*, July 6, https://nationaljeweler.com/articles/12088-here-are-the-details-on-the-lab-grown-diamond-given-to-jill-biden
Fisher D., Sibley S.J., Kelly C.J. (2009) Brown colour in natural diamond and interaction between the brown related and other colour-inducing defects. *Journal of Physics: Condensed Matter*, Vol. 21, No. 36, article no. 364213, http://dx.doi.org/10.1088/0953-8984/21/36/364213
Fritsch E., Phelps A.W. (1993) Type IIb diamond thin films deposited onto near-colorless natural gem diamonds. *Diamond and Related Materials*, Vol. 2, No. 2-4, pp. 70–74, http://dx.doi.org/10.1016/0925-9635(93)90033-X
Gaillou E., Post J.E., Rost D., Butler J.E. (2012) Boron in natural type IIb blue diamonds: Chemical and spectroscopic measurements. *American Mineralogist*, Vol. 97, No. 1, pp. 1–18, http://dx.doi.org/10.2138/am.2012.3925
Gao B., Song Z., Lu T., Ma Y. (2021) HPHT-grown near-colourless synthetic diamond with detected GR1 defect. *Journal of Gemmology*, Vol. 37, No. 5, pp. 467–469.
Howell D., Collins A.T., Loudin L.C., Diggle P.L., D'Haenens-Johansson U.F.S., Smit K.V., Katrusha A.N., Butler J.E., Nestola F. (2019) Automated FTIR mapping of boron distribution in diamond. *Diamond and Related Materials*, Vol. 96, pp. 207–215, http://dx.doi.org/10.1016/j.diamond.2019.02.029
Jeffay J. (2023) Two-colored lab growns - in blue and yellow of Ukraine flag. *IDEX Online*, http://www.idexonline.com/FullArticle?Id=48616
Johnson P., Myagkaya E. (2017) Lab Notes: HPHT synthetic diamond with intense green color. *G&G*, Vol. 53, No. 1, pp. 96–98.
Johnson P., Moe K.S., Persaud S., Odake S., Kazuchits N.M., Zaitsev A.M. (2023) Spectroscopic characterization of yellow *gem* quality CVD diamond. *Diamond and Related Materials*, Vol. 140, article no. 110505, http://dx.doi.org/10.1016/j.diamond.2023.110505
Jones R., Hounsome L.S., Fujita N., Öberg S., Briddon P.R. (2007) Electrical and optical properties of multivacancy centres in diamond. *Physics Status Solidi (a)*, Vol. 204, No. 9, pp. 3059–3064, http://dx.doi.org/10.1002/pssa.200776311
Khan R.U.A., Martineau P.M., Cann B.L., Newton M.E., Twitchen D.J. (2009) Charge transfer effects, thermo and photochromism in single crystal CVD synthetic diamond. *Journal of Physics: Condensed Matter*, Vol. 21, No. 36, article no. 364214, http://dx.doi.org/10.1088/0953-8984/21/36/364214
Khan R.U.A., Martineau P.M., Cann B.L., Newton M.E., Dhillon H.K., Twitchen D.J. (2010) Color alterations in CVD synthetic diamond with heat and UV exposure: Implications for color grading and identification. *G&G*, Vol. 46, No. 1, pp. 18–26, http://dx.doi.org/10.5741/GEMS.46.1.18
Khan R.U.A., Cann B.L., Martineau P.M., Samartseva J., Freeth J.J.P., Sibley S.J., Hartland C.B., Newton M.E., Dhillon H.K., Twitchen D.J. (2013) Colour-causing defects and their related optoelectronic transitions in single crystal CVD diamond. *Journal of Physics: Condensed Matter*, Vol. 25, No. 27, article no. 275801, http://dx.doi.org/10.1088/0953-8984/25/27/275801
Kitawaki H., Emori K., Hisanaga M., Yamamoto M., Okano M., Zhao Z., Sonani J., Harada H. (2023) Gemmological studies of "hybrid diamond" (natural + CVD synthetics). *37th International Gemmological Conference*, Tokyo, pp. 34–36.
Lai M.Y., Breeding C.M. Stachel T., Stern R.A. (2020) Spectroscopic features of natural and HPHT-treated yellow diamonds. *Diamond and Related Materials*, Vol. 101, article no. 107642, http://dx.doi.org/10.1016/j.diamond.2019.107642
Liang Q., Yan C.-S., Meng Y., Lai J., Krasnicki S., Mao H.-K., Hemley R.J. (2009) Recent advances in high-growth rate single-crystal CVD diamond. *Diamond and Related Materials*, Vol. 18, No. 5-8, pp. 698–703, http://dx.doi.org/10.1016/j.diamond.2008.12.002
Linde O., Epstein A., Kravchenko S., Rentmeesters K. (2021) Brilliant under pressure: The global diamond industry 2020–21. Bain & Company, https://www.bain.com/insights/global-diamond-industry-2020-21
Loudin L.C. (2017) Photoluminescence mapping of optical defects in HPHT synthetic diamond. *G&G*, Vol. 53, No. 2, pp. 180–188, http://dx.doi.org/10.5741/GEMS.53.2.180
Lu T., Ke J., Lan Y., Song Z., Zhang J., Tang S., Su J., Dai H., Wu X. (2019) Current status of Chinese synthetic diamonds. *Journal of Gemmology*, Vol. 36, No. 8, pp. 748–757.
Mäki J.-M., Tuomisto F., Kelly C., Fisher D., Martineau P. (2007) Effects of thermal treatment on optically active vacancy defects in CVD diamonds. *Physica B: Condensed Matter*, Vol. 401–402, pp. 613–616, http://dx.doi.org/10.1016/j.physb.2007.09.034
Markham M., Twitchen D. (2020) The diamond quantum revolution. *Physics World*, Vol. 33, No. 4, http://dx.doi.org/10.1088/2058-7058/33/4/31
Martineau P.M., Lawson S.C., Taylor A.J., Quinn S.J., Evans D.J.F., Crowder M.J. (2004) Identification of synthetic diamond grown using chemical vapor deposition (CVD). *G&G*, Vol. 40, No.1, pp. 2–25, http://dx.doi.org/10.5741/GEMS.40.1.2
Meng Y.F., Yan C.S., Lai J., Krasnicki S., Shu H., Yu T., Liang Q., Mao H.K., Hemley R.J. (2008) Enhanced optical properties of chemical vapor deposited single crystal diamond by low-pressure/high-temperature annealing. *Proceedings of the National Academy of Sciences*, Vol. 105, No. 46, pp. 17620–17625, http://dx.doi.org/10.1073/pnas.0808230105
Meylor Global offers extraordinarily large laboratory-grown diamonds and LGD jewellery with customised cuts (2020) Jewellery

Outlook.com, November 2, https://jewelleryoutlook.com/meylor-global-offers-extraordinarily-large-laboratory-grown-diamonds-and-lgd-jewellery-with-customised-cuts/
Moe K.S., Johnson P., D'Haenens-Johansson U., Wang W. (2017) Lab Notes: A synthetic diamond overgrowth on a natural diamond. *G&G*, Vol. 53, No. 2, pp. 237–239.
Myagkaya E., Johnson P. (2021) Lab Notes: New CVD material submitted for analysis. *G&G*, Vol. 57, No. 3, pp. 262–263.
Nad S., Gu Y., Asmussen J. (2015) Growth strategies for large and high quality single crystal diamond substrates. *Diamond and Related Materials*, Vol. 60, pp. 26–34, http://dx.doi.org/10.1016/j.diamond.2015.09.018
Nad S., Charris A., Asmussen J. (2016) MPACVD growth of single crystalline diamond substrates with PCD rimless and expanding surfaces. *Applied Physics Letters*, Vol. 109, No. 16, article no. 162103, http://dx.doi.org/10.1063/1.4965025
Natural Diamond Council (2023) ASSURE Directory 2.0, https://www.naturaldiamonds.com/council/assure-diamond-verification/
Odake S., Kadam P. (2023) Lab Notes: CVD diamonds with invisible markings. *G&G*, Vol. 59, No. 2, pp. 214–215.
Ord S. (2024) World's largest lab-created diamond displayed at US trade show. *Jeweller Magazine*, June 4, www.jewellermagazine.com/Article/13100/Worlds-largest-lab-created-diamond-displayed-at-US-trade-show
Rego S. (2023) India's lab-grown diamond industry is growing up. *National Jeweler*, March 15, https://nationaljeweler.com/articles/11774-india-s-lab-grown-diamond-industry-is-growing-up
Robins L.H., Cook L.P., Farabaugh E.N., Feldman A. (1989) Cathodoluminescence of defects in diamond films and particles grown by hot-filament chemical-vapor deposition. *Physical Review B*, Vol. 39, No. 18, pp. 13367–13377, http://dx.doi.org/10.1103/PhysRevB.39.13367
Robinson A. (2018) Irradiated HPHT-grown diamonds might escape detection as synthetics, says lab. *IDEX Online*, http://www.idexonline.com/FullArticle?Id=43871
Shigley J.E., Abbaschian R., Clarke C. (2002) Gemesis laboratory-created diamonds. *G&G*, Vol. 38, No. 4, pp. 301–309, http://dx.doi.org/10.5741/GEMS.38.4.301
Shigley J.E., McClure S.F., Breeding C.M., Shen A.H.-T., Muhlmeister S.M. (2004) Lab-grown colored diamonds from Chatham Created Gems. *G&G*, Vol. 40, No. 2, pp. 128–145, http://dx.doi.org/10.5741/GEMS.40.2.128
Smith E.M., Shirey S.B., Nestola F., Bullock E.S., Wang J., Richardson S.H., Wang W. (2016) Large gem diamonds from metallic liquid in Earth's deep mantle. *Science*, Vol. 354, No. 6318, pp. 1403–1405, http://dx.doi.org/10.1126/science.aal1303
Smith F. (2023) Record breaking 50.25-carat lab-grown diamond unveiled in Vegas. *Jewellery Monthly Magazine*, June 5, https://www.jewellerymonthly.com/record-breaking-50-carat-lab-grown-diamond
Stachel T., Luth R.W. (2015) Diamond formation—Where, when and how? *Lithos*, Vol. 220-223, pp. 200–220, http://dx.doi.org/10.1016/j.lithos.2015.01.028
Stoupin S., Antipov S., Butler J.E., Kolyadin A.V., Katrusha A. (2016) Large-surface-area diamond (111) crystal plates for applications in high-heat-load wavefront-preserving X-ray crystal optics. *Journal of Synchrotron Radiation*, Vol. 23, No. 5, pp. 1118–1123, http://dx.doi.org/10.1107/S1600577516011796
Sumiya H., Harano K., Tamasaku K. (2015) HPHT synthesis and crystalline quality of large high-quality (001) and (111) diamond crystals. *Diamond and Related Materials*, Vol. 58, pp. 221–225, http://dx.doi.org/10.1016/j.diamond.2015.08.006
Tallaire A., Collins A.T., Charles D., Achard J., Sussmann R., Gicquel A., Newton M.E., Edmonds A.M., Cruddace R.J. (2006) Characterisation of high-quality thick single-crystal diamond grown by CVD with a low nitrogen addition. *Diamond and Related Materials*, Vol. 15, No. 10, pp. 1700–1707, http://dx.doi.org/10.1016/j.diamond.2006.02.005
Tallaire A., Mille V., Brinza O., Thi T.N.T., Brom J.M., Loguinov Y., Katrusha A., Koliadin A., Achard J. (2017) Thick CVD diamond films grown on high-quality type IIa HPHT diamond substrates from New Diamond Technology. *Diamond and Related Materials*, Vol. 77, pp. 146–152, http://dx.doi.org/10.1016/j.diamond.2017.07.002
Tam K.W., Poon T. (2023) Lab Notes: CVD diamond over 34 carats. *G&G*, Vol. 59, No. 2, pp. 213–214.
Tang S., Su J., Lu T., Ma Y., Ke J., Song Z., Zhang J., Liu H. (2018) A thick overgrowth of CVD synthetic diamond on a natural diamond. *Journal of Gemmology*, Vol. 36, No. 2, pp. 134–141.
Tsai T., D'Haenens-Johansson U.F.S. (2019) Gemstone screening and identification using fluorescence spectroscopy. In *Frontiers in Optics + Laser Science APS/DLS*, OSA Technical Digest, Optical Society of America, paper JTu3A.109, http://dx.doi.org/10.1364/FIO.2019.JTu3A.109
Wang W., Moses T., Linares R.C., Shigley J.E., Hall M., Butler J.E. (2003) Gem-quality synthetic diamonds grown by a chemical vapor deposition method. *G&G*, Vol. 39, No. 4, pp. 268–283, http://dx.doi.org/10.5741/GEMS.39.4.268
Wang W., Tallaire A., Hall M.S., Moses T.M., Achard J., Sussmann R.S., Gicquel A. (2005) Experimental CVD synthetic diamonds from LIMHP-CNRS, France. *G&G*, Vol. 41, No. 3, pp. 234–244, http://dx.doi.org/10.5741/GEMS.41.3.234
Wang W., Hall M.S., Moe K.S., Tower J., Moses T.M. (2007) Latest-generation CVD-grown synthetic diamonds from Apollo Diamond Inc. *G&G*, Vol. 43, No. 4, pp. 294–312, http://dx.doi.org/10.5741/GEMS.43.4.294
Wang W., Doering P., Tower J., Lu R., Eaton-Magaña S., Johnson P., Emerson E., Moses T.M. (2010) Strongly colored pink CVD lab-grown diamonds. *G&G*, Vol. 46, No. 1, pp. 4–17, http://dx.doi.org/10.5741/GEMS.46.1.4
Wang W., D'Haenens-Johansson U.F.S., Johnson, P., Moe K.S., Emerson E., Newton M.E., Moses T.M. (2012) CVD synthetic diamonds from Gemesis Corp. *G&G*, Vol. 48, No. 2, pp. 80–97, http://dx.doi.org/10.5741/GEMS.48.2.80
Wang W., Persaud S., Myagkaya E. (2022) Lab Notes: New record size for CVD laboratory-grown diamond. *G&G*, Vol. 58, No. 1, pp. 54–56.
Watanabe K., Lawson S.C., Isoya J., Kanda H., Sato Y. (1997) Phosphorescence in high-pressure synthetic diamond. *Diamond and Related Materials*, Vol. 6, No. 1, pp. 99–106, http://dx.doi.org/10.1016/S0925-9635(96)00764-9
Welbourn C.M., Cooper M., Spear P.M. (1996) De Beers natural versus synthetic diamond verification instruments. *G&G*, Vol. 32, No. 3, pp. 156–169, http://dx.doi.org/10.5741/GEMS.32.3.156
Zaitsev A.M., Kazuchits N.M., Kazuchits V.N., Moe K.S., Rusetsky M.S., Korolik O.V., Kitajima K., Butler J.E., Wang W. (2020) Nitrogen-doped CVD diamond: Nitrogen concentration, color and internal stress. *Diamond and Related Materials*, Vol. 105, article no. 107794, http://dx.doi.org/10.1016/j.diamond.2020.107794
Zaitsev A.M., Kazuchits N.M., Moe K.S., Butler J.E., Korolik O.V., Rusetsky M.S., Kazuchits V.N. (2021) Luminescence of brown CVD diamond: 468 nm luminescence center. *Diamond and Related Materials*, Vol. 113, article no. 108255, http://dx.doi.org/10.1016/j.diamond.2021.108255
Zimnisky P. (2021) Lab-grown diamond jewelry market forecast to almost double in size by 2025. Paul Zimnisky Diamond Analytics, October 26, https://www.paulzimnisky.com/Lab-Grown-Diamond-Jewelry-Market-Forecast-to-Almost-Double-in-Size-by-2025
——— (2024) LGD forecasted to generate $10B in incremental diamond jewelry demand by 2026. Paul Zimnisky Diamond Analytics, January 9, https://www.paulzimnisky.com/LGD-Forecasted-to-Generate-10B-in-Incremental-Diamond-Jewelry-Demand-by-26

Gemological and Trace Element Characteristics of Cassiterite from Yunling, China

Wenqing Huang, Jungui Zhou, Ting Shui, Junyi Pan, Fanwei Meng, Rui Zuo, Shuxin Dong, and Suqiao Cao

The Yunling area in Yongde County of China's Yunnan Province is a significant source of gem-quality cassiterite. This study is an initial report on the gemological characteristics, internal features, absorption spectra, and trace element chemistry of this material.

Cut stones from Yunling typically range from 1 to 2 ct, and larger ones exceeding 20 ct are generally rare. Their colors range from near-colorless to various tones of brown, light brown, brownish pink, light gray, and black. Red color, resulting from iron oxide staining within fractures, is rare and was observed in only one of the stones we examined. The samples from this study had a specific gravity of 6.85–7.04 and did not fluoresce under long-wave or short-wave UV light. Internal features included concentric brown bands, irregular zones of gray to black colors, and multiphase fluid inclusions, with tourmaline and beryl as the primary mineral inclusions. Mica inclusions, though less frequent, were also observed.

Among the seven color groups identified for this cassiterite, chemical analyses revealed variable levels of titanium (8.08–1155 ppmw) and iron (26–425 ppmw); these were the most abundant trace elements in all color groups except black. Tungsten and uranium were only enriched in the black samples. Variations in the ultraviolet/visible/near-infrared absorption spectra for the observed color differences in the cassiterite point to possible causes. Specifically, the black coloration is associated with tungsten and oxygen vacancies, while brown and red colors are influenced by oxygen vacancies and iron oxide staining, respectively. When comparing the chemical composition profiles of cassiterite from Yunling and Viloco (Bolivia), notable differences were observed in the trace element ranges and averages. Trace element plots of Sb-Ni and Fe-Nd can be useful in distinguishing between cassiterite from the two localities.

Cassiterite (SnO_2) is a common ore mineral found in tin deposits that are spatially and genetically related to highly evolved granites (Lehmann, 2021; Ni et al., 2023). These granites originate from melts that have undergone intensive fractional crystallization (Wu et al., 2017). However, cassiterite crystals are typically opaque or small, making them unsuitable for use as gem material. In rare cases, gem-quality cassiterite has been found. One well-known example is the Viloco deposit in Bolivia (Hyršl and Petrov, 1998; Hyršl, 2002). Two lesser-known locations in China, specifically Yunling in Yongde County and Amo in Ximeng County, both situated in the Yunnan Province, also produce gem-quality cassiterite (figure 1) (Moore, 2004; Ottens, 2008, 2021; Wu, 2013; Huang and Pan, 2021; Huang et al., 2023).

Cassiterite has a structure similar to that of rutile, where each tin ion is surrounded by six oxygen ions at the corners of a regular octahedron. It exhibits uniaxial characteristics and displays exceptionally high refractive index (RI; n_ω=1.990–2.010, n_ε=2.093–2.100) and birefringence values (0.096–0.098) (Deer et al., 1992). Additionally, cassiterite has a very high specific gravity (SG) of approximately 7 and strong dispersion (0.071, roughly twice that of diamond). Its hardness is 6.5 on the Mohs scale, and twinning is common on {011} planes, resulting in the formation of the recognizable geniculate twin (also known as an "elbow" or "knee-shaped" twin). It is important to note that confusion with synthetic moissanite is possible because of that ma-

See end of article for About the Authors and Acknowledgments.
Gems & Gemology, Vol. 60, No. 2, pp. 168–193,
http://dx.doi.org/10.5741/GEMS.60.2.168

Figure 1. Left: A gem-quality cassiterite crystal, measuring 3.9 cm in length, in greisen matrix from the Yunling deposit. Photo by Yongming Shi. Right: This sterling silver ring features a Yunling cassiterite measuring 6 mm in diameter. Photo by Wenqing Huang.

terial's high birefringence (0.043) and dispersion (0.104).

The Yunling mine is situated near the village of Yunling in Yongde County in western Yunnan Province (figure 2). Cassiterite extracted from the mine was initially used for industrial purposes as the main ore mineral for tin in the early 1980s. However, it was later discovered that some of these ore pieces were of gem quality. In 2006, a mining company authorized by the local government began exploring tin ore until the mining rights expired in 2013 (Gu, 2010). Today, cassiterite specimens are occasionally extracted and collected by local villagers.

Considerable quantities of cassiterite have been mined as mineral specimens over the past three decades, and specimens on matrix rocks are highly sought after by mineral collectors (Ottens, 2008, 2021; Wu, 2013). Recently, a significant amount of faceted cassiterite, reportedly from the Yunling region, has appeared on the Chinese market, mainly in the provinces of Yunnan and Guangxi. However, the supply of gem-quality cassiterite is inconsistent, and it remains more of a collector's gemstone. These stones are commonly near-colorless and brown, though other color varieties such as black and brownish pink are occasionally encountered.

Documentation of the Yunling deposit has been limited, focusing mainly on the regional and deposit geology as well as the nature of the host granite (Nie et al., 2012; Wang et al., 2014; Xiao et al., 2022). Wu (2013) briefly documented the color categories and dimensions of rough cassiterite crystal specimens from the Yunling mine. However, the detailed gemological properties and chemical compositions that are

In Brief

- The Yunling area in Yunnan Province, China, represents a significant source of gem-quality cassiterite.
- Gemological examination reveals internal features such as concentric color bands, irregular gray to black domains, and mineral inclusions like tourmaline, beryl, and mica, along with multiphase fluid inclusions.
- Yunling cassiterite exhibits a wide variety of hues, caused either by lattice impurities or by iron oxide staining within fractures (for the red variety).
- LA-ICP-MS trace element analyses can provide insights into the substitutional mechanism of trace elements and separate Yunling cassiterite from those from Viloco, Bolivia.

Figure 2. A map showing the Yunling cassiterite occurrence. The nearby Amo deposit is also known to produce gem-quality cassiterite.

critical for identification, evaluation, and geographic origin determination remained lacking.

This article provides an overview of the geology of the Yunling cassiterite deposit and offers a detailed description of gemological properties, inclusion scenes, absorption spectra, and geochemical composition analysis by laser ablation–inductively coupled plasma–mass spectrometry (LA-ICP-MS).

GEOLOGICAL SETTING

Regional Geology. The Yunling cassiterite deposit is situated in the Changning-Menglian Belt of the Sanjiang Tethys tectonic region, which is at the southeastern margin of the Tibetan Plateau (figure 3, A and B). This region is recognized as one of China's significant tin belts. Tin deposits in the Sanjiang Tethys domain are found mainly in the Tengchong block, followed by the Baoshan block and the Changning-Menglian orogenic belt (e.g., Wang et al., 2014). The granitoids in the first two terranes span from the Early Paleozoic to the Paleogene periods (figure 3B). The Changning-Menglian Belt is delineated by the Kejie fault to the west and the Shuangjiang fault to the east (figure 3C), and it originated from the collision between the Tengchong-Baoshan block and the Simao block (Wang et al., 2014). Granitic rocks in the Changning-Menglian Belt (figure 3C) are primarily granodiorite in composition and fall into the high-potassium calc-alkaline series (Nie et al., 2012; Wang et al., 2014). Based on geochronological studies, the granitoids in this belt exhibit ages ranging from the Late Triassic to the

Figure 3. A: Tectonic framework of the Tibetan Plateau showing the location of the Sanjiang Tethys region; modified from Chen et al. (2014). B: Map showing major tectonic units of the Sanjiang Tethys in western Yunnan Province. The collision between the Tengchong-Baoshan block and Simao block gave rise to the Changning-Menglian Belt, representing the primary Paleo-Tethys Suture Zone. Modified from Deng et al. (2014). C: A closer view of the Changning-Menglian suture belt reveals the distribution of granitic rocks that primarily consist of Triassic-aged granodiorite (Nie et al., 2012). Two deposits of gem-quality cassiterite are found in the northern and southern portions of this metallogenic belt. These are located in the villages of Yunling in Yongde County and Amo in Ximeng County. Modified from Nie et al. (2012) and Wang et al. (2014).

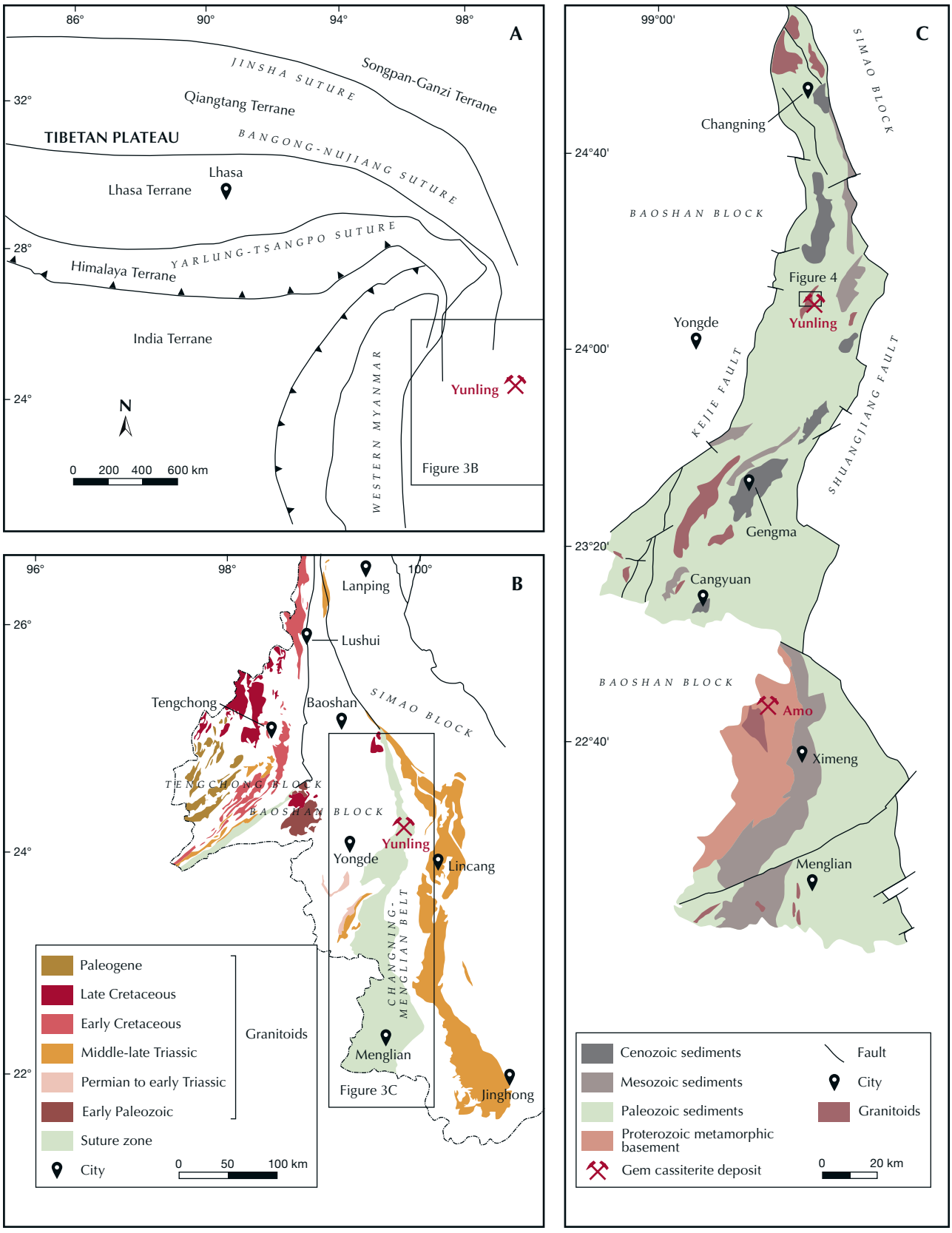
A
86°
90°
94°
98°
32°
28°
24°
JINSHA SUTURE
Songpan-Ganzi Terrane
Qiangtang Terrane
TIBETAN PLATEAU
BANGONG-NUJIANG SUTURE
Lhasa
Lhasa Terrane
YARLUNG-TSANGPO SUTURE
Himalaya Terrane
India Terrane
WESTERN MYANMAR
Yunling
Figure 3B
N
0 200 400 600 km
B
96°
98°
100°
26°
24°
22°
Lanping
Lushui
Tengchong
Baoshan
SIMAO BLOCK
TENGCHONG BLOCK
BAOSHAN BLOCK
Yunling
Yongde
Lincang
CHANGNING-MENGLIAN BELT
Menglian
Figure 3C
Jinghong
Paleogene
Late Cretaceous
Early Cretaceous
Middle-late Triassic
Permian to early Triassic
Early Paleozoic
Granitoids
Suture zone
City
0 50 100 km
C
99°00'
24°40'
24°00'
23°20'
22°40'
SIMAO BLOCK
Changning
BAOSHAN BLOCK
Figure 4
Yongde
Yunling
KEJIE FAULT
SHUANGJIANG FAULT
Gengma
Cangyuan
BAOSHAN BLOCK
Amo
Ximeng
Menglian
Cenozoic sediments
Mesozoic sediments
Paleozoic sediments
Proterozoic metamorphic basement
Gem cassiterite deposit
Fault
City
Granitoids
0 20 km

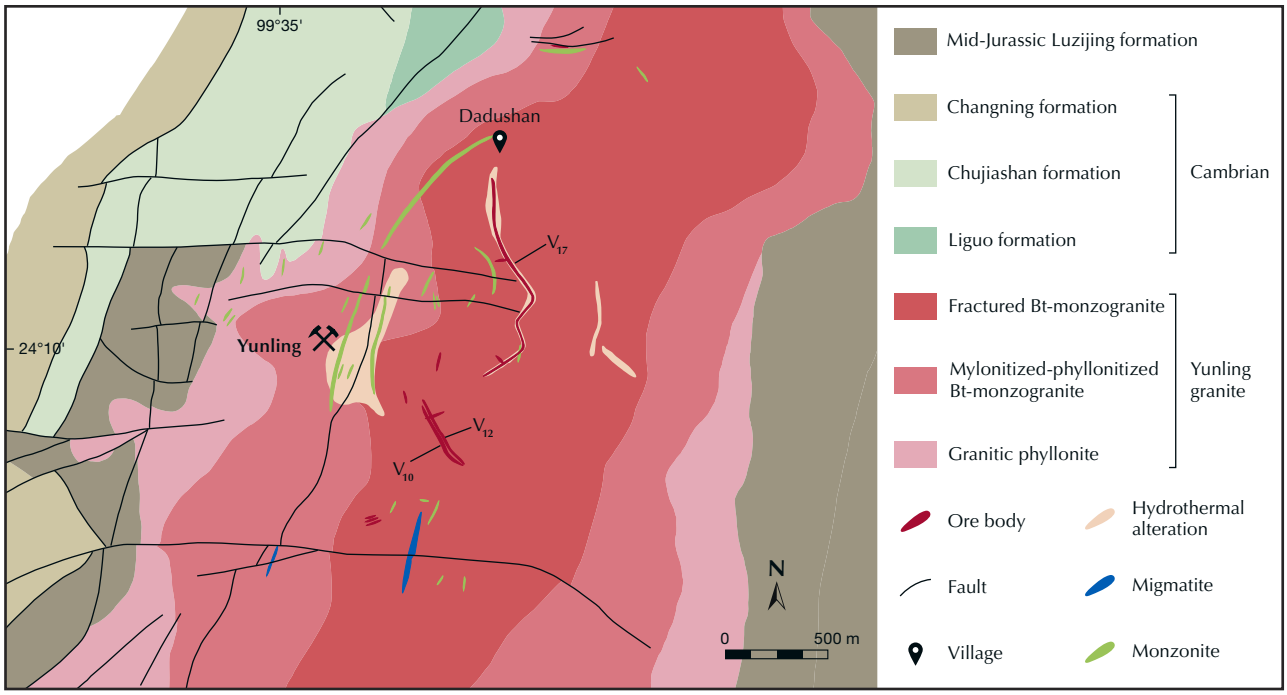

Figure 4. Geologic map of the cassiterite deposit in Yunling. Major structures in the area are EW- and NS-striking faults. The exposed plutons consist mainly of biotite monzogranite, which is of Triassic age. Additionally, there are minor occurrences of migmatite and monzonite veins. The major tin orebodies within this deposit are referred to as V_{10}, V_{12}, and V_{17}. Modified from Li (1985) and Yang et al. (1998).

Tertiary (Yu et al., 2008; Nie et al., 2012; Xiao et al., 2022). The Changning-Menglian Belt hosts several medium-sized tin deposits, including Haobadi, Yunling, and Damasa. The Amo deposit, located in the southern part of the belt (figure 3C), is also recognized for its gem-quality cassiterite (Huang and Pan, 2021).

Geology of the Deposit. The Yunling tin deposit is located in the northern section of the Changning-Menglian Belt, as shown in figure 3C. The stratigraphic sequence in this area is characterized by the Mid-Jurassic Luzijing formation, the Changning formation, the Chujiashan formation, and the Liguo formation, the latter three dating back to the Cambrian (figure 4). The intrusive rocks exposed in the region mainly consist of biotite monzogranite, referred to as Yunling granite in the Yunnan Geological Survey Report (Li, 1985), alongside minor occurrences of migmatite and monzonite veins (figure 4). The predominant rock type within the Yunling pluton is biotite monzogranite, classified as peraluminous S-type granite and belonging to the high-potassium calc-alkaline series (Nie et al., 2012; Zhang et al., 2012). Through zircon U-Pb dating, the age of the biotite monzogranite has been determined to be 231.4 ± 3.8 Ma (Nie et al., 2012).

Structurally, the major faults in the Yunling area strike in the east-west (EW) and north-south (NS) directions, with mineralization occurring mostly within the biotite monzogranite (figure 4). The primary tin orebodies, including V_{10}, V_{12}, and V_{17}, exhibit an average tin grade of 1.5%; orebody V_{17} is the largest, boasting a strike length of approximately 1000 m. Wall-rock alteration consists of greisenization, tourmalinization, and to a lesser extent, fluoritization. Ore types include cassiterite-mica-quartz-pyrite veins (figure 5) and greisen-type mineralization where cassiterite is distributed within greisenized granite. Cassiterite grains within the veins typically range from 0.1 to 1.0 mm in size, with some crystals reaching 10–20 mm or larger, characterized by high transparency and gem quality. Gem-quality cassiterite has also been reported from miarolitic cavities.

MATERIALS AND METHODS

Samples. Forty-one samples, reportedly from the Yunling area, were utilized for this study. They were acquired by author WH from Yongming Shi, a reputable collector and merchant in Yunnan Province.

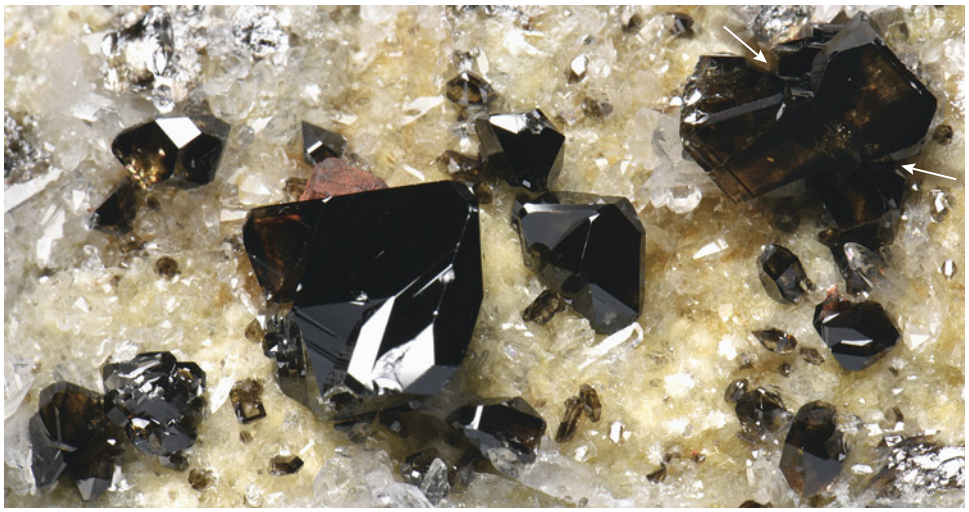

Figure 5. A cluster of transparent cassiterite crystals on the wall of a fissure vein in greisenized granite from Yunling. The presence of geniculate twins can be clearly observed at the twin interfaces, indicated by arrows. The mineral assemblage within the fissure veins consists of mica plates, cassiterite, and quartz. Some pyrite crystals with signs of ferritization are also found, though they are relatively minor. Photo by Junyi Pan; field of view 4.6 cm.

The cassiterite materials were sourced from orebody V_{17} and adjacent small-scale veins, located around 500–800 m east-southeast and 600–1100 m northeast of the Yunling village by local villagers hired by Yongming Shi. These samples comprised 17 faceted stones ranging from 0.54–2.14 ct (figure 6) and 24 rough stones weighing 10–38 ct (figure 7). Out of the 24 rough stones, 10 pieces (samples C-G1 to C-G10) underwent gemological characterization along with the 17 faceted stones, while all 24 rough stones were subsequently cut and polished into thin sections. The faceted samples were categorized into seven

Figure 6. The 17 faceted cassiterite samples from the Yunling mine (0.54–2.14 ct) examined in this study. They represent the seven color groups of cassiterite from this deposit. Photos by Wenqing Huang.

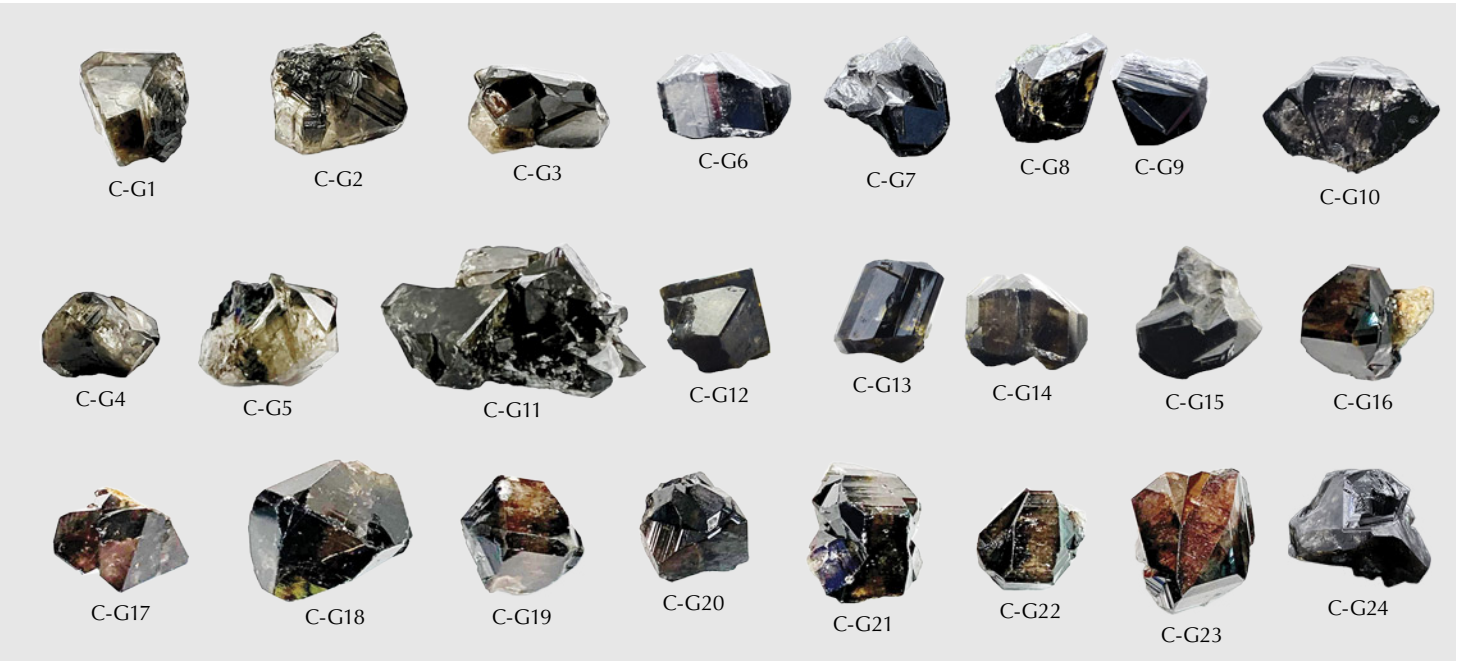

Figure 7. Rough cassiterite from Yunling. These samples typically exhibit euhedral morphologies and range from 10 ct to 38 ct. Photos by Wenqing Huang.

groups based on their color: near-colorless (two samples), light gray (two samples), light brown (five samples), brownish pink (three samples), red (one sample), brown (two samples), and black (two samples). These encompassed the full spectrum of cassiterite colors from the Yunling mine. The rough samples were cut into thin sections in specific orientations to preserve any color bands or domains and then double-side polished to a thickness of approximately 200 μm, primarily for microscopic observation and Raman spectroscopic analysis.

Standard Gemological Testing. Standard gemological analyses were completed on all 17 faceted stones and 10 of the 24 rough stones (samples C-G1 to C-G10) at the National Center of Inspection and Testing on Quality of Gold and Silver Products (NGSTC). RI was determined using an optical gem refractometer, and fluorescence reaction was determined using long-wave (365 nm) and short-wave (254 nm) UV lamps. Pleochroism was identified with a pocket dichroscope, and SG was measured through the hydrostatic method.

Microscopic Analysis and Spectroscopy. Microscopic features of the 24 cassiterite thin sections were observed using a Leica microscope attached to a digital camera, and photomicrographs were taken at magnifications ranging from 25× to 500×. To process the inclusion scenes, we employed the focus stacking technique, also known as extended depth of focus, as described by Renfro (2015). This method involves capturing a series of images at various focal planes and digitally combining them to create a single image with an extended depth of field, revealing intricate details of the inclusion scenes at different depths. For improved color distribution observation, the 17 faceted stones were immersed in methylene iodide. A gemological microscope MV5000 with diffused lighting, transmission light illumination, and a magnification of 20×–40× was utilized for observation.

To identify mineral inclusions and the compositions of fluid inclusions in cassiterite, spot analysis using Raman spectroscopy was applied on the 24 thin sections. Raman analysis was performed at the State Key Laboratory for Mineral Deposits Research, Nanjing University, using a Renishaw RM200 Raman system. An Ar^{+} laser with a surface power of 5 mW and a wavelength of 514.5 nm was used. The scanning range was set from 4000 to 100 cm^{-1}, with a grating of 1800 grooves/mm selected. Each measurement involved a 30-second accumulation time. Raman mapping was applied to measure a multi-solid inclusion using a Renishaw inVia Raman spectrometer at the Anhui Provincial Institute of Geological Experiments. The instrumental setup consisted of a 532 nm laser, a grating of 600

grooves/mm, and a spectral range of 4000–100 cm^{-1}. The mapping was conducted with a step size of 1 × 1 µm, a measurement time of 1 second per spot, and two measurements per spot. The spectrometers were calibrated daily using monocrystalline silicon at 520.7 cm^{-1}. The RRUFF database (Lafuente et al., 2016) and published literature by Wang et al. (2015) and Lensing-Burgdorf et al. (2017) were used as references for mineral phase identification.

Ultraviolet/visible/near-infrared (UV-Vis-NIR) absorption spectra were obtained on the 17 faceted stones using a BiaoQi Optoelectronics GEM-3000 spectrometer. The spectra were acquired at room temperature with a resolution of 1 nm, an integration time of 100 ms, an average of 15 measurements, a smoothing width of 1, and a scanning range of 220–1000 nm.

Trace Element Analysis. LA-ICP-MS trace element analyses were also conducted at the State Key Laboratory for Mineral Deposits Research, Nanjing University, using a Coherent 193 nm excimer laser ablation system coupled to a PerkinElmer NexION 350 ICP mass spectrometer. Both the sample and NIST 610 were loaded simultaneously into the ablation cell of a GeoLas HD system. The ICP-MS system was fine-tuned to achieve maximum sensitivity and reduce oxide production rate by maintaining ThO/Th ratios below 0.5%. The laser beam diameter was set at 32 µm with an energy density of 5 J/cm^2 and a repetition rate of 10 Hz. NIST 610 glass was applied as the bracketing external standard. A wide array of isotopes were analyzed, including ^{7}Li, ^{9}Be, ^{23}Na, ^{24}Mg, ^{27}Al, ^{29}Si, ^{39}K, ^{44}Ca, ^{45}Sc, ^{49}Ti, ^{51}V, ^{52}Cr, ^{55}Mn, ^{57}Fe, ^{59}Co, ^{60}Ni, ^{65}Cu, ^{66}Zn, ^{69}Ga, ^{72}Ge, ^{75}As, ^{85}Rb, ^{88}Sr, ^{89}Y, ^{90}Zr, ^{93}Nb, ^{95}Mo, ^{107}Ag, ^{111}Cd, ^{115}In, ^{121}Sb, ^{133}Cs, ^{137}Ba, ^{139}La, ^{140}Ce, ^{141}Pr, ^{146}Nd, ^{147}Sm, ^{151}Eu, ^{157}Gd, ^{159}Tb, ^{163}Dy, ^{165}Ho, ^{167}Er, ^{169}Tm, ^{173}Yb, ^{175}Lu, ^{178}Hf, ^{181}Ta, ^{182}W, ^{208}Pb, ^{209}Bi, ^{232}Th, and ^{238}U. Each spot measurement incorporated 20 s instrumental background, 20–30 s sample ablation, and 20 s washout time. Five to six spots devoid of inclusions were chosen for each sample ablation. A total of 91 analyses were conducted on the 17 faceted samples, using SILLS software for data reduction and tin as the internal standard (Guillong et al., 2008).

RESULTS

Gemological Properties. The gemological features of the 17 faceted samples and 10 rough stones (samples C-G1 to C-G10) show a range of hues, including brown, red, gray, and black. All were transparent, with RI values exceeding 1.78. SG values varied between 6.85 and 7.04, and this variability was broadly associated with the abundance of fractures and inclusions. Moreover, all samples showed an inert response to both long- and short-wave UV radiation. While most samples displayed no pleochroism, the brownish pink specimens exhibited moderate pleochroism of light brownish pink in one direction and pink in another. It is crucial to note that due to the rarity of cassiterite in gemological labs (Crowningshield, 1960; Gaievskyi and Iemelianov, 2012), its thermal conductivity (comparable to diamond's) along with its electricity conductivity and birefringence could lead to the misidentification of faceted colorless stones as moissanite (Hyršl, 2002).

Microscopic Characteristics. Examination with a gemological polarizer revealed that some of the thin sections of cassiterite crystals exhibited twinning, which was also present in a few of the faceted stones. Irregularities in color, such as bands and domains, were relatively common in the Yunling cassiterite

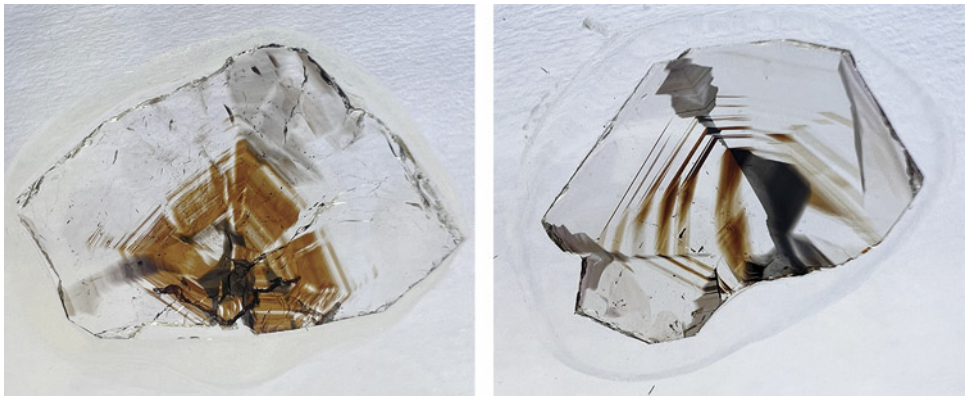

Figure 8. Alternating brown color bands and gray-black domains are relatively common in Yunling cassiterite, as shown in these two thin sections, measuring 1.81 × 1.21 cm (left) and 1.62 × 1.16 cm (right). Photos by Wenqing Huang.

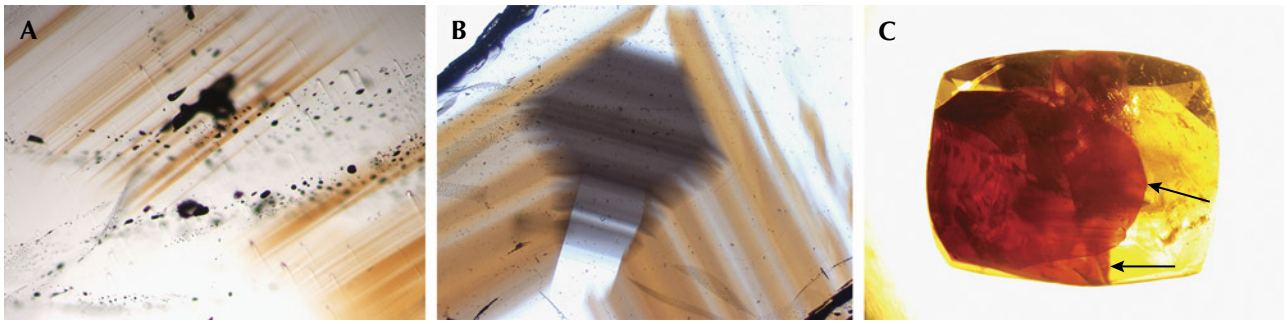

Figure 9. Color heterogeneity of cassiterite from Yunling. A: Fine brownish yellow color bands. B: Gray color domain. C: The red color observed in the red sample, viewed in immersion, appears to be confined to two fractures and distributed within planes (indicated by arrows). This distribution suggests that the red color is caused by iron oxide staining within the fractures. Photomicrographs by Wenqing Huang; fields of view 1.2 mm (A), 3.9 mm (B), and 10 mm (C).

(figures 8 and 9). The samples consistently displayed alternating color bands, typically appearing brown, while the color domains were gray to black with irregular to regular outlines (figures 8 and 9B). The red sample exhibited dark stripes, with the red color distributed exclusively along two fractures (figure 9C). Under strong fiber-optic illumination, the black samples exhibited a deep brown or deep yellowish gray color.

Microscopic observation, in combination with Raman spectroscopic analysis, revealed various mineral inclusions. The most prevalent inclusions were elongated and well-formed crystals (figure 10), identified as tourmaline by Raman spectroscopy (figure 11). The Raman bands of these tourmaline inclusions closely matched those of sodium-deficient schorl (Lensing-Burgdorf et al., 2017). These tourmaline inclusions were found as isolated occurrences (figure 10A) as well as clusters (figure 10, B–D). Further microscopic observation unveiled longitudinal striations on the column surface of these tourmaline crystals (figure 10, A and B), a characteristic feature of tourmaline.

Some mineral inclusions observed in these samples were positively identified by Raman as beryl (figures 12 and 13). The beryl inclusions presented two distinct appearances: one platy (figure 12, left) and the other prismatic (figure 12, right).

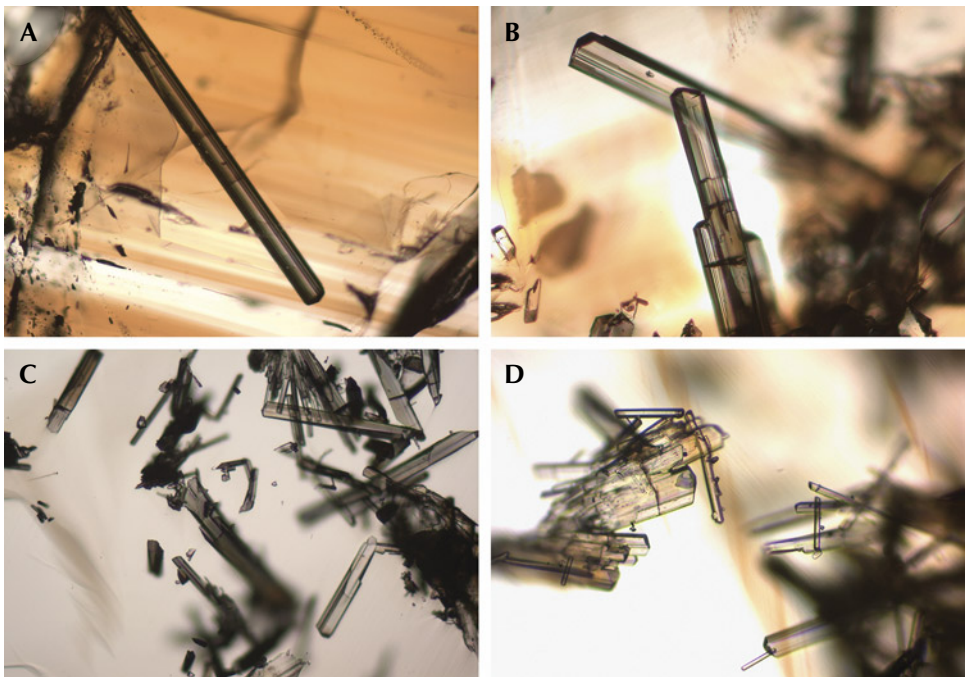

Figure 10. Internal features of Yunling cassiterite: an elongated tourmaline crystal in sample C-G8 (A) and clusters of tourmaline inclusions in samples C-G17 (B) and C-G16 (C and D). Photomicrographs by Wenqing Huang; fields of view 1.23 mm (A–C) and 0.6 mm (D).

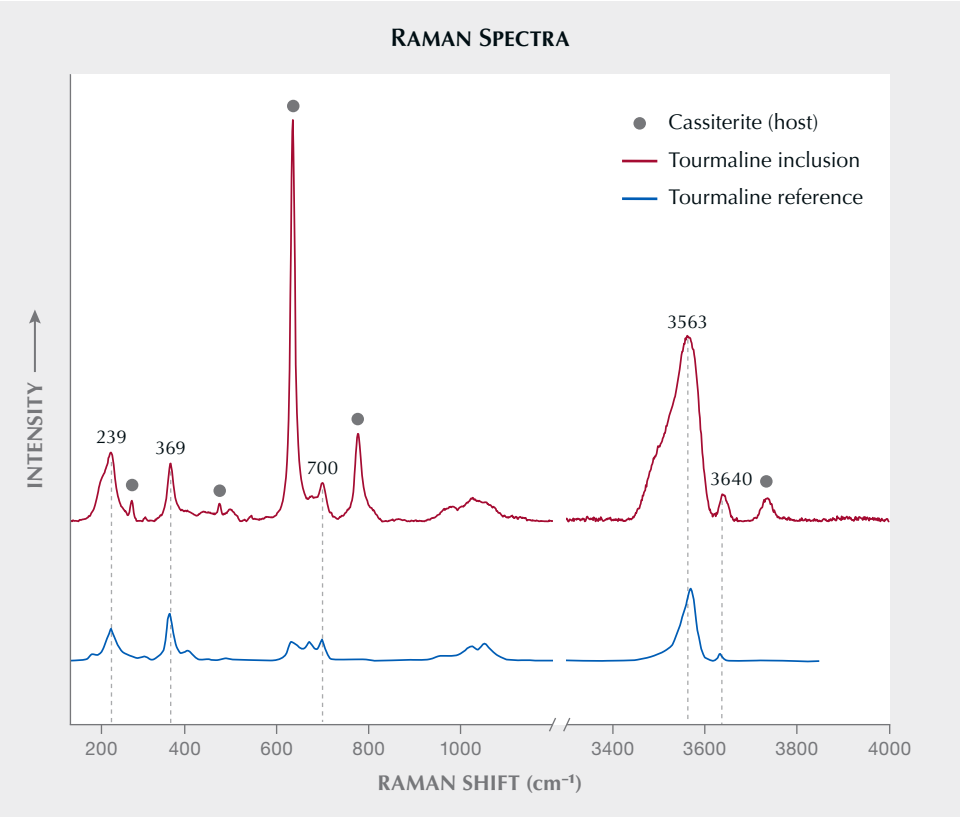

Figure 11. Baseline-corrected Raman spectra of a tourmaline inclusion in Yunling cassiterite sample C-G16 compared with the reference spectrum for tourmaline (sodium-deficient schorl) provided by Lensing-Burgdorf et al. (2017). Bands denoted by gray circles correspond to vibrations originating from the cassiterite host.

In addition, the Raman spectra of several solid inclusions such as the one shown in figure 14 matched the reference spectrum for muscovite (Wang et al., 2015) (figure 15), confirming their identification as mica. Differentiating between subgroups based on Raman spectra was challenging, as certain subgroups, such as muscovite and paragonite, displayed similar vibrational modes (Wang et al., 2015).

The Yunling cassiterite often displayed healed fissures containing fluid inclusions (figure 16). Upon

Figure 12. Internal features of Yunling cassiterite. Left: In sample C-G19, beryl inclusions showing a platy morphology. Right: A beryl inclusion occurring as a prismatic crystal in sample C-G21. Photomicrographs by Wenqing Huang; field of view 0.56 mm.

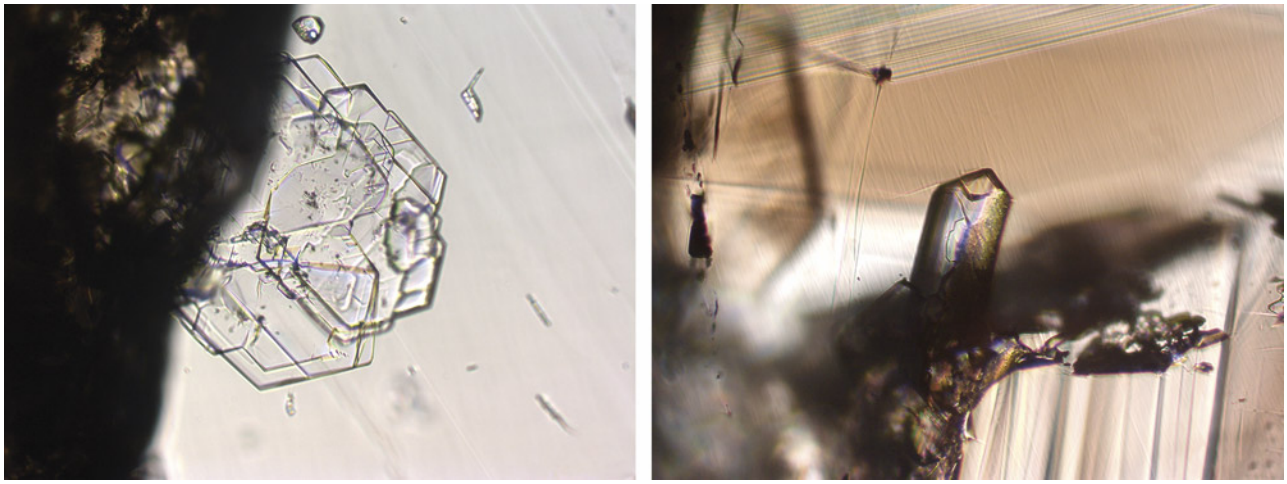

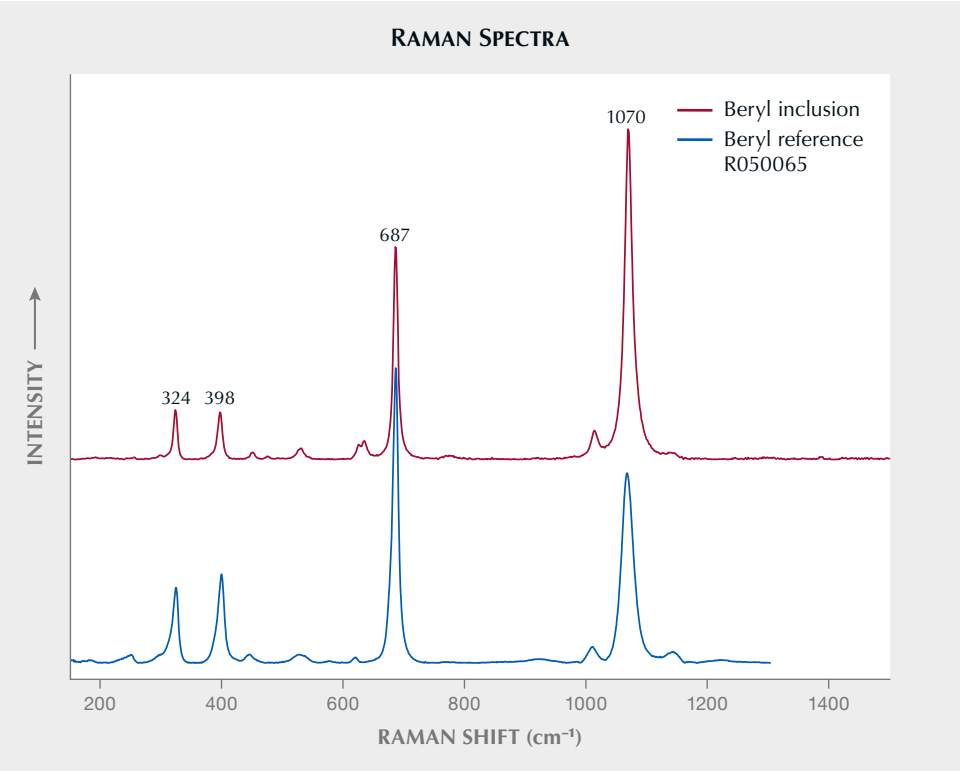

Figure 13. The baseline-corrected Raman spectrum of a beryl inclusion in sample C-G17 matches with the beryl spectrum from the RRUFF database. Spectra are offset vertically for clarity.

closer examination, these fluid inclusions consistently showed a distinct negative morphology and consisted of three phases: a bubble, a liquid, and a transparent mineral (figure 16, B, D, and E). Although the transparent mineral showed no Raman signal, this is common for halite within fluid inclusions (Frezzotti et al., 2012). The cubic morphology strongly suggests that the mineral is halite. The con-

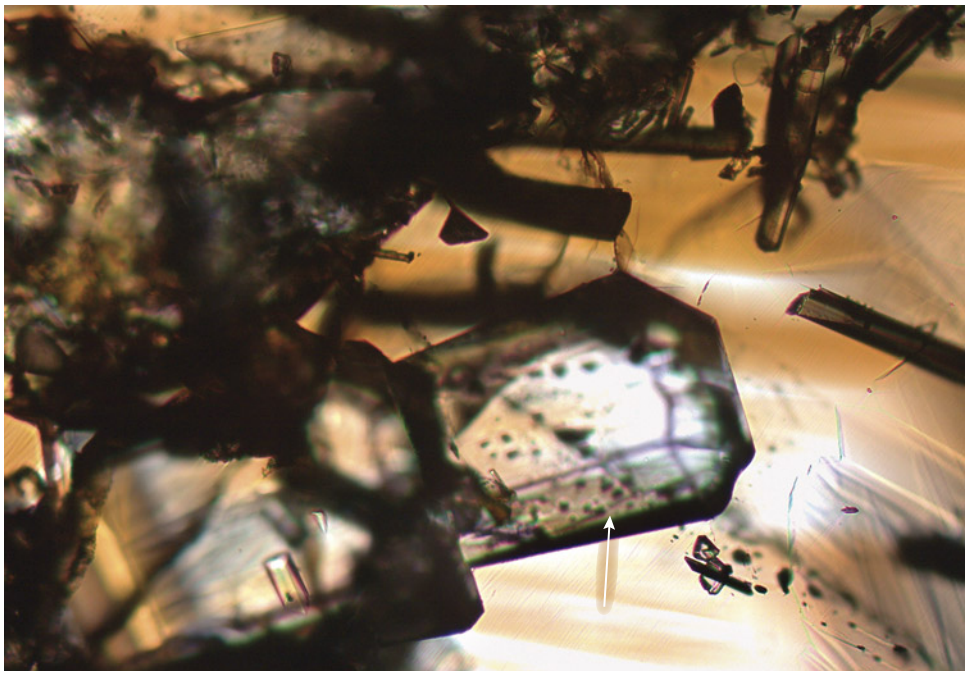

Figure 14. A mica inclusion (indicated by the arrow) in Yunling cassiterite sample C-G17. Photomicrograph by Wenqing Huang; field of view 1.13 mm.

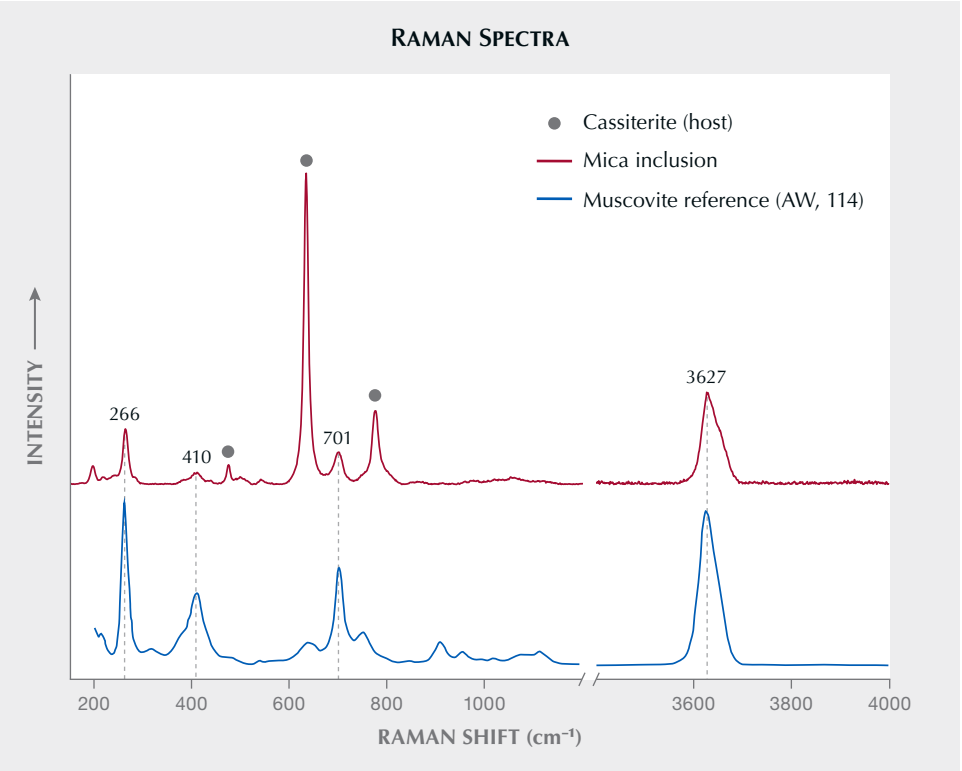

Figure 15. Raman spectrum of a mica inclusion in Yunling cassiterite sample C-G19 matched with the reference spectrum for muscovite from Wang et al. (2015). The bands marked by gray circles correspond to vibrations originating from the cassiterite host.

sistent phase ratios between the halite and the volatiles indicate that halite is a daughter mineral formed through the crystallization of the cooling fluid inclusions. Halite-bearing inclusions were the

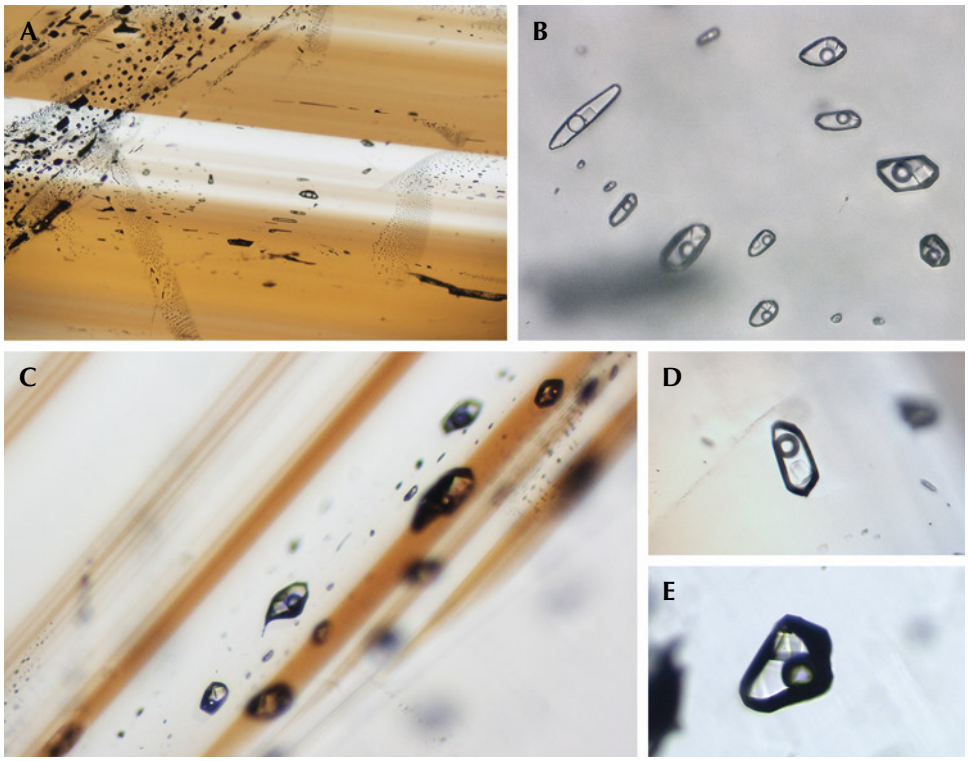

Figure 16. Fluid inclusions in cassiterite samples from Yunling. A and B: Fluid inclusions in healed fractures within samples C-G7 and C-G5, respectively. C: In sample C-G22, fluid inclusions occur parallel to the color bands. D and E: Representative three-phase inclusions in sample C-G24 show a cubic daughter mineral, a bubble, and a fluid phase. Photomicrographs by Wenqing Huang; fields of view 2.54 mm (A), 0.22 mm (B), 0.53 mm (C), 0.20 mm (D), and 0.15 mm (E). Image B was taken under transmitted light and enhanced with focus stacking techniques.

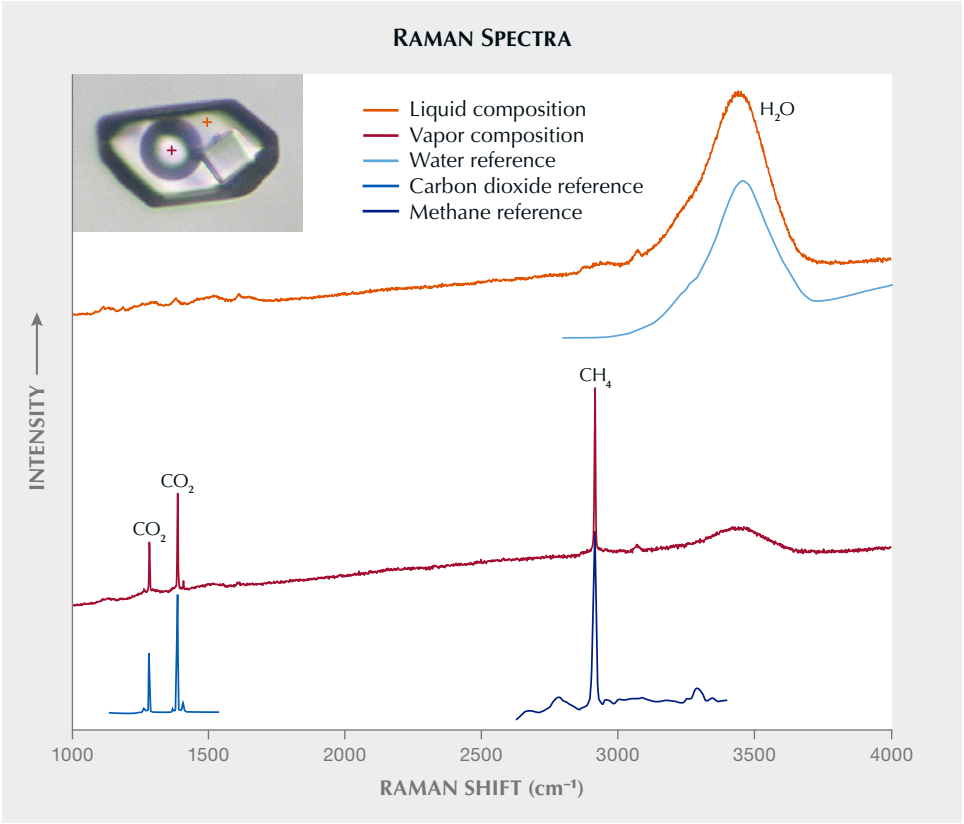

Figure 17. Representative Raman spectra showing the liquid composition and gas compositions of a fluid inclusion in Yunling cassiterite sample C-G5. These components were identified by reference to Frezzotti et al. (2012). Inset field of view 0.043 mm.

most abundant type in Yunling cassiterite. Raman spectroscopy revealed that the liquid was water, while the vapor primarily consisted of carbon dioxide and methane, identified by the characteristic bands around 1383/1282 cm^{-1} and 2916 cm^{-1}, respectively (Frezzotti et al., 2012) (figure 17).

Multiphase, multi-solid inclusions, shown in figure 18, were occasionally encountered. These oc-

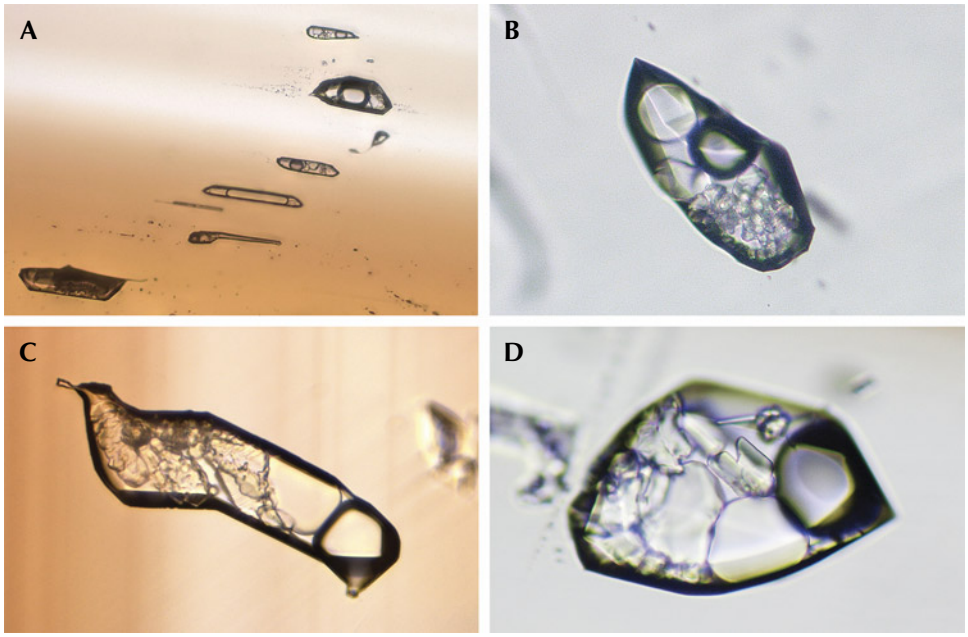

Figure 18. Multiphase, multi-solid inclusions were occasionally encountered, either in healed fractures (A, sample C-G7) or as isolated inclusions (B and D, sample C-G6; C, sample C-G8). Image A was taken using transmitted light and enhanced by focus stacking techniques. Photomicrographs by Wenqing Huang; fields of view 0.49 mm (A), 0.15 mm (B), 0.18 mm (C), and 0.14 mm (D).

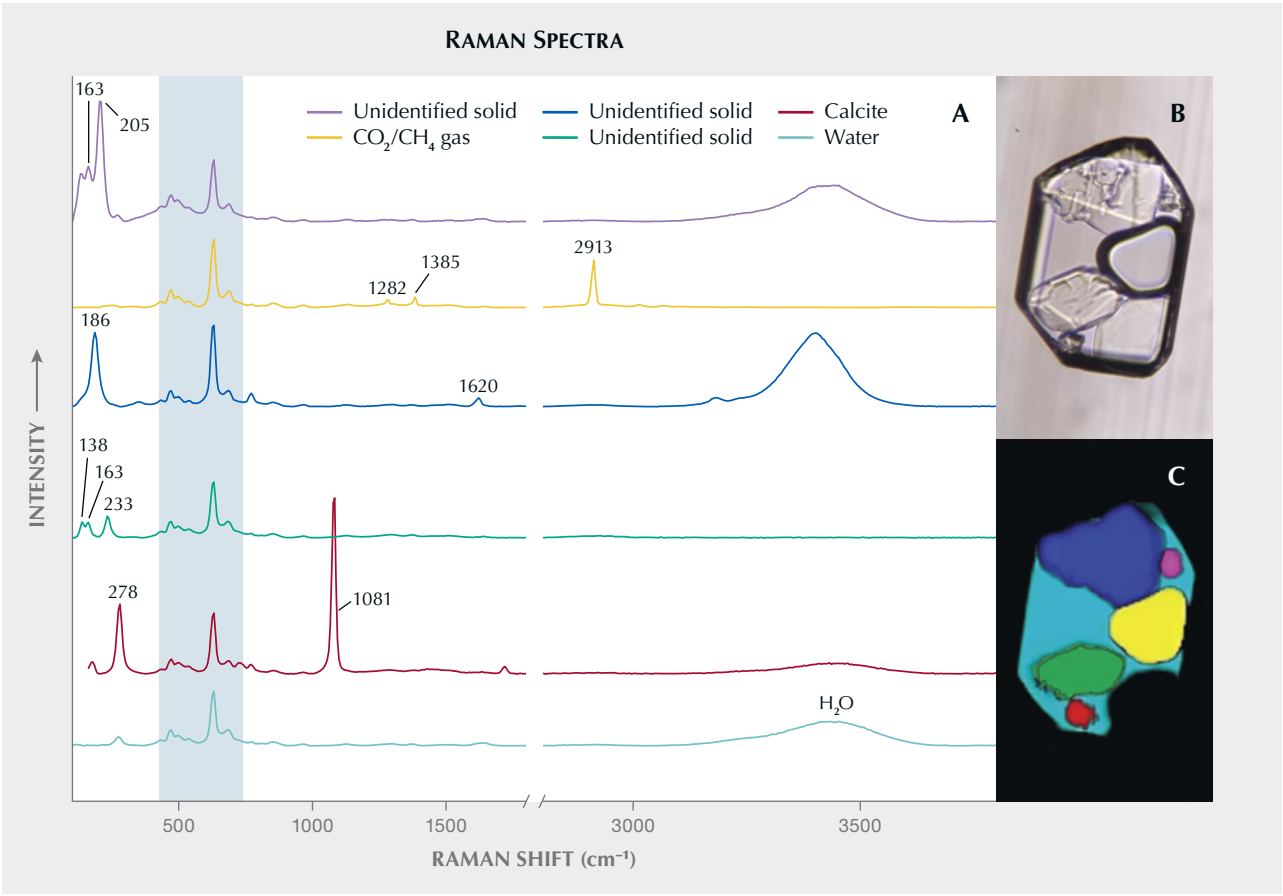

Figure 19. The Raman map (C) and corresponding baseline-corrected Raman spectra (A) of a selected multi-phase, multi-solid fluid inclusion in sample C-G8 (B; field of view 0.095 mm). The solid in the bottom right of the inclusion showed no Raman bands and is possibly halite. Three of the regions in the imaged inclusion (purple, blue, and green) could not be identified. Major Raman bands of the host cassiterite are highlighted in the light blue area of the plot.

curred either in healed fractures or as isolated inclusions. Raman analysis of a representative multi-solid inclusion indicated that the primary compositions of the liquid and vapor were water and carbon dioxide–methane, respectively (figure 19). Within this inclusion, five distinct solid phases were found. One of these solids exhibited characteristic bands at 1081 and 278 cm^{-1}, indicating a carbonate, possibly calcite. The transparent mineral located in the bottom right corner of figure 19B did not display any Raman signal, suggesting the possibility of halite. The other three solid phases showed vibrations at 163–205, 186, and 138–163–233 cm^{-1}, respectively (figure 19A), but we were unable to positively identify them based on the RRUFF database references.

Trace Element Compositions. The 17 faceted samples from Yunling were analyzed by LA-ICP-MS. Table 1 presents the representative trace elements for each sample, including their concentration ranges and corresponding averages. Other elements such as lithium, beryllium, sodium, zinc, and germanium were generally below or close to the detection limits. Notably, the high apparent values of indium were influenced by interference between ^{115}Sn and ^{115}In (Pavlova et al., 2015; Gemmrich et al., 2021). Therefore, these measurements are excluded from this report.

The titanium and iron contents ranged widely, from 8.08 to 1155 ppmw for titanium and from 25.7 to 425 ppmw for iron. The red sample had the highest iron values (see table 1). Titanium was more prevalent in black and light brown cassiterite. The concentrations of magnesium, aluminum, scandium, vanadium, chromium, antimony, cesium, and hafnium were mostly below 10 ppmw, with variations within each color group. The highest aluminum concentration, reaching 31.5 ppmw, was observed in the red sample. Among the various color

TABLE 1. Trace element concentrations[a] (in ppmw) of 17 faceted cassiterites in this study, compared with the Viloco mine, Bolivia (Gemmrich et al., 2021).

Element	Near-colorless		Light Brown					Brownish pink		
	Sample C1 (5 analyses)	Sample C2 (5 analyses)	Sample C3 (6 analyses)	Sample C4 (5 analyses)	Sample C5 (6 analyses)	Sample C6 (5 analyses)	Sample C7 (6 analyses)	Sample C8 (6 analyses)	Sample C9 (5 analyses)	Sample C10 (5 analyses)
Mg	0.03–0.10 (0.05)	bdl[b]–0.05 (0.04)	0.03–0.15 (0.08)	0.09–0.09 (0.07)	0.24–0.31 (0.28)	0.06–0.15 (0.10)	bdl–0.27 (0.16)	0.05–0.13 (0.09)	0.08–0.13 (0.09)	0.13–0.28 (0.19)
Al	11.2–14.6 (12.6)	4.75–5.26 (5.11)	5.70–6.54 (6.05)	5.37–5.88 (5.57)	4.64–5.97 (5.31)	6.87–8.94 (7.73)	2.68–9.43 (4.33)	1.47–2.03 (1.81)	4.51–6.25 (5.28)	5.87–12.2 (9.99)
Sc	2.69–3.69 (3.14)	1.04–1.30 (1.20)	0.69–1.02 (0.89)	2.07–2.47 (2.24)	3.75–4.61 (4.04)	1.80–4.23 (2.96)	1.68–6.04 (2.49)	1.14–1.75 (1.39)	1.40–1.74 (1.59)	1.15–3.89 (3.01)
Ti	162–217 (183)	77.3–114 (99.8)	138–205 (163)	193–285 (244)	989–1153 (1070)	171–566 (391)	142–723 (361)	301–390 (338)	223–318 (271)	494–875 (613)
V	2.63–4.58 (3.32)	0.97–1.22 (1.09)	1.43–2.08 (1.82)	6.74–7.68 (7.31)	14.8–19.5 (16.8)	2.98–6.27 (4.49)	6.26–9.73 (7.25)	0.70–1.47 (1.00)	1.12–1.72 (1.45)	3.19–18.8 (12.2)
Cr	1.39–2.33 (1.79)	bdl–2.51 (1.74)	bdl–2.50 (1.82)	1.53–2.70 (2.12)	7.14–9.61 (8.67)	bdl–3.28 (2.66)	1.45–2.96 (2.27)	1.20–2.42 (1.65)	bdl–3.40 (2.28)	1.83–4.27 (2.89)
Fe	173–217 (197)	78–87 (83)	77–81 (79)	108–117 (113)	94–113 (109)	123–163 (134)	61–170 (86)	48–65 (55)	93–133 (106)	106–218 (157)
Co	8.29–9.27 (8.63)	8.46–8.98 (8.75)	8.80–9.08 (8.94)	8.90–9.80 (9.23)	8.83–9.36 (9.09)	8.60–9.48 (9.11)	8.95–9.70 (9.37)	9.15–9.79 (9.41)	8.87–9.66 (9.28)	9.01–9.60 (9.25)
Ni	57.4–61.6 (59.7)	56.8–60.8 (59.4)	58.3–60.6 (59.4)	58.8–61.0 (60.2)	60.9–63.7 (62.6)	59.5–65.0 (61.4)	61.8–65.6 (63.8)	62.1–65.9 (63.7)	63.3–65.7 (64.2)	63.1–65.2 (64.2)
Ga	0.14–0.25 (0.22)	bdl–0.19 (0.14)	0.07–0.13 (0.10)	0.09–0.13 (0.11)	0.12–0.17 (0.13)	0.09–0.20 (0.16)	bdl–0.20 (0.13)	bdl–0.11 (0.09)	bdl–0.17 (0.12)	0.10–0.26 (0.18)
Zr	2.12–5.63 (4.21)	0.34–0.82 (0.60)	3.78–7.59 (5.17)	0.64–1.42 (1.19)	14.6–20.5 (16.4)	0.54–33.7 (19.6)	0.23–32.6 (6.97)	12.7–22.1 (17.4)	2.15–4.45 (3.12)	3.40–9.93 (6.18)
Nb	0.22–0.29 (0.25)	0.16–0.36 (0.24)	0.55–2.49 (1.02)	0.46–3.21 (1.87)	0.92–1.51 (1.23)	0.27–16.2 (9.30)	0.19–26.3 (6.71)	7.56–12.3 (9.68)	1.77–10.6 (6.76)	11.3–46.5 (28.1)
Sb	0.56–0.67 (0.63)	0.48–0.62 (0.55)	0.40–0.59 (0.51)	0.35–0.60 (0.51)	0.58–0.77 (0.65)	0.48–0.61 (0.54)	0.52–0.67 (0.58)	0.49–0.60 (0.55)	0.59–0.78 (0.68)	0.49–0.71 (0.59)
Cs	bdl–0.02 (0.02)	bdl–0.02 (0.02)	bdl–0.02 (0.02)	bdl–0.03 (0.02)	0.01–0.03 (0.02)	bdl–0.03 (0.02)	bdl–0.03 (0.02)	bdl–0.02 (0.02)	bdl–0.02 (0.02)	bdl–0.02 (0.01)
Ba	0.12–0.28 (0.18)	bdl–0.24 (0.17)	0.09–0.35 (0.16)	bdl–0.19 (0.15)	bdl–0.25 (0.17)	bdl–0.23 (0.19)	bdl–0.23 (0.17)	bdl–0.24 (0.19)	bdl	bdl–0.17 (0.15)
Hf	0.07–0.19 (0.14)	bdl–0.04 (0.02)	0.06–0.24 (0.13)	bdl–0.10 (0.06)	0.47–1.18 (0.76)	bdl–2.36 (2.04)	bdl–2.39 (0.66)	0.66–2.02 (1.44)	bdl–0.12 (0.06)	0.09–0.43 (0.20)
Ta	0.22–0.56 (0.33)	0.10–0.18 (0.16)	0.16–1.45 (0.45)	0.21–0.39 (0.29)	0.96–1.18 (1.08)	0.10–11.6 (5.46)	0.05–23.8 (4.46)	5.46–14.3 (7.91)	0.52–1.25 (0.76)	2.07–7.42 (4.45)
W	0.84–1.09 (0.95)	0.11–0.17 (0.14)	bdl–0.14 (0.05)	bdl–0.10 (0.07)	0.17–0.44 (0.35)	0.45–0.91 (0.65)	0.25–1.05 (0.41)	bdl–0.14 (0.10)	bdl–0.36 (0.26)	0.13–0.32 (0.22)
U	0.03–0.06 (0.04)	0.01–0.04 (0.02)	bdl–0.02 (0.02)	0.01–0.03 (0.02)	0.01–0.09 (0.05)	0.02–0.12 (0.07)	0.01–0.13 (0.04)	bdl–0.03 (0.02)	0.03–0.06 (0.04)	0.04–0.75 (0.45)

[a]*Data reported in minimum to maximum values, with averages in parentheses.*
[b]*bdl = below detection limit*

TABLE 1 (continued). Trace element concentrations[a] (in ppmw) of 17 faceted cassiterites in this study, compared with the Viloco mine, Bolivia (Gemmrich et al., 2021).

Element	Brown		Black		Red	Light gray		Yunling (China) in summary (91 analyses on 17 samples)		Viloco (Bolivia) (81 analyses on 24 samples)	
	Sample C11 (6 analyses)	Sample C12 (5 analyses)	Sample C13 (6 analyses)	Sample C14 (5 analyses)	Sample C15 (5 analyses)	Sample C16 (5 analyses)	Sample C17 (5 analyses)	Range	Detection limits	Range	Detection limits
Mg	bdl–0.19 (0.08)	bdl–0.04 (0.03)	0.07–0.33 (0.20)	0.27–0.32 (0.30)	bdl–0.03 (0.02)	bdl–0.07 (0.06)	0.05–0.13 (0.07)	bdl–0.33 (0.12)	0.005–0.07	bdl–4.63 (1.20)	0.04–4.20
Al	9.86–18.2 (14.5)	9.90–20.6 (13.7)	1.00–1.83 (1.34)	0.38–0.46 (0.43)	9.81–31.5 (21.6)	3.77–5.28 (4.61)	5.15–6.53 (5.75)	0.38–31.5 (7.27)	0.05–0.13	bdl–736 (96.0)	0.19–16.1
Sc	0.22–0.57 (0.41)	bdl–0.18 (0.12)	0.86–2.28 (1.37)	1.15–1.61 (1.42)	0.38–0.76 (0.50)	0.35–0.83 (0.52)	1.33–1.86 (1.64)	bdl–6.04 (1.74)	0.04–0.10	bdl–94.2 (9.79)	0.01–1.18
Ti	18.6–61.8 (37.5)	8.08–18.9 (13.2)	396–570 (475)	1026–1155 (1085)	22.6–52.7 (32.6)	64.1–186 (139)	208–264 (241)	8.08–1155 (343)	0.05–0.65	bdl–12172 (1156)	0.17–23.6
V	0.30–0.75 (0.52)	bdl–0.14 (0.10)	0.21–0.76 (0.46)	1.58–1.88 (1.68)	0.31–0.83 (0.51)	0.31–0.66 (0.46)	2.79–4.18 (3.28)	bdl–19.52 (3.89)	0.03–0.08	bdl–849 (70.1)	0.01–0.73
Cr	1.93–2.61 (2.28)	bdl–1.92 (1.71)	bdl–2.42 (2.08)	bdl–3.12 (1.91)	1.12–1.99 (1.55)	1.72–2.64 (2.23)	1.63–2.86 (2.32)	bdl–9.61 (2.56)	0.83–1.61	bdl–465 (19.4)	0.08–9.10
Fe	149–247 (219)	123–271 (174)	35–192 (84)	26–36 (31)	148–425 (297)	65–94 (80)	85–113 (102)	26–425 (122)	5–9	400–11200 (2623)	0.34–67.1
Co	9.23–9.61 (9.41)	8.89–9.94 (9.35)	9.25–9.58 (9.45)	9.39–9.85 (9.62)	9.48–9.77 (9.62)	9.30–9.59 (9.50)	9.08–10.1 (9.64)	8.29–10.1 (9.27)	0.004–0.05	0.54–76.7 (8.31)	0.003–0.37
Ni	62.5–66.7 (64.6)	62.2–64.1 (63.2)	63.8–66.4 (65.3)	63.5–66.4 (64.9)	63.5–66.7 (64.7)	64.6–69.3 (67.4)	63.9–67.8 (65.8)	56.8–69.3 (63.2)	0.02–0.34	3.11–416 (45.0)	0.12–19.5
Ga	bdl–0.35 (0.28)	0.19–0.55 (0.32)	bdl	bdl	0.19–0.43 (0.29)	bdl	0.09–0.21 (0.15)	bdl–0.55 (0.18)	0.03–0.10	0.42–42.5 (5.60)	0.005–0.67
Zr	1.44–3.18 (2.12)	0.60–0.86 (0.69)	29.3–43.1 (35.2)	3.58–12.7 (8.29)	0.25–2.54 (0.78)	4.46–12.6 (9.38)	2.12–3.84 (2.98)	0.23–43.1 (8.63)	0.005–0.06	bdl–350 (20.7)	0.01–1.08
Nb	0.04–0.08 (0.06)	0.07–0.17 (0.12)	224–911 (460)	180–234 (213)	0.24–1.46 (0.72)	0.40–3.16 (1.40)	0.82–1.44 (1.17)	0.04–911 (46.0)	0.004–0.04	bdl–1011 (36.1)	0.001–0.10
Sb	0.51–1.54 (0.72)	0.41–0.86 (0.57)	0.65–1.03 (0.85)	1.76–2.37 (2.05)	0.53–0.67 (0.60)	0.37–0.67 (0.49)	0.53–0.61 (0.56)	0.34–2.37 (0.68)	0.01–0.12	3.25–400 (43.3)	0.004–0.53
Cs	bdl–1.33 (0.35)	bdl–0.03 (0.02)	bdl–0.03 (0.02)	bdl–0.02 (0.01)	bdl–0.02 (0.02)	bdl–0.02 (0.02)	bdl–0.02 (0.02)	bdl–1.33 (0.04)	0.002–0.03	—	—
Ba	bdl–1.28 (0.58)	bdl–0.16 (0.13)	bdl–0.31 (0.25)	bdl–0.22 (0.20)	bdl–0.20 (0.14)	bdl–0.20 (0.15)	bdl–0.11 (0.11)	bdl–1.28 (0.19)	0.02–0.22	0.57–60.6 (7.75)	0.05–6.15
Hf	bdl–0.08 (0.06)	bdl–0.02 (0.02)	1.45–2.14 (1.73)	0.06–0.26 (0.14)	bdl–0.05 (0.04)	0.32–1.19 (0.84)	bdl–0.11 (0.09)	bdl–2.39 (0.57)	0.01–0.09	0.01–6.05 (0.30)	0.001–0.11
Ta	0.04–0.18 (0.09)	0.07–0.18 (0.10)	4.86–84.3 (35.1)	0.07–0.79 (0.41)	0.18–1.93 (0.56)	0.86–1.71 (1.25)	1.37–2.63 (1.98)	0.04–84.2 (4.10)	0.003–0.03	0.003–114 (1.78)	0.0004–0.05
W	0.34–2.19 (0.78)	0.48–0.86 (0.64)	115–327 (202)	149–176 (160)	bdl–0.11 (0.08)	0.16–0.26 (0.21)	0.27–0.52 (0.36)	bdl–327 (24.6)	0.01–0.17	0.05–33138 (2729)	0.001–0.11
U	0.01–0.05 (0.03)	0.01–0.04 (0.03)	6.48–12.1 (9.75)	14.1–17.8 (15.7)	0.02–0.11 (0.06)	bdl–0.04 (0.03)	0.02–0.05 (0.03)	bdl–17.8 (1.65)	0.004–0.02	0.01–332 (17.8)	0.0002–0.05

[a]*Data reported in minimum to maximum values, with averages in parentheses.*
[b]*bdl = below detection limit*

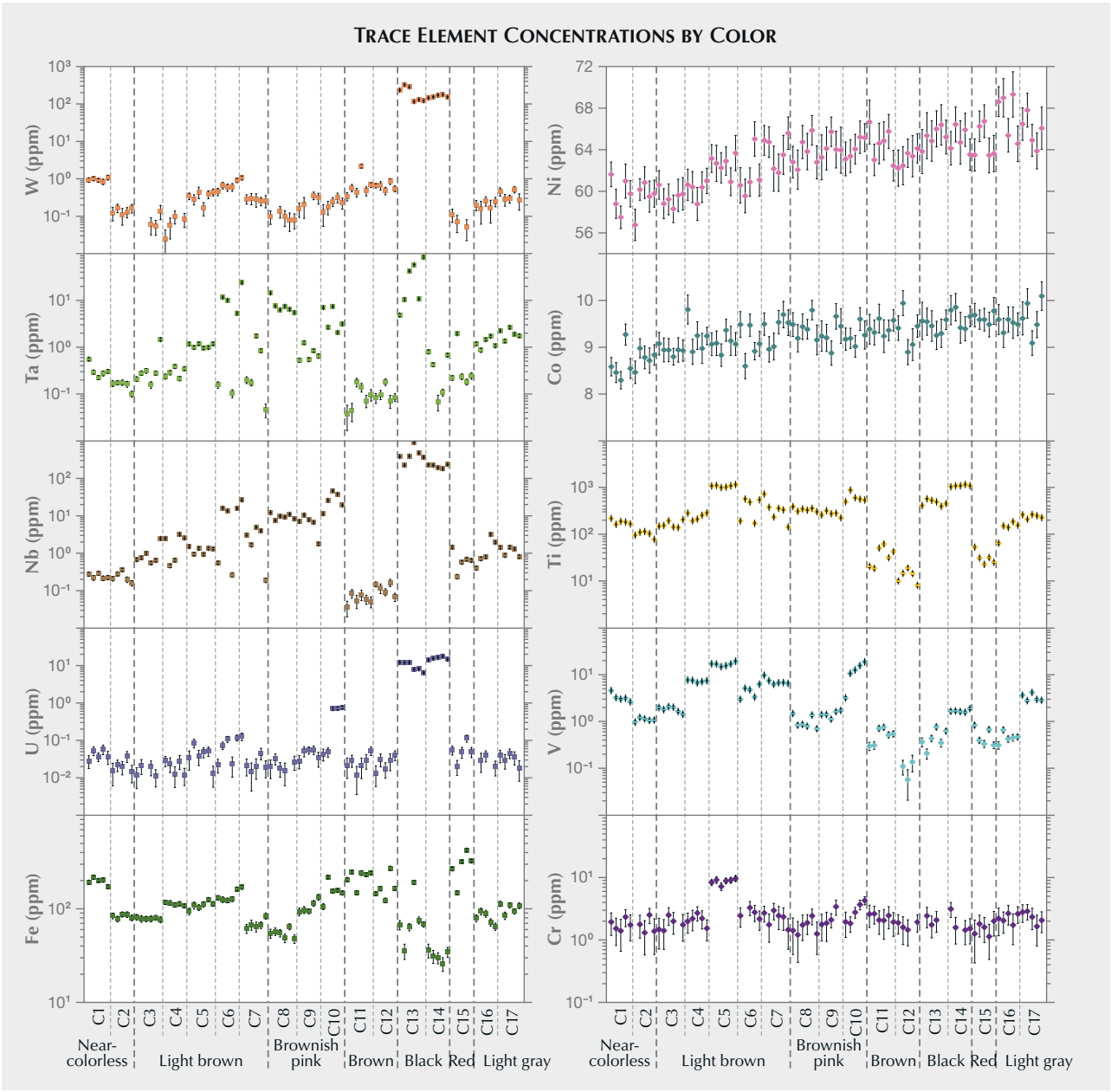

Figure 20. Selected trace element diagrams showing the geochemistry profiles of the most common chromophores in gem materials (iron, nickel, cobalt, titanium, vanadium, and chromium) and potential color-producing elements for cassiterite (tungsten, tantalum, niobium, and uranium). The individual data points represent trace element concentrations for test samples. Note that the vertical scales are different for the various elements: Nickel and cobalt are linear, while the other elements are log plots.

groups, vanadium exhibited the highest concentration in the light brown samples (19.5 ppmw) and brownish pink samples (up to 18.8 ppmw). Niobium and tungsten showed significant variation, ranging from 0.04 to 911 ppmw for niobium and from below detection limit to 327 ppmw for tungsten (table 1). The black cassiterite samples had the highest concentrations of tungsten (115–327 ppmw) and niobium (180–911 ppmw) (figure 20). The black samples also contained higher concentrations of uranium (6.48–17.8 ppmw) and zirconium (3.58–43.1 ppmw) than the other color groups (table 1). However, it is worth noting that the zirconium maximum was almost as high in the light brown (33.7 ppmw) and brownish pink (22.1 ppmw) samples. Cobalt and nickel compositions remained relatively constant across all color groups,

with ranges of 8.29–10.1 ppmw and 56.8–69.3 ppmw, respectively (figure 20).

UV-Vis-NIR Absorption Spectra. The UV-Vis-NIR spectra representative of the seven color groups are shown in figure 21 (left). A notable characteristic of near-colorless, light brown, brownish pink, and light gray cassiterite was a strong absorption band that shifted from the near-UV region (~350 nm) to the violet region (~400 nm). The brownish pink variety also showed a broad band centered around 490 nm. In contrast, the light brown and brown cassiterite exhibited increasing absorption from the red to violet regions, while the black samples displayed a relatively uniform absorption across the entire visible light range. The red cassiterite sample exhibited a broad transmission window spanning from 570 to 800 nm. Notably, the Vis-NIR reflectance spectrum of the red cassiterite closely resembled that of hematite and, to a lesser extent, goethite (figure 21, right).

DISCUSSION

Correlation Between Trace Elements and Colors. Gem materials derive their colors predominantly from dispersed metal ions, such as Cr^{3+}, Cu^{2+}, and Co^{2+}; their colors can also arise from combinations of ions, such as the intervalence charge transfer species Fe^{2+}–O–Fe^{3+} in beryl, or color centers like the GR1 center in diamond (Fritsch and Rossman, 1987, 1988a). In some cases, the presence of a colored mineral within the host can also contribute to a gem's color (Fritsch and Rossman, 1988b). However, the color-producing mechanism for cassiterite is rarely described, partly due to the scarcity of gem cassiterite with various colors.

Previous studies have attempted to establish the correlation between color variations and trace element compositions in natural cassiterite, leading to varying conclusions. Mossbauer spectroscopy has shown that cassiterite's color bears no relationship with the total iron composition but is instead influenced by the Fe^{2+}/Fe^{3+} ratios; the dark (black and brown) zones contain higher Fe^{2+}/Fe^{3+} ratios than the colorless ones (Grubb and Hannaford, 1966). On the other hand, some studies have shown that the dark zones contain higher concentrations of iron, niobium, tantalum, tungsten, and titanium (Goncharov and Filatov, 1971; Ollila, 1986; Nambaje et al., 2020). In certain cases, uranium (Swart and Moore, 1982) and uranium-tungsten (Guo et al., 2018) have been proposed as possible factors influencing the color, with higher contents corresponding to darker (dark brown) color zones. However, these interpretations are based solely on the geochemical perspective, and no optical absorption spectroscopy studies have been conducted.

Figure 21. Left: Representative UV-Vis-NIR absorption spectra for the seven colors of Yunling cassiterite. Right: Vis-NIR reflectance spectra of the red Yunling cassiterite sample, compared with those of hematite and goethite (from Harris et al., 2015).

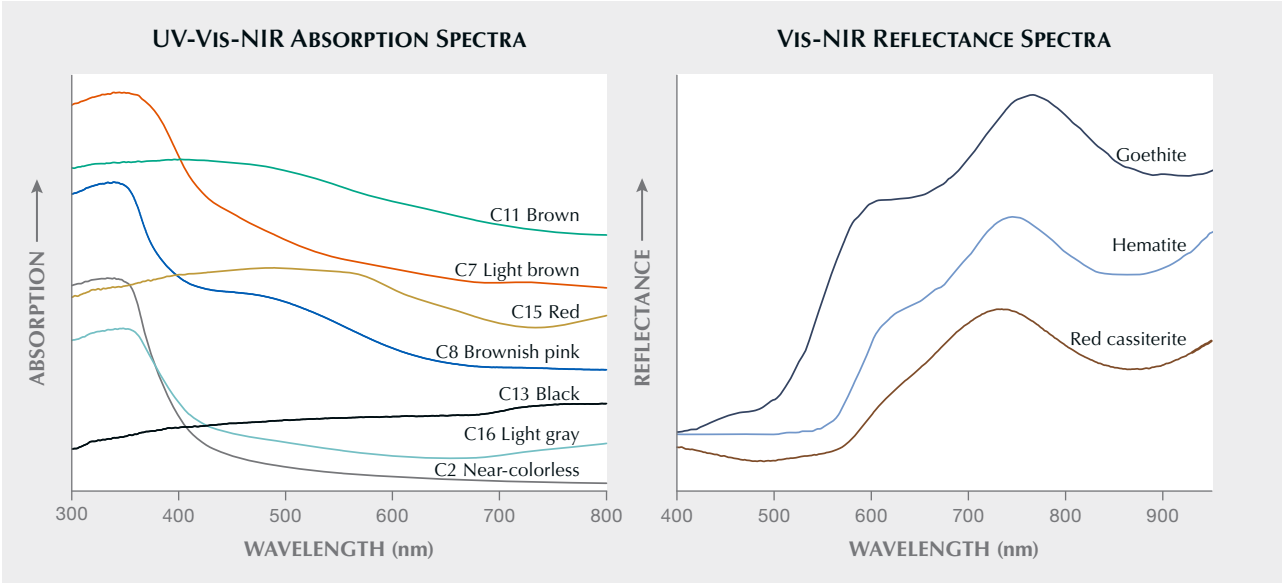

Meanwhile, the color mechanism of impurity-doped synthetic cassiterite, widely used as a pigment in the ceramics industry, has undergone extensive research. A violet color has been linked to the presence of Cr^{4+}, generating a characteristic band at 550 nm (Lopez-Navarrete et al., 2003; Serment et al., 2019). The contribution of Cr^{3+} and/or Cr^{4+} to the violet hue has also been suggested, with Cr^{3+} in cassiterite displaying characteristic bands at 650 and 470 nm (Ishida et al., 1987). Investigation by Matsushima et al. (2008) into dark brown films suggests that color origin may stem from chloride impurities and/or oxygen vacancies. Moreover, the incorporation of high field strength elements into cassiterite can alter its color appearance. For example, antimony imparts a light gray hue (Tena et al., 2005) or black (Kojima et al., 1996), attributed to charge transfer interactions between Sb^{3+} and Sb^{5+} within the matrix. These insights underscore the intricate nature of cassiterite's color mechanism, dictated by the interplay of the impurity species and their respective oxidation states.

Figure 20 shows common chromophores in gem materials (iron, nickel, cobalt, titanium, vanadium, and chromium), along with potential color-producing elements for cassiterite (tungsten, tantalum, niobium, and uranium). The consistently low cobalt and nickel concentrations across the seven color groups imply a limited role in cassiterite coloration. Notably, the iron concentrations in one near-colorless sample (sample C1) stood out from the other (sample C2; see table 1 and figure 20). Further microscopic examination of sample C1 revealed that high iron concentrations were associated with colorless areas rather than dark brown or brownish pink areas. This implies that iron does not significantly contribute to the color of pink and brown samples, as brownish pink sample C8 and light brown sample C3 were comparable in iron content to near-colorless sample C2, which had the lower iron content of the two near-colorless samples (figure 20). Although Guo et al. (2018) found higher uranium and tungsten compositions in the dark brown zones than in the light yellow domains, their low concentration in both the brown group and the light brown group suggests a minimal influence on the brown color (table 1; figure 20). In other words, impurities other than uranium-tungsten may be responsible for the brown color of Yunling cassiterite. Noticeably elevated tungsten contents are frequently found in the black cassiterite group (avg. 183 ppmw; table 1; see also Huang et al., 2023), suggesting that tungsten may contribute to the black coloration. This is supported by Zhou et al. (2018), in which doped tungsten was shown to enhance the visible light absorption of cassiterite. It is important to note that tungsten impurities in cassiterite often exist in hexavalent and tetravalent states (Möller et al., 1988; Bennett, 2021). While W^{4+} does not impact the color of cassiterite, W^{6+} can contribute to the black color through tungsten-oxygen charge transfer (Nomiya et al., 1987).

Further UV-Vis-NIR spectroscopic analysis revealed distinct absorption spectra among different colors of cassiterite (figure 21, left). Absorptions related to Cr^{3+} (650 and 470 nm) or Cr^{4+} (550 nm) were not observed in any of the samples. In brownish pink cassiterite, a broad absorption band centered at approximately 490 nm might account for its pink color; however, similar bands have not been previously reported, and the specific nature of this 490 nm band remains unclear. The absorption spectra of light brown and brown cassiterite, displaying a gradual decrease in absorption strength with wavelength, resembled the dark brown SnO_2 film presented in figure 3 of Matsushima et al. (2008). According to those authors, the dark brown coloration may stem from impurities such as chloride and/or oxygen vacancies. Oxygen vacancies are commonly found in magmatic-hydrothermal cassiterite, as reported by Grigor'yev et al. (1986), and these samples typically display a dark brown or black coloration that becomes more intense with an increased number of oxygen vacancies. Therefore, the origin of the brown (and possibly light brown) color in cassiterite from Yunling could be linked to the presence of oxygen vacancies. The color of the black cassiterite, which is influenced by tungsten, could also be associated with the presence of oxygen vacancies. The red cassiterite from Yunling exhibited a broad transmission at approximately 710 nm (figure 21, left). Microscopic examination revealed highly heterogeneous color distribution in the analyzed red cassiterite, in which the red color was concentrated exclusively in the fractures (figure 9C). Hence, iron oxide staining in the fractures, rather than trace elements or lattice defects, was likely responsible for this coloration. This inference is supported by its Vis-NIR reflectance spectrum (figure 21, right), which is highly consistent with that of hematite, a common red-colored iron oxide found in soil and sediments.

Substitutional Mechanism of Trace Elements. Cassiterite possesses a tetragonal lattice structure analogous to that of rutile, allowing the incorporation of

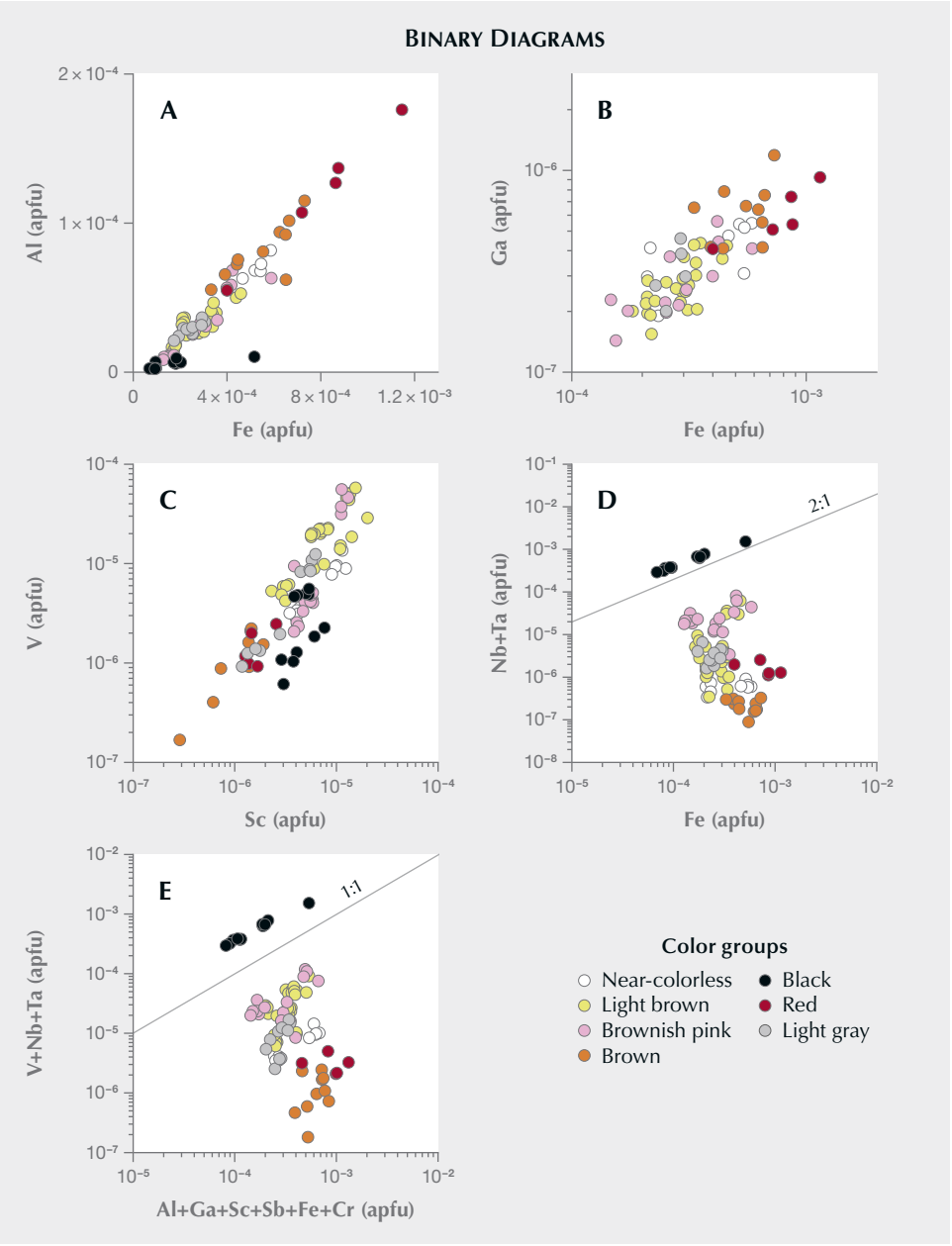

Figure 22. Binary diagrams of selected trace elements in cassiterite from Yunling, expressed in atoms per formula unit (apfu). A: The positive relationship between aluminum and iron is likely due to their similar trivalent ionic radii. B: Gallium and iron show a positive correlation, indicating a coupled substitution of $2Sn^{4+} \leftrightarrow Fe^{3+} + Ga^{5+}$. C: The positive relationship between scandium and vanadium implies that vanadium is in a valence state of +5, with a substitution mechanism of $2Sn^{4+} \leftrightarrow Sc^{3+} + V^{5+}$. D: A significant deviation from the 2:1 line in the Nb+Ta vs. Fe plot for most samples implies a significant iron excess. E: The plot comparing trivalent cations (aluminum, scandium, iron, gallium, chromium, and antimony) and pentavalent cations (vanadium, niobium, and tantalum) shows a significant excess of trivalent cations for most samples. Note that the scales are different for the various plots: A is linear, while B–E are log-log plots.

various trace elements such as iron, vanadium, scandium, titanium, tungsten, and uranium (Farmer et al., 1991; Tindle and Breaks, 1998; Bennett et al., 2020). However, the occurrence and substitution mechanisms of these trace elements are not well constrained and may vary among deposits (e.g., Gemmrich et al., 2021; He et al., 2022). The incorporation of trace elements into cassiterite depends largely on ionic charge, radius, and coordination, allowing compatibility with a wide range of elements in different valence states (e.g., Grubb and Hannaford, 1966; Möller et al., 1988; Murciego et al., 1997). Tetravalent elements such as Ti^{4+}, Zr^{4+}, and Hf^{4+} can directly substitute for Sn^{4+} without requiring additional ions for charge balance. In contrast, trivalent and pentavalent elements require other elements for charge compensation, as seen in examples such as $3Sn^{4+} \leftrightarrow 2(Ta, Nb)^{5+} + Fe^{2+}$ or $3Sn^{4+} \leftrightarrow W^{6+} + 2Fe^{3+}$.

In figure 22 we use the unit apfu (atoms per formula units) and the conversion from ppmw to apfu as follows:

$$apfu = \frac{molecular\ weight\ of\ SnO_2 \times (ppmw \times 10^{-6})}{atomic\ weight\ of\ the\ element}$$

The Fe-Al (figure 22A) and Fe-Ga (figure 22B) pairs yield a positive relationship in the Yunling cassiterite samples. This positive correlation between iron and aluminum is likely due to the similarity in trivalent ion radii (Shannon, 1976). Similarly, the Yunling cassiterite exhibited a positive correlation between iron and gallium that is analogous to what has been observed in many granite-associated hydrothermal cassiterites (e.g., He et al., 2022). This correlation can be explained by the coupled substitution of $2Sn^{4+} \leftrightarrow Fe^{3+} + Ga^{5+}$. Furthermore, the positive relationship between scandium and vanadium (figure 22C) implies that vanadium is in a valence state of +5, considering that scandium occurs only in a +3 valence state in geological conditions. Therefore, a substitution mechanism of $2Sn^{4+} \leftrightarrow Sc^{3+} + V^{5+}$ is favored.

It is well established that niobium and tantalum are incorporated into cassiterite in the pentavalent state through a coupled substitutional mechanism involving iron (Möller et al., 1988; Neiva, 1996). Figure 22D shows a marked deviation from the 2:1 line in most of the sample analyses, implying a significant iron excess. This surplus iron indicates additional substitution in the samples. Considering a broader range of trivalent (aluminum, scandium, iron, gallium, chromium, and antimony) and pentavalent (vanadium, niobium, and tantalum) cations dominant in cassiterite, the data would be expected to plot along the 1:1 ratio. However, there appears to be a deviation indicating a significant excess of trivalent cations (figure 22E). The low concentrations of lithium, mostly below detection limits, make its compensation impossible. In order to balance the uncompensated trivalent cations, potential compensating cations could be H^+ (Tindle and Breaks, 1998; Mao et al., 2020) or interstitial Sn^{2+} (as proposed by Cohen et al., 1985). Moreover, the black samples in figures 22D and 22E stand out from the other color groups on these plots. Recent studies have shown that individual cassiterite crystals exhibit distinct chemistries within each zone that appears dark in cathodoluminescence imaging, driven by specific substitution mechanisms (Bennett, 2021; Huang et al., 2023). Therefore, the observed variations observed in figures 22D and 22E could be attributed to cathodoluminescence-dark zones in the black samples (Huang et al., 2023).

Geographic Origin Determination. Although large euhedral cassiterite of gem quality from the Viloco mine in Bolivia was documented more than 20 years ago (Hyršl, 2002), comprehensive gemological properties remained lacking. Nevertheless, trace element spectra of cassiterite from the Viloco mine (Gemmrich et al., 2021) allow comparative analysis with the Yunling deposit (table 1).

Box and whisker plots in figure 23 illustrate the concentration of 12 selected elements, revealing broader ranges for elements such as tantalum, uranium, cobalt, and titanium in Viloco cassiterite compared to Yunling. Yunling cassiterite typically has a lower iron concentration, but the ranges overlap (as they do for all elements). The low iron concentration of Yunling cassiterite (generally <200 ppmw) is atypical of granite-related cassiterite deposits worldwide (Hennigh and Hutchinson, 1999; Guo et al., 2018; Chen et al., 2019). However, a granite-related petrogenesis has been suggested for this deposit (Xiao et al., 2022), supported by the vein occurrence and mineralogy comparable to other granite-related deposits. High-salinity fluid inclusions (figure 16) provide further evidence for its magmatic-hydrothermal origin. To our knowledge, the low iron content in Yunling cassiterite is unique. Iron incorporation in the cassiterite lattice typically involves other cations through a coupled substitutional mechanism (e.g., Möller et al., 1988); hence, the low iron content in Yunling cassiterite may be related to the low content of other cations such as niobium, tantalum, and gallium. Notably, the concentrations of cobalt and nickel are consistent in cassiterite from Yunling, regardless of color, while their concentrations in Viloco cassiterite are highly variable, even within a single sample (Gemmrich et al., 2021). For example, in sample Vil2-sn-b examined by Gemmrich et al. (2021), the concentrations of cobalt and nickel varied by an order of magnitude, from 8 to 77 ppm and 45 to 416 ppm, respectively. Therefore, multiple spot measurements of cobalt and nickel concentrations are valuable in separating cassiterite from Yunling and Viloco.

Figure 24 displays discrimination plots for Yunling compared to Viloco for Cr-V, U-W, Nb-Fe, and Ni-Sb. Significant overlap is observed in the Cr-V plot (figure 24A), undermining its effectiveness for discrimination. Minor overlap between uranium and tungsten points in Yunling and Viloco cassiterite is also observed in figure 24B. Comparing iron concentrations (figure 24C) and antimony concentrations (figure 24D) in Yunling cassiterite with those in Viloco cassiterite helps to distinguish their origin.

Cassiterite samples from both deposits contain healed fissures and tourmaline needles (Hyršl, 2002), but the presence of beryl and mica inclusions is typical for Yunling and Viloco.

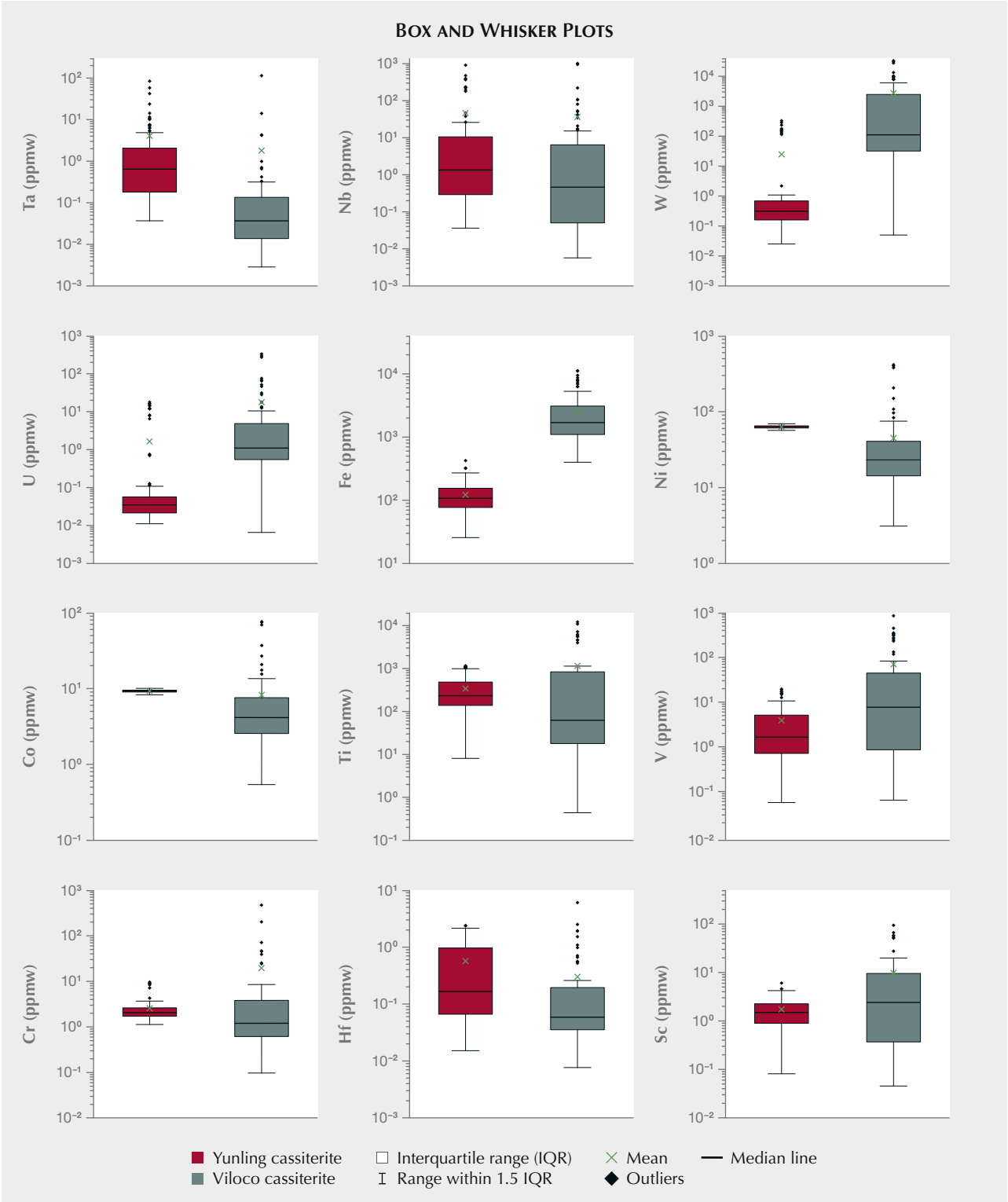

Figure 23. Selected box and whisker plots displaying trace element concentration comparisons in cassiterite from Yunling and Viloco deposits (data from Gemmrich et al., 2021). The number of analyses is 91 for Yunling and 81 for Viloco. Most elements in Viloco cassiterite (e.g., tantalum, uranium, scandium, and titanium) exhibit a wider range of spectra than those in cassiterite from Yunling. In Yunling cassiterite, the iron concentration is notably lower. Unlike Viloco cassiterite, which displays significant variations in cobalt and nickel contents, the concentrations of those elements in Yunling cassiterite remain rather consistent.

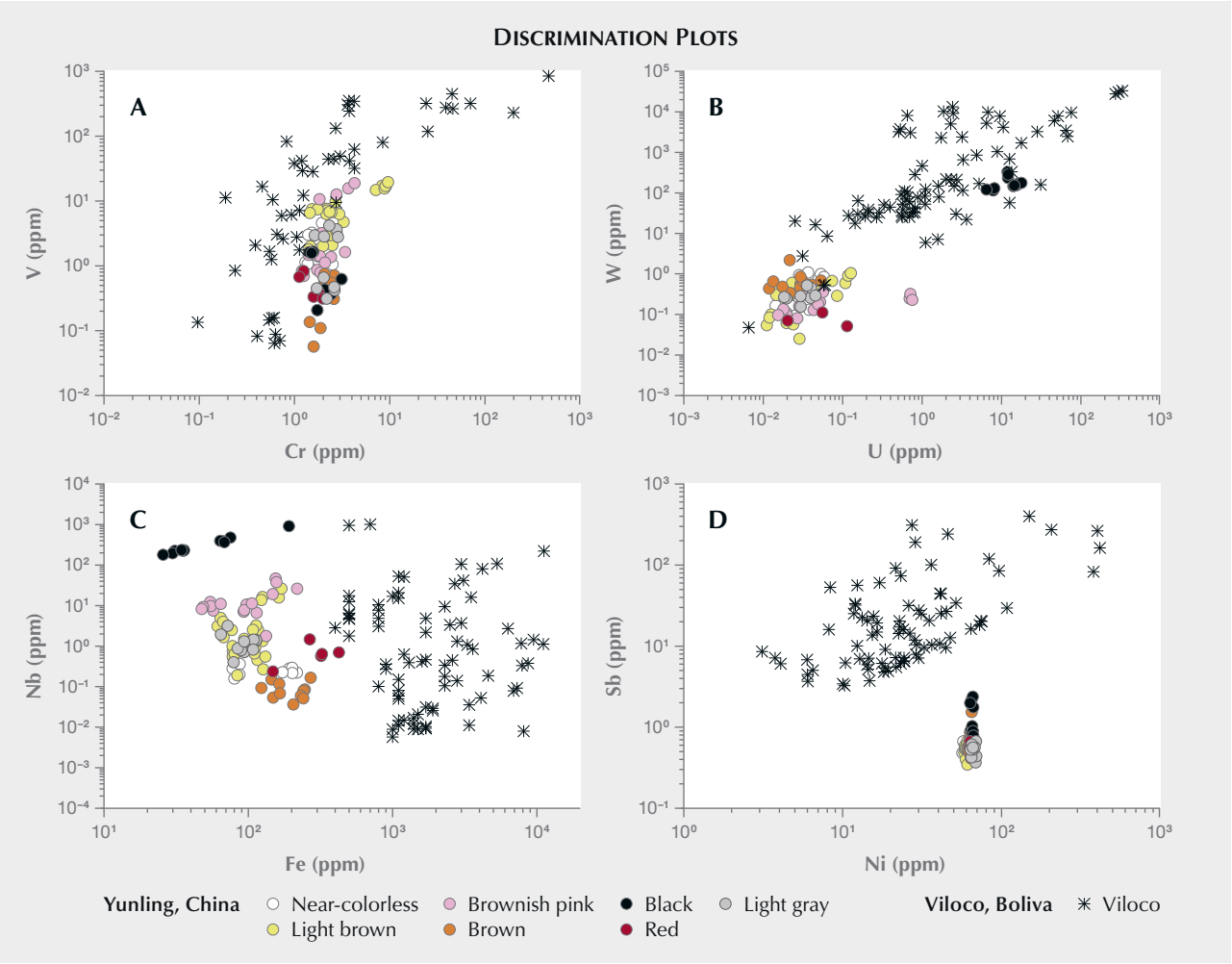

Figure 24. A: Plot of V vs. Cr showing significant overlap between Yunling and Viloco cassiterite. B: Compared to Viloco cassiterite, Yunling cassiterite (except the black samples) contains lower tungsten-uranium. C and D: Trace element plots potentially separating cassiterite from the two deposits, based on lower concentrations of iron and antimony in Yunling cassiterite.

CONCLUSIONS

The Yunling area in Yunnan Province, China, is among the few sources of gem cassiterite, producing mineral specimens since the 1980s. Despite the influx of faceted stones on the Chinese market in recent years, a lack of knowledge of their gemological properties and trace element chemistry exists, a gap this article addresses.

A detailed gemological investigation shows various hues of cassiterite, including near-colorless, light brown, brown, brownish pink, red, light gray, and black. Color bands displaying an oscillatory nature and irregular gray-black color domains are common. Notable mineral inclusions are tourmaline, beryl, and mica. Three-phase fluid inclusions, frequently found in healed fissures, consist of liquid, vapor, and a daughter mineral, probably halite.

Quantitative chemical analysis using LA-ICP-MS showed that the trace elements in the seven color groups of Yunling cassiterite are dominated by titanium (avg. 343 ppmw) and iron (avg. 122 ppmw). Additionally, black samples exhibited significant enrichment in tungsten (avg. 183 ppmw) and uranium (avg. 12 ppmw). The UV-Vis-NIR absorption spectra of the various samples exhibited significant differences, illustrating different sources for the various colors. The black color can be attributed to the presence of trace element tungsten and oxygen vacancies, while the brown color may result from the presence of oxygen vacancies alone. The color of the red sample could be attributed to the contribution of iron

oxide staining within fractures, so this color is not inherently from the host crystal. The underlying cause of pink color remains unresolved and requires further investigation.

Yunling cassiterite typically shows a narrower range of trace element concentrations (e.g., titanium, cobalt, nickel, and chromium) than samples from the renowned deposit in Viloco, Bolivia. Trace element plots of Sb-Ni and Fe-Nb can efficiently discriminate Yunling and Viloco cassiterite. The refinement of geographic origin determination for cassiterite, through additional reliable samples and data from this and other sites, remains an area for further study.

ABOUT THE AUTHORS

Dr. Wenqing Huang (corresponding author, 67019822@qq.com), Professor Jungui Zhou, and Shuxin Dong are affiliated with the National Center of Inspection and Testing on Quality of Gold and Silver Products, Nanjing Institute of Product Quality Inspection in Nanjing. Ting Shui is a professor at Nanjing Center, China Geological Survey in Nanjing. Dr. Junyi Pan (as well as Dr. Huang) is affiliated with State Key Laboratory for Mineral Deposits Research, Institute of Geo-Fluids, Frontiers Science Center for Critical Earth Material Cycling, School of Earth Sciences and Engineering, Nanjing University. Professor Fanwei Meng is affiliated with the School of Resources and Geosciences, China University of Mining and Technology in Xuzhou. Rui Zuo and Suqiao Cao are with the Anhui Provincial Institute of Geological Experiments in Hefei.

ACKNOWLEDGMENTS

The authors would like to thank Yongming Shi for providing valuable photos and related information. This work is financially supported by the National Nature Science Foundation of China (grant number 42272094), the Natural Science Foundation of Jiangsu Province (grant number BK20221171), the Open Foundation of State Key Laboratory for Mineral Deposits Research, Nanjing University (grant number 2023-LAMD-K03), and Natural Resources Science and Technology Project of Anhui Province (grant number 2022-K-12). We sincerely thank the anonymous peer reviewers for feedback that substantially improved the quality of this article.

REFERENCES

Bennett J.M. (2021) On the geochemistry of cassiterite. PhD thesis. University of Western Australia, 191 pp.

Bennett J.M., Kemp A.I.S., Roberts M.P. (2020) Microstructural controls on the chemical heterogeneity of cassiterite revealed by cathodoluminescence and elemental X-ray mapping. *American Mineralogist*, Vol. 105, No. 1, pp. 58–76, http://dx.doi.org/10.2138/am-2020-6964

Chen L.L., Ni P., Dai B.Z., Li W.S., Chi Z., Pan J.Y. (2019) The genetic association between quartz vein-and greisen-type mineralization at the Maoping W–Sn deposit, southern Jiangxi, China: Insights from zircon and cassiterite U–Pb ages and cassiterite trace element composition. *Minerals*, Vol. 9, No. 7, article no. 411, http://dx.doi.org/10.3390/min9070411

Chen X.C., Hu R.Z., Bi X.W., Li H.M., Lan J.B., Zhao C.H., Zhu J.J. (2014) Cassiterite LA-MC-ICP-MS U/Pb and muscovite $^{40}Ar/^{39}Ar$ dating of tin deposits in the Tengchong-Lianghe tin district, NW Yunnan, China. *Mineralium Deposita*, Vol. 49, pp. 843–860, http://dx.doi.org/10.1007/s00126-014-0513-8

Cohen A.J., Adekeye J.I.D., Hapke B., Partlow D.P. (1985) Interstitial Sn^{2+} in synthetic and natural cassiterite crystals. *Physics and Chemistry of Minerals*, Vol. 12, No. 6, pp. 363–369, http://dx.doi.org/10.1007/BF00654347

Crowningshield G.R. (1960) Developments and Highlights at the Gem Trade Lab in New York: Unusual stones. *G&G*, Vol. 10, No. 2, pp. 61–62.

Deer W.A., Howie R.A., Zussman J. (1992) *An Introduction to the Rock-Forming Minerals*. Longman Group UK Ltd., Harlow, UK.

Deng J., Wang Q., Li G., Li C., Wang C. (2014) Tethys tectonic evolution and its bearing on the distribution of important mineral deposits in the Sanjiang region, SW China. *Gondwana Research*, Vol. 26, No. 2, pp. 419–437, http://dx.doi.org/10.1016/j.gr.2013.08.002

Farmer C.B., Searl A., Halls C. (1991) Cathodoluminescence and growth of cassiterite in the composite lodes at South Crofty mine, Cornwall, England. *Mineralogical Magazine*, Vol. 55, No. 380, pp. 447–458, http://dx.doi.org/10.1180/minmag.1991.055.380.14

Frezzotti M.L., Tecce F., Casagli A. (2012) Raman spectroscopy for fluid inclusion analysis. *Journal of Geochemical Exploration*, Vol. 112, pp. 1–20, http://dx.doi.org/10.1016/j.gexplo.2011.09.009

Fritsch E., Rossman G.R. (1987) An update on color in gems. Part 1: Introduction and colors caused by dispersed metal ions. *G&G*, Vol. 23, No. 3, pp. 126–139, http://dx.doi.org/10.5741/GEMS.23.3.126

——— (1988a) An update on color in gems. Part 2: Colors involving multiple atoms and color centers. *G&G*, Vol. 24, No. 1, pp. 3–15, http://dx.doi.org/10.5741/GEMS.24.1.3

——— (1988b) An update on color in gems. Part 3: Colors caused by band gaps and physical phenomena. *G&G*, Vol. 24, No. 2, pp. 81–102, http://dx.doi.org/10.5741/GEMS.24.2.81

Gaievskyi I., Iemelianov I. (2012) Gem News International: Black cassiterite. *G&G*, Vol. 48, No. 1, p. 63.

Gemmrich L., Torró L., Melgarejo J.C., Laurent O., Vallance J., Chelle-Michou C., Sempere T.P.A. (2021) Trace element composition and U-Pb ages of cassiterite from the Bolivian tin belt. *Mineralium Deposita*, Vol. 56, No. 8, pp. 1491–1520, http://dx.doi.org/10.1007/s00126-020-01030-3

Goncharov G.N., Filatov S.K. (1971) Typical structural features of cassiterite from Sherlovaya Gora. *Geochemistry International*, Vol. 8, No. 2, pp. 268–275.

Grigor'yev I.F., Dolomanova Y.I., Podol'skiy A.M., Solntseva L.S., Solntsev B.N. (1986) Dependence of the structural type of cassiterite on its origin. *International Geology Review*, Vol. 28, No. 6, pp. 662–669, http://dx.doi.org/10.1080/00206818609466306

Grubb P.L.C., Hannaford P. (1966) Ferromagnetism and colour zoning in some Malayan cassiterite. *Nature*, Vol. 209, No. 5024, pp. 677–678, http://dx.doi.org/10.1038/209677a0

Gu J.S. (2010) Verification report on the reserves of mineral resources in the Yunling tin mine mining area, Yongde County, Yunnan Province. *Yunnan Geological Survey Report*, 127 pp. [in Chinese].

Guillong M., Meier D.L., Allan M.M., Heinrich C.A., Yardley B.W. (2008) Appendix A6: SILLS: A MATLAB-based program for the reduction of laser ablation ICP-MS data of homogeneous materials and inclusions. *Mineralogical Association of Canada Short Course*, Vol. 40, pp. 328–333.

Guo J., Zhang R., Li C., Sun W., Hu Y., Kang D., Wu J. (2018) Genesis of the Gaosong Sn–Cu deposit, Gejiu district, SW China: Constraints from *in situ* LA-ICP-MS cassiterite U–Pb dating and trace element fingerprinting. *Ore Geology Reviews*, Vol. 92, pp. 627–642, http://dx.doi.org/10.1016/j.oregeorev.2017.11.033

Harris J.R., Williamson M.C., Percival J.B., Behnia P., Macleod R.F. (2015) Detecting and mapping gossans using remotely-sensed data. In M.C. Williamson, Ed., *Environmental and Economic Significance of Gossans*. Geological Survey of Canada, Open file 7718, Ottawa, Ontario, Canada, pp. 3–13.

He X., Zhao J., Zhou R., Feng Y., Leonard N., Li F., Liu Z., Li W., Tan S. (2022) The distribution and substitution mechanism of trace elements in cassiterites: Constraints from LA-ICP-MS U-Pb dating, elemental mapping and *in situ* trace element analyses of the Gejiu tin polymetallic deposit, SW China. *Chemical Geology*, Vol. 609, article no. 121063, http://dx.doi.org/10.1016/j.chemgeo.2022.121063

Hennigh Q., Hutchinson R.W. (1999) Cassiterite at Kidd Creek: An example of volcanogenic massive sulfide-hosted tin mineralization. In M.D. Hannington and C.T. Barri, Eds., *The Giant Kidd Creek Volcanogenic Massive Sulfide Deposit, Western Abitibi Subprovince, Canada*. Economic Geology Publishing Co., Inc., Littleton, Colorado, pp. 431–440.

Huang W.Q., Pan J.Y. (2021) Gem Notes: Cassiterite from Yunnan Province, China. *Journal of Gemmology*, Vol. 37, No. 8, pp. 766–767.

Huang W.Q., Ni P., Pan, J.Y., Zhou J.G., Shui T., Chen H., Fan M.S., Cui J.M., Meng F.W., Ding J.Y. (2023) Relationship between cathodoluminescence response and trace element characterization of cassiterite from the Yunling tin deposit in western Yunnan, China: Implications for substitution mechanism and ore genesis. *Ore Geology Reviews*, Vol. 161, article no. 105610, http://dx.doi.org/10.1016/j.oregeorev.2023.105610

Hyršl J. (2002) Gem News International: Cassiterite from Viloco, Bolivia. *G&G*, Vol. 38, No. 2, pp. 175–176.

Hyršl J., Petrov A. (1998) Gemstones and ornamental stones from Bolivia: A review. *Journal of Gemmology*, Vol. 26, No. 1, pp. 41–47.

Ishida S., Hayashi M., Kato I. (1987) Spectroscopic study of chemical state and coloration of chromium in tin oxide. *Journal of the Ceramic Association, Japan*, Vol. 95, No. 3, pp. 303–308, http://dx.doi.org/10.2109/jcersj1950.95.1099_303 [in Japanese with English abstract].

Kojima M., Kato H., Gatto M. (1996) Optical and electrical properties of amorphous Sb-Sn-O thin films. *Philosophical Magazine B*, Vol. 73, No. 2, pp. 277–288, http://dx.doi.org/10.1080/01418639609365824

Lafuente B., Downs R.T., Yang H., Stone N. (2016) The power of databases: The RRUFF project. In T. Armbruster and R.M. Danisi, Eds., *Highlights in Mineralogical Crystallography*, pp. 1–29. W. de Gruyter GmbH, Berlin.

Lehmann B. (2021) Formation of tin ore deposits: A reassessment. *Lithos*, Vol. 402–403, article no. 105756, http://dx.doi.org/10.1016/j.lithos.2020.105756

Lensing-Burgdorf M., Watenphul A., Schlüter J., Mihailova B. (2017) Crystal chemistry of tourmalines from the Erongo Mountains, Namibia, studied by Raman spectroscopy. *European Journal of Mineralogy*, Vol. 29, No. 2, 257–267, http://dx.doi.org/10.1127/ejm/2017/0029-2607

Lopez-Navarrete E., Caballero A., Orera V.M., Lázaro F.J., Ocaña M. (2003) Oxidation state and localization of chromium ions in Cr-doped cassiterite and Cr-doped malayaite. *Acta Materialia*, Vol. 51, No. 8, pp. 2371–2381, http://dx.doi.org/10.1016/S1359-6454(03)00044-2

Li Y.N. (1985) Geological reconnaissance report of tin prospecting in Yunling area, Yongde County, Yunnan Province. *Yunnan Geological Survey Report*, 178 pp. [in Chinese].

Mao W., Zhong H., Yang J., Tang Y., Liu L., Fu Y., Zhang X., Sein K., Myint Aung S., Li J., Zhang L. (2020) Combined zircon, molybdenite, and cassiterite geochronology and cassiterite geochemistry of the Kuntabin tin-tungsten deposit in Myanmar. *Economic Geology*, Vol. 115, No. 3, pp. 603–625, http://dx.doi.org/10.5382/econgeo.4713

Matsushima Y., Maeda K., Suzuki T. (2008) Nature of dark-brown SnO_2 films prepared by a chemical vapor deposition method. *Journal of the Ceramic Society of Japan*, Vol. 116, No. 1357, pp. 989–993, http://dx.doi.org/10.2109/jcersj2.116.989

Möller P., Dulski P., Szacki W., Malow G., Riedel E. (1988) Substitution of tin in cassiterite by tantalum, niobium, tungsten, iron and manganese. *Geochimica et Cosmochimica Acta*, Vol. 52, No. 6, pp. 1497–1503, http://dx.doi.org/10.1016/0016-7037(88)90220-7

Moore T. (2004) What's new in minerals: Tucson Show 2004. *Mineralogical Record*, Vol. 35, No. 3, pp. 249–263.

Murciego A., Sanchez A.G., Dusausoy Y., Pozas J.M.M., Ruck, R. (1997) Geochemistry and EPR of cassiterites from the Iberian Hercynian Massif. *Mineralogical Magazine*, Vol. 61, No. 406, pp. 357–365, http://dx.doi.org/10.1180/minmag.1997.061.406.03

Nambaje C., Eggins S.M., Yaxley G.M., Sajeev K. (2020) Microcharacterisation of cassiterite by geology, texture and zonation: A case study of the Karagwe Ankole Belt, Rwanda. *Ore Geology Reviews*, Vol. 124, article no. 103609, http://dx.doi.org/10.1016/j.oregeorev.2020.103609

Neiva A.M.R. (1996) Geochemistry of cassiterite and its inclusions and exsolution products from tin and tungsten deposits in Portugal. *Canadian Mineralogist*, Vol. 34, No. 4, pp. 745–768.

Ni P., Pan J.Y., Han L., Cui J.M., Gao Y., Fan M.S., Li W.S., Chi Z., Zhang K.H., Cheng Z.L., Liu Y.P. (2023) Tungsten and tin deposits in South China: Temporal and spatial distribution, metallogenic models and prospecting directions. *Ore Geology Reviews*, Vol. 157, article no. 105453, http://dx.doi.org/10.1016/j.oregeorev.2023.105453

Nie F., Dong G.C., Mo X.X., Zhu D.C., Dong M.L., Wang X. (2012) Geochemistry, zircon U-Pb chronology of the Triassic granites in the Changning-Menglian suture zone and their implications. *Acta Petrologica Sinica*, Vol. 28, No. 5, pp. 1465–1476 [in Chinese with English abstract].

Nomiya K., Sugie Y., Amimoto K., Miwa M. (1987) Charge-transfer absorption spectra of some tungsten (VI) and molybdenum (VI) polyoxoanions. *Polyhedron*, Vol. 6, No. 3, pp. 519–524, http://dx.doi.org/10.1016/S0277-5387(00)81018-9

Ollila J.T. (1986) Origin of colour zoning in cassiterites from tin deposits within the Bushveld complex, South Africa. *Bulletin of the Geological Society of Finland*, Vol. 58, No. 2, pp. 3–11, http://dx.doi.org/10.17741/bgsf/58.2.001

Ottens B. (2008) *China: Mineralien - Fundstellen - Lagerstätten*, Christian Weise Verlag, Munich [in German].

——— (2021) *China II: Mineralien - Fundstellen - Lagerstätten*. Christian Weise Verlag, Munich [in German].

Pavlova G.G., Palessky S.V., Borisenko A.S., Vladimirov A.G., Seifert T., Phan L.A. (2015) Indium in cassiterite and ores of tin deposits. *Ore Geology Reviews*, Vol. 66, pp. 99–113, http://dx.doi.org/10.1016/j.oregeorev.2014.10.009

Renfro N. (2015) Digital photomicrography for gemologists. *G&G*, Vol. 51, No. 2, pp. 144–159, http://dx.doi.org/10.5741/GEMS.51.2.144

Serment B., Gaudon M., Toulemonde O., Duttine M., Brochon C., Demourgues A. (2019) Tuning the Cr^{IV}/Cr^{III} valence states in purple Cr-doped SnO_2 nanopowders: The key role of Cr^{IV} centers and defects. *Inorganic Chemistry*, Vol. 59, No. 1, pp. 678–686, http://dx.doi.org/10.1021/acs.inorgchem.9b02943

Shannon R.D. (1976) Revised effective ionic radii and systematic studies of interatomic distances in halides and chalcogenides. *Acta Crystallographica Section A*, Vol. 32, No. 5, pp. 751–767, http://dx.doi.org/10.1107/S0567739476001551

Swart P.K., Moore F. (1982) The occurrence of uranium in association with cassiterite, wolframite, and sulphide mineralization in South-West England. *Mineralogical Magazine*, Vol. 46, No. 339, pp. 211–215, http://dx.doi.org/10.1180/minmag.1982.046.339.07

Tena M.A., Sorlí S., Llusar M., Badenes J.A., Forés A., Monrós G. (2005) Study of Sb-doped SnO_2 gray ceramic pigment with cassiterite structure. *Journal of Inorganic and General Chemistry*, Vol. 631, No. 11, pp. 2188–2191, http://dx.doi.org/10.1002/zaac.200570038

Tindle A.G., Breaks F.W. (1998) Oxide minerals of the Separation Rapids rare-element granitic pegmatite group, northwestern Ontario. *Canadian Mineralogist*, Vol. 36, No. 2, pp. 609–635.

Wang A., Freeman J.J., Jolliff B.L. (2015) Understanding the Raman spectral features of phyllosilicates. *Journal of Raman Spectroscopy*, Vol. 46, No. 10, pp. 829–845, http://dx.doi.org/10.1002/jrs.4680

Wang C.M., Deng J., Carranza E.J.M., Santosh M. (2014) Tin metallogenesis associated with granitoids in the southwestern Sanjiang Tethyan Domain: Nature, deposit types, and tectonic setting. *Gondwana Research*, Vol. 26, No. 2, pp. 576–593, http://dx.doi.org/10.1016/j.gr.2013.05.005

Wu S.Z. (2013) *Gems and Mineral Crystals from Yunnan Province*. Yunnan Technology Publishing House, Kunming, China, 221 pp. [in Chinese].

Wu F., Liu X., Ji W., Wang J., Yang L. (2017) Highly fractionated granites: Recognition and research. *Science China Earth Sciences*, Vol. 60, pp. 1201–1219.

Xiao K., Sun X., Li Q., Si X.B., Zheng X., Lu L.L., Zhao Z.Y. (2022) Geological characteristics and zircon U-Pb geochronology of granite in Yunling tin deposit, southwestern Yunnan. *Mineral Deposits*, Vol. 41, No. 1, pp. 21–34 [in Chinese with English abstract].

Yang L.G., Dong W.W., Tan B.F., Chen S.L., Deng Y., Wang Q.H. (1998) Geological reconnaissance of the tin deposits in the Yunling area, Yalian Country, Yongde County, Yunnan Province. *Yunnan Geological Survey Report*, 39 pp. [in Chinese].

Yu X.H., Xiao X.N., Yang G.L., Mo X.X., Zeng P.S., Wang J.L. (2008) Zircon SHRIMP dating of several granites and geological significance in southern part of "Sanjiang" area, western Yunnan Province. *Acta Petrologica Sinica*, Vol. 24, No. 2, pp. 377–383 [in Chinese with English abstract].

Zhang X.Y., Peng R.M., Li Z.L., Luo P.H., Li J.W., Yi A.W. (2012) Geochemical characteristics of Yunling granodiorite in the Damaidi Sn ore district, southwest Yunnan. *Geophysical & Geochemical Exploration*, Vol. 36, No. 4, pp. 567–572 [in Chinese with English abstract].

Zhou C., Li Y., Chen Y., Lin J. (2018) Hydrothermal synthesis of tungsten doped tin dioxide nanocrystals. *Materials Research Express*, Vol. 5, No. 1, article no. 015911, http://dx.doi.org/10.1088/2053-1591/aaa7a4

Gem-Quality Anorthoclase Feldspar From Southeast Vietnam

Le Ngoc Nang, Pham Minh Tien, Pham Minh, and Pham Trung Hieu

In southeast Vietnam, gem-quality anorthoclase is found as megacrysts in Cenozoic alkali basalt. The crystals are transparent to translucent with vitreous luster and can be near-colorless, yellow, or brownish gray. Gemological testing confirmed this mineral is alkali feldspar, but the data cannot specify the alkali feldspar subgroup (orthoclase, anorthoclase, microcline, or sanidine). Based on X-ray diffraction analysis and a feldspar composition ternary diagram created from energy-dispersive X-ray fluorescence analysis, this material was identified as anorthoclase. Energy-dispersive X-ray fluorescence determined the composition to be $An_{3.50–8.02}$, $Ab_{58.83–81.69}$, and $Or_{11.94–36.96}$. The Raman spectra displayed differences when compared to those of other alkali feldspars such as sanidine, orthoclase, and microcline. Fourier-transform infrared spectra of this material are similar to those of anorthoclase from around the world and lack any distinctive features that would allow for its separation. Gem-quality anorthoclase from southeast Vietnam has commercial potential, as it is abundant and evenly distributed in the basaltic weathering products.

The feldspar group of minerals are rock-forming aluminum tectosilicates that include a wide range of well-known gemstone varieties such as moonstone (orthoclase), sunstone, labradorite (plagioclase), and amazonite (microcline) (Bonewitz, 2008). Alkali feldspar is a subgroup that ranges between sodium-rich feldspar ($NaAlSi_3O_8$) and potassium-rich feldspar ($KAlSi_3O_8$) and includes the monoclinic varieties sanidine and orthoclase as well as the triclinic varieties anorthoclase, albite, and microcline (Deer et al., 2001; Bonewitz, 2008). Variety classification is not possible using standard gemological methods because of overlapping properties such as specific gravity (SG), refractive index (RI), optic figure, fluorescence reaction, and absorption spectrum in the visible region. However, each of these varieties has distinct crystallographic structures, making it possible to identify them using X-ray diffraction methods (Harlow, 1982). Chemical composition also plays a vital role in establishing the alkali feldspar variety.

Anorthoclase, $(Na,K)AlSi_3O_8$, is an uncommon variety of alkali feldspar that is the potassium-rich variety of high albite, distinguished from sanidine by its triclinic symmetry (Jones and Taylor, 1961; Bendel and Schmidt, 2008). The entire solid solution between high albite and sanidine can form at high temperature. The color palette ranges from near-colorless to yellow and brownish gray (figure 1). Anorthoclase has a Mohs hardness of 6.5 and is characterized by albite-law twinning with perfect cleavage in two directions (Anthony et al., 2001). It is rarely used in the jewelry industry.

In Brief

- The feldspar species anorthoclase has been found in southeast Vietnam, originating from Cenozoic alkali basalt.
- The Vietnamese anorthoclase crystals studied here are yellow, brownish gray, or near-colorless, with a transparent to translucent appearance and vitreous luster, and sometimes they display chatoyancy and asterism.
- FTIR, Raman, and XRD spectroscopy, together with standard gemological properties, can confirm the anorthoclase variety (potassium-rich albite).
- Vietnamese anorthoclase is suitable for cutting into faceted and cabochon gems for use in jewelry.

In the Cenozoic alkali basalt of southeast Vietnam, anorthoclase megacrysts are enclosed in the host rock or scattered in the soil formed from basaltic weathering. These megacrysts are concentrated on ancient volcanic slopes that are currently used for farming. Previous studies have reported on the exis-

See end of article for About the Authors and Acknowledgments.
Gems & Gemology, Vol. 60, No. 2, pp. 194–207,
http://dx.doi.org/10.5741/GEMS.60.2.194

Figure 1. Yellow, brownish gray, and near-colorless anorthoclase feldspar from southeast Vietnam. The rough stones range from 96.5 to 144.8 ct and the cut samples from 3.64 to 11.07 ct. Photos by Le Ngoc Nang.

tence of anorthoclase in the region but with very limited descriptions, especially with regard to its gemological properties (Hoang and Flower, 1998). Earlier authors only categorized their samples as alkali feldspar without specifying the variety, as no structural and chemical composition analyses were performed at the time.

To date, anorthoclase has yet to be applied in the jewelry industry. Nang and Tien (2021) first recorded gem-quality anorthoclase in Dong Nai Province of southeast Vietnam. The article also reported two translucent samples that displayed chatoyancy and sheen effects. Although anorthoclase has received little attention in the past, we believe there is potential economic value in the gem-quality material from Dong Nai. This paper aims to provide new data on samples to identify the alkali feldspar variety and characterize this material in order to assess its gem quality and commercial potential.

GEOLOGICAL SETTING

Vietnam experienced two primary tectonic events. The first was the Indosinian orogeny during the Triassic (250–240 Ma). This resulted from the tectonic collision between the Indochina Plate and the Yangtze Plate, which lifted the northwest portion of the Indochina block toward the adjacent continents originating from the Gondwana supercontinent (Carter et al., 2001; Lepvrier et al., 2008). The second occurred when the Indian Plate collided with the Eurasian Plate in the Paleogene (50–55 Ma) (Clift et al., 2002; Leech et al., 2005). The large-scale basaltic eruptions along the eastern and southeastern coast of Asia, including the West Pacific offshore, played a fundamental role in regional geology (Barr and MacDonald, 1981). The eruptions consisted of several basaltic phases, later forming structures separated by faults and developed mainly in east Indochina, including southeast Vietnam (Rangin et al., 1995).

Southeast Vietnam has a total area of 23,000 km^2, and approximately 10,000 km^2 is covered by basaltic formations with thicknesses ranging from a few meters to over a hundred meters (figure 2) (Hoang and Flower, 1998). Two periods of magmatic eruption have been recorded in the region. The first eruption, dating 8 Ma to the Neogene, included quartz and olivine tholeiitic magmatic series. This was followed by olivine tholeiite, alkali basalt, and basalt in the second eruption, during the Quaternary (Hoang et al., 1996; Tich et al., 2004). The quartz and olivine tholeiitic magmatic series consists of basalt, two-pyroxene basalt, dolerite basalt, and olivine-poor hyalobasalt. These have massive and vesicular structure, black to gray color, and a low potassium content of <1% (Hoang et al., 1996). The series of olivine tholeiite, alkali basalt, and basalt contains xenoliths that may be associated with gemstones, as well as individual megacrysts such as garnet, zircon, augite, corundum, peridot, and feldspar.

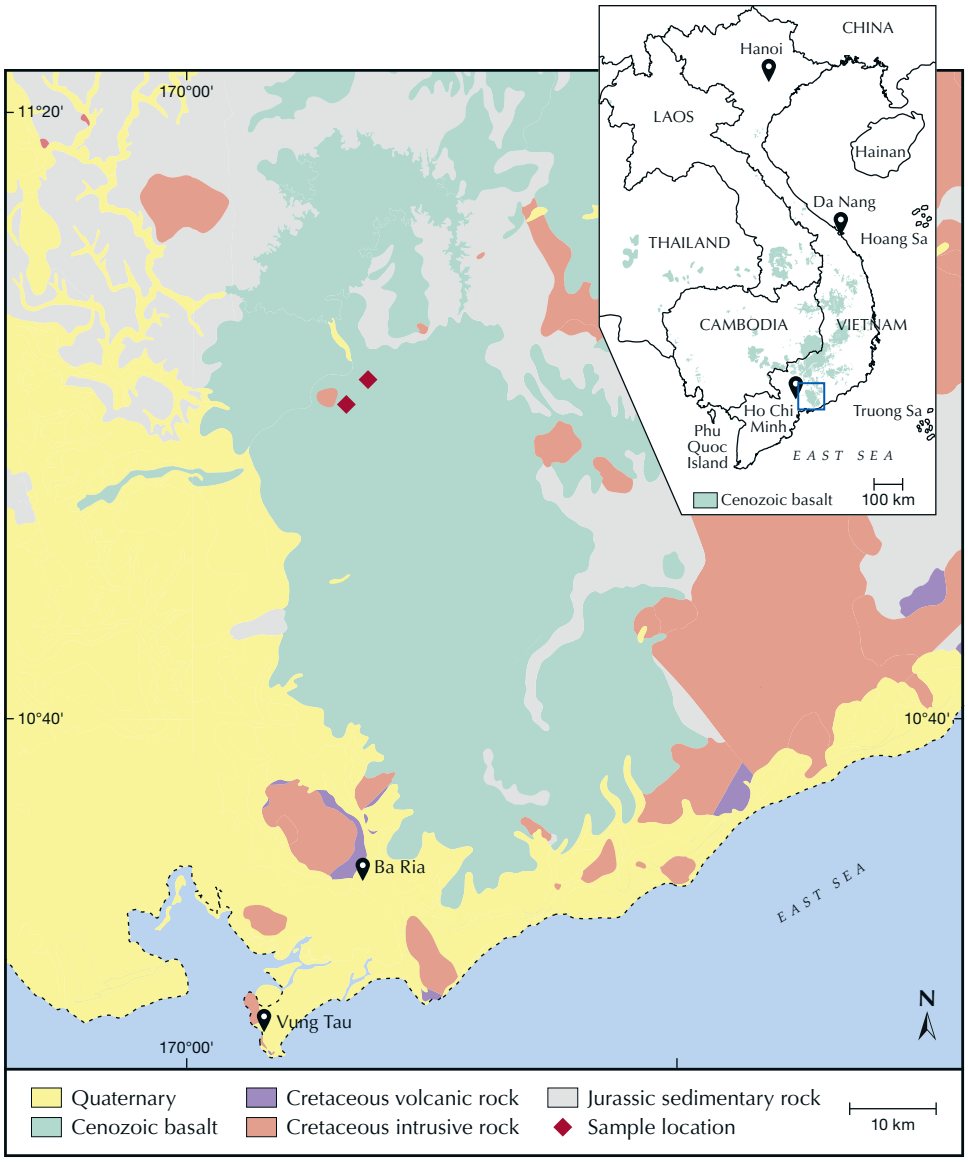

Figure 2. Geological map of southeast Vietnam. Anorthoclase is found in the middle of Cenozoic basalt. From Son (2005), modified by Le Ngoc Nang.

The anorthoclase in this study occurs as megacrysts within the alkali basalt. Weathering of these basaltic layers made it easier to access the anorthoclase (figure 3; visit https://www.gia.edu/gems-gemology/summer-2024-anorthoclase-feldspar).

MATERIALS AND METHODS

Samples. A total of 96 samples were obtained from two locations (see figure 2) in 2020 and 2022. They ranged from 5 to 1550 ct and consisted of 65 near-colorless, 17 brownish gray, and 14 yellow pieces (author LNN collected 34 samples, and 62 were provided by locals). Of the 96 samples, 33 were selected for faceting and cabochon cutting. We chose 14 rough specimens weighing over 6 ct in all available colors (near-colorless, brownish gray, and yellow), two transparency levels (transparent and translucent, including some chatoyant and four-rayed star samples; visit https://www.gia.edu/gems-gemology/summer-2024-anorthoclase-feldspar), most with good clarity. These were used to establish gemological properties, chemical composition, and spectroscopic features. The 14 samples consisted of eight faceted stones (AF1–AF8), two cabochons (AF9–AF10), and four rough samples (AF11–AF14) (figure 4). The faceted and cabochon specimens were cut by Nguyen Tri Duc, an expert cutter working in collaboration with Liu Gemological Research and Application Center (LIULAB) in Ho Chi Minh City. In addition, portions of samples AF12 (yel-

Figure 3. Nodules of anorthoclase were discovered in massive basalt by the lead author in sizes up to 22 cm (A), 6 cm in vesicular basalt (B), and 4 cm as fragments in alluvial deposits (C). Photos by Pham Minh Tien.

low), AF14 (near-colorless), and AF9 (brownish gray; the leftover material from cutting) were ground to powder for X-ray diffraction (XRD) analysis.

Methods. *Standard Gemological Testing*. Standard gemological testing was performed at LIULAB. The physical appearance of the samples was observed under a 60W GLS LED daylight bulb with a light temperature of approximately 5000–6000K. The SG of all 14 samples was measured using the hydrostatic method. A refractometer with a sodium light source and an optical coupling liquid of methylene iodide and

Figure 4. Anorthoclase samples from this study consisted of eight faceted stones, two cabochons, and four rough samples within three color groups: near-colorless, brownish gray, and yellow. Photos by Le Ngoc Nang.

tetraiodoethylene (RI of 1.81) was employed to measure the refractive index of the cut stones (AF1–AF10). Optical properties and pleochroism of high-transparency gems were observed using a polariscope and a dichroscope, respectively. All samples were exposed to ultraviolet light to determine their fluorescence reaction to long-wave (365 nm) and short-wave (254 nm) UV. A scratch test was performed to determine Mohs hardness. A Carton SPZV50 gemological microscope was used to view the internal features of the cut samples (AF1–AF10), with a magnification of 7× to 50×.

X-Ray Diffraction (XRD). Samples AF9, AF12, and AF14 were exposed to incident X-ray radiation to determine their crystallographic structures, which defines the variety of feldspar for each. The technique was performed using a Bruker D2 Phaser benchtop X-ray powder diffractometer, with Cu Kα radiation in the range of 5–75° 2θ with a scan speed of 0.02°/s, at 40 kV and 30 mA. The analyzed data were interpreted using X'Pert Highscore Plus software, which compared the analyzed results to the standard data in the Inorganic Crystal Structure Database (ICSD; Levin, 2018). XRD was conducted on near-colorless, yellow, and brownish gray powdered samples, with an average particle size of about 0.05 mm. These were processed and analyzed at the Institute of Chemical Technology, Vietnam Academy of Science and Technology in Ho Chi Minh City.

Energy-Dispersive X-Ray Fluorescence (EDXRF). We analyzed 14 samples (AF1–AF14) using a Shimadzu EDX-8100 operated with a voltage of 30 kV and a current of 10 mA. The reference standards for Al_2O_3, SiO_2, TiO_2, MgO, MnO, FeO, Na_2O, CaO, K_2O, and Cr_2O_3 were corundum, quartz, titanium dioxide, periclase, manganosite, fayalite, jadeite, wollastonite, potassium titanium phosphate, and eskolaite, respectively. The detection limits were calculated based on the system of Glascock (2020): 0.02 wt.% for Al_2O_3 and SiO_2; 0.01 wt.% for MgO and Na_2O; and 0.0002 wt.% for TiO_2, MnO, FeO, CaO, K_2O, and Cr_2O_3. EDXRF was conducted at the Center of Analytical Services and Experimentation in Ho Chi Minh City.

Raman Spectroscopy. A Horiba Xplora One was employed to obtain the Raman spectra in the 0–3750 cm^{-1} range for samples AF1, AF3, and AF7. Measurements were performed at a laser excitation wavelength of 532 nm, laser mode power at 50%, and 900 lines/mm diffraction grating, with a spectral resolution of 5 cm^{-1}. The objective selected was of 50× magnification. Raman spectra were collected over 15 s with two signal accumulations. The analysis was conducted at the Institute of Chemical Technology, Vietnam Academy of Science and Technology.

Fourier-Transform Infrared (FTIR) Spectroscopy. A Cary 630 FTIR instrument with attenuated total reflection (ATR) was used to efficiently collect the FTIR spectra of samples AF1, AF2, and AF7. Measurements were obtained in a spectral range of 4000–400 cm^{-1} with a resolution of <2 cm^{-1} and a scanning time of 3 s. The analysis was performed at LIULAB.

RESULTS AND DISCUSSION

Appearance. From the total of 96 samples collected during field trips, three colors were noted: near-colorless, brownish gray, and yellow (figures 1 and 4). Near-colorless samples were most common, followed by brownish gray, while yellow was comparatively rare. The majority of the gems collected were transparent to semitransparent; a few were translucent, and opaque samples were also found but rarely used because of their poor quality (figures 1 and 4; table 1). These materials were subhedral and anhedral fragments with good cleavage and conchoidal fracture. Some specimens bore etch marks on the surface due to surface corrosion. The samples showed vitreous luster. The yellow and brownish gray samples accounted for 5% and 7% of all of the collected samples, respectively. They had better clarity and transparency than the near-colorless samples, with few feathers along the cleavage. However, the brownish gray samples had lower clarity (i.e., a more cloudy appearance) than the yellow samples. The yellow and brownish gray stones were easier to cut than the near-colorless samples, which often developed deep cracks along the cleavage. Among the translucent samples, we encountered an anorthoclase with a cat's-eye effect (Nang and Tien, 2021).

Gemological Properties. The refractive indices measured on eight faceted stones (AF1–AF8) were n_α = 1.518–1.523 and n_γ = 1.526–1.531, with a birefringence of 0.007–0.008. The specific gravity of 14 samples determined by the hydrostatic method ranged from 2.59 to 2.62 (table 1). The Mohs hardness of the rough anorthoclase was 6.0–6.5. These properties were consistent with alkali feldspar (Bonewitz, 2008) but cannot help distinguish between orthoclase, microcline, sanidine, albite, and anorthoclase.

TABLE 1. Gemological properties of anorthoclase from Dong Nai, Vietnam.

Sample no.	Color	Form	Transparency	Weight (ct)	SG	RI (birefringence)	Fluorescence reaction
AF1	Light yellow	Faceted cushion	Transparent	25.99	2.61	1.520–1.528 (0.008)	Long-wave: Inert Short-wave: Weak pink
AF2	Yellow	Faceted oval	Transparent	12.24	2.59	1.518–1.525 (0.007)	Inert to long-wave and short-wave
AF3	Brownish gray	Faceted octagon	Transparent	10.95	2.61	1.520–1.528 (0.008)	Inert to long-wave and short-wave
AF4	Yellow	Faceted rectangle	Transparent	3.81	2.60	1.518–1.526 (0.008)	Inert to long-wave and short-wave
AF5	Yellow	Faceted oval	Transparent	11.07	2.61	1.520–1.528 (0.008)	Inert to long-wave and short-wave
AF6	Light yellow	Faceted lozenge	Transparent	4.67	2.60	1.517–1.525 (0.007)	Inert to long-wave and short-wave
AF7	Near-colorless	Faceted round	Transparent	3.64	2.62	1.523–1.531 (0.008)	Inert to long-wave and short-wave
AF8	Near-colorless	Faceted trilliant	Transparent	1.48	2.61	1.520–1.527 (0.007)	Inert to long-wave and short-wave
AF9	Brownish gray	Round cabochon	Translucent	3.27	2.61	1.52[a]	Inert to long-wave and short-wave
AF10	Brownish gray	Oval cabochon	Translucent	7.50	2.60	1.52[a]	Inert to long-wave and short-wave
AF11	Grayish yellow	Rough	Transparent	144.80	2.60	n/a	Inert to long-wave and short-wave
AF12	Grayish yellow	Rough	Transparent	54.90	2.60	n/a	Inert to long-wave and short-wave
AF13	Very light yellow	Rough	Transparent	37.28	2.69	n/a	Inert to long-wave and short-wave
AF14	Near-colorless	Rough	Transparent	52.60	2.59	n/a	Long-wave: Inert Short-wave: Weak pink

[a]*Measured using a spot reading method*

Twelve of the 14 samples were inert under UV light, while the other two (AF1 and AF14) emitted weak pink fluorescence under short-wave UV light. This differs from some alkali feldspars such as plagioclase and orthoclase, which fluoresce red or pink to long-wave UV (Morrison and Cox, 2014). Transparent samples displayed a biaxial pattern under the polariscope and did not show pleochroism. These features have been observed in more than one variety of alkali feldspar, with no clearly defined boundaries to distinguish them based on gemological properties.

Hence, the samples' appearance and gemological properties confirmed these were all alkali feldspars but could not differentiate which varieties they were.

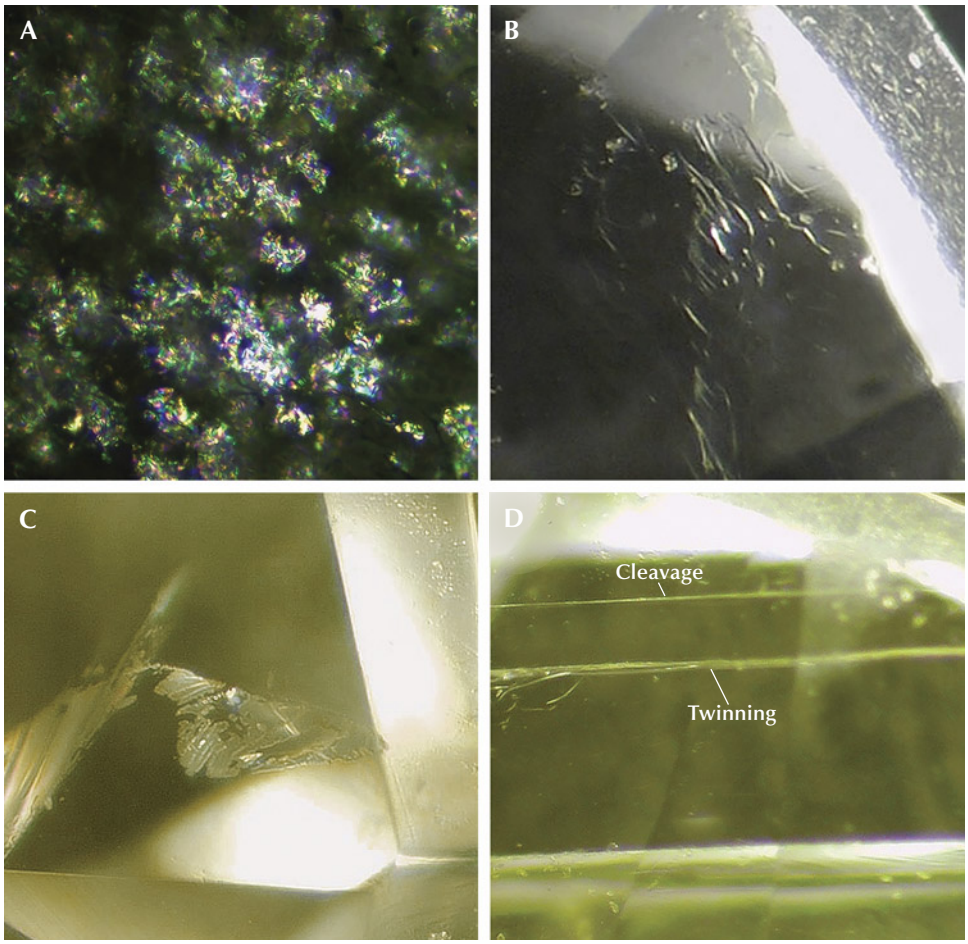

Figure 5. Inclusions in anorthoclase from southeast Vietnam. A: A myriad of incomplete thin, flat fluid inclusions reflecting interference colors (sample AF9). B: Worm-like fluid inclusions (sample AF7). C: Colorless healed fractures along the cleavage (sample AF5). D: Cleavage planes accompanied by albite-law twinning, identified using a polariscope (sample AF4). Photomicrographs by Le Ngoc Nang; fields of view 1.8 mm (A) and 2.5 mm (B–D).

Internal Features. Examining the cut gems, we detected fluid inclusions, healed fractures, cleavage planes, and twinning planes (twinning and cleavage planes were distinguished with a polariscope) (figure 5). Tiny fluid inclusions formed incomplete reflective and flat thin films that were directionally distributed in most near-colorless and brownish gray samples (figure 5A, sample AF9). Worm-like fluid inclusions were found in two samples (e.g., figure 5B, sample AF7), and these grew along the plane identified as albite-law twinning using a polariscope. Healing of fractures, which formed during rapid cooling from high temperature (Gübelin and Koivula, 2005), was observed in samples AF1–AF7, developing along the cleavages of the feldspar host (figure 5C, sample AF5). Characteristic perfect cleavage was observed in most of the samples along with the albite-law twin planes, as seen in figure 5D (sample AF4). Unfortunately, we could not determine the fluid inclusions by Raman analysis.

X-Ray Diffraction. While standard gemological testing methods are not effective for distinguishing alkali feldspar varieties, XRD can separate them based on their different crystal structures. Our XRD analyses for three samples (near-colorless, yellow, and brownish gray) from southeast Vietnam were consistent with the anorthoclase sample 01-075-1630 from the ICSD database (Levin, 2018) (figure 6). This result helped us confirm that the samples in all three colors were anorthoclase.

Chemical Composition. The chemical composition of 14 anorthoclase specimens determined with EDXRF is shown in table 2, in which Al_2O_3 ranges from 17.82 to 25.94 wt.%, SiO_2 from 60.10 to 67.12 wt.%, CaO from 0.64 to 1.51 wt.%, Na_2O from 5.90 to 9.52 wt.%, and K_2O from 2.15 to 6.13 wt.%. The concentration of main oxides, especially sodium and potassium, varied from sample to sample. In all measured samples, the sodium concentrations were higher than those for potassium. The transition from anorthoclase to sanidine occurs during the replacement of sodium by potassium, accompanied by increasing structural disorder. The K/(K+Na) in our

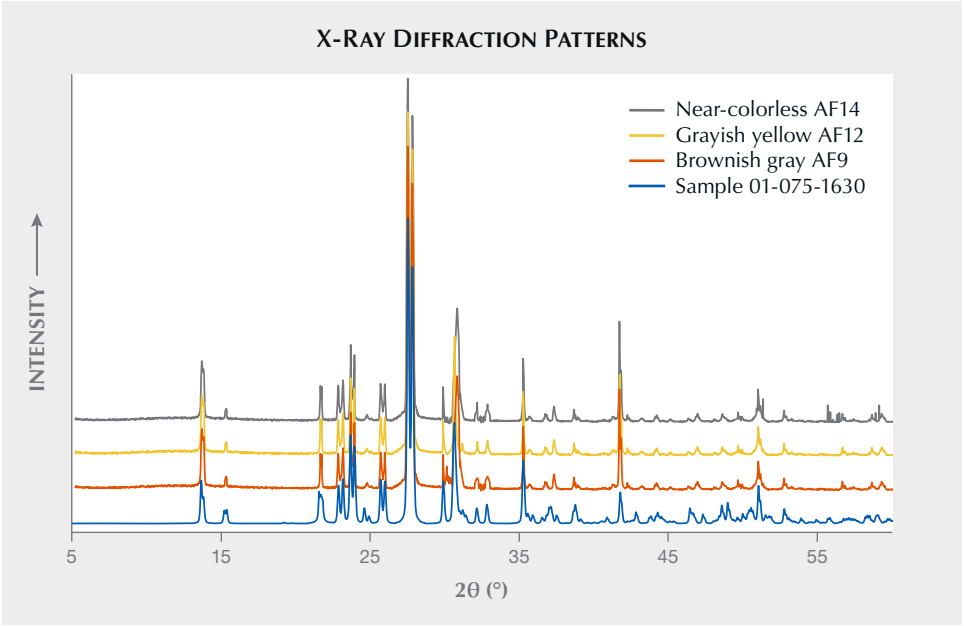

Figure 6. X-ray diffraction patterns of anorthoclase samples from southeast Vietnam and an ICSD reference sample included for comparison. Spectra are offset vertically for clarity.

samples ranged between 0.12 and 0.38, corresponding to anorthoclase rather than sanidine (Bendel and Schmidt, 2008). In addition, we noted a low calcium content (0.031–0.073) that corresponded with potassium-rich albite instead of calcium-potassium-rich albite (where the albite is more enriched in calcium than potassium). Meanwhile, we also determined there were very minor amounts of the trace elements iron, magnesium, titanium, and manganese. We calculated the following ratios: anorthite (An) 3.50–8.02%, albite (Ab) 58.83–81.69%, and orthoclase (Or) 11.94–36.96%. In all, 13 of the 14 samples fell within the anorthoclase (potassium-rich albite) region, and one sample (AF6) belonged to the albite field on the plotted An-Ab-Or system (figure 7).

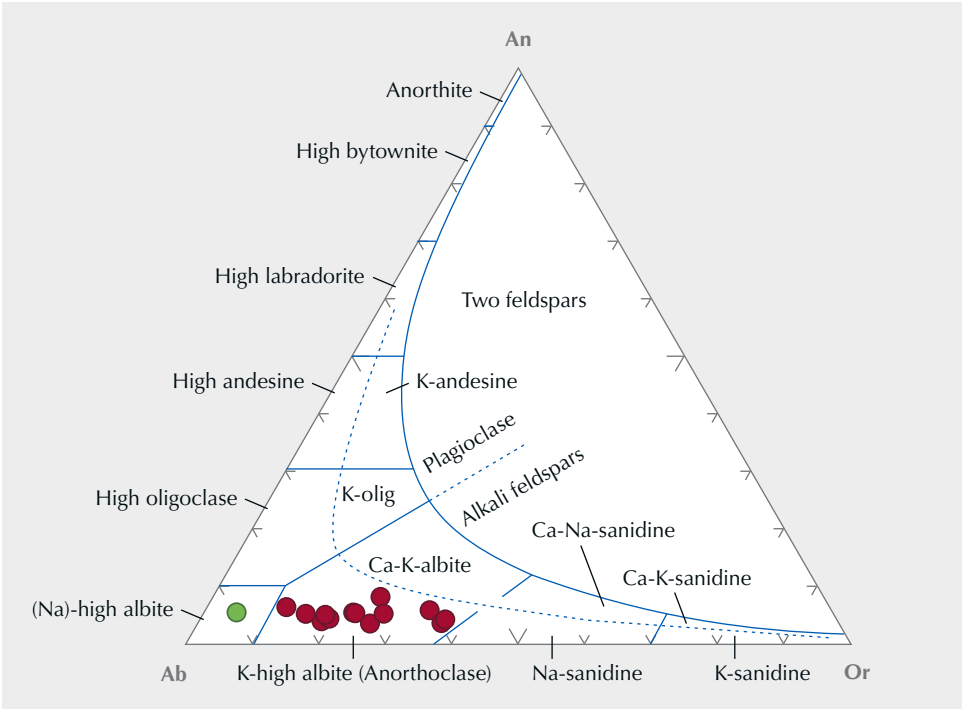

Figure 7. In the An-Ab-Or (anorthite-albite-orthoclase) composition diagram, all but one of the samples are concentrated in the range of anorthoclase (potassium-rich albite) (Smith and Brown, 1988). Note that the green dot corresponds to sample AF6.

TABLE 2. Chemical composition of anorthoclase from Dong Nai, Vietnam, obtained by EDXRF.

	AF1	AF2	AF3	AF4	AF5	AF6	AF7	AF8	AF9	AF10	AF11	AF12	AF13	AF14
Oxide (wt.%)														
SiO_2	63.96	63.57	65.54	66.14	61.13	67.12	60.10	63.45	62.78	66.55	65.05	64.35	66.01	67.10
TiO_2	0.01	bdl[b]	bdl	0.01	0.02	bdl	0.01	bdl	bdl	bdl	bdl	bdl	bdl	bdl
Al_2O_3	22.90	23.01	20.54	19.04	25.94	18.94	25.74	23.70	22.80	19.19	20.89	21.47	20.12	17.82
FeO[a]	0.77	0.61	0.56	0.46	0.557	0.46	0.65	0.65	0.81	0.32	0.03	0.39	0.47	0.55
MnO	bdl	bdl	bdl	bdl	bdl	bdl	bdl	bdl	bdl	bdl	bdl	bdl	bdl	bdl
MgO	0.12	0.50	0.39	0.46	0.60	0.35	0.50	0.32	0.72	0.41	0.22	0.40	0.53	0.42
CaO	0.76	0.83	1.09	1.19	0.91	1.34	0.64	0.97	1.51	0.73	0.77	0.83	1.06	1.10
Na_2O	8.35	8.03	8.03	6.83	7.65	9.52	5.90	8.20	6.99	8.11	7.01	6.42	7.92	7.90
K_2O	3.02	3.10	3.84	5.81	2.82	2.15	5.51	2.43	3.92	4.57	5.44	6.13	3.83	4.83
Atoms per formula unit, 8 O (charge balance)														
Si	2.839	2.828	2.916	2.964	2.719	2.973	2.706	2.821	2.813	2.962	2.915	2.879	2.939	3.000
Al	1.198	1.207	1.077	1.005	1.359	0.988	1.375	1.242	1.204	1.007	1.103	1.133	1.056	0.939
Fe^{2+}	0.022	0.020	0.020	0.017	—	0.012	0.021	0.024	0.030	0.080	0.011	—	0.018	0.021
Fe^{3+}	0.006	0.003	—	—	0.021	0.005	0.004	—	—	0.004	—	0.013	—	—
Mg	0.008	0.033	0.026	0.031	0.039	0.023	0.034	0.021	0.048	0.027	0.015	0.027	0.035	0.028
Ca	0.036	0.040	0.052	0.057	0.043	0.064	0.031	0.046	0.073	0.035	0.037	0.040	0.051	0.053
Na	0.718	0.693	0.692	0.593	0.659	0.815	0.515	0.707	0.607	0.700	0.609	0.557	0.684	0.685
K	0.171	0.177	0.216	0.332	0.159	0.119	0.316	0.138	0.224	0.258	0.311	0.350	0.218	0.275
K/(K+Na)	0.192	0.203	0.238	0.360	0.194	0.127	0.380	0.163	0.270	0.269	0.338	0.386	0.242	0.286
Ternary system of anorthite-albite-orthoclase														
An	3.91	4.35	5.41	5.81	5.028	6.37	3.58	5.19	8.02	3.50	3.86	4.20	5.31	5.20
Ab	77.62	76.22	72.09	60.39	76.49	81.69	59.72	79.34	67.19	70.52	63.64	58.83	71.83	67.60
Or	18.47	19.43	22.50	33.80	18.49	11.94	36.69	15.47	24.79	25.97	32.49	36.96	22.86	27.19

[a]*FeO = total iron*
[b]*bdl = below detection limit. Detection limits = SiO_2 and Al_2O_3: 0.002; TiO_2, FeO, MnO, and CaO: 0.0002; MgO and Na_2O: 0.01; and K_2O: 0.001.*

Raman Spectroscopy. Raman and FTIR spectra were measured on three faceted anorthoclase samples with different colors: light yellow (AF1), brownish gray (AF3), and near-colorless (AF7). In the 100–600 cm^{-1} range, the samples displayed four strong peaks at 165, 283, 476, and 510 cm^{-1} (figure 8). These peaks are typical of tectosilicate structure (Freeman et al., 2008) and matched with those of Mexican and Chinese alkali feldspar specimens. However, the 455 cm^{-1} peak that appeared in orthoclase and microcline (Freeman et al., 2008) was absent in the Vietnamese anorthoclase. According to Bendel and Schmidt (2008), the increase in peak intensities at 165 and 474 cm^{-1} coupled with the decrease at 120 and 450 cm^{-1} corresponds to the transition from sanidine to anorthoclase. In addition to these features, the mole percent K/(Na+K) of alkali feldspar ranged between 0.11 and 0.38, representing a shift from monoclinic to triclinic crystal structure and thus indicating anorthoclase rather than sanidine. The 510 cm^{-1} band was attributed to a mixed Si-O-Si (or Si-O-Al) bending/stretching mode (Mernagh, 1991). The absence of the 450 cm^{-1} peak points to anorthoclase rather than microcline and orthoclase, in which the peak is present (Mernagh, 1991).

Figure 8. Raman spectra of anorthoclase samples from southeast Vietnam include peaks at 165, 283, 476, and 510 cm^{-1} corresponding to alkali feldspar (Freeman et al., 2008). The absence of the 450 cm^{-1} peak with the mole percent K/(Na+K) ranging between 0.11 and 0.38 indicates the anorthoclase variety.

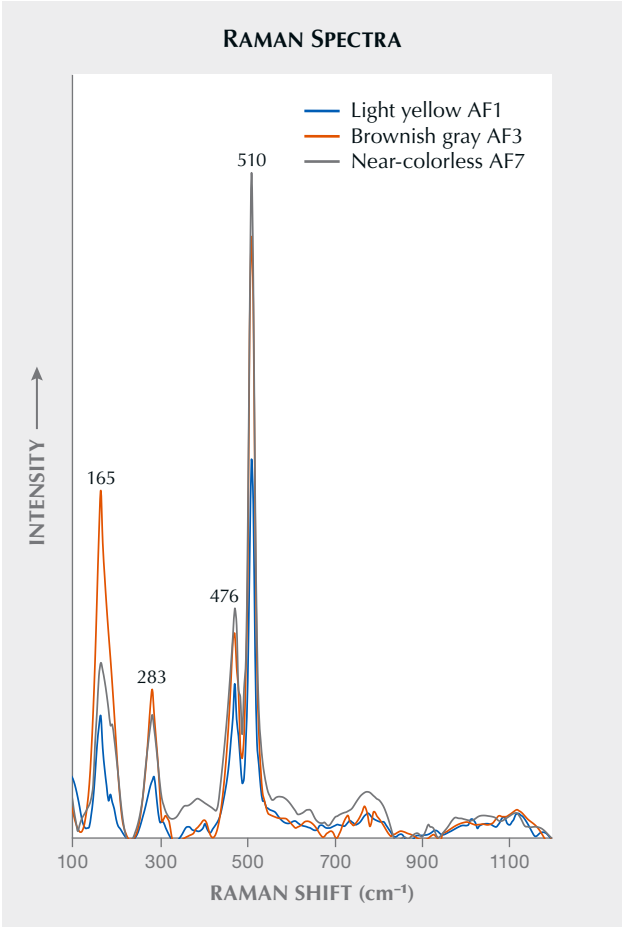

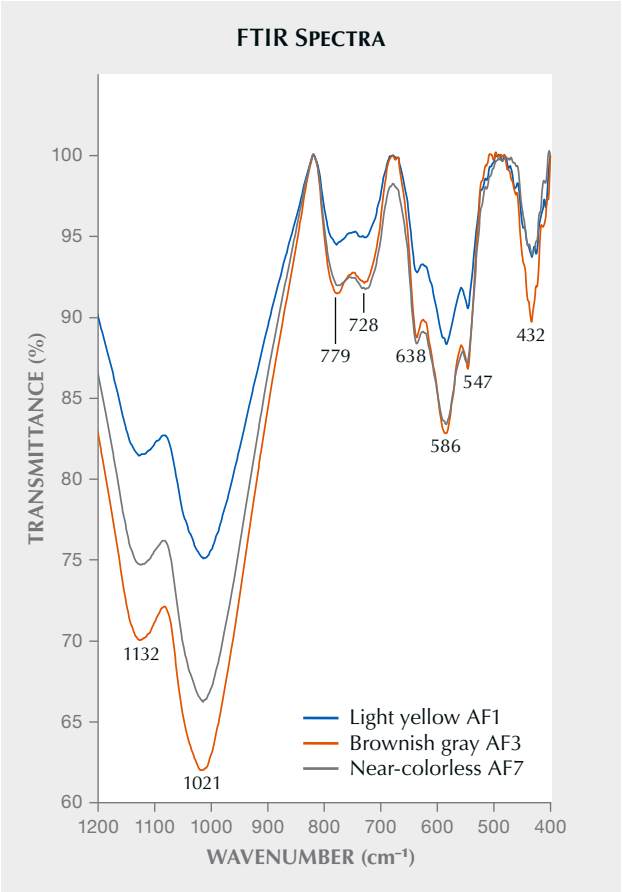

Figure 9. FTIR spectra of anorthoclase samples from southeast Vietnam indicate feldspar but cannot classify the anorthoclase variety. Note that transmittance mode was used due to the high scattering of samples.

Infrared Spectroscopy. The FTIR spectra of samples AF1, AF3, and AF7 (figure 9) showed relatively similar absorption bands in the 1200–400 cm^{-1} range, including 1132, 1021, 779, 728, 638, 586, 547, and 432 cm^{-1}. The 432 cm^{-1} peak was related to Si-O-Si deformation. The 547 cm^{-1} peak was associated with O-Si-O bending and M-O stretching (where M is the metal iron, magnesium, or manganese substituting for silicon). Peaks at 586 and 638 cm^{-1} were attributed to O-Si(Al)-O bending. Meanwhile, the 728 cm^{-1} peak corre-

Figure 10. A large anorthoclase mass (7.1 × 6 9 × 3.0 cm) weighing 1550 ct was cut in half, and the two pieces are shown in these photos. The opaque section on the left is suitable for a cabochon, while the more transparent section on the right could be used for faceting. Photos by Le Ngoc Nang.

sponded to Si-Al(Si) stretching and the 779 cm^{-1} peak to Si-Si stretching. Peaks at 1021 and 1132 cm^{-1} indicated Si-O stretching and Si(Al)-O stretching, respectively (Zhang et al., 1996). Hence, the infrared spectra of feldspar from southeast Vietnam are also typical of both sodium-rich and potassium-rich feldspars (Bosch-Reig et al., 2017), and therefore they are not useful for distinguishing anorthoclase from other feldspars.

GEM QUALITY AND POTENTIAL JEWELRY APPLICATION

Gem and non-gem anorthoclase have been reported from several locations, including Australia (Bahat, 1979), Portugal (Zanon et al., 2013), Antarctica (Sun and Hanson, 1976), the United States (Irving and Frey, 1984), and Cuba (Yin and Dai, 2021). It has not traditionally been used in jewelry because of its low transparency and easily split cleavages. Anorthoclase is rarely mentioned as a gem material, partly because it is mistaken for other alkali feldspars such as orthoclase or sanidine due to their similar appearance and gemological properties. This confusion could contribute to its unfamiliarity among many gem dealers.

Nang and Tien (2021) previously evaluated anorthoclase from southeast Vietnam for its color, transparency, stability to cutting and polishing, and chatoyant phenomenon. All three hues were appropriate for jewelry making, but yellow is traditionally a favorite color in the gem markets of Ho Chi Minh City (the same is true for other gem species such as sapphire and quartz). Some 70% of the anorthoclase collected was transparent. We also obtained several semitransparent samples, while the rest were translucent to opaque. The sizes were relatively large, usually around 15 ct up to more than 1500 ct (10–50 mm in size). High-quality anorthoclase is suitable for faceting into gems (again, see figures 1–4 and figure 11), while less-transparent material is more suitable for cutting into cabochons. Only 8% of the samples could be faceted to produce stones larger than 1 ct. More than 30% of the samples, which included the largest crystal at a weight of 1550 ct (figure 10), were suitable for cabochons. In the study group, the largest facet-quality rough anorthoclase was 144.80 ct (AF11), and the largest faceted stone to date was sample AF1, which weighed 25.99 ct and was mounted as a pendant (figure 11).

The samples had a Mohs hardness of 6.0–6.5, indicating moderate durability. However, perfect cleavage and multiple albite-law twinning planes in anorthoclase make gem manufacturing difficult and require extra care during use.

Low-quality feldspar can be treated to enhance its color, durability, and clarity. Examples include impregnating moonstone and amazonite with plastic to improve transparency (Jianjun et al., 2013; Sun and Renfro, 2017) and diffusing copper to create red labradorite imitations of andesine (Zhou et al., 2022). Anorthoclase from Dong Nai is still too novel for any known treatment practices. But it is a promising candidate for treatment, given the abundance of samples in the area.

Figure 11. This 25.99 ct light yellow anorthoclase (sample AF1) is set in a 14K gold pendant. Photo by Le Ngoc Nang.

The anorthoclase-bearing basalt and its weathering products cover approximately 1000 km^2 in southeast Vietnam, with depths of 30 to 100 m (Tich et al., 2004). Its weathering products, which range from 1 to 3 m in thickness, are a rich source of anorthoclase. On average, a cubic meter of basaltic material might contain three to five anorthoclase crystals, while the concentration is higher in weathering products because the gems are released from the bedrock by erosion and accumulated along the hill slopes. In Dong Nai, the weathering products are easily accessible by dirt roads surrounded by arable lands.

The gem quality, distribution, and mining feasibility of anorthoclase from southeast Vietnam suggests a potentially valuable deposit. In addition, the locality could become a geotourism attraction with basalt-related gemstones across the region.

CONCLUSIONS

Anorthoclase from Dong Nai Province in southeast Vietnam presents as transparent to translucent crystals that are brownish gray, yellow, and near-colorless. It is not practical to distinguish feldspar varieties using only standard gemological methods. The composition determined for the samples was $An_{3.50–8.02}$, $Ab_{58.83–81.69}$, and $Or_{11.94–36.96}$, which falls within the anorthoclase field on the An–Ab–Or ternary diagram. Interpretation of XRD results firmly concluded the anorthoclase variety. The Raman and FTIR spectra of anorthoclase from southeast Vietnam are similar to those from other regions in the world. Vietnamese anorthoclase has commercial potential, as there are significant amounts of gem-quality material suitable for faceting and cutting into cabochons. Lastly, these materials have a widespread distribution across the region, with a high concentration in the basaltic weathering products.

ABOUT THE AUTHORS

Le Ngoc Nang is a postgraduate in the geology faculty at the University of Science, Vietnam National University in Ho Chi Minh City, and CEO of Liu Gemological Research and Application Center (LIULAB), where Pham Minh Tien is a technical specialist. Pham Minh is a lecturer, and Dr. Pham Trung Hieu is an associate professor, in the geology faculty at the University of Science, Vietnam National University.

ACKNOWLEDGMENTS

We express gratitude to Tran Ngoc Vien for leading us to the sampling areas during our field trips to Dong Nai. This research was funded by the National Foundation for Sciences and Technology Development of Vietnam (NAFOSTED) under grant number 105.01-2021.18.

REFERENCES

Anthony J.W., et al. (2001) Anorthoclase. In *Handbook of Mineralogy*, Mineralogical Society of America, Chantilly, Virginia.

Bahat D. (1979) Anorthoclase megacrysts: Physical conditions of formation. *Mineralogical Magazine*, Vol. 43, No. 326, pp. 287–291, http://dx.doi.org/10.1180/minmag.1979.043.326.11

Barr S.M., MacDonald A.S. (1981) Geochemistry and geochronology of late Cenozoic basalts of Southeast Asia. *Geological Society of America Bulletin*, Vol. 92, No. 8 (part II), pp. 1069–1142, http://dx.doi.org/10.1130/GSAB-P2-92-1069

Bendel V., Schmidt B.C. (2008) Raman spectroscopic characterisation of disordered alkali feldspars along the join $AlSi_3O_8$–$NaAlSi_3O_8$: Application to natural sanidine and anorthoclase. *European Journal of Mineralogy*, Vol. 20, No. 6, pp. 1055–1065, http://dx.doi.org/10.1127/0935-1221/2009/0021-1856

Bonewitz R.L. (2008) *Rock and Gem: The Definitive Guide to Rocks, Minerals, Gemstones, and Fossils*. DK Publishing, New York.

Bosch-Reig F., Gimeno-Adelantado J.V., et al. (2017) Quantification of minerals from ATR-FTIR spectra with spectral interferences using the MRC method. *Spectrochimica Acta Part A*, Vol. 181, pp. 7–12, http://dx.doi.org/10.1016/j.saa.2017.02.012

Carter A., Roques D., et al. (2001) Understanding Mesozoic accretion in Southeast Asia: Significance of Triassic thermotectonism (Indosinian orogeny) in Vietnam. *Geology*, Vol. 29, No. 3, pp. 211–214, http://dx.doi.org/10.1130/0091-7613(2001)029%3C0211:UMAISA%3E2.0.CO;2

Clift P.D., Carter A., et al. (2002) Constraints of India–Eurasia collision in the Arabian Sea region taken from the Indus Group, Ladakh Himalaya, India. *Geological Society, London, Special Publications*, Vol. 195, pp. 97–116, http://dx.doi.org/10.1144/GSL.SP.2002.195.01.07

Deer W.A., Howie R.A., Zussman J. (2001) *Rock-Forming Minerals*, 2nd ed., Volume 4A. The Geological Society, London.

Freeman J.J., Wang A., et al. (2008) Characterization of natural feldspars by Raman spectroscopy for future planetary exploration. *Canadian Mineralogist*, Vol. 46, No. 6, pp. 1477–1500, http://dx.doi.org/10.3749/canmin.46.6.1477

Glascock M.D. (2020) Tables to support the analytical methods in use at MURR: NAA, XRF, and ICP-MS. University of Missouri Research Reactor (MURR), Columbia.

Gübelin E.J., Koivula J.I. (2005) *Photoatlas of Inclusions in Gemstones, Volume 2*. Opinio Publishers, Basel, Switzerland.

Harlow G.E. (1982) The anorthoclase structures: The effects of temperature and composition. *American Mineralogist*, Vol. 67, No. 9-10, pp. 975–996.

Hoang N., Flower M.F.J. (1998) Petrogenesis of Cenozoic basalts from Vietnam: Implication for origins of a "diffuse igneous province." *Journal of Petrology*, Vol. 39, No. 3, pp. 369–395, http://dx.doi.org/10.1093/petroj/39.3.369

Hoang N., Flower M.F.J., Carlson R.W. (1996) Major, trace element, and isotopic compositions of Vietnamese basalts: Interaction of hydrous EM1-rich asthenosphere with thinned Eurasian lithosphere. *Geochimica et Cosmochimica Acta*, Vol. 60, No. 22, pp. 4329–4351, http://dx.doi.org/10.1016/S0016-7037(96)00247-5

Irving A.J., Frey F.A. (1984) Trace element abundances in megacrysts and their host basalts: Constraints on partition coefficients and megacryst genesis. *Geochimica et Cosmochimica Acta*, Vol. 48, pp. 1201–1221, http://dx.doi.org/10.1016/0016-7037(84)90056-5

Jianjun L., Xiaofan W., et al. (2013) Infrared spectroscopic study of filled moonstone. *G&G*, Vol. 49, No. 1, pp. 28–34, http://dx.doi.org/10.5741/GEMS.49.1.28

Jones J.B., Taylor W.H. (1961) The structure of orthoclase. *Acta Crystallographica*, Vol. 14, No. 5, pp. 443–456, http://dx.doi.org/10.1107/S0365110X61001479

Leech M.L., Singh S., et al. (2005) The onset of India–Asia continental collision: Early, steep subduction required by the timing of UHP metamorphism in the western Himalaya. *Earth and Planetary Science Letters*, Vol. 234, No. 1-2, pp. 83–97, http://dx.doi.org/10.1016/j.epsl.2005.02.038

Lepvrier C., Vuong N.V., et al. (2008) Indosinian tectonics in Vietnam. *Comptes Rendus Geoscience*, Vol. 340, No. 2-3, pp. 94–111, http://dx.doi.org/10.1016/j.crte.2007.10.005

Levin I. (2018) NIST Inorganic Crystal Structure Database (ICSD). National Institute of Standards and Technology, http://dx.doi.org/10.18434/M32147

Mernagh T.P. (1991) Use of the laser Raman microprobe for discrimination amongst feldspar minerals. *Journal of Raman Spectroscopy*, Vol. 22, No. 8, pp. 453–457, http://dx.doi.org/10.1002/jrs.1250220806

Morrison N., Cox R. (2014) An investigation into UV fluorescence in feldspar group minerals. *Atlantic Geology*, Vol. 50, No. 1, pp. 24–35.

Nang L.N., Tien P.M. (2021) Chatoyant anorthoclase feldspar from Dong Nai Province, Vietnam. *Journal of Gemmology*, Vol. 37, No. 7, pp. 672–673.

Rangin C., Klein M., et al. (1995) The Red River fault system in the Tonkin Gulf, Vietnam. *Tectonophysics*, Vol. 243, No. 3-4, pp. 209–222, http://dx.doi.org/10.1016/0040-1951(94)00207-P

Smith J.V., Brown W.L. (1988) *Feldspar Minerals*, 2nd ed. Springer-Verlag, Berlin.

Son N.D., Du D.C., et al. (2005) Geological mapping of mineral resource and prospective zoning of Dong Nai Province, scale 1:50.000, Dong Nai Department of Science and Technology.

Sun S.S., Hanson G.N. (1976) Rare earth element evidence for differentiation of McMurdo volcanics, Ross Island, Antarctica. *Contributions to Mineralogy and Petrology*, Vol. 54, pp. 139–155, http://dx.doi.org/10.1007/BF00372120

Sun Z., Renfro N.D. (2017) Gem News International: Impregnated amazonite. *G&G*, Vol. 53, No. 3, pp. 384–385.

Tich P.X., Hoang N., Lee H.K. (2004) Geochemistry of late Cenozoic basalts in Vietnam and its tectonic significances. *Journal of Geology, Series B*, No. 24, pp. 65–76 [in Vietnamese].

Yin F., Dai D. (2021) Petrology and mineralogy of the Viñales meteorite, the latest fall in Cuba. *Science Progress*, Vol. 104, No. 2, http://dx.doi.org/10.1177/00368504211019859

Zanon V., Kueppers U., et al. (2013) Volcanism from fissure zones and the Caldeira central volcano of Faial Island, Azores archipelago: Geochemical processes in multiple feeding systems. *Geological Magazine*, Vol. 150, No. 3, pp. 536–555, http://dx.doi.org/10.1017/S0016756812000702

Zhang M., Wruck B., et al. (1996) Phonon spectra of alkali feldspars: Phase transitions and solid solutions. *American Mineralogist*, Vol. 81, No. 1-2, pp. 92–104, http://dx.doi.org/10.2138/am-1996-1-212

Zhou Q., Wang C., Shen A.H. (2022) Fluorescence characteristics of two copper-diffused plagioclase feldspars: Labradorite and andesine. *G&G*, Vol. 58, No. 4, pp. 424–437, http://dx.doi.org/10.5741/GEMS.58.4.424

CHARTS

MICRO-FEATURES OF TOURMALINE

Nathan Renfro, Tyler Smith, John I. Koivula, Shane F. McClure, and James E. Shigley

This chart focuses primarily on the types of natural inclusions found in tourmaline, as well as the minerals in which tourmaline can be found as an inclusion. Treatments such as enhancement of fractures, low-temperature heating, and irradiation are rare, and fracture filling is generally the only one of these that leaves any visible evidence. Because tourmaline treatments have little visual impact with regard to microscopic observations, they will not be covered in this chart, which is intended to serve as a broad overview of the micro-world of tourmaline. No synthetic gem tourmaline exists.

Tourmaline is a borosilicate mineral supergroup with a trigonal crystal structure and a wide range of chemical compositions. Tourmalines generally form elongate prismatic crystals with a triangular cross section, and they are often significantly color zoned. This color zoning results from modifications in the nutrient solution from which the tourmaline crystallizes. Due to the wide range of chemical variations possible in this mineral group, more than 40 tourmaline mineral species are now recognized.

While tourmaline is a common mineral, it is generally not abundant (London, 2008). Most gem-quality tourmalines are the lithium-rich species elbaite, found in granitic pegmatites where elements such as boron and lithium have been concentrated. Tourmalines can also form in metamorphic rock, including marbles and schists; however, many of those are schorl or dravite and may not be suitable for gem use. Notable sources are Brazil, the United States, Madagascar, Nigeria, and Mozambique. The most highly prized gem tourmalines are the vividly colored green to blue copper-bearing variety known in the trade as "Paraíba" tourmaline, named after the state in Brazil where it was first discovered (Fritsch et al., 1990). Today, these copper-bearing tourmalines are also found in Mozambique and Nigeria. "Paraíba-type" tourmalines are usually elbaite, but liddicoatite examples have also been documented (Katsurada and Sun, 2017).

Examining gem tourmaline in the microscope often reveals growth tubes resulting from a localized interruption of crystal growth, leaving behind hollow or fluid-filled tubes. These features are sometimes referred to as growth blockages. When these tubes are sufficiently dense and oriented properly, they produce a cat's-eye effect in a cabochon.

Solid mineral inclusions reflecting the growth environment are also found in gem tourmaline. Elbaite gems that formed in pegmatites may contain minerals such as lepidolite, feldspar, zircon, or pyrochlore. Tourmalines from metamorphic deposits may contain other minerals such as graphite or apatite. Tourmaline inclusions are sometimes seen in pegmatite minerals, including beryl, quartz, mica, and spodumene.

Fluid inclusions are often encountered in gem tourmalines, and these are referred to as "trichites" when they show a thready or hairlike structure. Some of these may be three-phase inclusions, containing liquid, gas, and solid components. When tourmalines containing fluid inclusions are heat treated, the fluid inclusions tend to rupture, leaving fractures that can be hidden by filling them with oils or resins.

Pink tourmalines can be irradiated to increase their color saturation, and many blue and green stones undergo low-temperature heating to improve or lighten their colors. Such treatments are often undetectable.

The tourmaline group is available in an extraordinary range of colors (figure 1). The inclusions encapsulated inside these gems are equally remarkable and can be appreciated by any gemologist who examines them with a microscope.

ABOUT THE AUTHORS

Nathan Renfro is senior manager of colored stone identification, John Koivula is analytical microscopist, Shane McClure is global director of colored stone services, and James Shigley is distinguished research fellow, at GIA in Carlsbad, California. Tyler Smith is a senior staff gemologist at GIA in New York.

Gems & Gemology, Vol. 60, No. 2, pp. 208–210,
http://dx.doi.org/10.5741/GEMS.60.2.208

Figure 1. This collection of 50 tourmalines showcases the gem's wide-ranging color palette. Photo by Robert Weldon; courtesy of Bruce A. Fry.

REFERENCES

Fritsch E., Shigley J.E., Rossman G.R., Mercer M.E., Muhlmeister S.M., Moon M. (1990) Gem-quality cuprian-elbaite tourmalines from São José da Batalha, Paraíba, Brazil. *G&G*, Vol. 26, No. 3, pp. 189–205.

Katsurada Y., Sun Z. (2017) Cuprian liddicoatite tourmaline. *G&G*, Vol. 53, No. 1, pp. 34–41.

London D. (2008) *Pegmatites*. *Canadian Mineralogist*, Special Publication No. 10, Mineralogical Association of Canada, Québec, 347 pp.

ADDITIONAL READING

Abduriyim A., Kitawaki H., Furuya M., Schwarz D. (2006) "Paraíba"-type copper-bearing tourmaline from Brazil, Nigeria, and Mozambique: Chemical fingerprinting by LA-ICP-MS. *G&G*, Vol. 42, No. 1, pp. 4–21.

Beesley C.R. (1975) Dunton mine tourmaline: An analysis. *G&G*, Vol. 15, No. 1, pp. 19–24.

Brandstätter F., Niedermayr G. (1994) Copper and tenorite inclusions in cuprian-elbaite tourmaline from Paraíba, Brazil. *G&G*, Vol. 30, No. 3, pp. 178–183.

Dirlam D.M., Laurs B.M., Pezzotta F., Simmons W.B. (2002) Liddicoatite tourmaline from Anjanabonoina, Madagascar. *G&G*, Vol. 38, No. 1, pp. 28–53.

Furuya M. (2007) Copper-bearing tourmalines from new deposits in Paraíba State, Brazil. *G&G*, Vol. 43, No. 3, pp. 236–239.

Hainschwang T., Notari F., Anckar B. (2007) Trapiche tourmaline from Zambia. *G&G*, Vol. 43, No. 1, pp. 36–46.

Johnson M.L., Wentzell C.Y., Elen S. (1997) Multicolored bismuth-bearing tourmaline from Lundazi, Zambia. *G&G*, Vol. 33, No. 3, pp. 204–211.

Johnson P.W. (1969) Common gems of San Diego County, California. *G&G*, Vol. 12, No. 12, pp. 358–371.

Katsurada Y., Sun Z., Breeding C.M., Dutrow B.L. (2019) Geographic origin determination of Paraíba tourmaline. *G&G*, Vol. 55, No. 4, pp. 648–659.

Laurs B.M., Simmons W.B., Rossman G.R., Fritz E.A., Koivula J.I., Anckar B., Falster A.U. (2007) Yellow Mn-rich tourmaline from the Canary mining area, Zambia. *G&G*, Vol. 43, No. 4, pp. 314–331.

Laurs B.M., Zwaan J.C., Breeding C.M., Simmons W.B., Beaton D., Rijsdijk K.F., Befi R., Falster A.U. (2008) Copper-bearing (Paraíba-type) tourmaline from Mozambique. *G&G*, Vol. 44, No. 1, pp. 4–30.

Long P.V., Pardieu V., Giuliani G. (2013) Update on gemstone mining in Luc Yen, Vietnam. *G&G*, Vol. 49, No. 4, pp. 233–245.

Martin J.G.M. (1958) Historical Himalaya tourmaline mine resumes production. *G&G*, Vol. 9, No. 6, pp. 163–173.

Merkel P.B., Breeding C.M. (2009) Spectral differentiation between copper and iron colorants in gem tourmalines. *G&G*, Vol. 45, No. 2, pp. 112–119.

Nhung N.T., Huong L.T.T., Thuyet N.T.M., Häger T., Quyen N.T.L., Duyen T.T. (2017) An update on tourmaline from Luc Yen, Vietnam. *G&G*, Vol. 53, No. 2, pp. 190–203.

Pezzotta F., Adamo I., Diella V., Gatta G.D., Danisi R.M. (2011) The Pederneira pegmatite, Minas Gerais, Brazil: Geology and gem tourmaline. *G&G*, Vol. 47, No. 2, pp. 141–142.

Proctor K. (1985) Gem pegmatites of Minas Gerais, Brazil: The tourmalines of the Araçuaí Districts. *G&G*, Vol. 21, No. 1, pp. 3–19.

——— (1985) Gem pegmatites of Minas Gerais, Brazil: The tourmalines of the Governador Valadares District. *G&G*, Vol. 21, No. 2, pp. 86–104.

Shaub B.M. (1955) Recent discovery of fine gem tourmalines in Maine. *G&G*, Vol. 8, No. 5, pp. 131–136.

Shigley J.E., Cook B.C., Laurs B.M., Bernardes M.O. (2001) An update on "Paraíba" tourmaline from Brazil. *G&G*, Vol. 37, No. 4, pp. 260–276.

Simmons W.B., Laurs B.M., Falster A.U., Koivula J.I., Webber K.L. (2005) Mt. Mica: A renaissance in Maine's gem tourmaline production. *G&G*, Vol. 41, No. 2, pp. 150–163.

Sinkankas J. (1957) Recent gem mining at Pala, San Diego County, California. *G&G*, Vol. 9, No. 3, pp. 80–87, 95.

Slawson C.B., Bastos F.M. (1955) The gemstones of Minas Gerais, Brazil. *G&G*, Vol. 8, No. 8, pp. 227–230, 253–254.

Sun Z., Palke A.C., Breeding C.M., Dutrow B.L. (2019) A new method for determining gem tourmaline species by LA-ICP-MS. *G&G*, Vol. 55, No. 1, pp. 2–17.

Taylor M.C. (1999) The first California gem tourmaline locality. *G&G*, Vol. 35, No. 3, pp. 153–154.

A Brilliant Future Is Here.

Online Courses from GIA Experts

Start learning from anywhere with self-paced online courses created by the leader in gemological research. Designed for working professionals, GIA® courses on diamonds, colored stones, pearls, and jewelry deliver knowledge you need to advance your career.

Choose Your Sample Lesson

GIA.edu/online-ed

Lab Notes

Editors

Thomas M. Moses | Shane F. McClure
Sally Eaton-Magaña | Artitaya Homkrajae

Bicolor CHRYSOBERYL with Chrysoberyl and Alexandrite Zones

Recently, the Tokyo laboratory received for identification service a bicolor 0.73 ct octagonal step cut measuring 5.33 × 4.37 × 2.74 mm. One zone was greenish yellow, and the other was blue-green in fluorescent light and red-purple in incandescent light (figure 1).

Standard gemological testing results, including a refractive index of 1.747 to 1.753, and Raman spectroscopy proved that this stone was zoned chrysoberyl, and more notably an extremely rare zoned chrysoberyl and alexandrite gem. Microscopic examination revealed the presence of fingerprints, straight graining, and two-phase fluid inclusions (figure 2). No evidence of coating or clarity enhancement was observed. This is the first time GIA has documented a stone composed of chrysoberyl and alexandrite.

Hikaru Sato

Figure 1. This 0.73 ct octagonal step cut was composed of chrysoberyl and alexandrite. The alexandrite portion showed a color change from blue-green in fluorescent light to red-purple in incandescent light.

Large Natural DIAMONDS with Asteriated Cloud Inclusions

The Carlsbad laboratory recently received for scientific examination two natural diamonds that displayed remarkable light brown cloud inclusions resembling stars (figure 3, left). Such diamonds are sometimes referred to as "asteriated" or "star" diamonds in the literature. Clouds are found in sectors correlating with high hydrogen and nickel concentrations and are thought to consist of graphite inclusions (B. Rondeau et al., "Three historical 'asteriated' hydrogen-rich diamonds: Growth history and sector-dependent

Figure 2. Two-phase fluid inclusions in the bicolor chrysoberyl; field of view 2.00 mm.

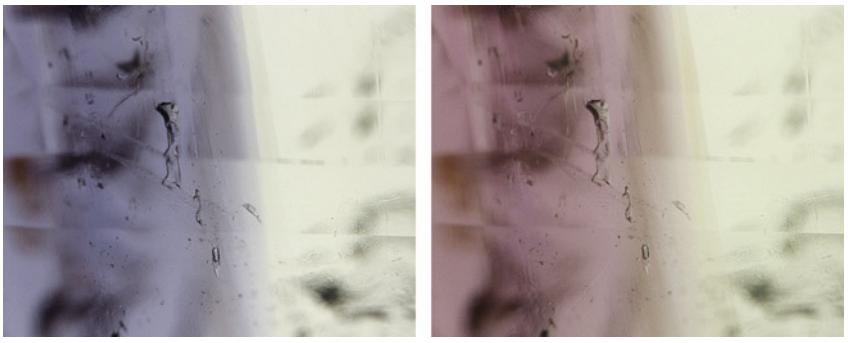

Editors' note: All items were written by staff members of GIA laboratories.

GEMS & GEMOLOGY, Vol. 60, No. 2, pp. 212–225.

Figure 3. Left: An 8.14 ct and an 8.57 ct diamond containing brown asteriated cloud inclusions with sixfold symmetry. Right: The clouds fluoresced green when exposed to long-wave UV. The purple reflections of the UV source are likely caused by surface imperfections on the rough surface.

impurity incorporation," *Diamond and Related Materials*, Vol. 13, No. 9, 2004, pp. 1658–1673; A.R. Lang et al., "Is dispersed nickel in natural diamonds associated with cuboid growth sectors in diamonds that exhibit a history of mixed-habit growth?" *Journal of Crystal Growth*, Vol. 263, No. 1-4, 2004, pp. 575–589; K.V. Smit et al., "Diamond growth from C-H-N-O recycled fluids in the lithosphere: Evidence from CH_4 micro-inclusions and $\delta^{13}C$-$\delta^{15}N$-N content in Marange mixed-habit diamonds," *Lithos*, Vol. 265, 2016, pp. 68–81).

While asteriated diamonds are occasionally submitted to GIA (Fall 2019 Lab Notes, p. 417; Fall 2019 Gem News International, p. 443), the two recently examined stones were particularly notable for their large size and preserved natural forms. The 8.14 ct diamond was resorbed and maintained most of its rough form on one side, and it was sliced to reveal the underlying inclusion pattern on the other. The preserved rough surfaces also displayed brown radiation stains, indicating their past history of natural alpha irradiation followed by annealing in the earth. The 8.57 ct diamond was a polished stone with bruted edges. In both stones, and consistent with similar asteriated diamonds previously studied, the clouds fluoresced green when subjected to long-wave UV (figure 3, right).

Both diamonds had high hydrogen concentrations, as detected by bulk Fourier-transform infrared spectroscopy. Photoluminescence (PL) mapping using 455 nm laser excitation showed a prominent wide S3 center (496.7 nm), correlating directly with the green fluorescing clouds (figure 4). This peak is associated with nickel (A.M. Zaitsev, *Optical Properties of Diamond: A Data Handbook*, Springer-Verlag, Berlin, 2001). Other nickel-related peaks in the cloud region were detected in both stones via 633 nm laser excitation at 694.2, 700.5, 787.3, and 793.4 nm (figure 5). Unattributed peaks at 709.1 and 729.6 nm were also detected. Higher peak intensities at 793.5 and 801.8 nm in the cloud inclusion sectors were revealed using 785 nm laser excitation. The former peak is associated with the S2 and S3 centers (Zaitsev, 2001), and the latter is potentially NE8, a nickel-nitrogen complex center (T. Gaebel, "Stable

Figure 4. A: The 8.14 ct diamond maintained much of its textured rough surface on one side and had a sliced surface to reveal the underlying cloud. B: The cloud fluoresced green when exposed to long-wave UV, correlating to the peak area intensity of the S3 center; field of view 7.19 mm. C: The false-color heat map showing the peak area intensity of the S3 center was collected using 455 nm laser excitation and included 43,976 spectra.

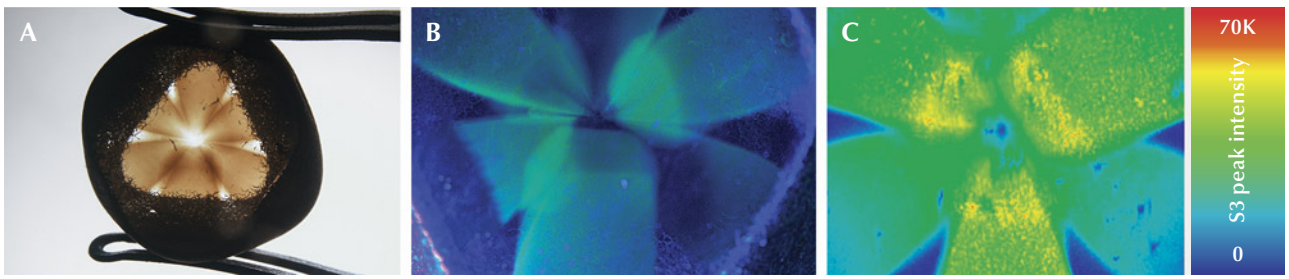

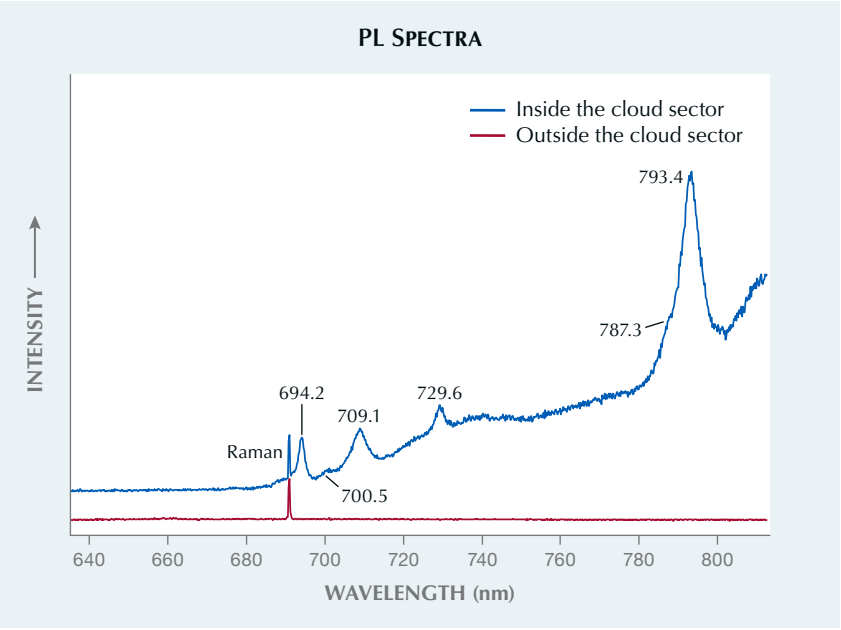

Figure 5. PL spectra for the 8.14 ct diamond when mapped with 633 nm laser excitation. Several nickel-related defects were detected inside the cloud inclusion sector but not outside of it. The spectra are stacked for clarity, and the Raman peaks are scaled as equal.

single-proton source in the near infrared," *New Journal of Physics*, Vol. 6, 2004, article no. 98).

Both diamonds were analyzed by X-ray computed microtomography (µ-CT), in which the asteriated growth sectors, ~{100}, were visible in three-dimensional reconstructions (figure 6; see video at https://www.gia.edu/gems-gemology/summer-2024-lab-notes-diamonds-asteriated-cloud-inclusions). The contrast in the µ-CT reconstruction should be mainly a function of the mean atomic number of the material. The asteriated regions more strongly absorb X-rays than the rest of the diamond, an indication that the combined signal from the diamond and inclusions likely had a higher atomic number.

These aesthetically pleasing and scientifically interesting diamonds provide stunning examples of what the natural world has to offer.

Taryn Linzmeyer, Henry Towbin, and Sally Eaton-Magaña

Figure 6. Left: µ-CT cross section of the 8.57 ct diamond. Asteriated growth sectors are observed following the <100> crystallographic directions. While the cloud sectors appear solid, they are actually composed of microscopic inclusions. Right: 3D rendering of the segmented µ-CT image highlighting the asteriated sectors in yellow within the semi-transparent diamond.

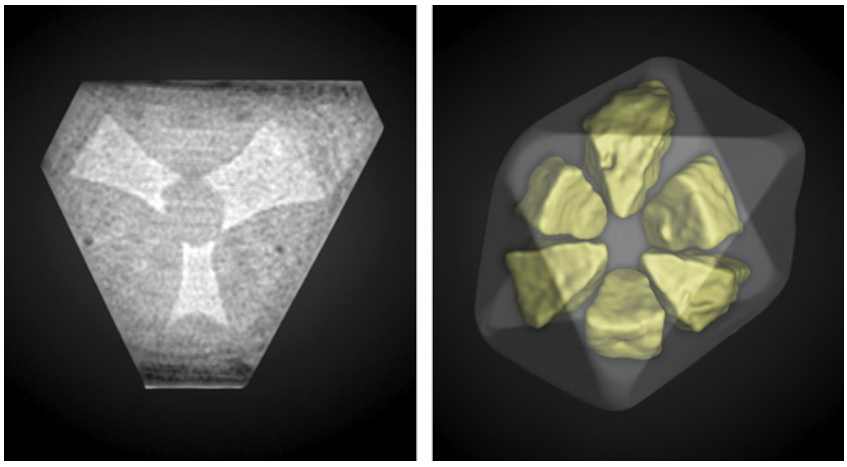

Cat's-Eye HEXAGONITE

A 0.50 ct purplish pink cabochon displaying chatoyancy (figure 7) was recently submitted to the New York laboratory as a ruby. Standard gemological testing revealed a spot refractive index of 1.63 and a hydrostatic specific gravity of 3.02, neither of which were consistent with the expected values for corundum. Raman analysis, along with the specific gravity and refractive index, confirmed the identity of this mineral as tremolite (figure 8).

Hexagonite, a variety of tremolite, ranges in color from red to pink to purple. Initially believed to be a hexagonal form of tremolite, and named

Figure 7. This 0.50 ct purplish pink cabochon is a rare chatoyant example of hexagonite.

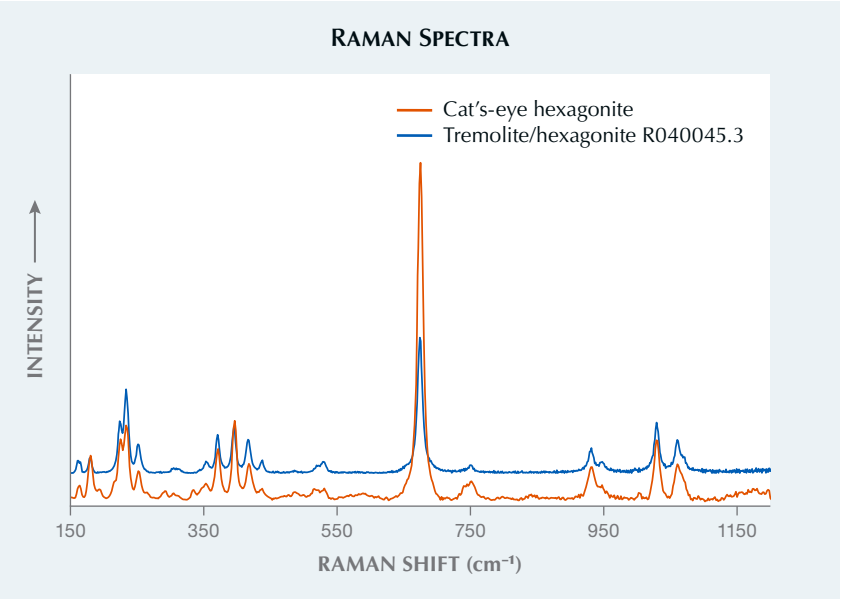

Figure 8. Raman spectrum of the cat's-eye hexagonite compared to a known tremolite reference spectrum. Spectra are offset vertically for clarity.

accordingly, the mineral was later confirmed to be monoclinic (Summer 1985 Lab Notes, p. 110). This mineral can be found in facetable sizes in St. Lawrence County and Lewis County, both in the state of New York. Though typically under a carat and heavily included, a few large transparent stones have been unearthed.

Under magnification, the densely included stone displayed long silk and needles (figure 9). These inclusions, when oriented parallel to each other and the base of a cabochon, create the cat's-eye phenomenon.

Courtney Robb

Metallic See-Through Backing on Omphacite JADE

The Carlsbad laboratory recently received for identification an omphacite jade carving in the shape of a pea pod (figure 10) with an unusual effect created by its backing. Adhered on the back of the carving, which measured 23.71 × 9.67 × 2.59 mm and weighed 4.52 ct, was a thin layer of plastic-like material with a metallic luster. Standard gemological testing revealed a spot refractive index of 1.66 and weak blue fluorescence due to the plastic layer; microscopic observation showed the film in reflected light. A metallic film of 0.10 mm thickness was found to be adhered on the back of the piece to create a metallic look. It had a see-through quality, shown in figure 11. Raman analysis of the thin film closely matched with a plastic used in Mylar.

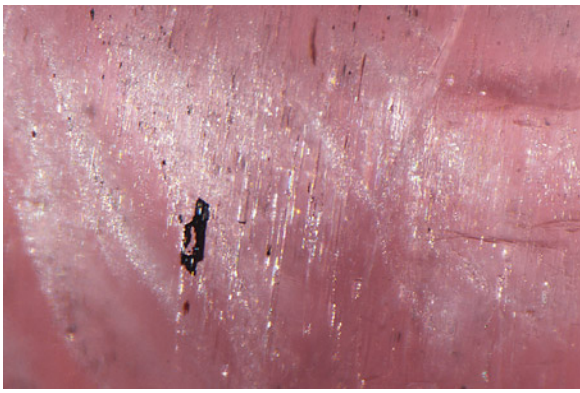

Figure 9. Light reflects off densely packed silk, needles, and particles to create the cat's-eye effect. Field of view 1.31 mm.

Figure 10. A: Face-up view of the 23.71 × 9.67 × 2.59 mm jade carving. B: The profile view shows the thickness of the thin film lining. C: The back of the carving shows the reflective metallic luster of the film.

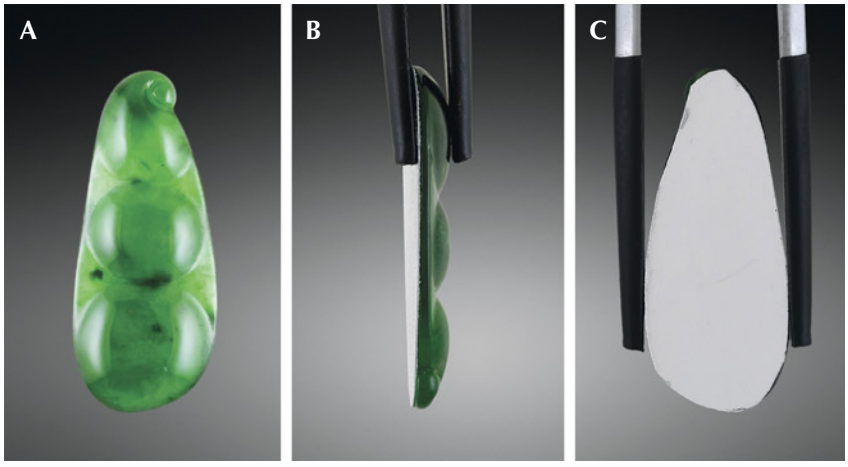

Figure 11. The see-through nature of the carving and thin reflective film backing.

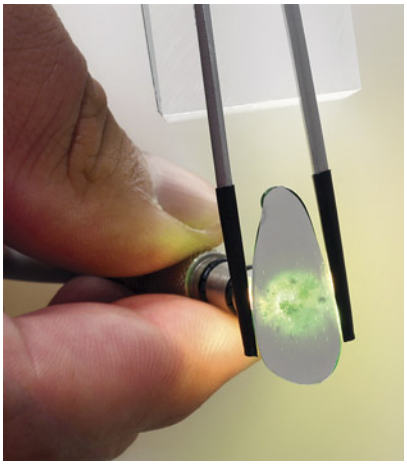

Figure 12. The five CVD-grown diamond samples set in variously designed metal rings: ~5.00 ct orange heart brilliant (A), ~5.58 ct greenish blue pear brilliant (B), ~2.30 ct greenish blue cushion modified brilliant (C), ~1.65 ct yellowish orange square emerald cut (D), and ~3.08 ct grayish green emerald cut (E).

Analysis for polymer impregnation with Fourier-transform infrared spectroscopy revealed the importance of direction in testing the piece. If the laser was positioned perpendicular to the metallic film so that the laser went through the film, the glue layer would be detected, creating a false positive for polymer impregnation. Analysis parallel to the metallic film proved the piece was not polymer impregnated. Understanding and identifying all components of such a piece is very important in the determination of jade treatment types.

Maxwell Hain

Large Treated-Color CVD LABORATORY-GROWN DIAMOND Rings

Laboratory-grown diamonds have become a prominent sector of the jewelry market. Part of the consumer appeal relates to the availability of stones with vibrant colors and the range of carat sizes. The New York laboratory received one submission of five laboratory-grown diamonds produced by chemical vapor deposition (CVD) set in variously designed metal rings (figure 12). These samples represent the wide range of stone colors and sizes created using CVD growth technology. CVD diamonds commonly undergo post-growth treatments to improve clarity and color. Post-growth treatments such as high-pressure, high-temperature (HPHT) processing, irradiation, and annealing are often necessary for a more desirable color result. High-temperature treatment may remove internal synthetic graining patterns to improve clarity. Gemologists identify the treatments based on subtle indicators using several methods, specifically spectroscopic data analysis.

Infrared absorption spectroscopy showed no absorption related to nitrogen or boron, classifying these CVD diamonds as type IIa. The visible/near-infrared absorption spectrum, taken at room temperature, displayed GR1 absorption in all five samples (e.g., figure 13). Photoluminescence spectroscopy revealed a GR1 emission and silicon-vacancy doublet at 736.6 and 736.9 nm in samples B–E. The SiV^- doublet is usually indicative of CVD growth since it is rarely seen in natural diamonds or HPHT-grown diamonds. The presence of the SiV^- reveals CVD growth but does not contribute to the color within these stones. The GR1 defect in these CVD diamonds is evidence of post-growth treatment that included irradiation causing alterations in bodycolor.

The data suggest the samples underwent various treatments including HPHT annealing, irradiation, and possible post-irradiation annealing. Based on spectroscopic data, sample A shows evidence of HPHT treat-

Figure 13. Four of the five CVD diamond samples are shown with a clear GR1 defect. Spectra are offset vertically for clarity.

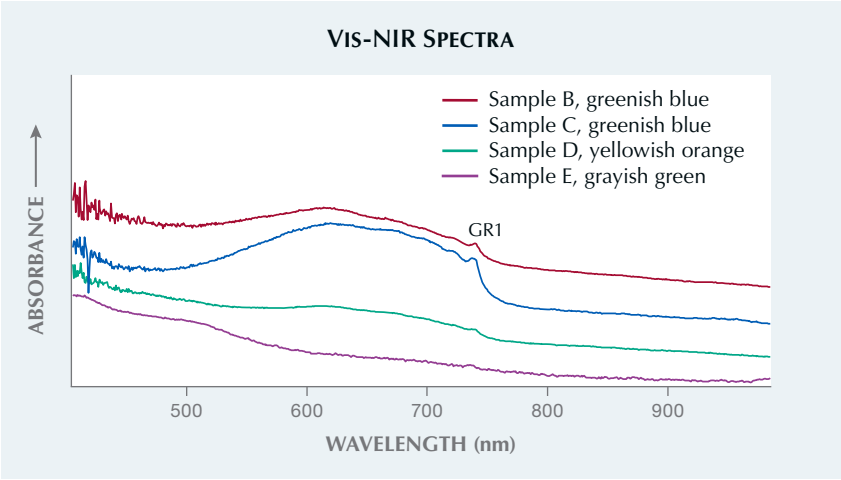

ment due to the lack of the 468 nm peak, irradiation, and low-temperature annealing to create the orange color. The greenish blue colors for samples B and C were created with irradiation and possibly annealing. Both samples contained strong absorption from the GR1 center and a weak 666.5 nm peak that can be annealed out at temperatures ranging from 420° to 540°C (see A.T. Collins, "Spectroscopy of defects and transition metals in diamond," *Diamond and Related Materials*, Vol. 9, Nos. 3–6, 2000, pp. 417–423). Sample D likely underwent irradiation and subsequent low-temperature treatment to create the yellowish orange color. The grayish green color in sample E was likely the result of HPHT treatment and irradiation with subsequent annealing. We consider the annealing temperatures to be low to moderate because of the lighter color result in sample E.

Gemological and spectroscopic analysis revealed that all five samples were type IIa CVD-grown diamonds that underwent post-growth treatment to achieve fancy colors. The laboratory-grown diamond market continues to develop, driven by consumer demand for these affordable mined diamond alternatives.

Stephanie Persaud and Erica Watts

Figure 14. The white saltwater nacreous pearl weighing 1.90 ct and measuring 6.75 × 6.55 × 6.19 mm.

PEARLS

Seed Features in an Akoya Keshi Pearl

Recently, GIA's Mumbai laboratory received a white button-shaped saltwater nacreous pearl weighing 1.90 ct and measuring 6.75 × 6.55 × 6.19 mm for pearl identification (figure 14). When observed under high magnification, the pearl's surface showed fine fingerprint-like overlapping platelets typical of aragonite. Energy-dispersive X-ray fluorescence revealed a manganese level below the detection limit and a strontium level of 857 ppm, confirming the pearl's saltwater origin. Under long-wave ultraviolet light, the pearl exhibited a moderate greenish yellow reaction, which is typical for pearls from the *Pinctada* species.

Real-time X-ray microradiography (RTX) analysis revealed a small oval-shaped core surrounded by a dark gray organic-rich concentric structure displaying an acicular (or radial) pattern

Figure 15. A: RTX image showing an oval core in an organic-rich concentric structure surrounded by an acicular pattern. An elongated, irregular Tokki-like feature with a linear structure is positioned on the top of the concentric growth structure. B: µ-CT image showing the oval core with a seed feature on the inner growth arc. C: µ-CT image showing another seed feature on the outer growth arc.

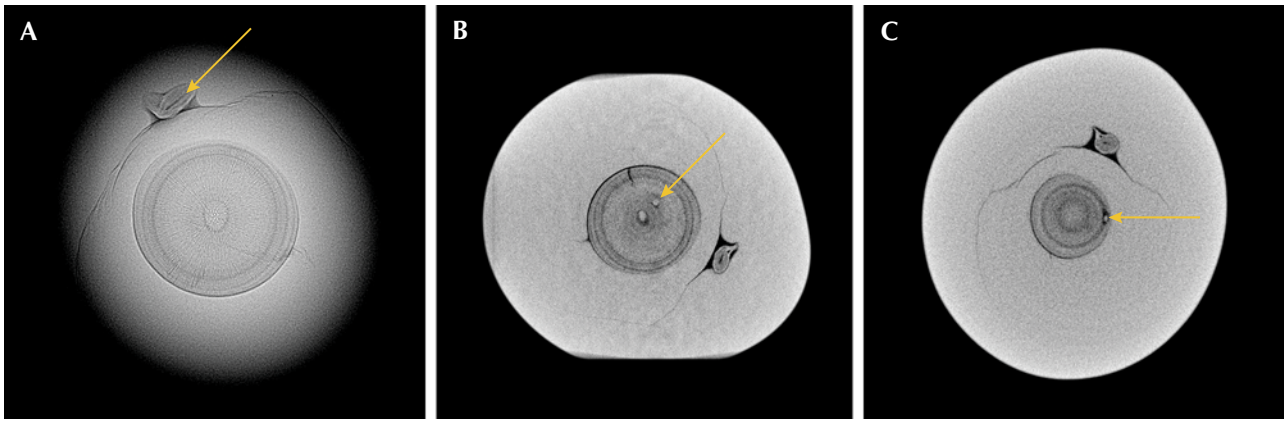

(figure 15A). An additional elongated, irregular feature with a linear structure at its center was positioned above the central structure, as indicated by the arrow in figure 15A. The growth characteristic of this additional feature looked similar to the internal structure of surface protuberances that sometimes form on bead cultured pearls. Bead cultured pearls with additional surface protuberances are sometimes referred to as Tokki pearls (M.S. Krzemnicki et al., "Tokki pearls: Additional cultured pearls formed during pearl cultivation: External and internal structures," *32nd International Gemmological Conference*, 2011; https://www.ssef.ch/wp-content/uploads/2018/01/SSEF_Tokki_pearls.pdf). Owing to the existence of an elongated feature, it was questionable whether this was a non-bead cultured (NBC) pearl.

Further examination using X-ray computed microtomography (µ-CT) revealed two light gray seed features in the main concentric growth structure: a larger one near the core in the acicular area and a smaller one close to the outline of the concentric growth structure (figure 15, B and C). Previous studies of saltwater NBC pearls, known as keshi cultured pearls, produced from various *Pinctada* mollusk species have shown that NBC pearls with organic-rich concentric growth structures sometimes contain seed features made up of a calcium carbonate substance; these seed features appeared light gray in microradiographs. The seed features can be different sizes and shapes, and they are typically found within organic-rich areas in loose concentric ring structures (A. Homkrajae et al., "Internal structures of known *Pinctada maxima* pearls: Cultured pearls from operated marine mollusks," Fall 2021 *G&G*, pp. 186–205).

Conversely, organic-rich concentric structures with acicular patterns are typically associated with calcite formation in some natural pearls. It is therefore unusual to observe seed features in an acicular organic-rich structure. The presence of both seed features and the elongated Tokki-like feature in this pearl indicated an NBC pearl formation, most likely produced from the *Pinctada fucata* (akoya) oyster based on internal structure and external appearance.

While seed features can be found in natural pearls, they are usually located on the outer concentric rings closer to the pearl's surface and, in some cases, may contain fine growth arcs (A. Homkrajae et al., "Internal structures of known *Pinctada maxima* pearls: Natural pearls from wild marine mollusks," Spring 2021 *G&G*, pp. 2–21). In addition, they have a different radiopacity compared to their cultured counterparts.

Differentiating between natural and cultured pearls poses a significant challenge, given that pearls are unique products of living organisms. µ-CT has enabled gemologists to provide conclusive results on certain features associated more with NBC pearls that are not visible on RTX images, such as the seed features in this example. Seed features are more commonly observed in cultured pearls originating from *Pinctada maxima*. This pearl is noteworthy due to the rarity of seed features in akoya keshi pearls and in this case its combination with an acicular structure.

Jayesh Surve and Abeer Al-Alawi

A Large Multicolored Natural Blister Pearl

Pearls have always been renowned for their beauty and mystical allure. From the wide range of pearls examined in GIA's Mumbai laboratory, one recent submission was highlighted for its remarkable size and unique multicolored appearance. The baroque-shaped natural blister pearl weighed 90.08 ct and measured 28.66 × 22.19 × 18.50 mm (figure 16).

The surface exhibited an array of colors. The top was an attractive silvery white with strong orient, while the sides displayed various shades of red ranging from orangy red to dark red with a yellowish cream hue on the base. Under high magnification, a nacreous area with a fine platy structure was observed on the top, and a non-nacreous area on the side and base displayed a complex crystalline structure along with minor surface-reaching cracks (figure 17, A–C). When exposed to long-wave ultraviolet radiation, the red part of the pearl was inert, while the silvery white area emitted a moderate greenish yellow reaction, which is a common reaction for unprocessed and untreated pearls.

Energy-dispersive X-ray fluorescence spectrometry on multiple spots of the surface revealed a magnesium range from below detection limits up

Figure 16. The multicolored pearl weighing 90.08 ct and measuring 28.66 × 22.19 × 18.50 mm.

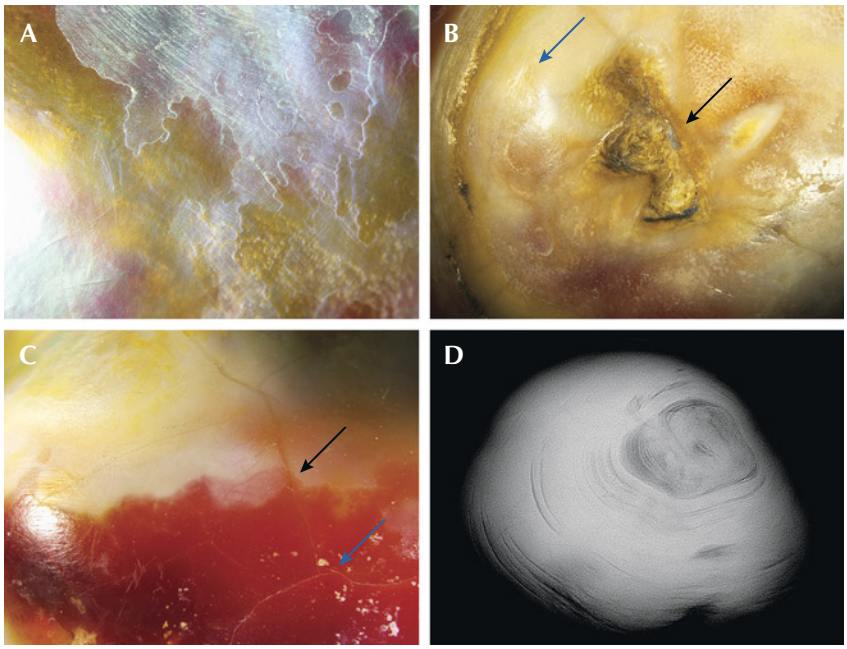

Figure 17. A: Nacreous platy structure on the top portion of the pearl. B: Nacreous structure (blue arrow) and non-nacreous structure (black arrow). C: Surface-reaching cracks (blue arrow) and boundary between two colored portions of the non-nacreous surface (black arrow). D: RTX image showing the organic-rich concentric natural growth pattern following the shape of the pearl. Fields of view: 0.80 mm (A), 2.20 mm (B), and 1.5 mm (C).

to 35 ppm and strontium levels ranging from 1031 to 2646 ppm, indicating a saltwater origin. Real-time X-ray microradiography (RTX) imaging showed an off-center organic-rich core surrounded by concentric growth arcs following the pearl's shape (figure 17D). This distinctive internal structure corresponded to those observed in natural whole pearls. However, the presence of a worked area on the base indicated the pearl had once been attached to a mollusk's shell. Therefore, it was identified as a natural blister pearl ("Natural shell blisters and blister pearls: What's the difference?" *GIA Research News*, August 26, 2019).

Raman analysis was conducted on two spots using an 830 nm laser excitation due to higher background fluorescence in this sample. The nacreous area showed peaks at 701, 704, and 1085 cm^{-1} indicative of aragonite, while the non-nacreous orangy red area revealed peaks at 283, 712, and 1085 cm^{-1} indicative of calcite (figure 18). Ultraviolet/visible reflectance spectra on the same spots showed reflectance minima at around 280 nm and an area of lower reflectance between 420 and 500 nm, similar to that observed in pearls from the *Pinctada maxima* mollusk.

Since no indication of color pigments was observed on the nacreous portion of the pearl, the various colors seen on the nacreous surface were likely due to the iridescent effect in the multilayered aragonite platelet structure, similar to abalone pearls. The cause of the red coloration on the non-nacreous area remains unclear; however, no indications of treatment were identified. According to previous studies on pen pearls (e.g., Fall 2009 Gem News International, pp. 221–223), red coloring in pen pearls is associated with carotenoid pigments, and porphyrins may be responsible for imparting a red color. However, the Raman peaks reported in those studies were not detected in this sample.

This large multicolored natural blister pearl with both nacreous and non-nacreous surfaces is an intriguing product of nature.

Anukul Belanke, Roxane Bhot Jain, and Abeer Al-Alawi

Figure 18. The Raman spectra showed peaks at 283 and 712 cm^{-1} indicative of calcite and typical aragonite features at 701, 704, and 1085 cm^{-1} at 830 nm excitation.

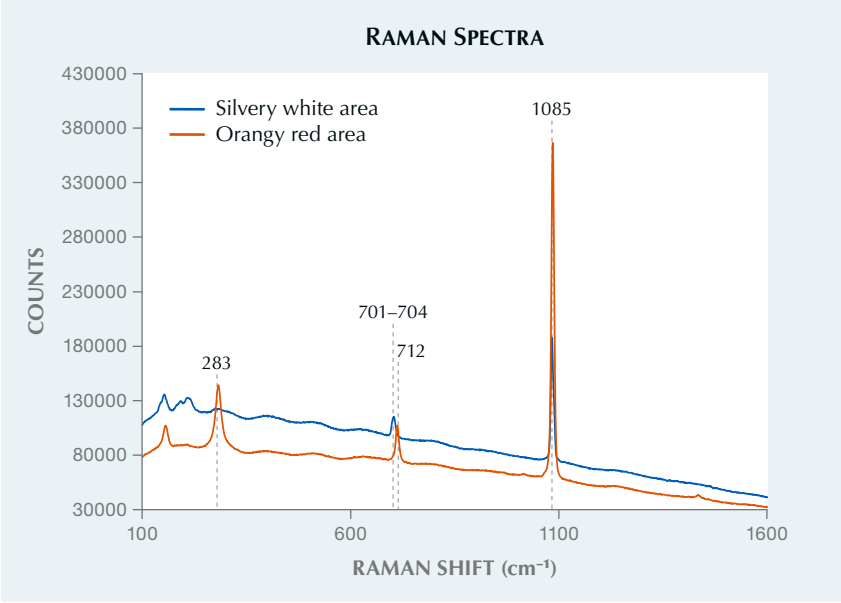

Figure 19. A white saltwater natural calcite pearl weighing approximately 0.12 ct and measuring 2.55 mm in diameter.

Calcite Pearl with Red X-Ray Fluorescence

GIA's Mumbai laboratory recently received for identification seven strands containing 1,170 variously shaped white to cream-colored pearls. Real-time X-ray microradiography (RTX) revealed that most of the pearls were of natural origin, and a few were non-bead cultured pearls. All the natural pearls showed an inert reaction when exposed to X-ray excitation due to their saltwater origin, except for one white near-round pearl that measured 2.55 mm in diameter and weighed approximately 0.12 ct (figure 19). The pearl exhibited a very unusual deep red fluorescence (figure 20, left).

RTX analysis showed a minimal growth structure with a few faint growth arcs in the outer area of the pearl and one distinct growth ring closer to the center near the drill hole (figure 21, left). X-ray computed microtomography (μ-CT) further revealed a very fine growth arc within the center ring (figure 21, right). These were consistent with structures observed in natural pearls from the *Pinctada* species.

Figure 20. Left: An X-ray fluorescence image of the pearl showing a deep red fluorescence. Right: This photomicrograph of the pearl's inner layer reveals a network of blue subsurface vein-like features; field of view 1 mm.

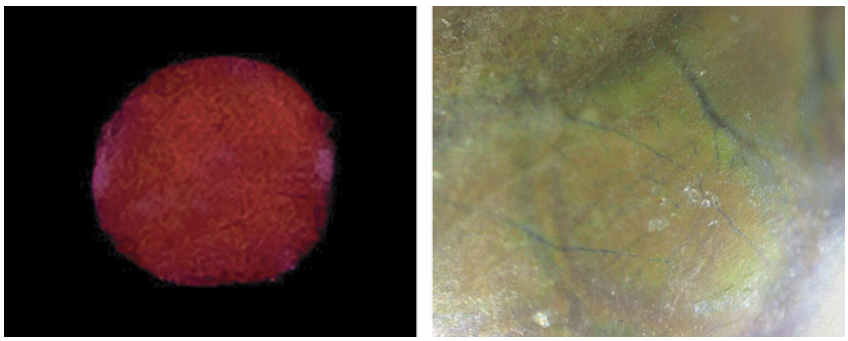

Externally, the pearl looked similar to the other pearls in the strands, possessing a medium surface luster with orient. Examination at high magnification exposed a translucent layer showing characteristic fingerprint-like overlapping surface platelets with blue subsurface vein-like features branching out in a dendritic pattern beneath it (figure 20, right). Interestingly, similar blue vein-like features have been observed in some research pearl samples reportedly produced from *Pinctada radiata* mollusks from the Persian (Arabian) Gulf. No visual indications of treatment on the surface were observed. Under long-wave ultraviolet light, the pearl exhibited a moderate chalky bluish green reaction. Energy-dispersive X-ray fluorescence revealed a manganese level of 76 ppm and a strontium level of 1599 ppm, characteristic of saltwater origin.

Raman analysis conducted on two randomly chosen spots using 514 nm laser excitation revealed peaks at 154, 282, 712, 1085, and 1437 cm^{-1}, indicating calcite composition. Saltwater calcite pearls with a "nacreous-looking" surface have been previously examined by GIA laboratories (Winter 2022 Lab Notes, pp. 477–478; Spring 2024 Lab Notes, pp. 69–71). However, they lacked visible fluorescence to X-ray excitation and exhibited a clear, evenly spaced fine concentric ring structure, contrasting with the minimal growth structure of this pearl.

Spectroscopic analysis combined with microscopic examination suggested that the red fluorescence was not a result of any surface treatment, but rather a natural phenomenon. Orange to red fluorescence has been previously recorded in freshwater pearls containing calcite and vaterite (both of which are polymorphs of calcium carbonate) when activated by cathodoluminescence or X-ray excitation. This luminescence has been associated with the presence of Mn^{2+} in either calcite or vaterite in freshwater non-bead cultured pearls from China (S. Karampelas et al., "Chemical characteristics of freshwater and saltwater natural and

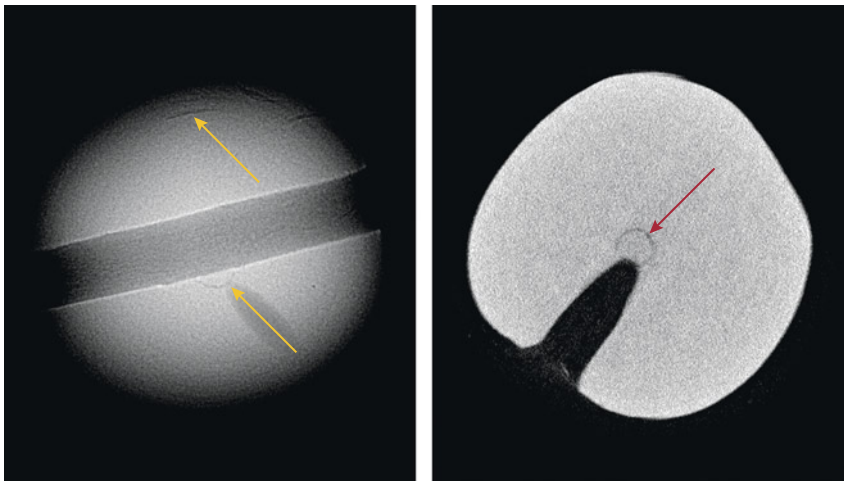

Figure 21. Left: RTX image displaying very fine growth arcs (yellow arrows). Right: µ-CT image showing a center ring with a very fine growth arc inside (red arrow).

cultured pearls from different bivalves," *Minerals*, Vol. 9, No. 6, 2019, article no. 357). Although such red fluorescence in saltwater pearls has not been previously recorded, we suspect a connection to the presence of calcite on the pearl's surface, though the existence of vaterite in the inner nacre layers remains a possibility.

Further research on the chemical composition of the surface and inner cross-sectional layers of this sample is required to understand the exact formation and the specific cause of this reaction in saltwater pearls. This is the first time GIA has encountered a nacreous-looking calcite pearl that exhibited red fluorescence when subjected to X-ray excitation.

Rajesh Patel and Abeer Al-Alawi

Large *Tridacna* Shell with a Blister Pearl and a Shell Blister

A collection of various shells was recently submitted to the Mumbai laboratory. Among these was a large shell from the *Tridacna* species, featuring an attached blister pearl and a shell blister (figure 22). The shell was sawn on three sides to create a stable base for display and weighed approximately 1.37 kg.

Externally, the off-white shell exhibited a wavy pattern of thin, sharp ridges in rows, along with several parasitic holes. Unlike shells from other mollusks, *Tridacna* shells exhibit thick growth layers of calcium carbonate in a rippling, overlapping pattern. In the thick cross section of this shell, the growth layers opened into a large cavity at one end, divided into two parts by a thin, wavy layer of calcium carbonate (figure 23A).

The interior surface was white to light cream in color, with a smooth porcelain-like surface featuring two protuberances that appeared to be a blister pearl and a shell blister, each naturally attached and displaying distinct striations toward their respective outer edges. The light gray blister pearl with brownish patches on its body, measuring approximately 37.31 × 25.42 mm, displayed a relatively smooth porcelaneous surface with a short and patchy flame-like structure (figure 23B). The dull cream-colored shell blister, measuring 28.93 × 16.63 mm, protruded outward and resembled a cone, with a concave opening at its apex encircled by a brown area rich in organic matter (figure 23C).

Figure 22. Tridacna *shell with a natural blister pearl measuring 37.31 × 25.42 mm (left) and a shell blister measuring 28.93 × 16.63 mm (right).*

Figure 23. A: Cross section of the shell in the cut area. B: The porcelain-like surface of the blister pearl was characterized by a short and patchy flame-like structure; field of view 16.3 mm. C: The concave opening encircled by a brown organic-rich area on the shell blister; field of view 16.3 mm.

Under long-wave ultraviolet radiation, the shell and shell blister exhibited a moderate to strong chalky blue reaction, while the blister pearl displayed reddish purple patches on its surface. Energy-dispersive X-ray fluorescence analysis could not be conducted due to the size of the specimen. Raman analysis of both the blister pearl and the shell blister showed a weak doublet at 701 and 704 cm^{-1} and a peak at 1086 cm^{-1}, indicative of aragonite, with no indication of color treatment.

The identity of both the blister pearl and the shell blister was confirmed by real-time X-ray microradiography (RTX) analysis. Both features exhibited cavity or void-like structures that have previously been observed in whole pearls and blister pearls from the *Tridacna* species (Summer 2017 Lab Notes, pp. 231–233). The blister pearl revealed a globule-like structure at its base, with a dark void of varying opacity and organic-rich material (figure 24, left). Its firm attachment to the shell was visible at one end, with discernible shades of gray indicating organic material, confirming its identity as a blister pearl. Conversely, the shell blister displayed a faint void lacking distinct features and contained light gray tubular features indicative of the parasitic boreholes and channels that contributed to its formation (figure 24, right). Parasite channels in the shell were displayed as dark gray lines in random patterns and different thicknesses.

Studies have shown that blister pearls develop as whole pearls within the mantle, normally appearing as tall domes fused with the shell, while shell blisters are caused by foreign bodies and appear as shallow bumps on the shell's inner surface ("Natural shell blisters and blister pearls: What's the difference?" *GIA Research News*, August 26, 2019). Differentiating between blister pearls and shell blisters can be challenging as they can have a similar surface appearance; thus, identification must be confirmed using internal growth structures. The presence of both within the submitted shell pro-

Figure 24. Left: RTX image of the larger blister pearl with a globule-like structure (indicated by the arrow) and a dark void following the shape of the pearl. Right: RTX image of the smaller shell blister with a faint void and white tubes (indicated by the arrow).

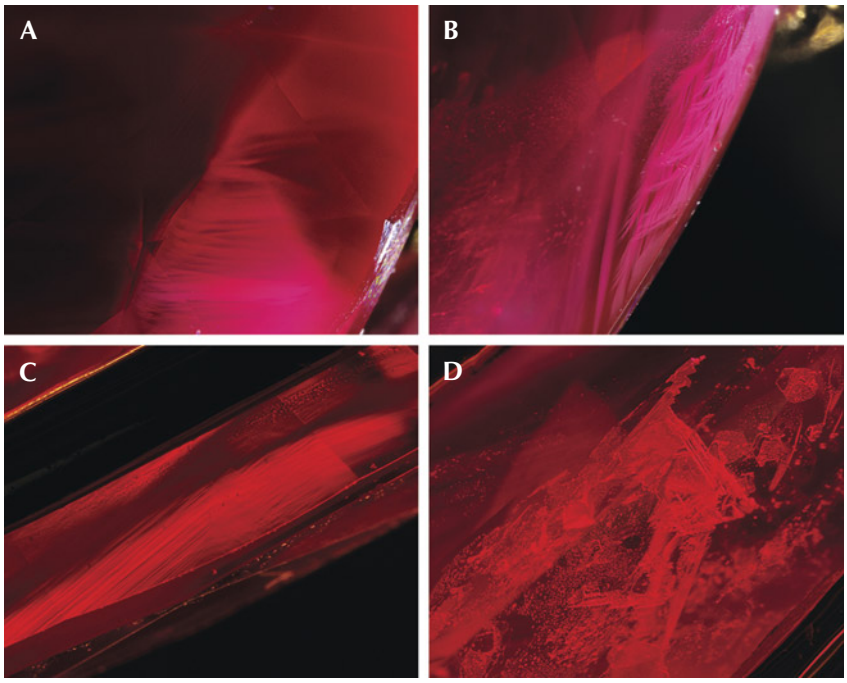

Figure 25. Inclusions in a Ramaura flux-grown synthetic ruby: angular milky clouds (A), wispy veil-like irregular hazy clouds (B), strong angular graining (C), and triangular flux inclusions (D). Fields of view 2.96 mm (A, B, and D) and 3.99 mm (C).

vided gemologists with valuable insights on their unique appearance and formation, offering significant gemological and scientific information for future reference.

Andrew Aron, Abeer Al-Alawi, and Roxane Bhot Jain

Natural-Looking Inclusions in a Ramaura SYNTHETIC RUBY

GIA's Tokyo laboratory recently observed a vivid red stone mounted in a ring that was submitted for an identification and origin report. This stone measured 14.13 × 5.41 × 3.60 mm, with an estimated weight around 2.14 ct. It showed two strong specific absorption lines around 468 and 476 nm in the blue area through a handheld spectroscope, and its gemological properties confirmed ruby.

The ruby fluoresced strong red to long- and short-wave ultraviolet light. It contained natural-looking angular milky clouds (figure 25A), unusual wispy veil-like milky clouds (figure 25B), strong angular graining (figure 25C), and triangular negative crystals containing flux-like materials and minute bubbles (figure 25D). Although the pattern of milky clouds gave the appearance of a natural origin, the wispy veil-like clouds and triangular flux-like inclusions are characteristics of flux-grown synthetic ruby.

Laser ablation–inductively coupled plasma–mass spectrometry (LA-ICP-MS) was used to determine the chemical nature of the stone. The analysis revealed lower concentrations of magnesium and gallium and much higher concentrations of lanthanum, platinum, and lead than those found in natural rubies (table 1). Vanadium was not detected. These chemical features, especially the absence of vanadium and the detection of lanthanum, platinum, and lead, were abnormal for natural ruby. The inclusions and trace element chemistry, particularly the presence of lanthanum, suggested a Ramaura flux-grown synthetic ruby (e.g., S. Muhlmeister et al., "Separating natural and synthetic rubies on the basis of trace-element chemistry," Summer 1998 *G&G*, pp. 80–101). The inclusions were consistent with those in Ramaura flux-grown rubies except for the presence of natural-looking milky clouds (R.E. Kane, "The Ramaura synthetic ruby," Fall 1983 *G&G*, pp. 130–148).

The Ramaura flux process, first reported in 1983, can produce red corundum by spontaneous nucleation of a crystal from a high-temperature flux. Ramaura synthetic rubies are formed using a flux of Bi_2O_3 and PbF_2

TABLE 1. Trace element concentrations (in ppma) of the clean and cloudy areas of the Ramaura flux-grown ruby, measured by LA-ICP-MS.

	Mg	Cr	Fe	Ni	Ga	La	Pt	Pb
Clean area SP1	5.33	2851	51	2.27	8.83	6.65	1.02	5.58
Clean area SP2	0.83	4706	68	4.20	10.12	0.01	5.10	0.02
Cloudy area SP3	0.65	3153	61	2.03	9.77	55.20	1.04	57.77
Cloudy area SP4	0.74	3287	64	2.15	1.97	74.88	1.09	243.07
Detection limit (ppma)	0.02	0.22	3	0.1	0.01	0.001	0.001	0.001

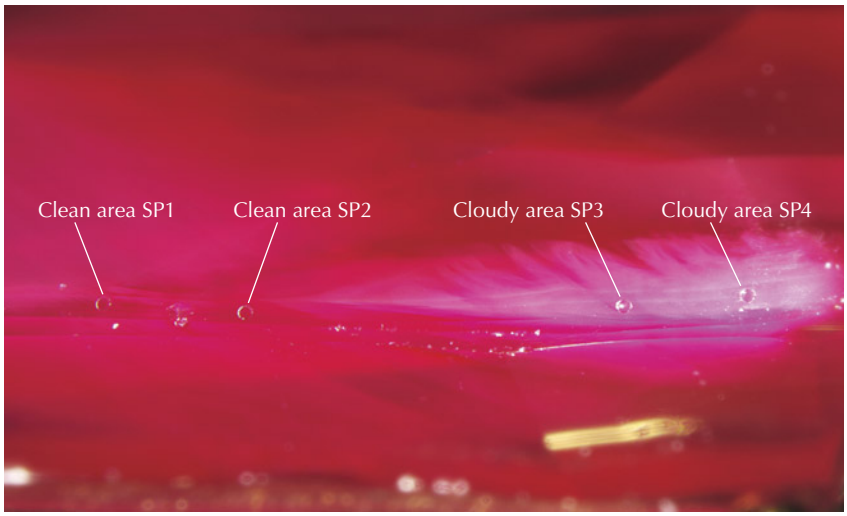

Figure 26. LA-ICP-MS analysis spots located in clean and cloudy regions within the ruby. Field of view 3.99 mm.

within a platinum crucible (Muhlmeister et al., 1998). The La_2O_3 is intentionally added to the flux, and thus the presence of lanthanum is a specific signature of Ramaura synthetic ruby. Most of this stone's inclusions and chemical features supported a synthetic origin, but the natural-looking milky inclusions were unusual and have not been reported until now.

In order to clarify the cause of the natural-looking clouds, LA-ICP-MS results from the clean areas and the cloudy areas reaching the girdle were compared (figure 26). The chemical comparison suggested that the cloudy area was extremely rich in lanthanum and lead relative to the clean area (table 1). How lanthanum and lead are incorporated into this synthetic ruby is not clear, as there were no obvious inclusions that could be tested (such as particles or flakes within the clouds). However, the natural-looking clouds were clearly formed by partial enrichment of lanthanum and lead within this Ramaura synthetic ruby.

Surprisingly, such milky clouds and flux inclusions could be confused with heated natural ruby and might cause misidentification. Careful observation of inclusions in the stone and chemical analysis were both needed to confirm that this was a laboratory-grown ruby.

Makoto Miura

Unique Moiré-Pattern Metallic Inclusion in Paraíba TOURMALINE

The Tokyo laboratory received a 0.33 ct greenish blue oval modified brilliant measuring 5.48 × 3.60 × 2.37 mm (figure 27). Gemological properties, as well as trace element analysis collected with laser ablation–inductively coupled plasma–mass spectrometry (LA-ICP-MS), identified this gem as a Paraíba tourmaline from Brazil.

Microscopic observation revealed planar inclusions consisting of minute particles in the area marked in figure 27. Under fiber-optic illumination, these minute particles had a pink metallic luster. The particles were clustered together, but circular to teardrop-shaped voids in these clusters contained no observable particles (figure 28). Further magnification showed that the particles were arranged in a moiré pattern (figure 29). A moiré pattern occurs when two sets of parallel lines are superimposed, which is sometimes observed in gemstone inclusions (e.g., Fall 2023 *G&G* Micro-World, pp. 375–376). These planar inclusions did not reach the surface of the stone. No fissure was observed along the inclusion. Based on the particles' pinkish color and metallic luster, as well as the stone's high copper content (17095–22700 ppmw), we assume they were native copper. This data was not collected directly from the inclusions but from the girdle of the stone by LA-ICP-MS. Considering the high range of copper concentration compared to the reported copper level of Brazilian Paraíba tourmaline from 119 to 38800 ppmw (Y. Katsurada et al., "Geographic origin determination of Paraíba tourmaline," Winter 2019 *G&G*, pp. 648–659), it is possible they are native copper just

Figure 27. A moiré-pattern metallic inclusion was observed in the marked area of the 0.33 ct Paraíba tourmaline.

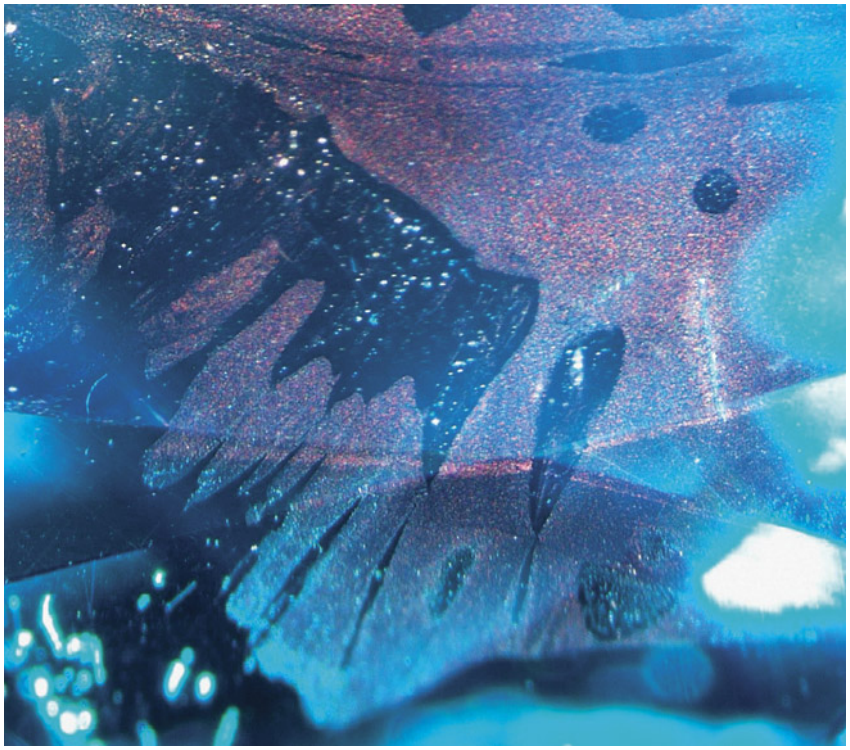

Figure 28. Fiber-optic light showed particles with metallic luster distributed in planar form. Under brightfield or darkfield illumination, the particles' low relief made them almost invisible at first glance. Field of view 1.55 mm.

like the metallic platelets sometimes found in high-copper Paraíba tourmalines (e.g., F. Brandstätter and G. Niedermayr, "Copper and tenorite inclusions in cuprian-elbaite tourmaline from Paraíba, Brazil," Fall 1994 *G&G*, pp. 178–183; Fall 2022 Lab Notes, pp. 362–363; H.A.O. Wang et al., "Further characterisation of native copper inclusions in Cu-bearing tourmaline," *Journal of Gemmology*, Vol. 38, No. 5, 2023, pp. 427–429).

Figure 29. Further magnification revealed the arrangement of particles in a moiré pattern. Field of view 0.93 mm.

Some studies have discussed formation scenarios of dendritic copper inclusions. Brandstätter and Niedermayr (1994) suggested epigenetic exsolution formation because the concentration of CuO decreased toward the native copper inclusions, which were located along the planes corresponding to the trigonal symmetry of tourmaline. On the other hand, Wang et al. (2023) suggested syngenetic formation rather than epigenetic formation, based on the distribution of valence states of copper (metallic copper/Cu^{2+}) and the presence of liquid inclusions similar in shape to dendritic native copper.

The inclusions we observed were different from the dendritic inclusions discussed in previous studies in terms of pattern and orientation in the host tourmaline. Consequently, there could be other mechanisms or scenarios at play with these inclusions, including the possibility of a material other than native copper.

Kanako Otsuka and Yusuke Katsurada

PHOTO CREDITS
Shunsuke Nagai—1; Hikaru Sato—2; Annie Haynes—3; Taryn Linzmeyer—4; Jian Xin (Jae) Liao—7, 12; Courtney Robb—9; Diego Sanchez—10, 11; Gaurav Bera—14, 16, 19, 20, 22, 23A; Andrew Aron—23 (B and C); Lubna Sahani—17; Makoto Miura—25, 26; Shunsuke Nagai—27, 29; Kanako Otsuka—28

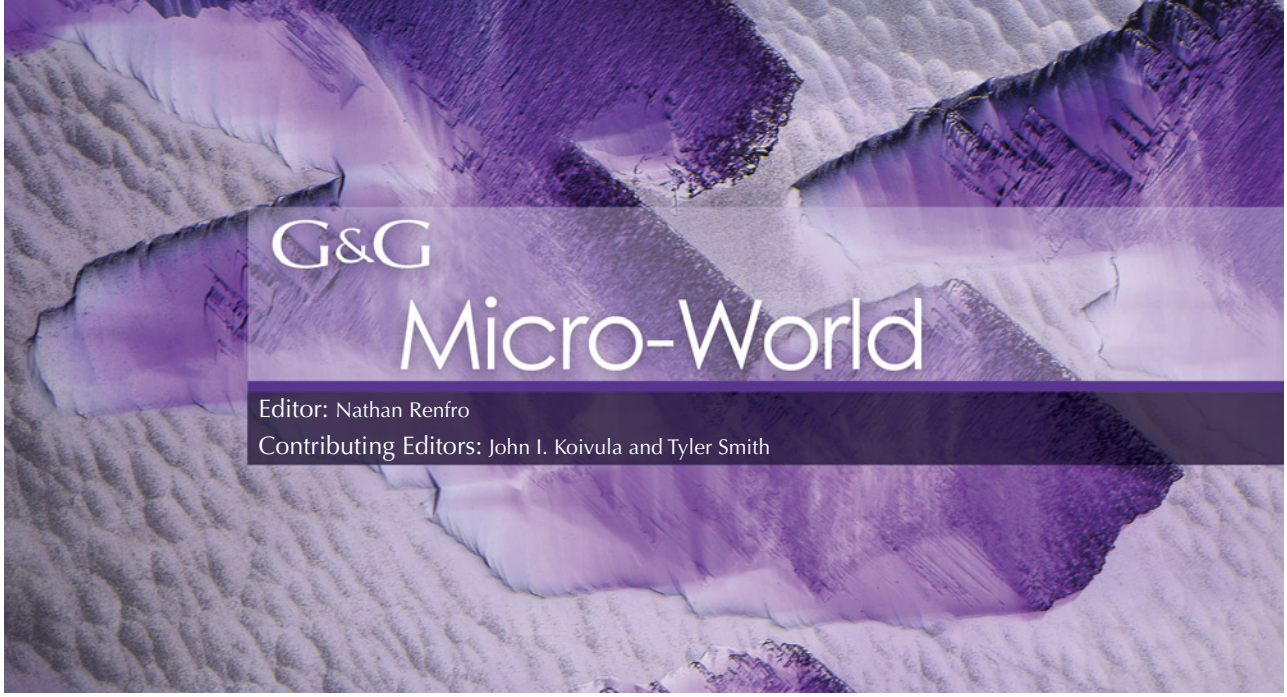

"Conch Shell" in Diamond

Surface-reaching fractures or breaks in diamonds are commonly known as feathers. The authors recently came across a feather with a surprising anatomy in a 0.41 ct natural diamond with G color and I_1 clarity. This structure resembled a conch shell (figure 1). The conch shell, also called a *shankha* in India, is used for religious purposes and as a musical instrument, and it is thought to bring good luck.

Tejas Jhaveri and Russel Carvalho
GIA, Mumbai

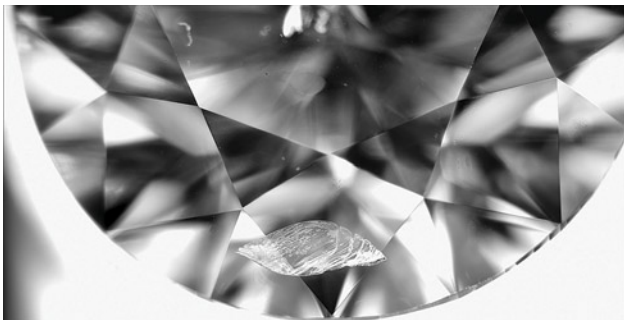

Figure 1. This transparent feather with noticeable depth, observed in a natural diamond, suggests a conch shell. The image was captured in monochrome. Photomicrograph by Tejas Jhaveri; field of view 2.50 mm.

Square-Shaped Cloud in Diamond

Polishers occasionally recognize a distinctive inclusion within a rough diamond and orient the faceting to highlight the unusual feature. One such example is the recently examined 0.34 ct round brilliant with I color shown in figure 2. Due to the prominent square-shaped cloud under the table (figure 2, left), the clarity grade of the stone was SI_2. Previously, gemologists have reported other natural diamonds with nominally similar-looking clouds oriented under the table facet (N. Renfro et al., "Inclusions in natural, synthetic, and treated diamond," Winter 2018 *G&G*, pp. 428–429; Spring 2021 *G&G* Micro-World, pp. 65–66).

The cloud appeared as a perfect square shape (the measured length along one side of the square was ~0.9 mm) when viewed through the table facet, but it appeared significantly more scattered when viewed through the pavilion (figure 2, right). Such features highlight the beneficial synergy between natural inclusions and skilled polishers.

Deepak Raj and Hardik Rathod
GIA, Surat

Sally Eaton-Magaña
GIA, Carlsbad

Heliodor and Aquamarine with Surface Etching

During an ongoing beryl characterization project, aquamarine and heliodor beryl samples from the GIA Museum col-

About the banner: This synthetic amethyst shows a flame-like color zoning along the rhombohedral crystal direction. These patterns are only seen in synthetic amethyst. Photomicrograph by Nathan Renfro; field of view 15.61 mm. Courtesy of the John Koivula inclusion collection.

Gems & Gemology, Vol. 60, No. 2, pp. 226–237.

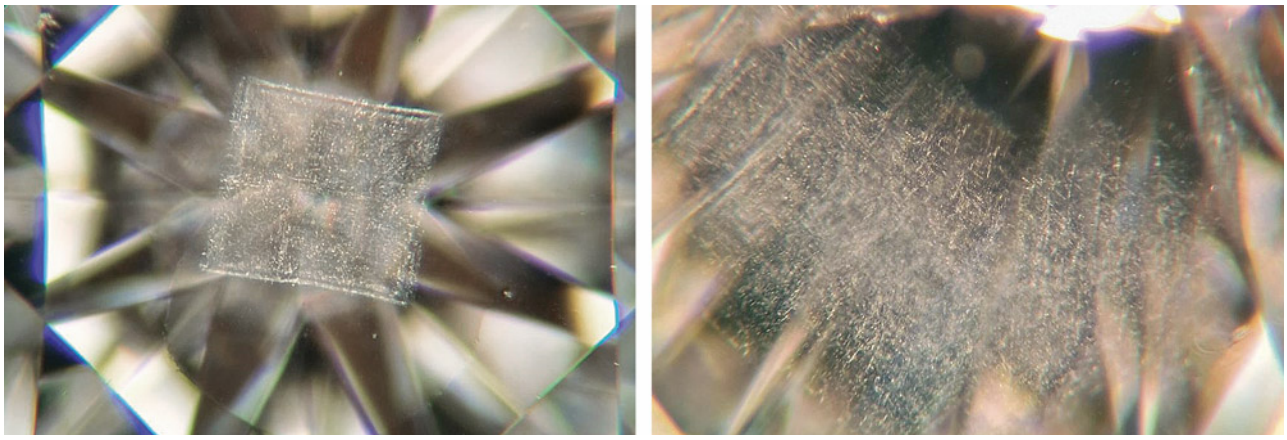

Figure 2. Left: Table-up view of a 0.34 ct round brilliant with SI_2 clarity possessing a square-shaped cloud; field of view ~2.9 mm. Right: When viewed through the pavilion, the cloud feature appears much less ordered; field of view ~1.6 mm. Photomicrographs by Deepak Raj.

lection (figure 3) revealed distinctive etch features on each of their crystal faces. These two samples were reported by the donor as being from China.

The etch pits seen on these samples are markedly different from those of Ukrainian heliodor (G. Franz et al., "Etch pits in heliodor and green beryl from the Volyn pegmatites, northwest Ukraine: A diagnostic feature," Fall 2023 *G&G*, pp. 324–339). While Ukrainian heliodor exhibits a more rectangular etching, these specimens have rounded six-sided shapes akin to a compressed hexagon

Figure 3. These aquamarine (left) and heliodor (right) crystals reported to be from China, measuring approximately 2 cm long and 0.4 cm wide, display distinctive etch pits. Photo by Adriana Robinson. Gift of Zeng Jiliang, GIA Museum nos. 20633 (left) and 20630 (right).

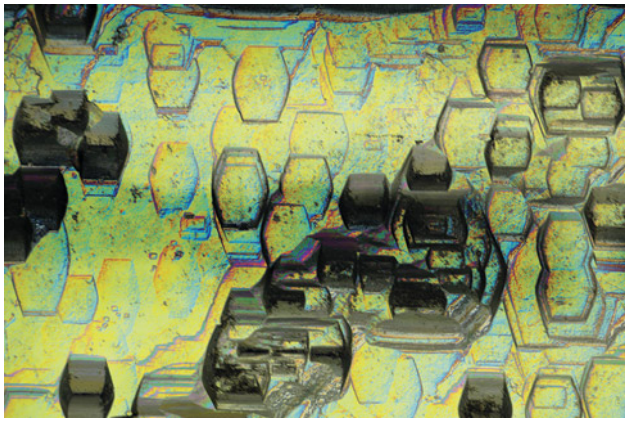

Figure 4. Heliodor viewed with differential interference contrast filters. Compressed hexagonal etch features exist on every prismatic face and run the length of the crystal. Photomicrograph by Rhiana Henry; field of view 2.88 mm.

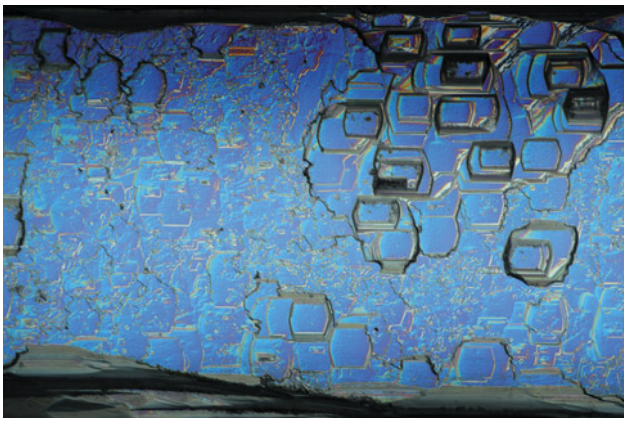

Figure 5. Aquamarine viewed with differential interference contrast filters. Hexagonal, pseudorectangular, and uneven etch features exist on every prismatic face and run the length of the crystal. Photomicrograph by Rhiana Henry; field of view 2.88 mm.

adorning their prismatic faces (figure 4). The six-sided deeper etch features are sometimes superimposed upon irregularly shaped etch features, or have ragged edges, and these are displayed more prominently on the aquamarine sample (figure 5) than on the heliodor. In both samples, the six-sided shapes are superimposed on each other in some cases, creating deep grooves within the crystal. Some etch shapes exhibit a line separating regions, which runs parallel to the *c*-axis of the crystal. The etch pits are detectable to the eye but require a microscope to see the compressed hexagons in detail.

Rhiana Elizabeth Henry and Adriana Robinson
GIA, Carlsbad

Hammered Effect in a Worked Pearl

The authors recently examined a white button-shaped pearl weighing 9.92 ct and measuring 11.76 × 11.20 × 10.62 mm (figure 6), which was identified as a natural pearl formed in a saltwater environment. One intriguing feature of the pearl was a distinctive pattern resembling the hammered surface commonly seen on brass and copper ornaments. The pearl's surface appeared to show a series of closely packed shallow indentations on the nacre surface, forming ridges in a mosaic pattern (P. Southgate and J. Lucas, *The Pearl Oyster*, 2008, p. 296).

Microscopic examination revealed that the hammered effect was subsurface and did not actually result in any ex-

Figure 6. This 9.92 ct white natural pearl displayed a subsurface hammered effect. Photo by Gaurav Bera.

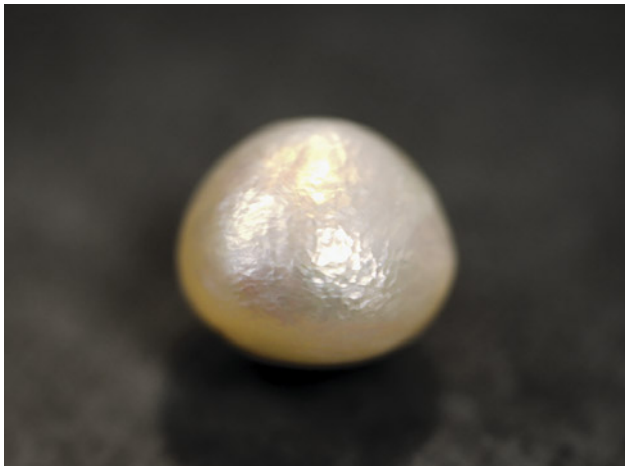

Figure 7. Worked lines observed on the pearl's surface along with a subsurface hammered effect. Photomicrograph by Nishka Vaz, field of view 1.8 mm.

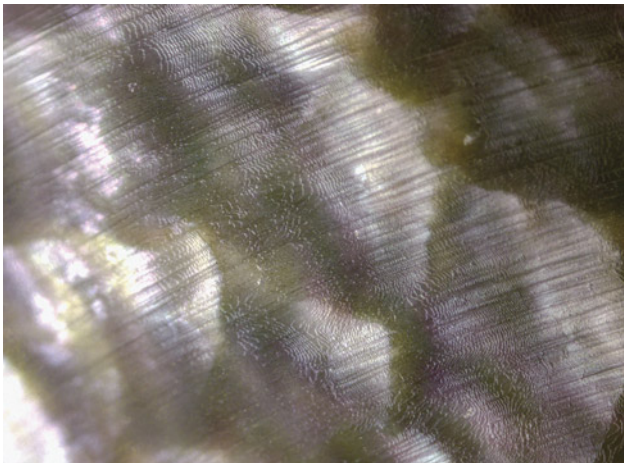

terior indentations. However, the pearl's surface was covered in shallow worked lines, crisscrossing in angular directions with an attempt to create a smoother surface without any irregularities (figure 7).

The surface nacre layer of the pearl was translucent, making it easier to observe the pattern in the underlying nacre layers along with the strong orient caused by these subsurface indentations. Due to the worked surface of the pearl, the interaction of light with these layers created an optical illusion of a bumpy texture when viewed without magnification.

While the authors have previously encountered pearls with a subsurface hammered appearance, this effect combined with extensive working was notable.

Nishka Vaz and Abeer Al-Alawi
GIA, Mumbai

"Ruffles" on a Freshwater Pearl

Surface is one of GIA's 7 Pearl Value Factors describing the appearance of pearls. Because pearls are a product of nature, it is rather common to find blemishes or irregularities on the surface. However, the "ruffle" pattern exhibited by one particular pearl was fascinating.

The 4.61 ct non-bead cultured freshwater pearl's surface appeared unusually bumpy to the eye (figure 8). Microscopic examination under fiber-optic light revealed an interesting finding: a rainbow-colored wavy pattern under a translucent surface with no indication of treatment. Surprisingly, these ruffles were not caused by actual blemishes or irregularities on the pearl's outermost surface, but were formed by interactions between light and the unique nacre platelet arrangement under the pearl's surface (figure 9).

When light is projected onto a pearl's surface, iridescence can be observed due to diffraction and interference of white light caused by the layered arrangement of the nacre platelets (E. Fritsch and G.R. Rossman, "An update on color in gems. Part 3: Colors caused by band gaps and physical phenomena," Summer 1988 *G&G*, pp. 81–102). This underlying botryoidal feature on the surface may be explained by the special arrangement of nacre platelets that was determined by nature.

Figure 8. A 4.61 ct non-bead cultured freshwater pearl with a bumpy surface. Photo by Wing Kiu Fan.

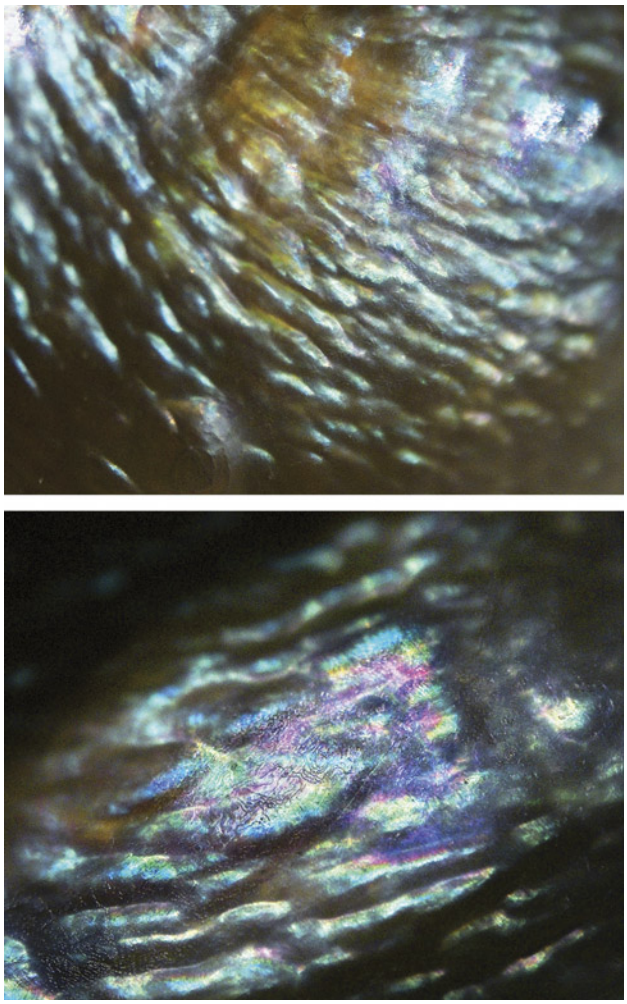

Figure 9. An iridescent wavy pattern and an overlapping nacre platelet structure (center part of the bottom image) were observed on the freshwater nacreous pearl. Photomicrographs by Wing Kiu Fan; field of view 4.00 mm (top) and 3.00 mm (bottom).

While similar features have previously been reported in akoya pearl (Fall 2021 *G&G* Micro-World, pp. 271–272), this is the author's first encounter with this intriguing appearance. The presence of these ruffles makes this freshwater pearl worth documenting.

Wing Kiu Fan
GIA, Hong Kong

Fascinating Snakeskin Pattern on a Pen Shell

The pen shell, a member of the Pinnidae family, is distinguished by its thin, fragile walls and fan-shaped outline. While typically ranging from 30 to 50 cm in length, the pen shell can reach sizes up to 120 cm, making it one of the largest endemic bivalve mollusks of the Mediterranean Sea. It is usually found in estuaries and coastal waters (T. Capello et al., "Pen shell *Pinna nobilis* L. (Mollusca: Bivalvia) from different peculiar environments: Adaptive mechanisms of osmoregulation and neurotransmission," *European Zoological Journal*, Vol. 86, No. 1, 2019, pp. 333–342).

Pen shells are known for their intricate pattern of concentric growth lines, which form a visually captivating display, and their coloration ranging from brown to vibrant hues of yellow. GIA's Mumbai laboratory occasionally receives shells with intriguing features, one of them a pen shell with broken edges from Bahrain, measuring approximately 11.9 × 7.4 cm (figure 10). When viewed under magnification with fiber-optic illumination, a small area revealed an organized translucent yellow to brown cellular pattern, with vivid yellow outlines around each cell. These resembled a scale pattern, akin to the skin of a snake. Interestingly, a thick, milky white material filled the boundaries between the cells, giving the shell a shiny appearance. It was evident that the shell had been coated with varnish to enhance its aesthetic appeal (figure 11).

Figure 10. Pen shell from Bahrain, showing broken ends due to its fragile nature. Photo by Gaurav Bera.

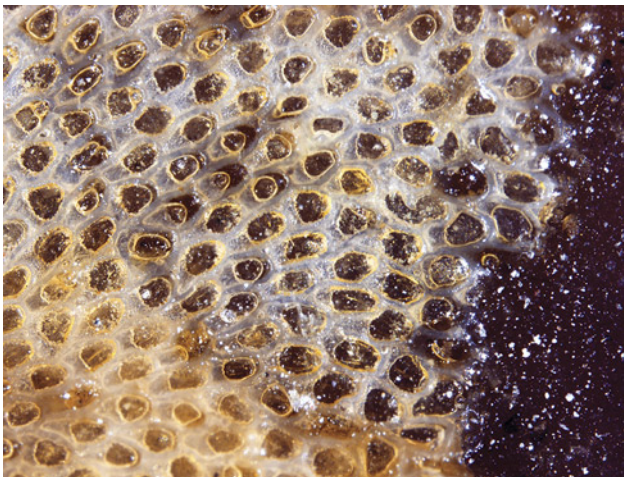

Figure 11. The pen shell's snakeskin pattern coated with varnish, shown under magnification. Photomicrograph by Pfokreni Nipuni; field of view 2.1 mm.

While shells can exhibit many different appearances, this snakeskin pattern is particularly fascinating.

Pfokreni Nipuni and Abeer Al-Alawi
GIA, Mumbai

Fireworks in Ruby

In the world of gemology, double-star corundum stands out as one of the rarest and most prized varieties of corundum, exhibiting two intersecting stars that dance across the surface. The effect resembles miniature fireworks in a gemstone. The double star is caused by needle-like inclusions of minerals such as rutile or hematite-ilmenite arranged in two orientations near the curved dome of the cabochon. When light reflects and scatters through these inclusions, it creates two intersecting white six-rayed stars.

Another type of double-star effect has two differently colored six-rayed stars, also known as dual-color double stars. One is a white star positioned near an upper layer of the cabochon's dome, while the other is a bodycolored star that seems to emanate from the back of the stone. This phenomenon occurs when light travels twice through the polished curved base of the cabochon, which contains needle-like inclusions and a matrix of corundum with trace elements determining its bodycolor. It produces a second star with color resulting from the host stone's color (K. Schmetzer et al., "Dual-color double stars in ruby, sapphire, and quartz: Cause and historical account," Summer 2015 *G&G*, pp. 112–143).

Figure 12. This unheated 11.43 ct purplish red round ruby cabochon displayed a white twelve-rayed double-star phenomenon. Photo by Nuttapol Kitdee.

Figure 13. A six-rayed streamer-like pattern in the double-star ruby. Photomicrograph by Aprisara Semapongpan; field of view 7.20 mm.

Recently, the author examined an unheated 11.43 ct purplish red round ruby cabochon that displayed a twelve-rayed double-star phenomenon (figure 12). The white color of this double star indicates that both stars formed near the curved dome surface. Alongside inclusions commonly found in rubies were interesting particle inclusions arranged in a streamer-like pattern revealed by fiber-optic illumination. These particles formed their very own six-rayed star pattern (figure 13), adding unexpected fireworks to the stone. This discovery serves as a reminder that nature is full of surprises just waiting to be uncovered.

Aprisara Semapongpan
GIA, Bangkok

Unique Fingerprint in Montana Sapphire

The group of fingerprint and crystal inclusions shown in figure 14 forms a unique and uncanny shape within a 6 × 4 mm heated Montana sapphire. The pattern displays a

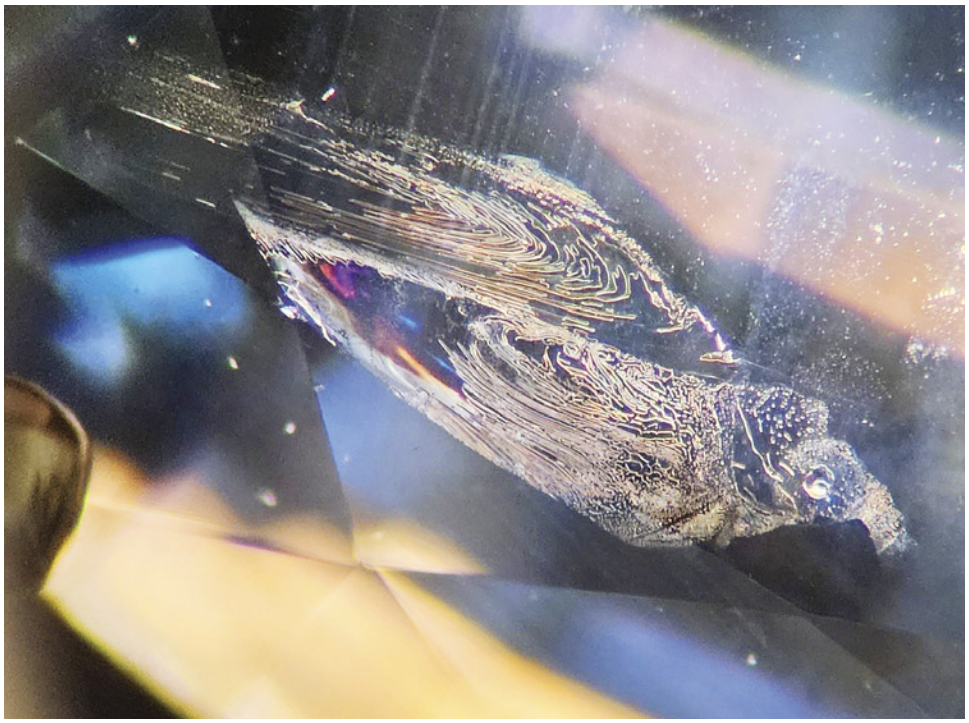

Figure 14. Inclusions combine to create a bird pattern inside a Montana sapphire. Photomicrograph by Isabelle Corvin; field of view 2.4 mm.

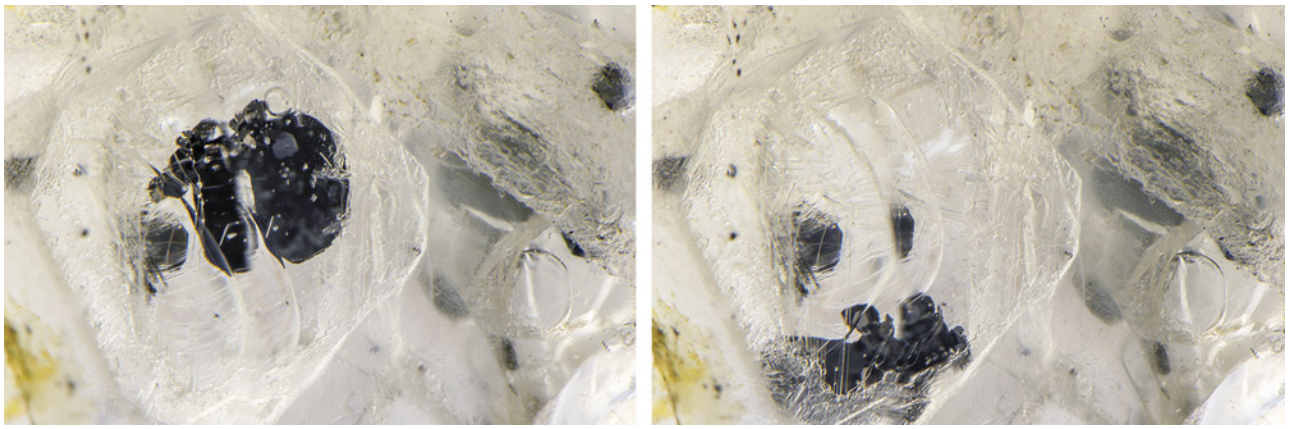

Figure 15. These two photomicrographs of a three-phase fluid inclusion in a Sri Lankan sapphire show that the opaque black graphite plates move freely within the void. Photomicrographs by Nathan Renfro; field of view 4.79 mm.

bird, complete with iridescence along the "wings" and a prominent included crystal as the "eye." The angle of the bird within the sapphire adds depth and movement to the pattern.

Isabelle Corvin
Olympia, Washington

Graphite in Sapphire

The gem deposits of Sri Lanka are known to contain graphite, which sometimes appears as inclusions in the sapphires Sri Lanka is famous for. We recently examined one such sapphire: a transparent to translucent, light brownish gray, waterworn single crystal section, with one polished window perpendicular to the optic-axis direction.

Weighing 4.94 ct and measuring 8.75 × 7.35 × 5.80 mm, the sapphire was purchased from Sajith Masilamani in Ratnapura, Sri Lanka. It was said to be from the Ratnapura District in Sabaragamuwa Province.

Under the microscope, the stone's inclusion scene proved quite interesting. On display was a large primary three-phase fluid inclusion containing water, liquid, and gaseous carbon dioxide, together with graphite as the solid phase. Of particular interest, as shown in figure 15, were loose graphite plates that moved freely in the confines of the fluid inclusion chamber.

In addition to the mobile graphite plates, the inclusion was quite active and appeared to "boil" while it homogenized under microscopic examination. A somewhat similar inclusion in a Sri Lankan sapphire is shown in *Photoatlas of Inclusions in Gemstones, Volume 3* (E.J. Gübelin and J.I. Koivula, 2005, Opinio Publishers, Basel, Switzerland, p. 280). Therefore, this particular inclusion with mobile graphite was unusual but not unique.

John I. Koivula and Nathan Renfro
GIA, Carlsbad

Transparent Spinel Inclusion in Pink Sapphire

The S Gemmological Institute Gem Lab recently examined 155 sapphires of assorted color, sourced from the Mogok Stone Tract in Myanmar. Among these, a pink sapphire weighing 1.166 ct exhibited a significant crystal inclusion extending to the table facet (figure 16). This transparent inclusion was identified by Raman spectroscopy as spinel. Internally, the inclusion appeared clear and smooth, while the surface-reaching face exhibited signs of scratching due to the low hardness of spinel compared to the sapphire host.

In the Mogok area, spinel inclusions in pink sapphire are not unusual, as both pink sapphire and spinel have been discovered in the marble-hosted formations. Although spinel inclusions have been previously reported in Burmese ruby (E.B. Hughes and W. Vertriest, "A canary in the ruby mine: Low-temperature heat treatment experiments on Burmese ruby," Winter 2022 *G&G*, pp. 400–423), and green gahnospinel inclusions have been documented in blue sapphire from Sri Lanka (Winter 2023 *G&G* Micro-World, p. 503), this spinel inclusion in a pink sapphire from Mogok was unusually large and distinct.

Sai Gon Khay and Kyaw Thu
S Gemmological Institute
Yangon, Myanmar

Star of David Pattern in Vietnamese Sapphire

Recently, the author examined a 3.18 ct bicolor yellow and blue-green basalt-related sapphire that was mined in southern Vietnam. Under brightfield illumination, the stone revealed partially healed fissures exhibiting an intriguing Star of David pattern matching the pinacoid face (figure 17).

This type of fissure often displays a geometric crystal structure, resembling either a hexagon or a triangle,

Figure 16. A large surface-reaching spinel inclusion in a Burmese pink sapphire from Mogok, shown in dark-field and oblique illumination. Photomicrograph by Kyaw Thu; field of view 1.3 mm.

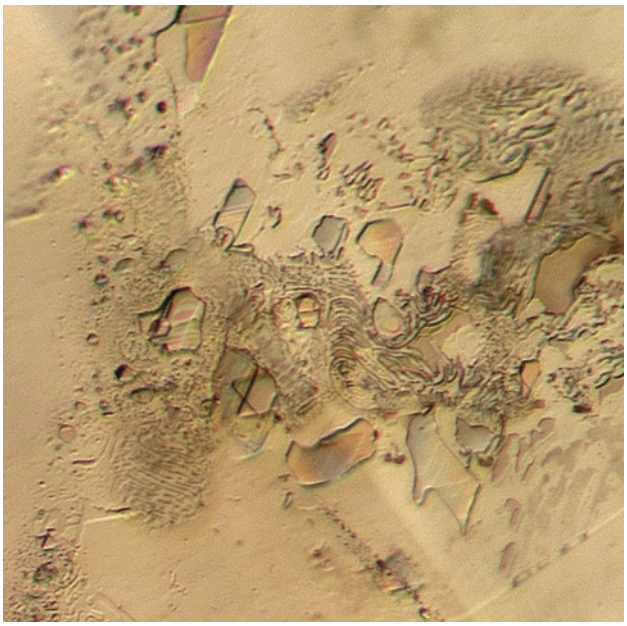

Figure 17. The fascinating Star of David pattern within partially healed fissures adds to the allure of this sapphire's micro-world. Under brightfield illumination, the grayish areas that remained unhealed were iridescent in some areas. Photomicrograph by Tinh Xuan Nguyen; field of view 1.8 mm.

when perpendicular to the *c*-axis. However, the pattern of interlocking triangles is rarely observed. These unique triangles probably resulted from defects in the crystal structure, which arose during oscillating growth between the rhombohedral and pinacoidal planes. The partial healing process made these features noticeable under the microscope.

Tinh Xuan Nguyen
PNJ Laboratory Company Limited
Ho Chi Minh City, Vietnam

Sapphire Displaying Tire Tracks in Snow

The author recently examined a 13.15 ct blue oval mixed-cut sapphire that contained a striking inclusion scene (figure 18). Careful microscopic observation revealed that the inclusions consisted of particle clouds close to the surface of the stone. The clouds featured a distinctive angular shape; they were aligned and stacked in a repeating pattern that suggested a Madagascar origin. The stone was faceted at an angle that accentuated these uniquely patterned particle clouds, which resembled tire tracks in snow.

Masumi Saito
GIA, Tokyo

Quartz with Sphalerite

The Taolin mine in Linxiang County, Hunan Province, China, is known to produce fine specimens of gemmy, brownish orange sphalerite, together with quartz. We re-

Figure 18. Clouds of particles in sapphire resembling tire marks in snow. Photomicrograph by Shunsuke Nagai, field of view 2.30 mm.

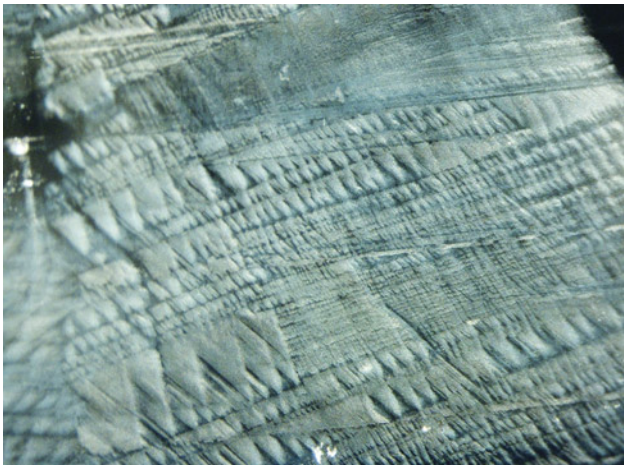

Figure 19. This 182.19 ct quartz cabochon hosts a brownish orange phantom with a netlike structural form. Photo by Adriana Robinson.

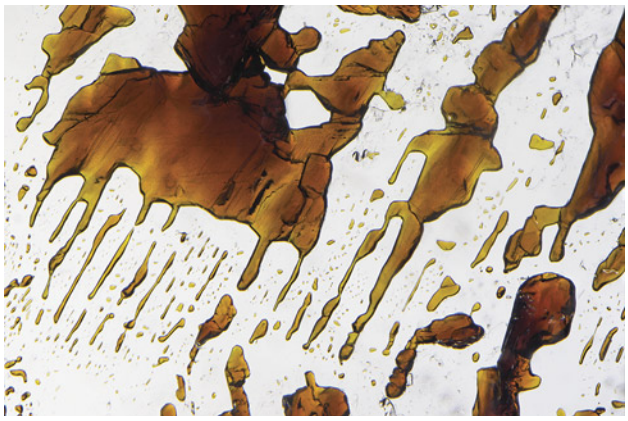

Figure 20. A network of rounded and stretched crystals, islands, and puddles of sphalerite that look as if they were once in a liquid state. Photomicrograph by Nathan Renfro; field of view 9.92 mm.

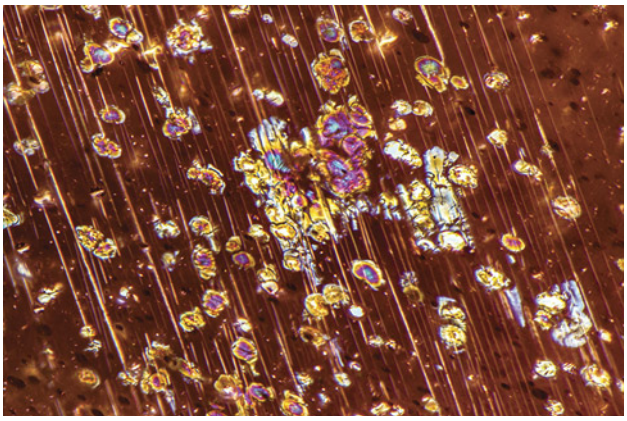

Figure 21. Reflected light reveals the metallic luster of these colorful inclusions in an Oregon sunstone. Photomicrograph by Rosie Young; field of view 1.26 mm. Courtesy of GIA Museum, collection no. 4735.

cently examined a transparent and colorless rectangular freeform double cabochon (figure 19) fashioned from a Taolin quartz crystal. The cabochon weighed 182.19 ct and measured 44.70 × 29.81 × 15.76 mm.

Interestingly, this specimen played host to a phantom of transparent brownish orange inclusions that formed as a network of rounded and stretched crystals, islands, and puddles. The appearance of these features suggested they were once in a liquid state (figure 20) and were originally deposited as a viscous liquid in the quartz.

Several parts of the phantom were near the surface of the host quartz, and some had been polished through and exposed at the surface. This made the inclusions ideal for Raman analysis, which proved that the phantom was made up of individual islands and tendrils of the mineral sphalerite.

John I. Koivula, Nathan Renfro, and Maxwell Hain
GIA, Carlsbad

Pyritic Inclusions in Oregon Sunstone

A sample of Oregon sunstone from the GIA Museum's collection was found to contain some unusual inclusions that appeared yellow in transmitted light and iridescent in reflected light. Vivid shades of yellow, blue, and purple were visible in a concentric pattern when illuminated with a fiber-optic light (figure 21). Some of the inclusions contained a metallic copper center and appeared darker than the surrounding inclusion under brightfield illumination (figure 22). The series of parallel lines pictured are also thought to be copper inclusions.

These inclusions looked pyritic in nature and possibly altered as a result of heating. This may well be natural heating from processes within the earth, as Oregon sunstone is not known to be treated.

Rosie Young
Gemmological Certification Services, London

Figure 22. Left: The yellow color of the inclusions can be seen with brightfield illumination, with those having a copper core appearing dark in the center. Right: The same view with reflected light shows the metallic luster of both the pyritic inclusions and the copper. Photomicrographs by Rosie Young; field of view 1.26 mm.

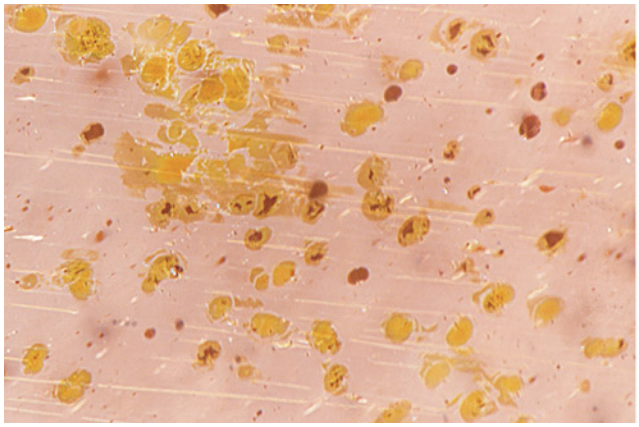

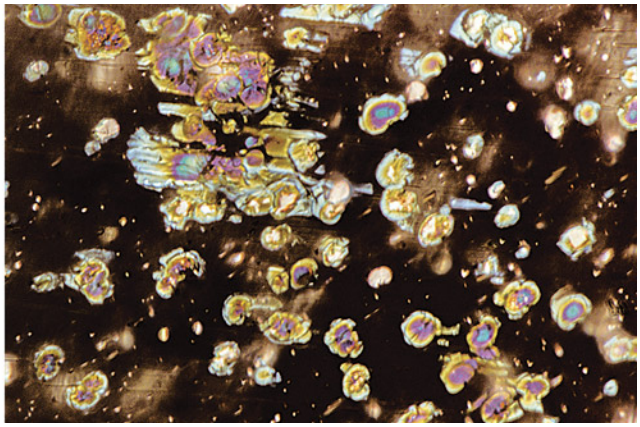

Figure 23. Weighing 178.42 ct and measuring 44.00 mm in length, this smoky brown quartz crystal from Ramona, California, hosts a 3.3 mm garnet. Photo by Annie Haynes.

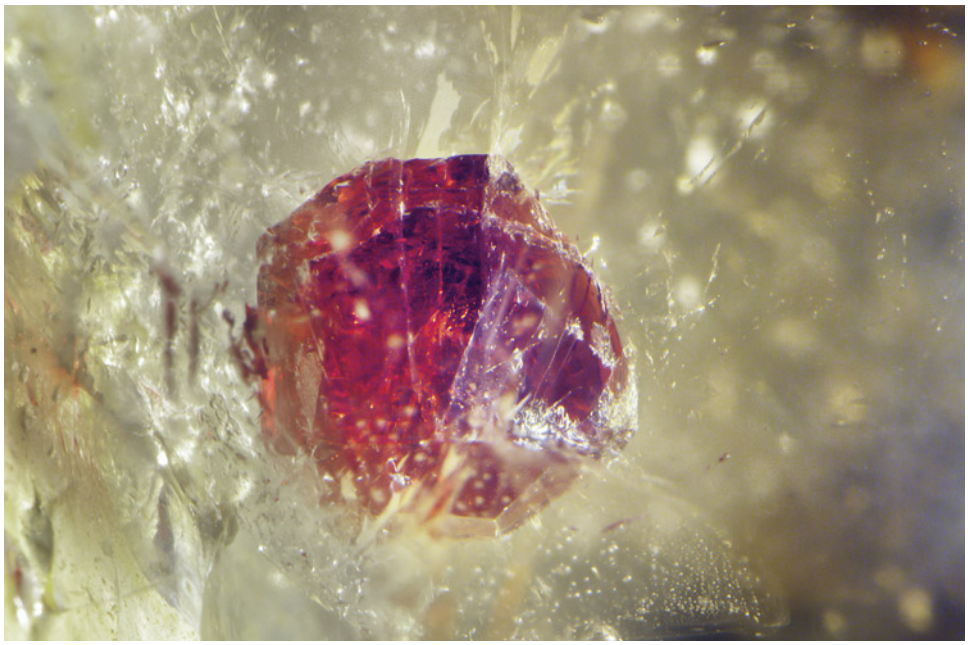

Figure 24. The 3.3 mm dark reddish orange isometric crystal in this smoky quartz was identified through Raman analysis as spessartine. Photomicrograph by Nathan Renfro; field of view 7.20 mm.

Quarterly Crystal: Spessartine in California Quartz

With silicon and oxygen as its building blocks, quartz is the single most abundant mineral in the earth's crust. When it forms as transparent crystals, it serves as an excellent and durable host for inclusions.

The 178.42 ct terminated smoky brown quartz crystal on a pegmatitic albite and muscovite matrix, measuring 44.00 mm long and shown in figure 23, came from the collection of noted gemologist, collector, and author Dr. John Sinkankas of San Diego, California. Dr. Sinkankas found the specimen at the Little Three mine in Ramona, near San Diego, while doing field research for his three-volume *Gemstones of North America*.

As shown microscopically in figure 24, the translucent, relatively large 3.3 mm dark reddish orange isometric inclusion appeared to be a garnet, since the pegmatitic Little Three mine is known to produce both quartz and spessartine. Raman analysis yielded an identification as spessartine, confirming our microscopic identification.

John I. Koivula, Nathan Renfro, and Maxwell Hain

Laboratory Growth of Gem Materials and the Attempt to Replicate Nature

Our last three installments of Colored Stones Unearthed have focused on geological processes that form gemstones naturally in the earth. We detailed gemstones formed in magmatic, metamorphic, and sedimentary geological environments. The separation of geologic processes into those involving molten rocks (magmatic), solid-state recrystallization at high pressure and temperature (metamorphic), and deposition and lithification of sediments (sedimentary) might seem intuitive to any modern student of geology. For most of human history, however, the forces involved in shaping the earth and forming these precious gemstones were almost entirely unknown.

Although laboratory-grown (synthetic) gemstones are commonplace today, the technological breakthroughs that enabled them were not feasible until scientists unraveled the geologic mysteries behind gem formation. This knowledge allowed researchers to replicate these conditions in a laboratory setting (figure 1). Early attempts to artificially reproduce the beauty of natural gemstones were mostly relegated to glass imitations or primitive treatments applied to natural stones. Laboratory processes for growing gemstones are very sophisticated today, but it was not until the 1800s that humankind was able to imitate, in some way, the geological processes that formed precious stones naturally. And yet, for the most part, the technology has not advanced far enough to perfectly replicate the gemological properties of natural stones using artificial growth methods. As a result, most synthetic colored stones are easily detectable by a gemological laboratory.

This installment of Colored Stones Unearthed gives an overview of processes for growing gem materials in a laboratory and how differences in the synthetic and natural growth environments enable laboratory-grown stones to be separated from natural materials. Note that this is not intended as an exhaustive overview of criteria to separate natural and laboratory-grown stones, nor is it an exhaustive overview of current methods for laboratory growth. Rather, it is meant to serve as a comparison between natural and artificial processes for the formation of gemstones. For historical reviews of crystal growth methods, see Bohm (1985) and Feigelson (2015, 2022).

Geological Processes Forming Gemstones

The geological processes forming natural gemstones can be roughly divided into magmatic (Palke and Shigley, 2022), metamorphic (Palke and Shigley, 2023), and sedimentary (Shigley et al., 2023). Magmatic gemstones are those that formed through igneous processes involving molten rocks, or magma, somewhere within the earth, likely in the crust or upper mantle. Examples include some sapphire and peridot associated with alkali basalts, some feldspar, some garnet, and topaz when including crystallization from vapor phases in cooling rhyolitic lava flows. Conditions may vary, especially the depth of formation, but the temperatures involved are generally at least 750°C, which is roughly the minimum temperature at which rocks composed of silicate minerals will begin to melt and form magma that can separate to form a free magma phase.

Editors' note: Questions or topics of interest should be directed to Aaron Palke (apalke@gia.edu) or James Shigley (jshigley@gia.edu).

Gems & Gemology, Vol. 60, No. 2, pp. 238–251.

Figure 1. Synthetic alexandrite, amethyst, beryl, corundum, diamond, and fire opal. The three smallest stones are synthetic diamonds ranging from 0.06 to 0.14 ct. Photo by Robert Weldon.

Metamorphic rocks, in the strictest sense, form by heating and compression of rocks in the solid state, recrystallizing the rock and forming a new texture and possibly new mineral phases. In reality, metamorphic processes rarely happen entirely in the solid state but involve some type of fluid flow, facilitating the transport of chemical components. Metamorphic gemstones include many rubies and sapphires, jade, tsavorite, tanzanite, and various garnets. Pressure and temperature conditions for metamorphic ruby and sapphire typically range from 2 kbar and 550°C to about 11 kbar and 825°C (figure 2).

Sedimentary gemstones are classified as those that formed not necessarily directly through sedimentation and compaction but rather through low-grade diagenetic processes, often involving fluid circulation, in sedimentary rock formations. Typical examples include opal, some turquoise, and malachite. While synthetic versions of these sedimentary gems have been produced, most of the synthetic gems available on the market are single-crystal laboratory-grown versions of magmatic and metamorphic gemstones, which will be the focus of this installment.

Processes for Growing Gem Materials In the Laboratory

Some of the first crystal growth experiments involved the production of salt through evaporation of seawater. Despite some intuitive understanding of crystallization processes that enabled this advancement, the technical framework for crystal growth did not come about until

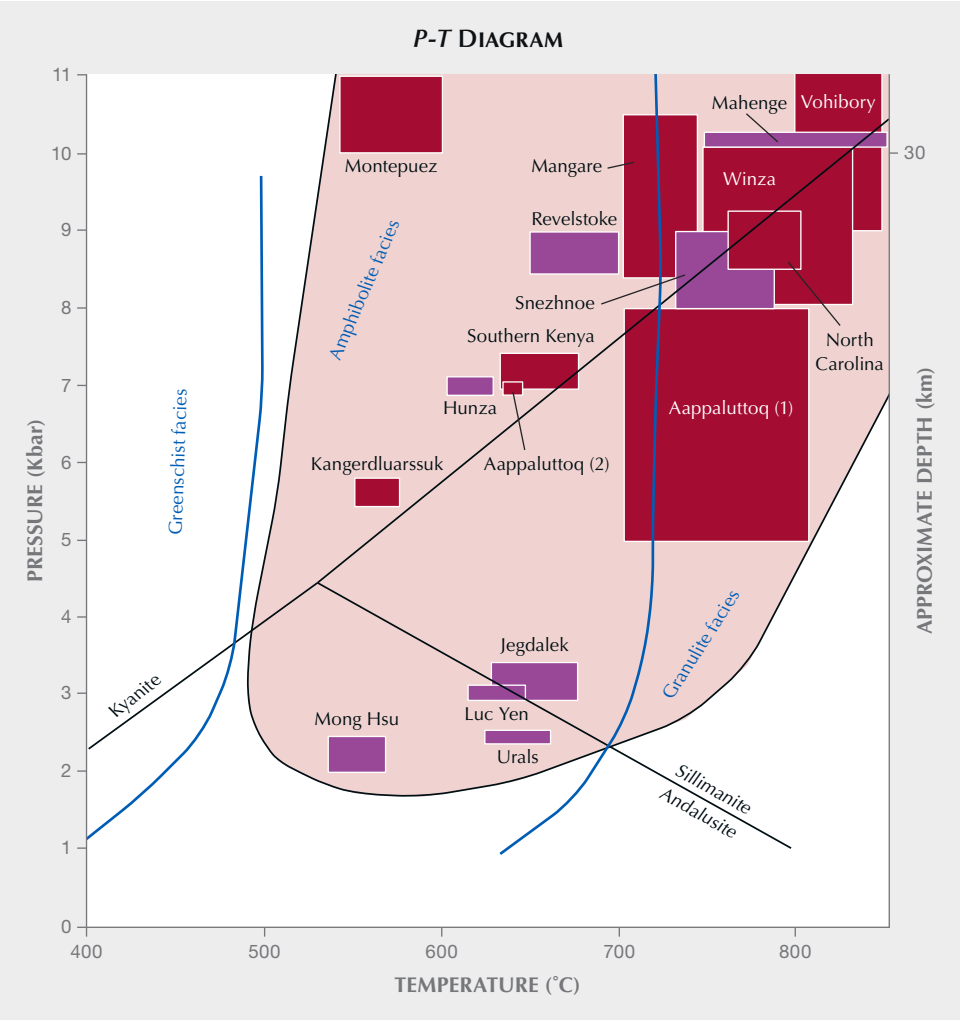

*Figure 2. This pressure-temperature (*P-T*) diagram shows geological formation conditions for some global ruby deposits. Purple rectangles show ranges of marble-hosted ruby deposits, while red rectangles show metamorphic deposits (*sensu stricto*). Reproduced from figure 21 of Giuliani et al. (2020).*

more recently. An important advancement in the scientific understanding of crystal growth came with the French mineralogist Haüy, who in 1801 observed the flat cleavage planes of a broken calcite specimen. Haüy developed the idea of the "molecule intégrante" (integrant molecule) as the tiny fundamental building block of a crystal, a concept modern mineralogists recognize as the "unit cell" of a crystal (Haüy, 1801; Authier, 2013). Other natural scientists such as Steno (Winter, 1916, p. 171), Lowitz (Bohm, 1985), and Gibbs (1878) recognized, for instance, that crystal growth occurs through the attachment of material from outside the crystal, in many cases from a supersaturated solution containing the necessary chemical components.

The earliest foray into laboratory-grown gemstones was in 1837, when Gaudin grew the first small ruby crystals by mixing potassium alum, potassium chromate, lead oxide, and silica, then melting the mixture with rubies forming by vapor recrystallization (Gaudin, 1837). In the late 1800s, Verneuil succeeded in growing much larger crystals (known as boules) of flame-fusion rubies, as detailed in the next section. From there, and with further advances in crystal growth science and technology and the widespread use of synthetic crystals for many applications, the field of laboratory-grown crystals that could be used as gemstones rapidly expanded. The following sections will describe the three main synthesis techniques: melt growth, flux growth, and hydrothermal growth.

Melt Growth. Perhaps the first true laboratory-grown gemstones observed were the "Geneva" rubies first examined by Jannettaz in 1886. In an exceptional instance of gemological insight, he concluded these stones to be synthetic based on the presence of spherical gas bubbles (Jannettaz, 1886). He was able to make this logical jump, despite never having seen synthetic gemstones, by comparison with manufactured glasses and inclusions in natural rubies. The "Geneva" rubies were grown by a melt method wherein pure aluminum oxide with added chromium oxide would have been brought beyond the melting point of corundum to melt the starting material with an oxygen-hydrogen torch, allowing it to recrystallize upon cooling.

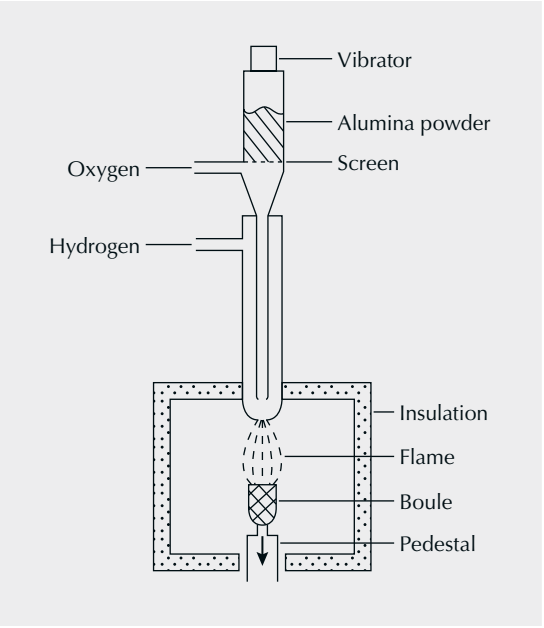

Figure 3. Drawing of a Verneuil (flame-fusion) apparatus (left) and a photo of flame-fusion crystal growth in the furnace (right). Photo courtesy of Hrand Djevahirdjian.

The true breakthrough, however, came in the latter part of the nineteenth century, when Verneuil perfected the flame-fusion method to produce synthetic ruby on a commercial scale (Verneuil, 1904; Nassau, 1972). His method utilized an oxygen-hydrogen torch to melt high-purity alumina powder mixed with chromium oxide that was being fed into the flame by a vibrating feeder. As the powdered starting material passes through, the flames turn the powder into small melt droplets. These melt droplets fall onto a pedestal where the temperature is lower, and the melt slowly crystallizes into a blob. As more of the alumina/chromium material is fed through the flame, the pedestal is slowly lowered, creating room for more ruby to grow, allowing the boule to elongate, and bringing it to lower and lower temperatures in a controlled manner (figure 3). This method creates a single crystal of corundum in the form of a cylindrical boule up to several inches in length (figure 4). The Verneuil crystal growth method (also

Figure 4. Flame-fusion synthetic sapphire boules and an oval-cut gem (2.45 ct). Photo by Robert Weldon. Cut stone gift of Aaland Gem Co. Inc., GIA Museum no. 24224.

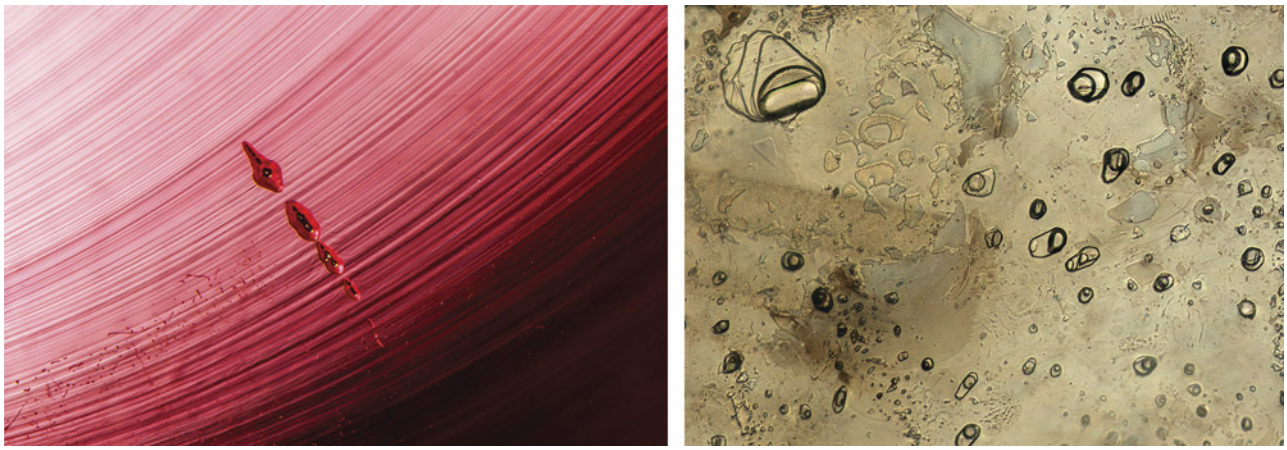

Figure 5. Left: Typical inclusions in flame-fusion rubies include curved striae and gas bubbles. Photomicrograph by Nathan Renfro; field of view 3.59 mm. Right: Melt-related natural gemstones may have melt inclusions with a composition different from that of the natural host, such as these silicate melt inclusions in a Montana sapphire. Photomicrograph by Aaron Palke; field of view 0.71 mm.

known as flame-fusion growth) is the most common method for laboratory-grown ruby and sapphire to this day, accounting for the bulk of modern production. (Note that the "Geneva" rubies mentioned above are now believed to have been produced by the Verneuil process.)

While large, well-crystallized gem corundum can be synthesized with the flame-fusion method, the growth conditions are quite different from those required to produce melt-related gems naturally (i.e., magmatic gemstones). In nature, magmatic corundum generally grows around 700°–900°C, much lower than the melting point of pure corundum of 2044°C required for flame-fusion growth. The reason for this is best summarized by a quote from GIA's John Koivula: "Nature plays in a dirty kitchen." In other words, the high melting point only applies in a laboratory setting with pure Al_2O_3. Where formation occurs in the earth, the chemical environment is full of impurities that lower the melting point of corundum. This melting point depression is similar to the familiar practice of adding salt to icy sidewalks in winter months to bring down the melting point of the ice, allowing it to melt at temperatures below 0°C. The other significant difference is the pressure of formation. Flame-fusion ruby and sapphire grow at ambient pressure, whereas natural magmatic ruby and sapphire grow at higher pressures deep within the earth.

Because of these significant differences in growth conditions, the properties of flame-fusion synthetics can generally be distinguished from those of their natural counterparts. The fact that flame-fusion synthesis happens at low pressure allows gas bubbles to be captured, which is not seen in magmatic gems formed at high pressure in the absence of a free gas phase (figure 5). The flame-fusion method also produces curved striae or curved color banding, a feature not found in natural gems where growth zoning is more angular and reflects slow and deliberate crystal growth. Flame-fusion ruby and sapphire also have so-called Plato lines, observed in immersion in cross-polarized light when looking down the optic axis. Inclusions found in natural magmatic (melt-related) gemstones are entirely different and may include natural inclusions like silk or angular particulate clouds, especially in sapphires, composed of a quenched glassy melt phase and a contraction bubble (figure 5). Finally, because chemical impurities will prevent the growth of high-quality flame-fusion crystals, producers only use very pure starting materials, resulting in crystals with a very pure trace element chemistry. On the other hand, natural rubies and sapphires grow in a "dirtier" chemical environment where the corundum can take in multiple different trace elements. Flame-fusion rubies then, typically have no detectable magnesium, iron, or gallium, all components that are readily detectable in natural ruby and sapphire using only X-ray fluorescence (XRF) spectrometry. Because the composition of the melt must exactly match that of the grown crystal, the compositions of melt-grown crystals tend to be relatively simple, and gem materials with a complex chemical formula are not generally grown with melt methods.

The melting process has been further refined to include the Czochralski method (Czochralski, 1918; Nassau, 1980) and the skull method (Nassau, 1977, 1980; Harrison and Honig, 1981). In the Czochralski method, high-purity starting material is melted in a large crucible typically made of iridium. A long rotating seed crystal is then placed in contact with the melt and slowly extracted, with melt continuously crystallizing on this interface, to form a large cylindrical crystal known as a boule. The skull method passes a flame back and forth over a charge loaded into a roughly cylindrical shape and slowly melts it into a single crystal. Czochralski melt-grown oxide crystals can be quite large, potentially up to 200 mm (approximately 8 inches) in diameter and up to 600 mm (about 2 feet) in length. There are several other direct melt crystal growth methods, but the ones described here are the most significant to the

Figure 6. Flux-grown synthetic ruby produced by the Douros method. The rough rhombohedral crystal weighs 44.74 ct, and the cut stones range from 2.14 to 4.93 ct. Photo by Robert Weldon; courtesy of John Douros.

synthetic gem industry. However, there are some materials that cannot be grown directly from the melt, as they do not melt congruently[1]. In these cases, such as with beryl, the flux and hydrothermal methods described below need to be used.

While the flame-fusion process was developed for ruby and then blue sapphire, it is now used to grow other materials such as spinel, rutile, and strontium titanate. Czochralski-grown gems include ruby and sapphire, chrysoberyl/alexandrite, spinel, garnets including YAG, and a multitude of other materials. This method is less common than flame fusion for most gem materials. The floating zone method is another melt-related technique used for gem synthesis but will not be covered here.

Flux Growth. Flux-grown gems (figure 6) represent another step toward more closely replicating natural geological growth conditions. As discussed above, early natural scientists began to understand gem formation as a gradual nucleation and growth of crystals by removing essential chemical components from a solution or melt. In nature, the solutions are generally either water-based hydrothermal fluids that dissolve an assortment of chemical components, including those needed to grow gems, or they are molten rocks (magmas) that contain the nutrients needed for gem growth. The flux method approaches these conditions through the use of solvents known as fluxes that are effective at dissolving the chemical components of certain gem materials at temperatures lower than those used for melt methods (i.e., the flux solution and the final crystal differ in composition) (Nassau, 1980; Elwell, 1989). Through careful control of temperature, these chemical components can nucleate to grow gem-quality crystals. The use of a flux allows the crystallization process to occur at a much lower temperature than the melting point of the gem material being grown. Additionally, flux-growth methods make it possible to grow certain gem materials that melt incongruently and therefore cannot be grown directly from a melt (e.g., beryl).

Flux-grown gem materials were first developed between 1920 and 1940 but entered the market significantly in the 1970s. However, the difficulty and expense of this method have made these materials increasingly uncommon today. Flux-grown rubies have been produced by several makers, including Chatham (Schmetzer, 1986), Douros

[1]Incongruent melting refers to situations where a mineral does not have a sharp melting point but instead disintegrates into other materials upon heating, thus making it impossible to melt and refreeze a crystal of such a mineral.

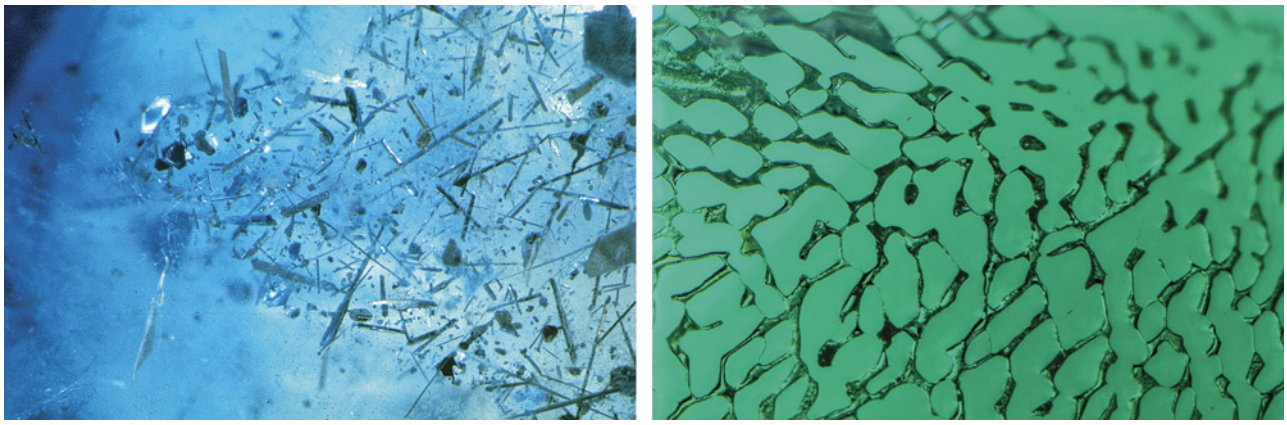

Figure 7. Needles and platelets of platinum crystals in flux-grown synthetic sapphire (left) and a partially healed fracture that trapped the flux-based growth medium in a flux-grown synthetic emerald (right). Photomicrographs by John I. Koivula (left) and Nathan Renfro (right; field of view 1.09 mm).

(Smith and Bosshart, 1993), Kashan (Schmetzer, 1986), Knischka (Knischka and Gübelin, 1980), Lechleitner (Schmetzer, 1986), and Ramaura (Kane, 1983). Chemical oxide components used in the fluxes are diverse: Li_2O, MoO_3, PbF_2, PbO_x, Na_3AlF_6, WO_3, $Na_2W_2O_7$, Ta_2O_5, and Bi_2O_3, among others (Muhlmeister et al., 1998). The flux method has also been used to grow gem-quality synthetic emerald, alexandrite, sapphire, spinel, and other materials. Flux-grown crystals are generally on the order of a few millimeters up to a few centimeters in size.

Because the growth environment is much more complex, flux-grown gemstones tend to be much more included than those produced by melt methods. Platelets of platinum or other platinum-group metals from the crucible can occur as inclusions (figure 7). These metals as well as other exotic elements can often be detected with trace element analysis using XRF or laser ablation–inductively coupled plasma–mass spectrometry (LA-ICP-MS). Their presence is considered proof of synthetic origin, as these elements are not found in any abundance in the geological environments where natural gemstones are formed.

Other typical inclusions in flux-grown gemstones are flux-filled fingerprints. These are generally similar to fluid-filled fingerprints seen in natural stones. But in flux-grown synthetic gems, these fingerprints represent fractures or fissures that are filled with the liquid flux material used as a growth medium. These features have a distinct appearance and are often distinguishable from fingerprints formed in natural stones (figure 7). Fingerprints in flux-grown gems generally have a higher relief and are translucent to opaque. However, there can be some overlap in the appearance of fingerprints between flux-grown and even natural, untreated gems (figure 8). A more significant area of overlap is between flux-filled fingerprints in synthetic stones and the residue in treated, flux-healed natural

Figure 8. Images showing the similarity between fingerprints in some natural sapphires (left) and flux-healed fingerprints in some flux-grown synthetic sapphires (right), which could lead to confusion between the two. Photomicrographs by John I. Koivula.

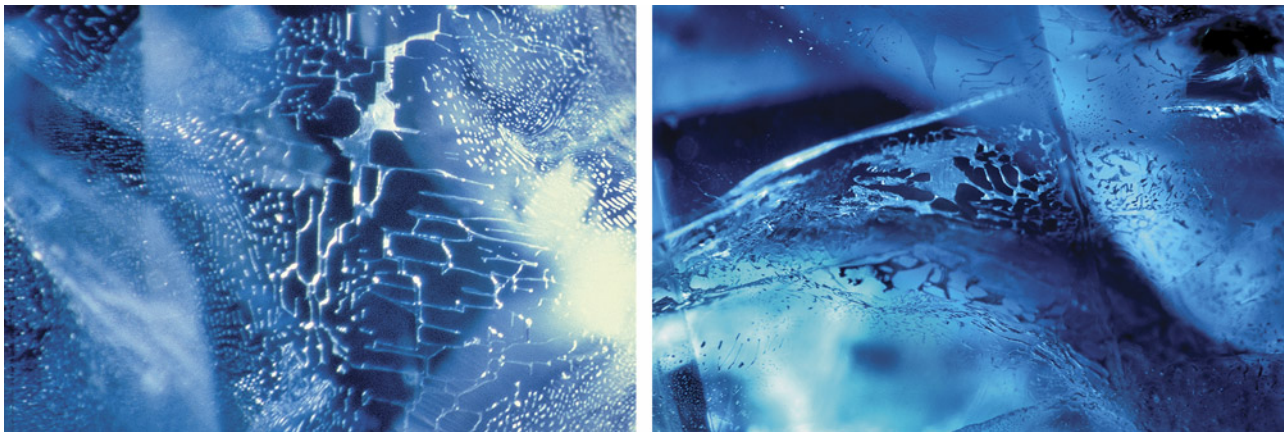

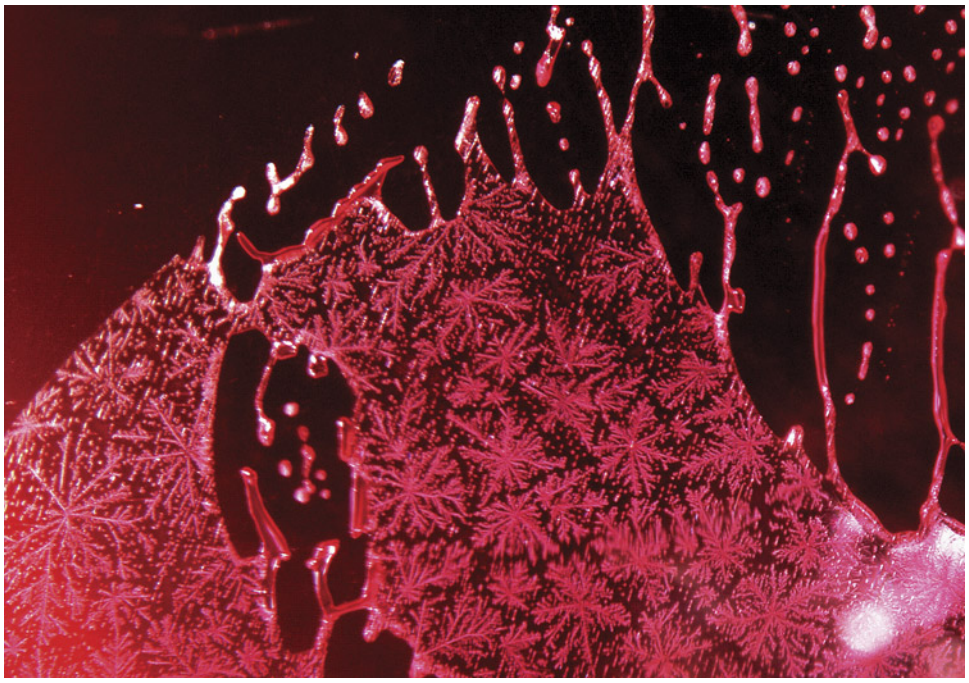

Figure 9. Partially healed fracture in a Mong Hsu ruby heated in the presence of a flux. The flux has infiltrated the fracture, partially recrystallizing the ruby and leaving behind a residue. Because the flux used to treat natural gemstones is similar to that used to produce flux-grown synthetic ruby, these types of inclusions can look similar. Photomicrograph by Nattida Ng-Pooresatien; field of view 1.3 mm.

stones. Many natural rubies in particular have significant fractures that detract from their clarity. Fluxes have been used during heat treatment of natural gemstones to penetrate fractures and partially fill and "heal" them, improving transparency (figure 9). After healing a fracture, the residue from a flux will remain trapped in the stone, leaving a fingerprint very similar to those seen in flux-grown gems (figure 10).

Figure 10. The process of flux healing of fractures during high-temperature heat treatment of ruby in the presence of a fluxing agent. Fractures naturally occurring in a ruby become filled with a molten flux during heating and partially recrystallize corundum. After treatment, some of the molten flux is trapped in these partially healed fractures and solidifies. Illustration by Peter Johnston.

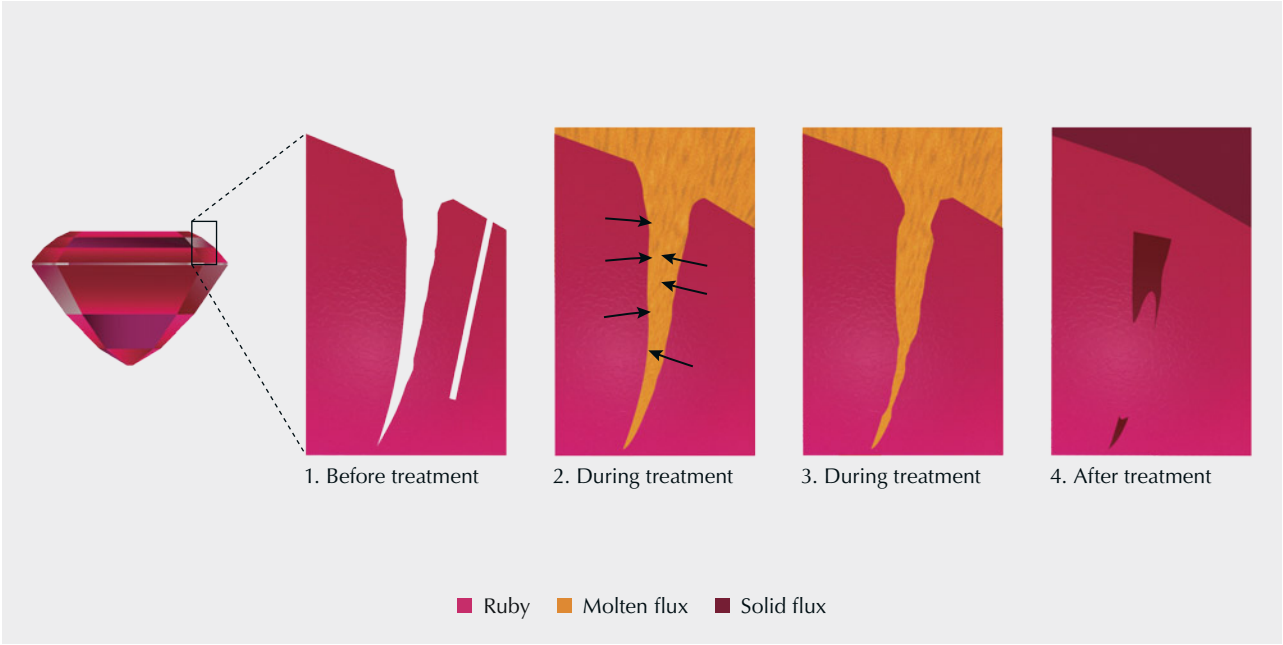

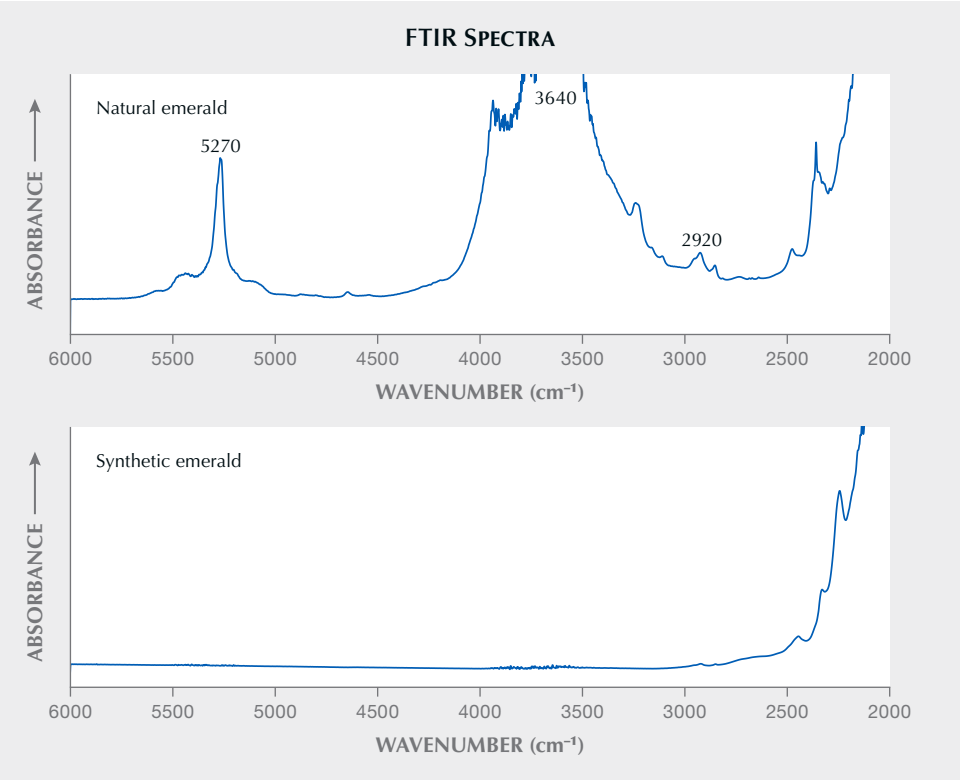

Figure 11. Typical FTIR spectra of natural emerald showing water-related features at ~3640 cm^{-1} (top) compared to a flux-grown synthetic emerald with no water features (bottom). The natural emerald spectrum also shows an overtone at 5270 cm^{-1} and oil peaks at ~2920 cm^{-1}.

In addition to inclusion features, spectroscopy can be a useful tool for identifying some flux-grown gemstones such as synthetic alexandrite and emerald. Natural alexandrite and emerald always grow from nucleation and pre-

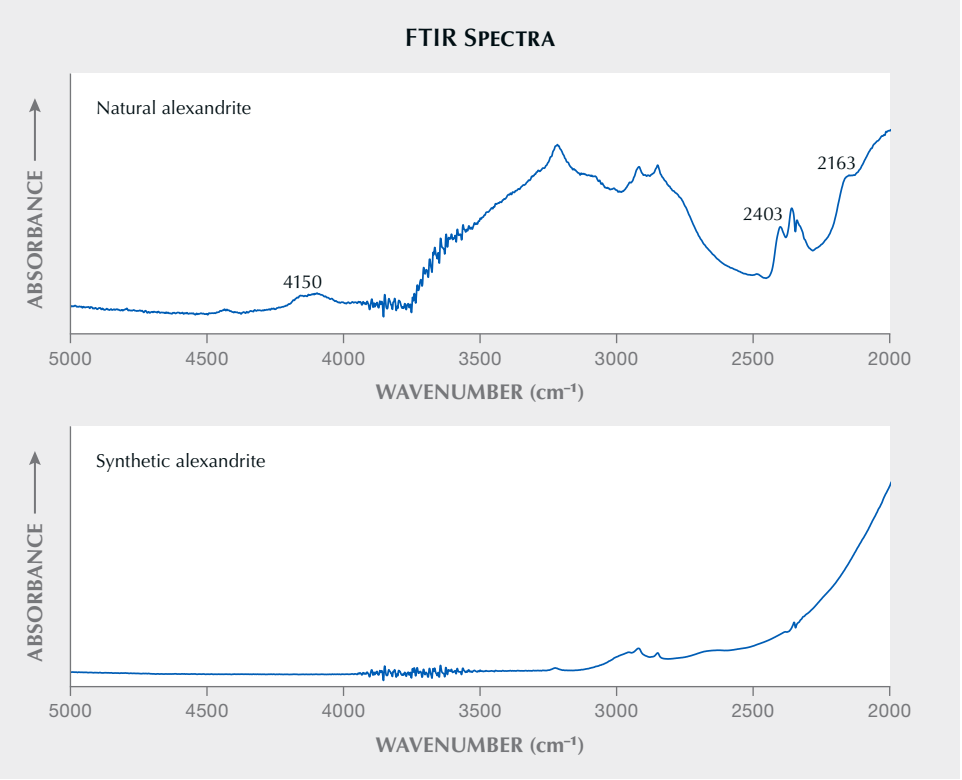

Figure 12. Typical FTIR spectra of natural alexandrite (top) showing hydrogen-related features at 2163, 2403, and 4150 cm^{-1} in comparison to flux-grown synthetic alexandrite (bottom), which does not have any of these features.

cipitation from some water-based hydrothermal fluid, and so these stones incorporate hydrogen derived from this water in their crystal structure. The fluxes used to grow synthetic alexandrite and emerald, on the other hand, are entirely dry (no water present). Fourier-transform infrared (FTIR) spectroscopy offers an excellent tool for detecting hydrogen species in gem materials. Natural emeralds show an intense absorption band at about 3640 cm^{-1} related to water in the beryl channels (figure 11, top), and natural alexandrite (figure 12, top) will show hydrogen-related peaks at 2163, 2430, and 4150 cm^{-1} (Malsy and Armbruster, 2012). Flux-grown emerald (figure 11, bottom) and alexandrite (figure 12, bottom) have none of these features and generally show a flat-line FTIR spectrum.

Hydrothermal Growth. Because many natural gemstones form through the action of hydrothermal fluids circulating through the earth, hydrothermally grown synthetic gemstones often pose a significant identification challenge. The first instance of hydrothermal crystal growth was by Robert Wilhelm Bunsen in 1839, when he grew crystals of barium and strontium carbonate in thick-walled glass tubes at >200°C and >100 bars (Bunsen, 1848; see also de Sénarmont, 1850). This field of research expanded, especially through efforts in the early 1900s by geologists and geochemists at the Carnegie Institution for Science and later at Harvard University (Bohm, 1985) in their attempts to understand phase equilibria in high-pressure, high-temperature environments in the earth. Use of the hydrothermal method grew rapidly from the need for high-purity quartz crystals for their piezoelectric properties, especially for radio components during World War II (McWhan, 2012). This important industrial product was historically mined from certain deposits known to yield high-quality, low-defect quartz crystals, such those in Brazil. Creating the same product artificially required hydrothermal growth (figure 13). Quartz crystals cannot be grown by melt methods, as the resulting melt is so viscous and the diffusion so slow that molten silica will quench to a glass upon cooling before crystallizing.

Hydrothermal growth takes advantage of the fact that water becomes a supercritical fluid at the conditions used in high-pressure autoclaves, enhancing diffusion by up to two orders of magnitude and allowing large crystals to grow. Hydrothermal growth of quartz and other gem minerals (figure 14) often uses mineralizers, salts, or other ions that increase the solubility of the gem material being grown. In quartz growth, sodium hydroxide is added to the water in the autoclave. Temperature gradients in the autoclave allow

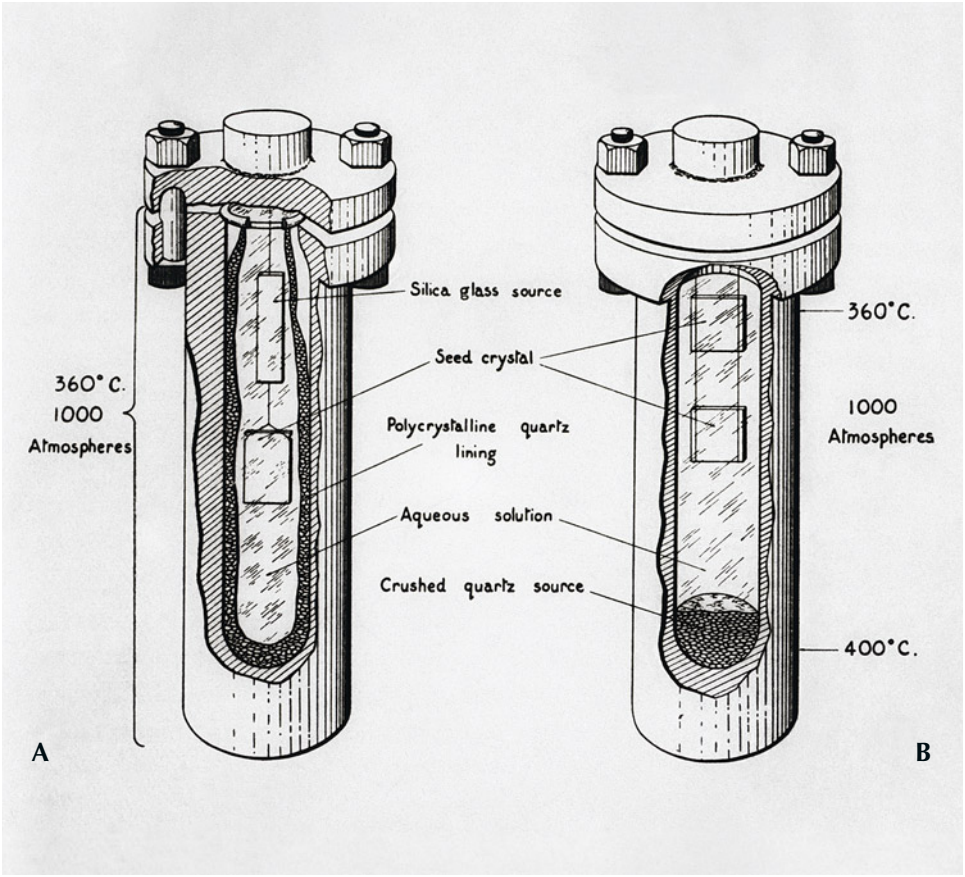

Figure 13. Isothermal (left) and temperature gradient (right) autoclaves used to grow hydrothermal quartz. From the Dr. Edward J. Gübelin Collection.

Figure 14. Hydrothermally grown synthetic beryl ranging from 1.08 to 6.32 g. Photo by Robert Weldon.

supersaturation to be achieved in the fluid, facilitating crystal growth. For industrial use, large crystals with controlled crystallographic orientation are grown using single-crystal seed plates (figure 15). In addition to quartz, hydrothermal growth methods can produce synthetic emerald (e.g., figure 16), ruby, sapphire, and spinel, among other gems.

While the conditions of hydrothermal gem synthesis often closely mimic those found in natural growth settings, most hydrothermal gems can be easily identified by an experienced gemologist. Characteristic inclusions in hydrothermal gems often include so-called chevron graining (figure 15), especially in emerald, but also features such as

Figure 15. Left: A colorless seed crystal inclusion in a synthetic hydrothermal beryl. Right: A chevron pattern in a synthetic hydrothermal emerald. Photomicrographs by John I. Koivula.

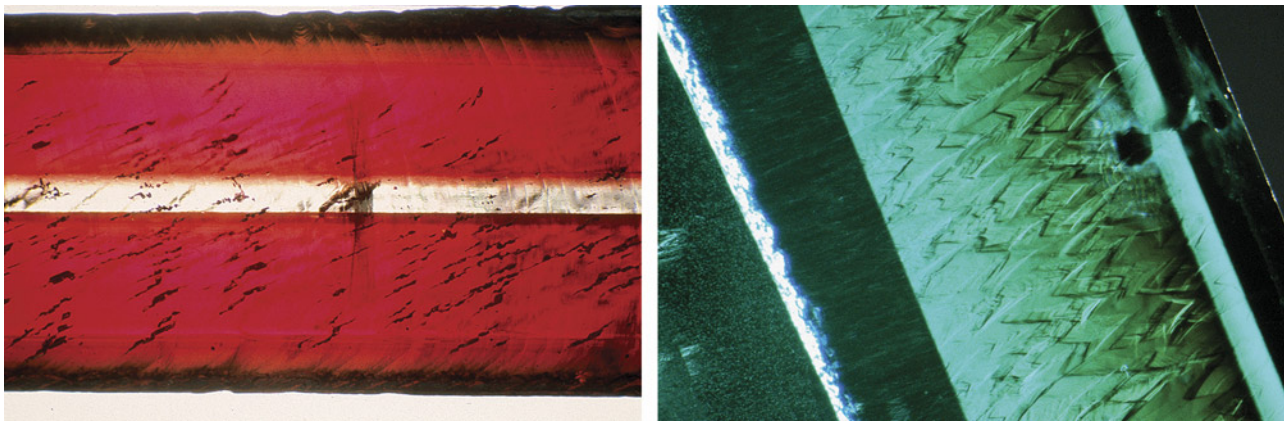

Figure 16. Synthetic crystals from the GIA Museum collection. Left to right: Russian hydrothermal synthetic emerald, flame-fusion pink synthetic spinel, hydrothermal synthetic amethyst with a colorless seed plate, titanium-doped Czochralski-grown purplish pink synthetic sapphire boule, flame-fusion blue synthetic spinel boule, and flux-grown Ramaura synthetic ruby. Photos by Robert Weldon.

nailhead spicules and mineral inclusions not found in nature such as phenakite in emerald. One of the most challenging identifications is that of hydrothermal quartz. Both natural and hydrothermal synthetic quartz tend to be quite clean, meaning there are few inclusions to identify their origin. In some cases, FTIR spectroscopy can be helpful, but water-based peaks tend to be poorly resolved and FTIR spectroscopy may not always offer a conclusive identification. Observation of a seed plate can help determine hydrothermal synthetic origin, but any remnants of the seed plate are usually cut away from finished gems. Natural amethyst of sufficient size will almost always have characteristic Brazil-law twinning, which is essentially never found in hydrothermal synthetic amethyst (except in rare cases where a Brazil-law twinned seed plate is used). Trace element chemistry can sometimes prove natural origin if sufficient gallium is present, but most natural and hydrothermal synthetic quartz is extremely pure silica (SiO_2) with few trace elements. As a result, chemical analysis often fails to distinguish between the two.

TABLE 1. Possible methods for synthetic growth of various common gem species.

	Melt			Solution		Other	
	Flame Fusion	Floating Zone	Crystal Pulling (Czochralski)	Flux	Hydrothermal	Vapor Growth	Sedimentation
Emerald				X	X		
Aquamarine					X		
Alexandrite		X	X	X	X		
Ruby	X	X	X	X	X		
Sapphire	X	X	X	X	X		
Diamond[a]				X		X	
Forsterite		X	X				
Opal							X
Rock crystal					X		
Amethyst					X		
Citrine					X		
Rose quartz					X		
Spinel	X		X	X			
Zircon				X	X		

[a]*Diamonds are not explicitly mentioned in the text, which is focused on colored stones, but laboratory-grown diamonds are produced by the high-pressure, high-temperature (HPHT; flux) and chemical vapor deposition (CVD; vapor growth) methods. Both methods are reviewed in S. Eaton-Magaña et al., "Laboratory-grown diamonds: An update on identification and products evaluated at GIA," pp. 146–167 of this issue.*

Synthetic Growth Processes Replicating Sedimentary Processes. Methods have also been developed to artificially grow gems that ordinarily form via sedimentary processes in the earth, such as opal, turquoise, and malachite. Of these, opal is probably the most important commercially. While the specifics of the growth methods are not fully disclosed, some solution-based method is used to dissolve SiO_2 and precipitate a nanostructured lattice approximating the natural opal structure that is capable of producing play-of-color. The appearance of synthetic opal can be easily distinguished (Renfro et al., 2019). While synthetic opal matches many of the gemological properties of natural opal, there is a debate about whether it is more accurately classified as "imitation opal" (Schmetzer, 1984; Schmetzer and Henn, 1987).

Conclusions

Scientific progress in understanding crystal growth and gem formation through geological processes has been a cornerstone in humankind's attempts to artificially grow gemstones in the laboratory. Early growth methods were sufficiently separated from nature to allow easy identification of these synthetic stones through basic observations of their inclusions and other properties. As synthesis methods became more sophisticated over time, growth conditions came to more closely approximate natural geological conditions of gem formation. An overview of different growth methods for various gem species is shown in table 1. Even with these significant technological advancements, humans have yet to fully replicate the rare conditions in the earth that produced fine natural gemstones.

REFERENCES

Authier A. (2013) *Early Days of X-ray Crystallography*. Oxford University Press, Oxford, UK, 464 pp.

Bohm J. (1985) The history of crystal growth. *Acta Physica Hungarica*, Vol. 57, No. 3-4, pp. 161–178, http://dx.doi.org/10.1007/BF03158886

Bunsen R. (1848) Bemerkungen zu einigen Einwürfen Gegen mehrere Ansichten über die chemisch-geologischen Erscheinungen in Island. *Annalen der Chemie und Pharmacie*, Vol. 65, No. 1, pp. 70–85.

Czochralski J. (1918) Ein neues Verfahren zur Messung der Kristallistaionsgeschwindigkeit der Metalle. *Zeitschrift für Physikalische Chemie*, Vol. 92, No. 1, pp. 219–221.

Elwell D. (1989) Fundamentals of flux growth. In H. Arend and J. Hulliger, Eds., *Crystal Growth in Science and Technology*, Vol. B210. Plenum Publishing Corp., New York, pp. 133–142.

Feigelson R.S. (2015) Crystal growth through the ages: A historical perspective. In T. Nishinaga, Ed., *Handbook of Crystal Growth: Fundamentals, Volume IA: Thermodynamics and Kinetics*. Elsevier, Amsterdam, pp. 1–83.

——— (2022) Crystal growth history: Theory and melt growth processes. *Journal of Crystal Growth*, Vol. 594, article no. 126800, http://dx.doi.org/10.1016/j.jcrysgro.2022.126800

Gaudin A. (1837) Note sur la formation artificielle du corindon. *Comptes Rendus Hebdomadaires des Séances de l'Académie des Sciences*, Vol. 4, No. 26, pp. 999–1000.

Giuliani G., Groat L.A., Fallick A.E., Pignatelli I., Pardieu V. (2020) Ruby deposits: A review and geological classification. *Minerals*, Vol. 10, No. 7, article no. 597, http://dx.doi.org/10.3390/min10070597

Harrison H.R., Honig J.M. (1981) Skull melting as a technique in the growth of single crystals. *Bulletin of Materials Science*, Vol. 3, No. 3, pp. 247–253, http://dx.doi.org/10.1007/BF02747589

Haüy R.J. (1801) *Traité de Minéralogie* (5 volumes). DeLance Printers, Paris.

Jannettaz E. (1886) Note sur les rubis artificiels. *Bulletin de la Société française de Minéralogie*, Vol. 9, No. 8, pp. 321–323, http://dx.doi.org/10.3406/bulmi.1886.2037

Kane R.E. (1983) The Ramaura synthetic ruby. *G&G*, Vol. 19, No. 3, pp. 130–148, http://dx.doi.org/10.5741/GEMS.19.3.130

Knischka P.O., Gübelin E. (1980) Synthetische Rubine mit Edelsteinqualität, isometrischem Habitus und hoher zahl unbeschädigter Kristallflächen. *Zeitschrift der Deutschen Gemmologischen Gesellschaft*, Vol. 29, No. 3-4, pp. 155–185.

Malsy A.K., Armbruster T. (2012) Synthetic alexandrite–Growth methods and their analytical fingerprints. *European Journal of Mineralogy*, Vol. 24, No. 1, pp. 153–162, http://dx.doi.org/10.1127/0935-1221/2012/0024-2181

McWhan D. (2012) *Sand and Silicon: Science that Changed the World*. Oxford University Press, Oxford, UK, 142 pp.

Muhlmeister S., Fritsch E., Shigley J.E., Devouard B., Laurs B.M. (1998) Separating natural and synthetic rubies on the basis of trace-element chemistry. *G&G*, Vol. 34, No. 2, pp. 80–101, http://dx.doi.org/10.5741/GEMS.34.2.80

Nassau K. (1972) Dr. A.V.L. Verneuil: The man and the method. *Journal of Crystal Growth*, Vol. 13-14, pp. 12–18, http://dx.doi.org/10.1016/0022-0248(72)90055-3

——— (1977) Cubic zirconia - The latest diamond imitation and skull melting. *Lapidary Journal*, Vol. 31, No. 4, pp. 900–904, 922–926.

——— (1980) *Gems Made by Man*. Chilton Book Company, Radnor, Pennsylvania, 364 pp.

Palke A.C., Shigley J.E. (2022) Colored Stones Unearthed: Gems formed in magmatic rocks. *G&G*, Vol. 58, No. 4, pp. 494–506.

——— (2023) Colored Stones Unearthed: Gems formed in metamorphic rocks. *G&G*, Vol. 59, No. 2, pp. 232–241.

Renfro N.D., Koivula J.I., Muyal J., McClure S.F., Schumacher K., Shigley J.E. (2019) Inclusions in natural, treated, synthetic, and imitation opal. *G&G*, Vol. 55, No. 2, pp. 244–245, http://dx.doi.org/10.5741/GEMS.55.2.244

Schmetzer K. (1984) An investigation of the synthetic products of Gilson showing a play of colours. *Journal of Gemmology*, Vol. 19, pp. 27–42.

——— (1986) *Natürliche und synthetische Rubine - Eigenschaften und Bestimmung*. E. Schweizerbart'sche Verlagsbuchhandlung, Stuttgart, 131 pp.

Schmetzer K., Henn U. (1987) Synthetic or imitation? An investigation of the products of Kyocera Corporation that show play-of-color. *G&G*, Vol. 23, No. 3, pp. 148–151, http://dx.doi.org/10.5741/GEMS.23.3.148

de Sénarmont H. (1850) Expériences sur la formation artificielle, par voie humide, de quelques espèces minérales qui ont pu se former dans les sources thermales sous l'action de chaleur et de la pression. *Annales de Chimie et de Physique*, Vol. 30, pp. 129–149.

Shigley J.E., Bassoo R., Palke A.C. (2023) Colored Stones Unearthed: Gems recovered from sedimentary rocks. *G&G*, Vol. 59, No. 4, pp. 510–523.

Smith C.P., Bosshart G. (1993) New flux-grown synthetic rubies from Greece. *JewelSiam*, Vol. 4, No. 4, pp. 106–114.

Verneuil A. (1904) Mémoire sur la reproduction du rubis par fusion. *Annales de Chimie et de Physique*, Vol. 8, No. 4, pp. 20–48.

Winter J.G. (1916) *The Prodromus of Nicolaus Steno's Dissertation Concerning a Solid Body Enclosed by a Process of Nature within a Solid* (1669), Macmillan Company, New York, 283 pp.

GEM NEWS INTERNATIONAL

Contributing Editors
Gagan Choudhary, *IIGJ-Research & Laboratories Centre, Jaipur, India* (gagan.choudhary@iigjrlc.org)
Christopher M. Breeding, *GIA, Carlsbad* (christopher.breeding@gia.edu)
Guanghai Shi, *School of Gemmology, China University of Geosciences, Beijing* (shigh@cugb.edu.cn)

COLORED STONES AND ORGANIC MATERIALS

New emerald production from the Curlew mine, Western Australia. Australian emeralds have been known for over a century but have always maintained a low profile. Small volumes, low clarity, and desaturated color were among the reasons for their lack of recognition in the global market.

One of Australia's emerald deposits is the Curlew mine in the Shire of East Pilbara in Western Australia. This area has been worked officially since the mid-1970s, but anecdotal evidence suggests that emeralds were known at least 50 years prior to that. During this initial period of mining, the focus was on specimen collecting. Any gem-quality material was sold to Indian-based emerald manufacturers and disappeared into the vast pool of emeralds with undetermined origin.

Figure 1. Emeralds in matrix and various cut stones from the Curlew mine in Western Australia. All stones were mined in 2023. The cut stones are untreated and range from 0.45 to 7.92 ct (triangular shape). Photo by Lhapsin Nillapat; courtesy of Matthew Allen (The Gemstone Trading Company).

From the 1980s to 2011, the mine was largely abandoned, although a few (unsuccessful) attempts were made to revitalize the deposit. In 2011, a prospecting license was passed between different groups with little success in emerald production. In recent years, the mining license was taken over by a small-scale mining group. They successfully produced gem-quality material from the existing pit during the 2023 mining season. Production was limited to a few kilograms of gem-quality material, but the owners intend to scale up the production in 2024.

GIA's Bangkok laboratory was able to study a suite of 69 emeralds from this recent production (figure 1) that was on loan from the miner. The rough emerald crystals showed a well-formed hexagonal outline, often coated with dark mica crystals. Other minerals associated with the emerald were identified as feldspar and quartz. One of the matrix specimens also contained significant volumes of purple fluorite (confirmed by Raman spectroscopy).

The combination of these matrix minerals, especially mica, suggests that these stones formed in the contact zone of a pegmatite intrusion into an (ultra-)mafic rock. Images from the emerald mineralization in the field confirmed this (figure 2). This type of geological environment, found at many other emerald deposits around the world, is responsible for the majority of emeralds in the marketplace, including Kafubu (Zambia), the Ural Mountains (Russia), Shakiso (Ethiopia), and Itabira (Brazil).

Editors' note: Interested contributors should send information and illustrations to Stuart Overlin at soverlin@gia.edu.

Gems & Gemology, Vol. 60, No. 2, pp. 252–270.

Figure 2. An emerald pocket at the reaction zone between the pale pegmatite intrusion (bottom right) and ultramafic greenish rock (top left). The emeralds are encrusted in dark mica crystals. Photo by Matthew Allen; field of view approximately 50 cm.

The refractive index of the stones was 1.580–1.586 ± 0.001, with a birefringence of 0.007. This is in the higher range for emerald and corresponds with other emeralds that form in a similar geological environment.

Chemical analysis using laser ablation–inductively coupled plasma–mass spectrometry (LA-ICP-MS; see table 1) and spectroscopic analysis confirmed that these emeralds were rich in iron. Ultraviolet/visible/near-infrared spectroscopy revealed chromium-related absorption features as well as a strong band around 810 nm, which is attributed to the higher iron concentration. This band is used to separate high-iron, schist-hosted emeralds from hydrothermal, low-iron emeralds (e.g., Colombia and Afghanistan).

Various inclusions were seen in the emeralds (figure 3). Very fine fluid inclusions had a blocky outline, sometimes elongated as tubes, with a single bubble inside. In many cases, they were surrounded by a frosty rim that was large enough to obscure the fluid inclusion. No color zoning was observed, but some of the cleaner stones showed wavy to straight graining.

Two types of crystal inclusions were observed, the most common being dark mica platelets and the other consisting

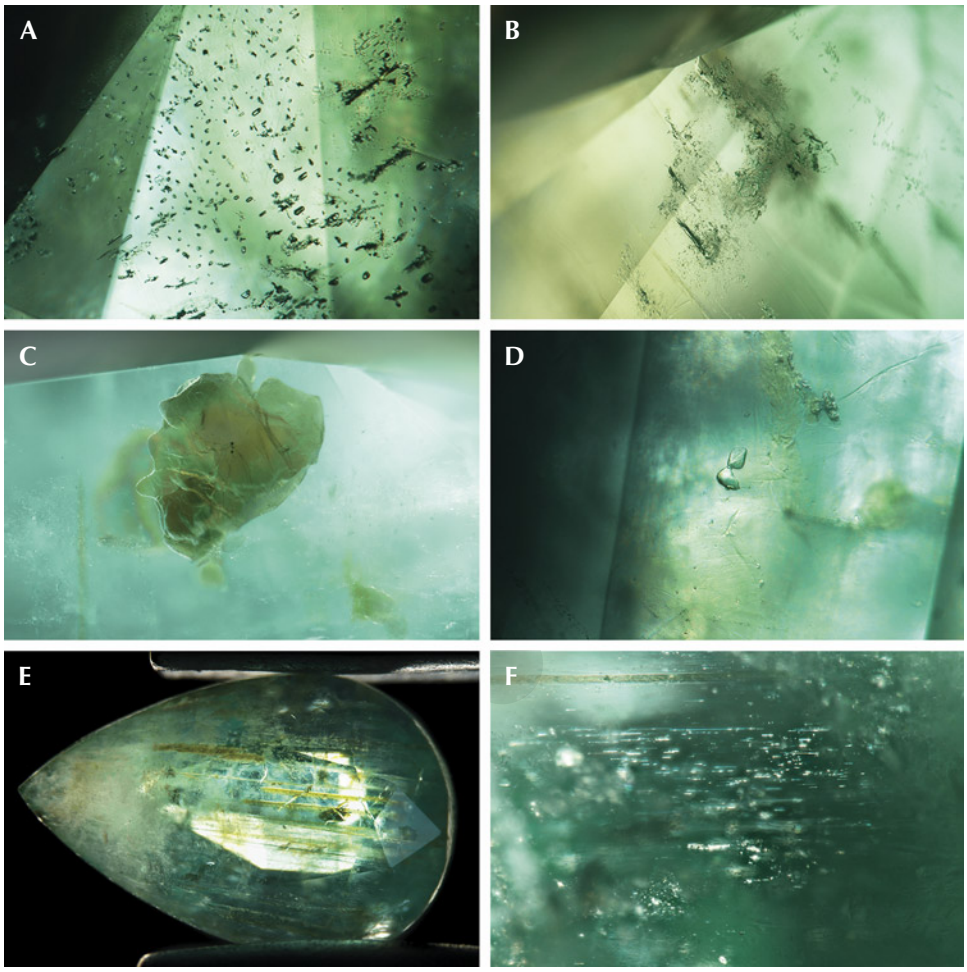

Figure 3. A: A field of blocky two-phase fluid inclusions. B: Elongated two-phase fluid inclusions with large frosty rims. C: An irregularly shaped platy mica crystal. D: Two small, transparent, and colorless feldspar crystals. E: Large tubes filled with a foreign orangy material. F: A cluster of short parallel needles. Photomicrographs by Suwasan Wongchacree; fields of view 1.07 mm (A), 1.80 mm (B, C, and F), 1.20 mm (D), and 10.8 mm (E).

of small transparent colorless crystals. With the use of confocal Raman spectroscopy, some of these transparent crystals were identified as feldspar and others as fluorite. Several stones also showed clusters of short needles mixed with smaller reflective particles, sometimes forming fields of "dusty" particles. A handful of stones had large, wide tubes stained with orangy brown iron mineralization.

Overall, this inclusion scene shares many similarities with samples from other high-iron emerald sources such as Kafubu and Itabira (S. Saeseaw et al., "Geographic origin determination of emerald," Winter 2019 *G&G*, pp. 614–646).

The trace element composition of Curlew emeralds (table 1) allows for separation from other high-iron emerald sources, although multiple elements should be taken into

TABLE 1. Trace element analysis (in ppmw) of 40 emerald samples from Western Australia, measured using LA-ICP-MS (three spots per stone).

	Li	Na	Mg	Sc	V	Cr	Fe	Rb	Cs
Range	260–603	2240–9990	891–7710	21–325	34–444	219–2750	916–4700	13–133	228–2270
Average	377	4093	2345	89	156	1367	1903	38	718
Standard deviation	73	1446	1205	69	85	549	780	22	385
Detection limit (ppmw)	0.05	0.9	0.02	0.09	0.03	0.5	2	0.02	0.01

Figure 4. Two strands of large Japanese akoya bead cultured pearls. The pearls range from 11.0 to 11.6 mm in the top strand and from 11.0 to 12.2 mm in the bottom strand. Photo by Artitaya Homkrajae.

account to clearly separate the Australian emeralds from those found in Russia and Nigeria.

Emeralds from this renewed activity at the Curlew mine in Australia only started to enter the global emerald trade in late 2023. Their appearance and characteristics are in line with other high-iron, schist-hosted emeralds such as those from Zambia, Brazil, and Russia. Inclusions offer limited clues for origin determination, which relies heavily on trace element analysis and correct interpretation of these results.

Wim Vertriest, Suwasan Wongchacree, and Polthep Sakpanich
GIA, Bangkok

Remarkably large akoya bead cultured pearls. Saltwater bead cultured pearls dominating the global pearl market are produced by mollusk species in the *Pinctada* genus, including *P. maxima* (South Sea), *P. margaritifera* (Tahitian), and *P. fucata matensii* (akoya). The size and color of these pearls depend mainly on the mollusk species. The majority of white saltwater bead cultured pearls are South Sea and akoya pearls. South Sea pearls are notable for their large sizes, ranging from 8 to 20 mm, and soft satiny luster. Akoya pearls are well known for their round shape, high degree of luster, and attractive rosé (pink) overtone (very often as a result of processing). Akoya pearls are generally smaller, averaging between 6 and 8 mm in diameter, with those above 10 mm considered rare.

At the 2024 AGTA GemFair in Tucson in February, the author spotted unusually large round akoya pearls that were comparable in size to South Sea bead cultured pearls. These were on display at the booth of Yen's Jewelry & Accessories Inc. (San Francisco). Eric Yen noted that the two strands in figure 4 consisted of the maximum available sizes of Japanese akoya bead cultured pearls. Those in the top strand ranged from 11.0 to 11.6 mm, and those in the bottom strand were

Figure 5. Left: The three-armed claw game (one play for 100 yen). Right: The pearl necklace prize, complete with a jewelry box. Photos by Mari Sasaki (left) and Shunsuke Nagai (right).

between 11.0 and 12.2 mm. Although the bead sizes were not specified, the cultivation process was presumably challenging and required extra caution due to the insertion of a large bead nucleus and possibly the need to nourish the mollusks for several years. Yen explained that these sizes for akoya pearls were extraordinary and multiple harvests were involved to create matching strands. Many mollusks die during the culturing process, which limits production and thus increases rarity and value. In addition to their remarkable sizes, the pearls appeared to have a rounded shape, a spotless surface, high luster, and an appealing rosé overtone.

Artitaya Homkrajae
GIA, Carlsbad

Akoya cultured pearl prize in an arcade-style claw game. Japan began producing pearls in the early 1900s with the successful cultivation of akoya pearls, which are deeply intertwined with the nation's customs. Once used in engagement rings in Japan, akoya pearls remain a jewelry staple for weddings, funerals, and other important occasions. Combining entertainment and product promotion, akoya pearl jewelry began showing up as a prize in Japanese arcades in 2019.

Author MS recently had the opportunity to play a coin-operated "claw" game (figure 5, left) for 100 yen (approximately US$0.65). The prizes offered included earrings, one-size-fits-all unclosed rings, and pendants, all containing akoya pearls. Gold or silver stickers on top of each box indicated the jewelry metal color. After 14 attempts, the author captured the prize shown in figure 5 (right): a pearl set in a 40 cm white metal necklace weighing 2.20 g, contained in a blue jewelry box with a silver sticker but no metal information. According to metal testing by energy-dispersive X-ray fluorescence (EDXRF) spectroscopy, the metal was composed mainly of copper, zinc, and nickel, suggesting an alloy of these metals.

The 8.20 × 8.01 × 7.92 mm pearl had a white bodycolor with pink overtone and was fully drilled with an approximately 1 mm drill hole. The bead was observed through the drill hole. A bumpy surface near the drill hole (figure 6, left) resulted in the pearl's semi-baroque shape. Nacre and terrace structures were observed on the surface (figure 6, right). The pearl's saltwater chemistry was confirmed by EDXRF. Its luster was excellent, and the surface was clean. The pearl fluoresced weak bluish yellow under short-wave UV and moderate bluish yellow under long-wave UV. The fluorescence feature indicates that the pearl had been subjected to a routine set of traditional processes for improving the appearance of cultured pearls (R. Shor, "From single source to global free market: the transformation of the cultured pearl industry," Fall 2007 *G&G*, pp. 200–226). The nacre thickness was measured by optical coherent tomography (OCT),

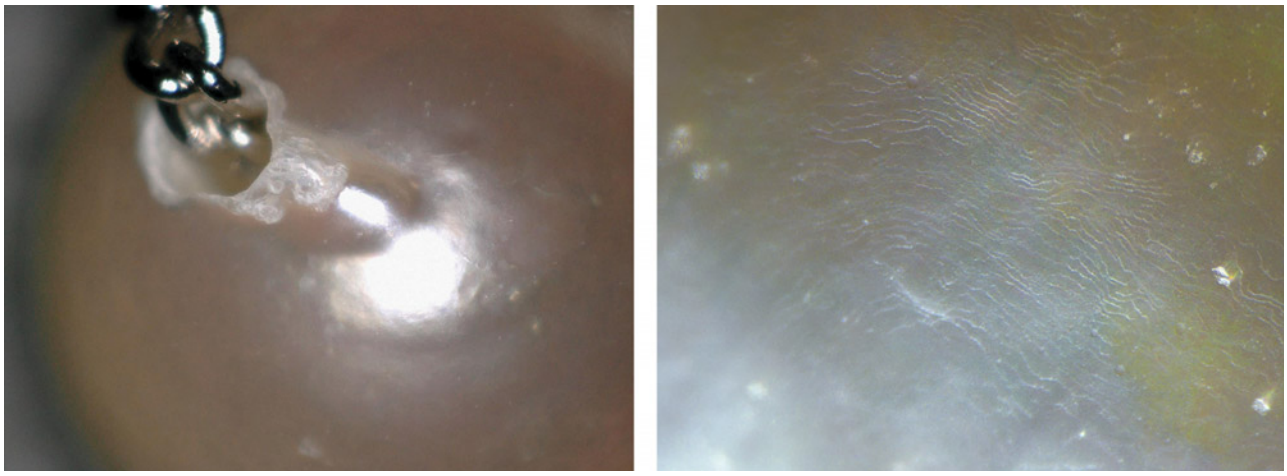

Figure 6. Left: The bumpy surface around the drill hole. Right: Magnification of the pearl surface showing the nacre's terrace structure. Photomicrographs by Mari Sasaki.

a nondestructive technique for cross-sectional imaging of various materials, including pearl and jade (J. Liu et al., "Pearl thickness measurements from optical coherence tomography images," *Applied Mechanics and Materials*, Vol. 421, 2013, pp. 415–420; S. Chang et al., "Detection and analysis of jade material using optical coherence tomography," *Photonics North 2010*, Vol. 7750, 2010, SPIE). The center of the pearl was round with a homogeneous nacre thickness of 0.35 mm ± 0.01 mm (figure 7, left). Toward the drill hole, the thickness was uneven, with some bumpy areas in the thinnest part measuring ~0.23 mm (figure 7, right). Although the quality was very good, the shape was not round and the size was less than 8 mm, which is probably why this pearl became a prize in the claw game.

In addition to arcade games, toy capsule vending machines in commercial locations throughout Japan offer jewelry prizes such as earrings, rings, and pendants using akoya pearls, rough and faceted colored stones, and even diamonds. These machines charge anywhere from 500 to 1,000 yen (approximately US$3.25–$6.50) per try. While claw games allow players to attempt to win the prize of their choice, often unsuccessfully, toy capsule machines dispense a prize every time but by luck of the draw. According to Japanese regulations, the value limit of prizes in crane games is about one thousand yen, so expensive jewelry is not available.

This may be an interesting new outlet for akoya pearls. Those who might not enter a jewelry store can still win a piece of pearl jewelry for themselves, or as small gifts for family and friends.

Mari Sasaki, Kazuko Saruwatari, Shoko Odake, and Tsutomu Takada
GIA, Tokyo

Blister pearl vs. shell blister from *Pteria sterna*. The saltwater mollusk *Pteria sterna*, also known as the rainbow-lipped pearl oyster, is widely distributed in the eastern Pacific, from Baja California to Peru. These mollusks can grow up to 14 cm, producing natural pearls ranging from 3 to 6 mm and rarely up to 11 mm (*CIBJO Pearl Guide*, 2020).

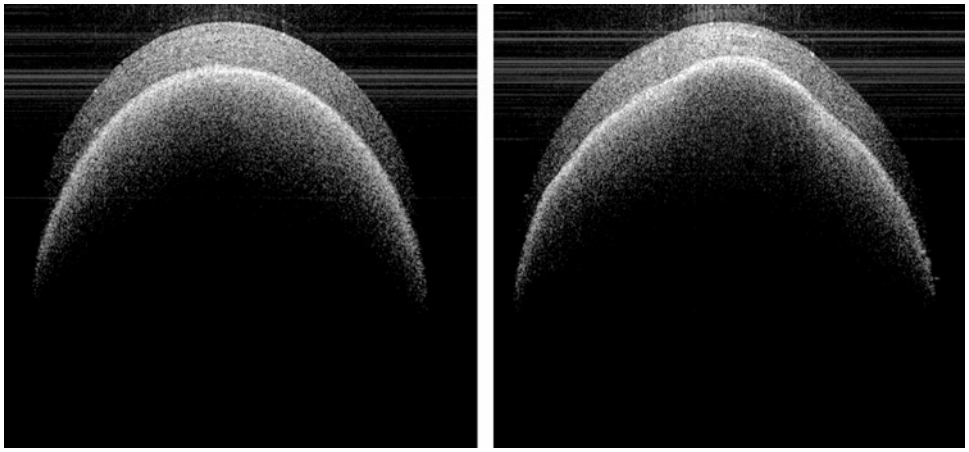

Figure 7. OCT images of the pearl. Left: The middle of the pearl, where the nacre thickness measured ~0.35 mm. Right: The bumpy area, where the nacre thickness measured ~0.23 mm. Images by Kazuko Saruwatari.

Figure 8. These three Pteria sterna *shells each have a visible protuberance, measuring approximately 20.22 × 13.78 × 13.55 mm, 23.49 × 19.06 × 15.62 mm, and 24.88 × 17.03 × 12.23 mm, respectively. Photo by Gaurav Bera.*

Externally, their shells are more concave than those of *Pinctada*-species mollusks, and the internal nacre exhibits vibrant multicolored hues with a metallic sheen. This characteristic is reflected in the wide range of colored pearls they produce.

GIA's Mumbai laboratory recently received a variety of shells for scientific examination. The submission included three shells from *Pteria sterna*, exhibiting nacre colors ranging from brown to gray, with vivid overtones of violet and blue and a strong orient with variations in saturation and tone. The shells weighed 63, 83, and 174 g; each had a prominent protuberance attached to its inner wall, measuring approximately 20.22 × 13.78 × 13.55 mm, 23.49 × 19.06 × 15.62 mm, and 24.88 × 17.03 × 12.23 mm, respectively (figure 8).

Upon examination, dried organic remnants from the aquatic habitat and various parasite intrusion boreholes of differing thickness were observed on all three. Shell 2 in particular had a noticeable cavity in the center of its exterior, which extended into the interior area of the protuberance. A distinct feature observed in all three samples was an irregular, patchy nacreous yellowish brown area, indicative of an adductor muscle scar (figure 9). Viewed under high magnification, the nacreous area revealed spiral patterns of aragonite platelets on the surface (figure 10), similar to those observed in most nacreous pearls from *Pteria*-species mollusks (L. Kiefert et al., "Cultured pearls from the Gulf of California, Mexico," Spring 2004 *G&G*, pp. 26–39).

Energy-dispersive X-ray fluorescence (EDXRF) spectrometry of samples 1 and 3 showed manganese levels of 26 and 110 ppm, and higher strontium levels of 1185 and 1915 ppm, respectively, indicative of their saltwater origin. Due to instrument limitations and the position of sample 2, it was not possible to collect EDXRF data from it. All three samples also exhibited a strong reddish reaction under long-wave ultraviolet light (figure 9) and a weak yellowish reaction under short-wave ultraviolet light. The reddish reaction is linked to a type of porphyrin pigment found in pearls originating from the *Pteria* species (Winter 2014 Lab Notes, pp. 295–296).

Ultraviolet/visible reflectance spectra were collected on multiple spots on the blisters as well as their shells. Absorption bands at identical positions but with different relative intensities were observed at around 405 and 495 nm, indicating a natural color characteristic of the *Pteria* mollusk. Photoluminescence analysis of the pearls revealed the triple bands at 620, 650, and 680 nm, corresponding to their natural coloration (S. Karampelas, "Spectral characteristics of natural-color saltwater cultured pearls from *Pinctada maxima*," Fall 2012 *G&G*, pp. 193–197).

Real-time X-ray microradiography (RTX) imaging of the samples revealed large voids of varying size and opacity, containing organic-rich material of lower opacity with a spotty and granular appearance. However, the images were not clear due to overlapping dark parasitic network structures beneath the growth within the host shells. All three protuberances within the shells displayed a pronounced boundary around the bulge, making them stand out prominently from their host shell. However, the irregularly shaped protuberance observed in shell 1 stood out due to its well-defined outline at the attachment point, forming a clear separation from the shell beneath it. In contrast, the protuberances from shells 2 and 3 appeared to have grown more together with the shell at their bases, lacking clearly

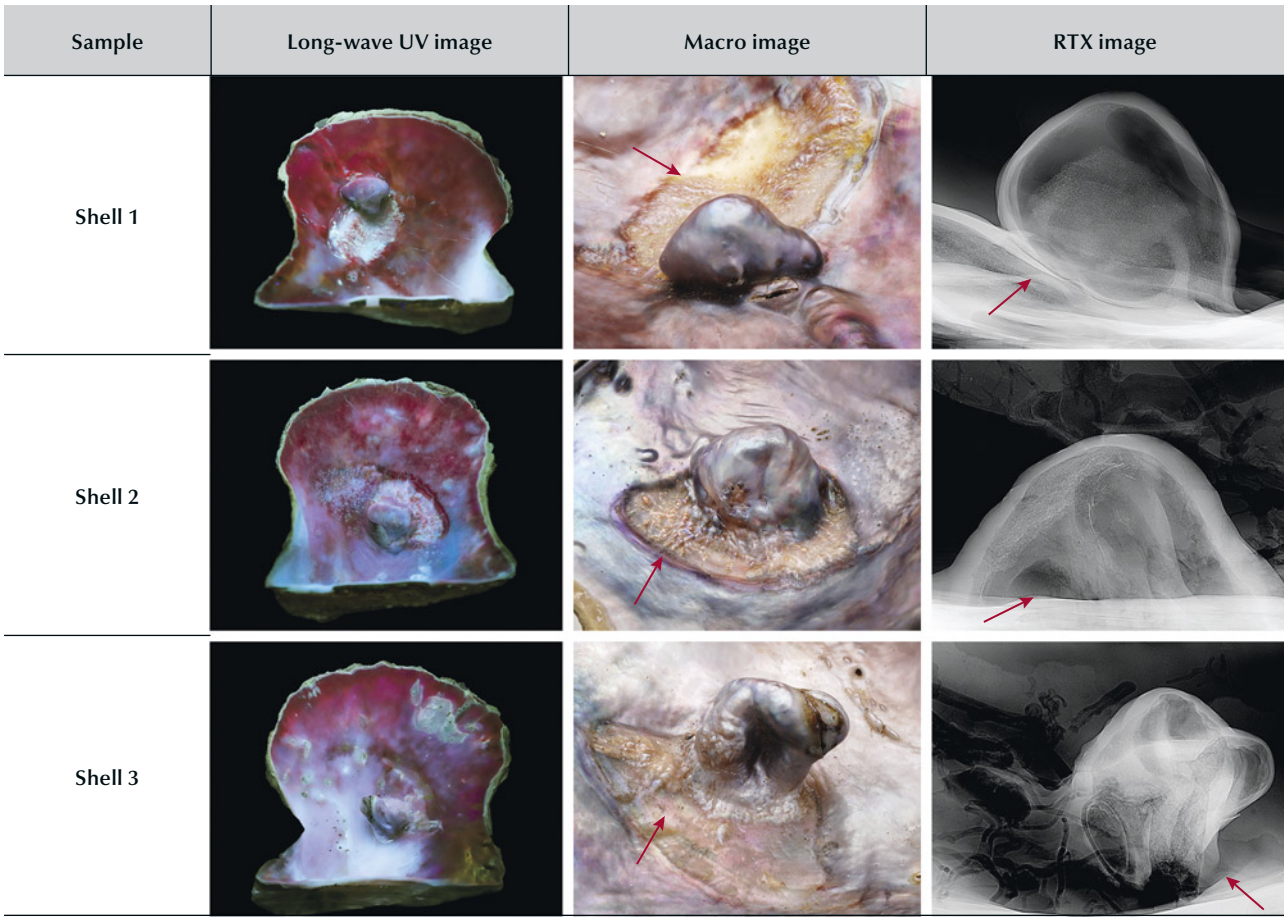

Figure 9. Long-wave UV images displaying a strong red fluorescence typical to that observed in the Pteria *species (left). Macro images showing protuberances and their attachment to the adductor tissue scar beneath (marked with arrows) (middle). RTX images revealing dark organic-rich voids, as well as parasite intrusion and nacre growth at the base (marked with arrows) (right). Photos by Gaurav Bera.*

defined outlines at the attachment points. These features are consistent with RTX observations; sample 1 showed a large organic-rich area followed by a more complete nacre growth around the base, while samples 2 and 3 showed a merging of the bases with the shell growth. Based on the characteristics shown in their base attachment, outline shapes, dome height, and internal growth features, it can be concluded that sample 1 is likely a blister pearl, while samples 2 and 3 lean more toward shell blisters.

Shell blisters result from foreign objects trapped in the space between the mantle tissue and shell, which is subsequently overgrown by layers of calcium carbonate, whereas blister pearls are whole pearls that have perforated from the mantle tissue and attached themselves to the shell (E. Strack, *Pearls*, 2006, Ruhle-Diebener-Verlag GmbH, Stuttgart, pp. 125–127). Previous studies have found that natural shell blisters show some similarities to natural blister pearls in that both have nacreous concre-

Figure 10. Spiral patterns formed by the platy layers of aragonite (nacre) observed on the surface. Photomicrograph by Lubna Sahani; field of view 1.44 mm.

Figure 11. Haeri Jang's design sketch for the "Blossom" necklace, featuring white gold, pink and colorless diamonds, lavender jade, and akoya pearls.

tions protruding from the inner shell wall ("Natural shell blisters and blister pearls: What's the difference?" *GIA Research News*, August 26, 2019). Differentiating between natural blister pearls and shell blisters remains complex and challenging, relying heavily on external examination and the experience of the gemologist, along with references from observations and research studies. This ongoing learning curve means that even experienced gemologists may reach different conclusions in such cases. GIA is privileged to study such intriguing shell samples, and hopefully these observations will promote a better understanding of natural blister pearls and shell blisters.

Gauri Sarvankar, Lubna Sahani, Roxane Bhot Jain, and Abeer Al-Alawi
GIA, Mumbai

JEWELRY DESIGN

GIA student design showcase. One of GIA's "student choice" awards was recently presented to Haeri Jang, a graduate of the Jewelry Design program at the New York campus. Figure 11 shows Jang's "Blossom" necklace design, which combines white gold, pink and colorless diamonds, lavender jade cabochons, and akoya pearls. Noted Jang, "The inspiration of this piece comes from the ethereal beauty of cherry blossoms. I hope to capture the subtle charm and the timeless elegance of these delicate blooms. I have drawn from my imagination and from both nature and tradition to create this symbol of beauty and purity. I have attempted to modernize the elements of traditional Korean accessories and blend them with a contemporary aesthetic."

SYNTHETICS AND SIMULANTS

A visit to Clarity Diamond's CVD facility. Laboratory-grown diamond sales have surged in the global gem and jewelry market over the past decade. With increased consumer demand, many in the trade are interested in learning more about these products and their supply chain. First-hand experience, such as visiting a laboratory-grown diamond factory, helps ensure the delivery of reliable information to industry professionals and consumers.

Figure 12. Clarity Diamond opened its CVD facility in Austin to a large group of 2024 AGS Conclave attendees. Scientists led the visitors through the CVD growth process and answered questions from the audience. Courtesy of Clarity Diamond.

Recently, the authors had the opportunity to visit Clarity Diamond's facility in Austin, Texas. We first joined a group tour of around 120 attendees from the 2024 American Gemological Society Conclave (figure 12) and then returned the next day for a more in-depth visit. On both occasions, the Clarity Diamond team openly shared their knowledge of chemical vapor deposition (CVD) diamond growth techniques and products, providing visitors with a rewarding learning experience.

For the majority of the group, including the authors, this was their first visit to a diamond growth facility and the first opportunity to see diamonds growing in a reactor. Attendees participated in engaging demonstrations exhibiting the unique physical properties of polycrystalline CVD-grown diamond. This type of diamond is generally produced as a thin plate composed of thousands of microscopic diamonds and has many applications in other industries such as engineering and electronics. For example, one demonstration showed that polycrystalline diamond could easily cut through ice due to its high thermal conductivity (five times higher than copper), efficiently melting through it (figure 13). Many visitors commented that they wished they had this learning opportunity earlier to help them better understand CVD-grown diamonds or even diamonds in general.

Clarity Diamond's facility hosts a number of reactors as well as a planning and cutting area for research purposes (figure 14). A diamond seed (also referred to as a substrate), a predetermined gas mixture, and extremely hot plasma are the three necessary components to grow CVD diamonds. These diamonds can be produced with interrupted or uninterrupted growth (figure 15). The former requires the grower to remove the crystal from the reactor to polish off unwanted growth and then return it to the reactor. This procedure can be repeated many times, depending on the needs of the grower. In comparison, uninterrupted growth keeps the substrates in the reactor from beginning to end. At Clarity Diamond, the crystals are produced by one un-

Figure 13. Mechanical engineer and product manager A.J. Brown demonstrated diamond's outstanding thermal conductivity for the visitors, who used polycrystalline CVD-grown diamond plates produced in the facility to cut through ice cubes with ease. Courtesy of Clarity Diamond.

interrupted growth cycle. According to founder and CEO Bob Basnett, one of the main challenges in uninterrupted growth is controlling the temperature for an extended time, up to a thousand hours, which allows the crystal to grow continuously to the thickness needed.

These laboratory-grown diamonds are cut and polished by Clarity's partner, HRA Group, at their cutting factory in Ho Chi Minh City, Vietnam. Planning is done by computer-aided tools, and plans are executed following the same cutting and polishing procedures applied to natural

Figure 14. A CVD-grown diamond factory such as Clarity's facility in Austin often has rows of reactors lined up (left). The reactors are carefully monitored throughout the growth period, as demonstrated by process engineer Dr. Amanda Charris (right). Courtesy of Clarity Diamond.

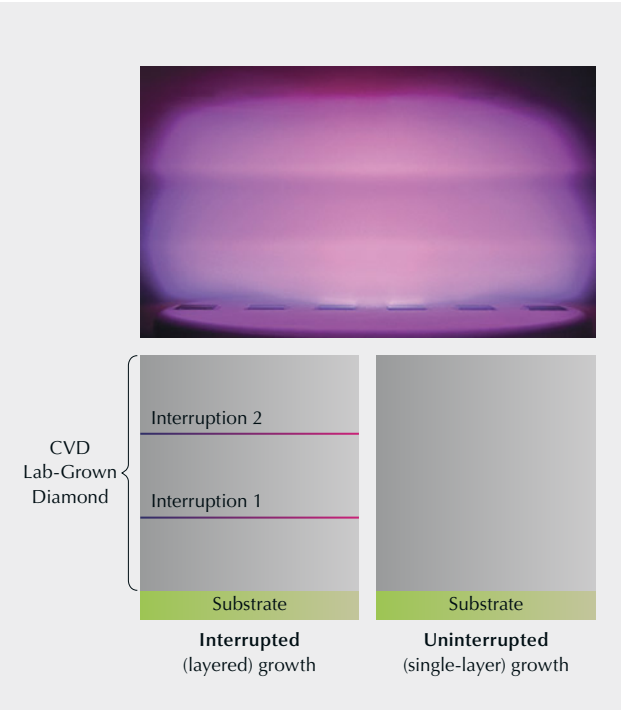

Figure 15. Top: CVD-grown diamond manufacturers grow diamond crystals using seeds (or substrates), a predetermined gas mixture, and plasma of extremely high temperature. Photo courtesy of Clarity Diamond. Bottom: Both interrupted and uninterrupted growth are applied in the industry, and each has advantages and unique challenges. Clarity Diamond uses the uninterrupted method, resulting in CVD-grown diamonds without growth lines, as displayed in this illustration.

diamonds (figure 16). HRA Group also distributes the finished products to retailers in North America, Australia, and Europe. The brand currently focuses on producing CVD-grown diamonds of high color grade (D–F) and clarity (VS_2 and above).

All visitors, many of whom are jewelry retailers throughout the country, had the chance to view finished jewelry mounted with CVD-grown diamonds manufactured in the facility (figure 17). This gave the retailers the opportunity to understand the product and the process behind the gem, so they can deliver accurate information to consumers. Clarity Diamond is committed to providing transparency about its growth process and business practices to retailers.

Retailer and consumer education remain at the core of our industry and GIA's mission. Education plays an even bigger role when relatively new products are brought to the market. As GIA researchers and educators diligently keep

Figure 16. Planning CVD-grown rough diamond for cutting is done by computer-aided tools, which usually propose options for the cutters—in this case, the two round brilliants to be produced from one rough (left). Then cutters follow processes similar to those used for cutting and polishing natural diamonds (right, 3.16–5.44 ct). Courtesy of Clarity Diamond and HRA Group.

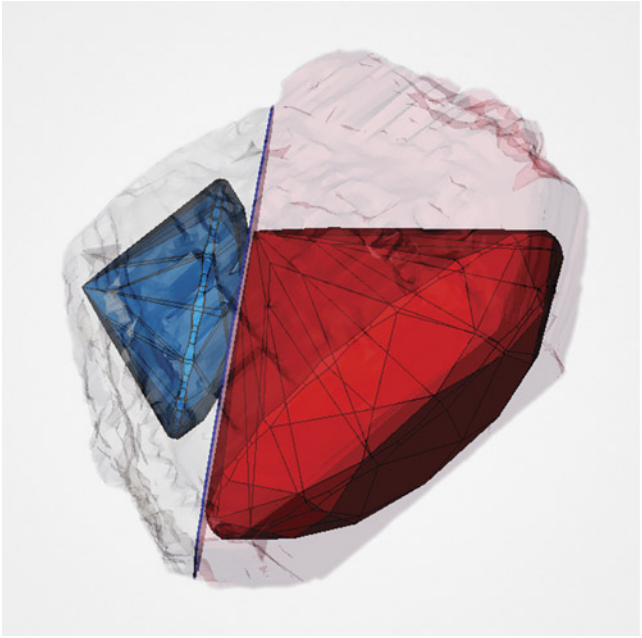

Figure 17. Clarity Diamond hosted a counter inside the facility to show some of its finished jewelry product lines. Courtesy of Clarity Diamond.

up with new developments, we also learn from industry practitioners through opportunities such as this visit to Clarity Diamond's CVD facility.

Tao Hsu and Lisa Kennedy
GIA, Carlsbad and New York

Unusually large flux-grown synthetic sapphire. IIGJ-Research & Laboratories Centre (formerly Gem Testing Laboratory) in Jaipur, India, recently received for identification a translucent blue rough stone weighing 64.70 ct. The specimen appeared transparent in transmitted light and displayed a typical bipyramidal (barrel-shaped) crystal habit along with distinct stepped striations across the surface (i.e., perpendicular to the longer *c*-axis, as shown in figure 18, left). In addition, some areas displayed a rhomb-shaped step pattern, and one side of the bipyramidal crystal had a large rhombohedral face (figure 18, right). This combination of crystal habit and surface features suggested corundum, which was confirmed by Raman spectroscopy.

Under magnification, the specimen displayed white and opaque flux residues in the form of wispy veils or flux fingerprints, along with flux-filled cavities (figure 19). No other inclusions associated with natural or synthetic

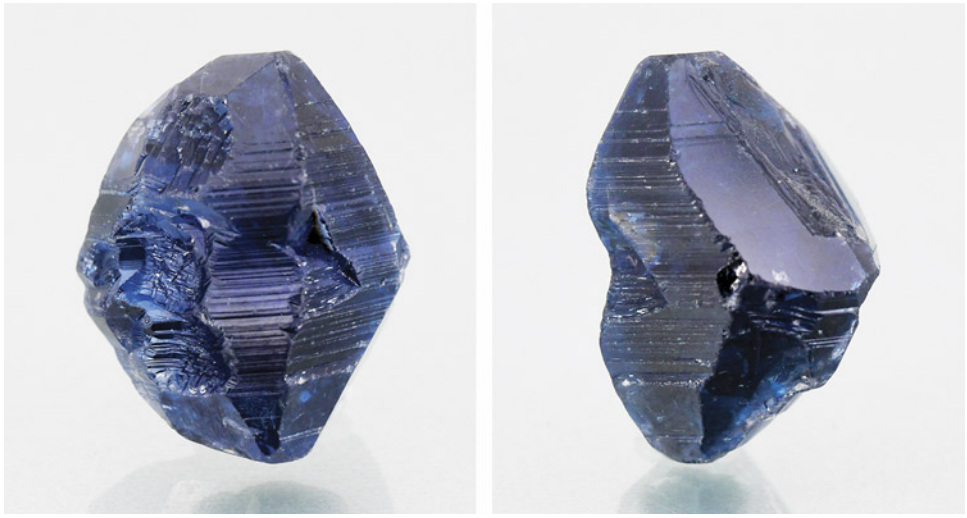

Figure 18. This unusually large 64.70 ct rough specimen displaying a bipyramidal crystal habit and stepped striations was identified as a flux-grown synthetic sapphire. Note the large rhombohedral face in the image on right. Photos by Gagan Choudhary.

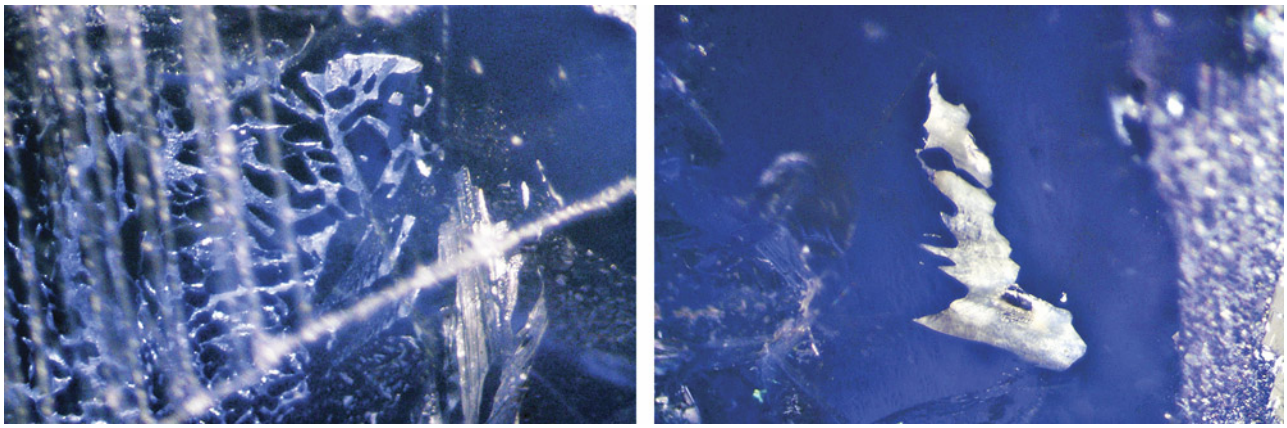

Figure 19. The flux-grown sapphire crystal contained white and opaque flux inclusions in the form of fingerprints (left) and flux-filled cavities (right). Photomicrographs by Gagan Choudhary; field of view 5.08 mm.

corundum were observed. However, the specimen exhibited strong color zoning when immersed in methylene iodide; blue color was mainly concentrated toward the center of the stone, while the rim of the crystal appeared colorless (figure 20). The presence of flux (in the form of fingerprints/cavities) and the absence of any natural inclusions pointed to a synthetic sapphire grown by the flux-fusion process. Under short-wave UV, the specimen displayed strong chalky yellowish green fluorescence while remaining inert under long-wave; such a fluorescence reaction is not observed in natural (heated or unheated) sapphire. Closer examination in the DiamondView revealed stronger yellowish green fluorescence from flux inclusions compared to the stone's body, although zonal greenish fluorescence was also visible. The exact cause of this yellowish green fluorescence remains unknown.

Figure 20. Viewed in immersion, the flux-grown sapphire crystal exhibited strong color zoning, with a deep blue center and a rim that appeared colorless. Photo by Gagan Choudhary.

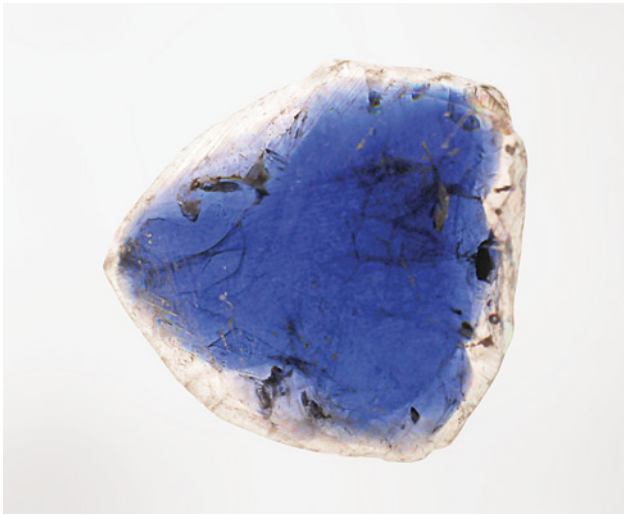

Consistent with an earlier report (Winter 2020 Lab Notes, pp. 524–525), this synthetic sapphire also displayed peaks at ~388 and 450 nm, along with a broad band at ~475–800 nm and an absorption maximum at ~615 nm in its ultraviolet/visible/near-infrared spectrum; these features are associated with Fe^{3+} and Fe^{2+}-Ti^{4+}. Semiquantitative energy-dispersive X-ray fluorescence analysis revealed the presence of molybdenum, tantalum, platinum, and silver, while vanadium and gallium were not detected; this chemistry further indicated a flux-grown synthetic.

This was the first time we had encountered such a large flux-grown synthetic sapphire, though the market availability of this size is unknown. Through careful microscopic observation, along with fluorescence reaction and chemistry, a laboratory gemologist should be able to correctly identify this type of flux-grown synthetic sapphire. But these sapphires, especially in their rough form, may pose a challenge for gem dealers who are generally equipped with a 10× loupe or only basic gemological tools.

Gagan Choudhary (gagan.choudhary@iigjrlc.org)
IIGJ-Research & Laboratories Centre, Jaipur, India

AUCTION REPORTS

Spring 2024 auction highlights. Yellow diamonds brought a ray of sunshine to Geneva for the spring auction season, which was full of excitement in mid-May. The Allnatt diamond, a 101.29 ct Fancy Vivid yellow brilliant set in a brooch designed by Cartier in 1952, was pulled from Sotheby's Magnificent Jewels sale just before it began. Another yellow diamond, the 202.18 ct "Yellow Rose" (figure 21), was the star of Christie's Magnificent Jewels auction the following day. The GIA-graded Fancy Intense yellow

Figure 21. The 202.28 ct "Yellow Rose" diamond sold in Geneva for $6.7 million. Courtesy of Christie's Images Ltd. 2024.

Figure 22. The "Argyle Phoenix," a 1.56 ct Fancy red diamond, fetched nearly three times its presale estimate. Courtesy of Phillips.

pear modified brilliant with SI_1 clarity sold for $6.7 million, the second-highest price ever paid at Christie's for a yellow stone weighing more than 200 ct.

Perhaps the most significant highlight in Geneva was the sale of the "Argyle Phoenix" (figure 22), a 1.56 ct Fancy red diamond offered by Phillips that nearly tripled its presale estimate. Selling for $4.2 million ($2.7 million per carat), the GIA-graded brilliant set in an 18K gold ring broke two auction records: highest price and highest per-carat price for a Fancy red diamond. Originating from the Argyle mine in Australia, the "Argyle Phoenix" is the largest known Fancy red round brilliant diamond.

The trend of exceeding presale estimates continued later in the month at Christie's Magnificent Jewels in Hong Kong. Cartier's multi-gem Tutti Frutti necklace "India" (figure 23) shattered its $4.9 million high estimate and fetched $8.7 million. Adorned with carved rubies, emeralds, sapphires, and round GIA-graded diamonds, as well as sapphire, ruby, and emerald beads, the piece sold after 10 minutes of competitive bidding. Christie's reported that more than half the lots in the auction surpassed their estimates, including a "pigeon's blood" Burmese ruby and diamond ring that garnered $6.4 million, doubling its $3.2 million high estimate.

At the close of the season in June, Christie's offered the 10.20 ct "Eden Rose" (figure 24) as their top lot in New York. The Internally Flawless Fancy Intense pink type IIa diamond was publicized not only for its size, but also for its pure pink hue and lack of secondary tones. Set in an 18K rose and white gold ring and surrounded by 12 carats of pear- and marquise-shaped colorless diamonds, the GIA-graded round brilliant exceeded its high estimate of $12 million, selling for $13.3 million, or $1.3 million per carat.

Figure 24. The "Eden Rose," a 10.20 ct Fancy Intense pink diamond, surpassed its presale estimate, selling for $13.3 million. Courtesy of Christie's Images Ltd. 2024.

Erica Zaidman
GIA, Carlsbad

Figure 23. The "India" necklace from Cartier's Tutti Frutti collection, featuring carved rubies, emeralds, sapphires, and diamonds, nearly doubled its upper presale estimate, garnering $8.7 million in Hong Kong. Courtesy of Christie's Images Ltd. 2024.

Figure 25. A: The show floor at the 2024 IJT. B and C: Yusuke Katsurada's Montana sapphire seminar and a presentation at the GIA booth. Photos by Kazuko Saruwatari (A) and Tomoko Narui (B and C).

CONFERENCE REPORTS

IJT 2024. International Jewelry Tokyo (IJT), held every January at the Tokyo International Exhibition Center, known as Tokyo Big Sight, is Japan's largest jewelry trade show (figure 25). This year, GIA organized a seminar presented by Dr. Yusuke Katsurada titled "The Tales of Montana Sapphire," which focused on colored stone origin and traceability. For the first time, on-site presentations were conducted at the GIA booth, with gemologists from GIA's Tokyo laboratory explaining colored stone treatments to the public.

A variety of items were on display this year. One jewelry maker, Kishun, exhibited AI-designed jewelry (figure 26, left). Spokesperson Hanako Minami noted that this was the company's first such venture. She observed that the AI-generated designs were quite novel but lacked practicality. The company expects AI to learn to produce practical and innovative jewelry designs in the future. Meanwhile, one traditional jeweler presented natural diamond engagement and wedding rings with elaborate designs in metal (figure 26, right). The designs were inspired by floral and other natural elements that have long been familiar in Japanese culture.

Figure 26. Left: These AI-designed rings showcase different themes. From left to right: satellite, cherry blossom, and civil engineering. Right: An engagement ring with a plum blossom design. The side stone is a pink sapphire. Photos by Kazuko Saruwatari; courtesy of Kishun (left) and Manji (right).

Figure 27. Left: Various gemstones with the 180-facet "kikyo" cut, sold loose or set in pendants and rings. Right: A kikyo-cut rutilated quartz. Photos by Kazuko Saruwatari; courtesy of Shimizu Kiseki.

Also on display were gemstones cut with 180 facets, enhancing the brightness of quartz and other materials containing various inclusions (figure 27, left). The facets are based on a dodecahedron structure, with 15 facets on each pentagonal face (figure 27, right). This style is called the "kikyo" cut because of its resemblance to the bellflower (*kikyo* in Japanese). The cut epitomizes the skill of master craftsman Yukio Shimizu, the sole artisan who executes this intricate 180-facet gemstone cut.

Meanwhile, akoya cultured pearls remain popular. Most notable were the akoya pearls from Vietnam, which possessed excellent luster and white color. Vietnamese akoya pearl jewelry was also featured in versatile designs (figure 28, left). Other highlights were South Sea and

Figure 28. Left: Vietnamese akoya pearls are featured in this flexible design for use as a double bracelet or a single choker. Right: Two large South Sea golden pearls and one white pearl larger than 21 mm along with a slightly smaller Tahitian pearl. Photos by Kazuko Saruwatari; courtesy of Spopel (left) and Fiore (right).

Tahitian pearls in sizes larger than 20 mm (figure 28, right).

Next year's IJT will be held January 15–18, 2025, also at Tokyo Big Sight.

Kazuko Saruwatari
GIA, Tokyo

ANNOUNCEMENTS

***G&G* Facebook group surpasses 40,000 members.** In early 2020, *Gems & Gemology* launched a Facebook group dedicated to the world of gemology. Since then, more than 40,000 jewelry professionals, researchers, students, and gem enthusiasts worldwide have joined to share and expand their knowledge. With regular posts from *G&G* contributors and GIA researchers (figure 29), along with posts from group members, followers enjoy a steady stream of content covering gemstone inclusions, treatments, identification, field gemology and mining, and more.

Ready to join? Visit https://www.facebook.com/groups/giagemsgemology to become a member of our growing community.

Figure 29. The Gems & Gemology *Facebook group is a growing community of more than 40,000 gem and jewelry enthusiasts worldwide, featuring posts from* G&G *contributors, GIA researchers, and members of the group.*

ERRATUM

In the Spring 2024 feature article "Nanoscale techniques for characterizing gemstone coatings" by Tsung-Jen Wu et al. (pp. 42–54), carbon and oxygen were inadvertently switched in the legends for figure 3 (left and right). The correct legends are shown below in figure 30. We regret the error.

Figure 30. Corrected legends are shown for the Auger electron spectroscopy plots in figure 3 of Wu et al., "Nanoscale techniques for characterizing gemstone coatings: A case study on synthetic moissanite," from the Spring 2024 issue.

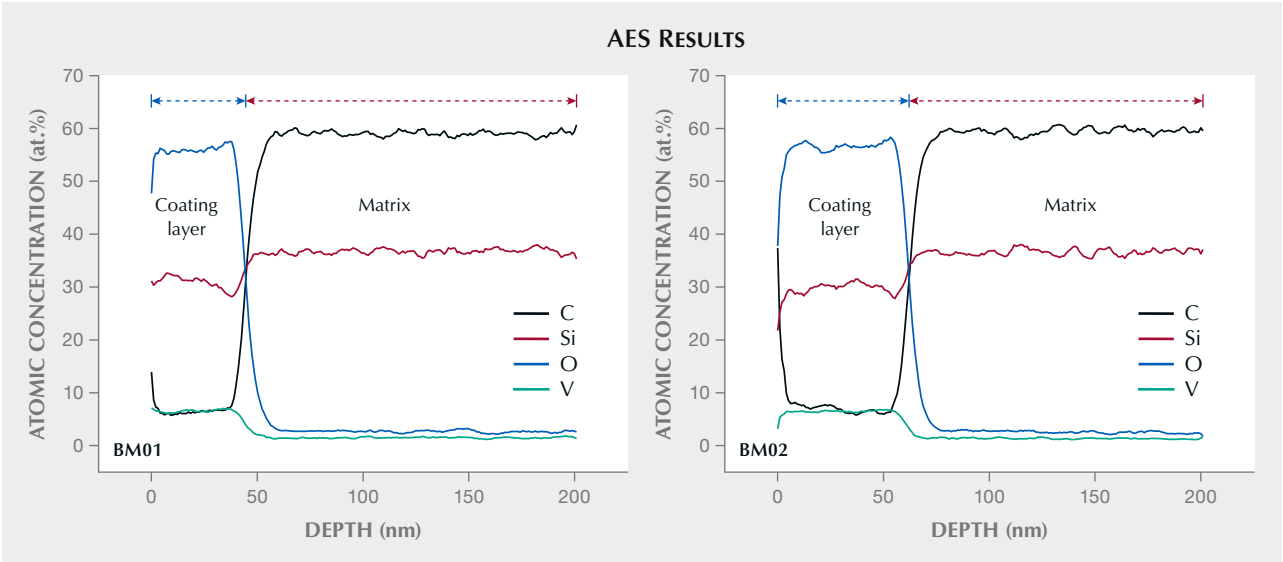

Trusted Innovation, Backed by Science.

GIA®

Science and innovation meet modern design to provide the technology you need to safeguard your customers and business.

GIA® Gemolite® NXT
Introducing GIA® Gemolite® NXT, where form meets function. Ergonomic design ensures comfort, while advanced proprietary LED lighting and clarity of optics provide unparalleled precision. GIA sets the new standard in gemological instruments.

Learn More

GIA.edu/gemolite

Dance of Light and Color: Painted Labradorite

Robert Weldon, Orasa Weldon, and Nathan Renfro

Valentina Fetisova's improbable path from trained ballerina to painter of gem labradorite has two common denominators: love of art and an unwavering dedication to the tiniest detail.

Born in Obninsk, Russia, Fetisova was enamored with ballet from the age of eight months, when she would stand in front of her mother's television, transfixed by the performance on screen. She went on to dedicate 24 years of her life to dance under the direction of ballet greats Gediminas Taranda and Maya Plisetskaya. Fetisova eventually fulfilled a childhood dream to tour with the Imperial Russian Ballet. Seven years into professional ballet, however, she decided it was time for a change.

From Fingernails to Stone

After leaving ballet, Fetisova launched a new career as a nail artist. "I wanted each tiny painting to look like a work of art," she says. After taking dozens of courses on painting and scouring the Internet for ideas and techniques, she eventually came upon the concept of painting on stones. She searched for a mentor who could teach her this art and found two master painters who agreed to give her private lessons—the second one for only two days. "The second master was invaluable for me because the man is a genius and was able to share so much," Fetisova says. In total, she has been painting for close to 20 years. "What I learned could have graduated me from the university!" she says.

"I painted my first panther on labradorite, and everyone who saw it loved it. It became my calling card. It somehow happened that more and more labradorites soon fell into my hands, and I boldly began to paint on them, too. I brought out my technique of painting on glowing stones; it is more complicated and time-consuming, but now you can evaluate the result yourself." (Visit www.gia.edu/gems-gemology/summer-2024-in-the-spotlight to view how the labradorescence phenomenon changes with the tilt of the stone.)

Fetisova, who left Russia in 2009 and now lives in Antalya, Turkey, has developed a technique that takes advantage of the glowing colors of the gem's labradorescence, particularly as a stone is tilted in relation to a light source, to give her paintings a dramatic effect. She enjoys watching people pick out a favorite painted labradorite from her collection, which includes beautiful landscapes, people, wildlife, flowers, and even science fiction scenes.

"Though it was not my goal to paint space items or fantastic stories—those pieces were ordered specially—they *did* turn out well, so I'll continue to paint them." For customers who aren't sure what they want, she refers to the "magic" of the stone. "A person is attracted to one, takes it in their hands, and no longer needs to see any other stones. The stone and its new owner have found each other." Her clientele includes members of royal families (she's not disclosing who) and notable jewelers.

Top: Gem artist Valentina Fetisova uses unique painting techniques to transform labradorite and other gem materials into works of art.

Technique

Fetisova says that most of her "canvases" come to her as prepolished cabochons. The first step is to remove the polished surface through

Below: A seagull over stormy waters in a 235 ct gem measuring 78 × 64 × 6 mm. Photo by Robert Weldon. Opposite page: Photomicrography reveals the stunning translucency of the painting, as the labradorescence phenomenon adds to the vivid coloration perceived. Photomicrograph by Nathan Renfro.

Left: A resplendent tiger in the late afternoon "labradorite sunset" rests on a rock in this piece measuring 72 × 36 × 7 mm and weighing 127 ct. Photo by Robert Weldon. Right: Magnification reveals Fetisova's mastery of the brush, as individual whiskers and strands of fur are highlighted. Photomicrograph by Nathan Renfro.

sanding with emery paper and other abrasives. To protect her intellectual property, Fetisova does not disclose the grit or brand of varnish or paint. However, she notes that a miniature image of her subject matter is then transferred onto the gem's sanded surface with tracing paper. After this step, a series of color spots are painted onto the surface, and the stone is placed in an oven to dry at a temperature not exceeding 70°C (158°F). This is followed by a layer of varnish and a drying phase. She mattes this surface again with sandpaper and paints a second layer onto the stone, to be dried again. "The transparency of the paint on the surface makes it possible to create different shadow effects and at the same time control the transparency of the image, especially on shiny stones."

Fetisova explains that the clarity and beauty of each painting evolves from layer to layer and through successive steps in the drying process. The number of layers can vary, but in most cases she can complete her painting in about four layers. Once the work is finished, she paints the date and her signature on the back of the gem. She then varnishes the stone again in several layers, on both sides.

Then it is time to evaluate her work. If Fetisova likes what she sees, the piece is finished and ready for sale and, ultimately, for a little "magic" with a buyer.

Photo Gallery

Fetisova makes use of the gems' labradorescence to add drama and color to her paintings. The effect is best captured as the photographer angles the light or the gem to exhibit this phenomenon. We would like to acknowledge Mike Bowers for bringing Fetisova's work to our attention and for generously allowing us to photograph his collection of her paintings on labradorite.

Left: Fighting fish shimmer against a watery background as the labradorescence is on full display in this 110 ct gem measuring 50 × 49 × 5 mm. Center: A light source exhibiting the phenomenon is turned off, showcasing Fetisova's brush and painting techniques. Photos by Robert Weldon. Right: Photomicrography demonstrates Fetisova's ability to mimic the movement and personality of her subject. Photomicrograph by Nathan Renfro.

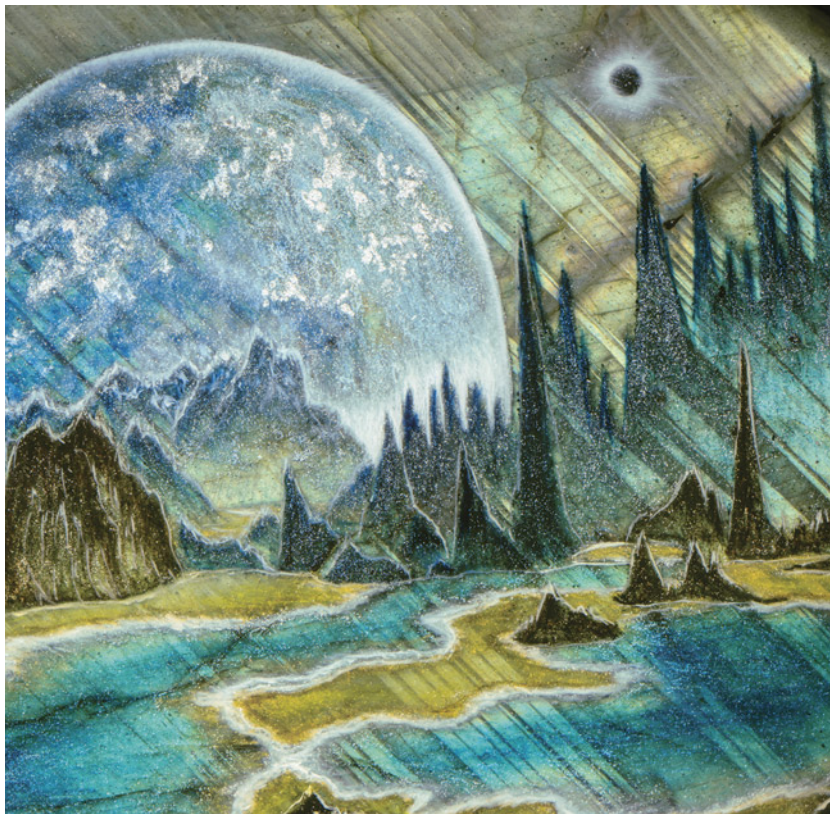

Above: A sci-fi scene in this oval measuring 48 × 72 × 8 mm and weighing 247 ct depicts streaks of light filtering through pine forests and reflecting in the lakes below. At the horizon, a giant moon emerges from behind the mountains. Photo by Robert Weldon. Right: Detail of variations in the perceived color, depending on the orientation of the light source. Photomicrograph by Nathan Renfro.

Left: A snowy owl in flight in this 114 ct gem. Right: Detail of the minutely realistic rendering of the owl's eyes. Photos by Orasa Weldon.

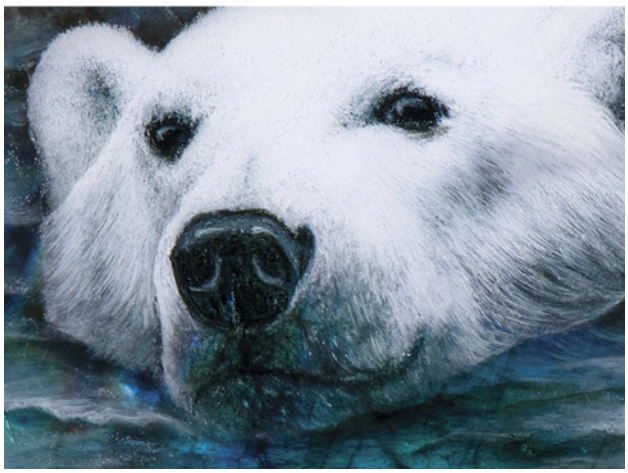

Top: This 80 ct labradorite, which measures 47 × 4 mm, shows a polar bear swimming. Bottom: Detail of the polar bear. Note the expression and the shiny eyes and nose, accentuating the Arctic cold. Photos by Orasa Weldon.

Above: An otherworldly sci-fi scene in this oval measuring 70 × 53 × 6 mm and weighing 214 ct. Photo by Robert Weldon. Opposite page: Detail reveals slight color variations as the light source is moved. Photomicrograph by Nathan Renfro.

Left: A polar bear with two cubs on an ice floe are illustrated in a 160 ct labradorite measuring 47 × 75 × 5 mm. Right: Close-up of the detail in the painting of the fur. Photos by Orasa Weldon.

Left: "The Cosmonaut," part of Fetisova's sci-fi series, captures the vast range of subject matter she is able to render with imagination and skill. This 71 × 52 × 6 mm labradorite weighs 231 ct. Photo by Robert Weldon. Right: Detail of the cosmonaut. Photomicrograph by Nathan Renfro.

Micro-Features of Tourmaline

Inclusions in Tourmaline

This pink tourmaline from Brazil shows color zoning and numerous growth blockages. An interesting spiral dislocation is also seen parallel to the *c*-axis of the crystal. Field of view 2.21 mm.

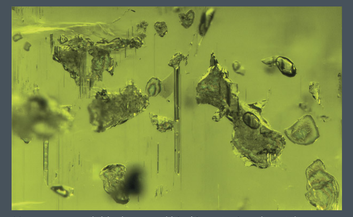

Numerous growth blockages and birefringent mineral crystals are notable features in this elbaite tourmaline from Brazil. Field of view 1.43 mm.

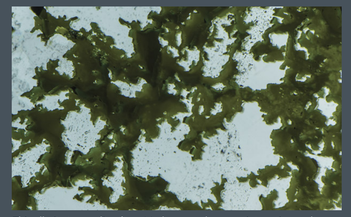

This elbaite tourmaline from Madagascar shows an interesting and complex moss-like pattern of color zoning. Field of view 8.29 mm.

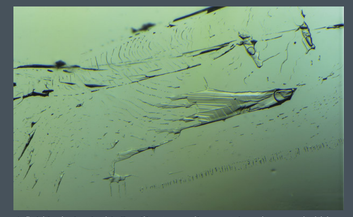

A fluid inclusion in this Brazilian tourmaline contains a large gas bubble, liquid, a delicate curved fiber, and small solid crystals. "Communicator tubes" and "necking down" structures are visible. Field of view 3.16 mm.

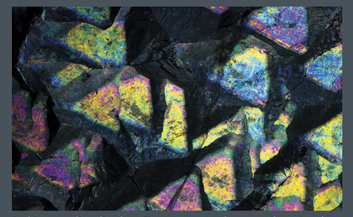

In this tourmaline slice from Fianarantsoa, Madagascar, vibrant interference colors are seen when looking parallel to the optic axis using cross-polarized light. Field of view 23.95 mm.

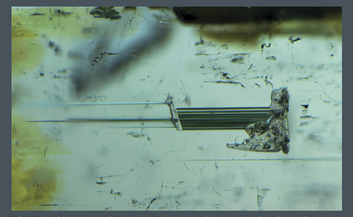

This Brazilian tourmaline contains an excellent example of a multistage growth blockage mechanism caused by what are probably mica crystals. Yellow epigenetic staining is also present. Field of view 4.11 mm.

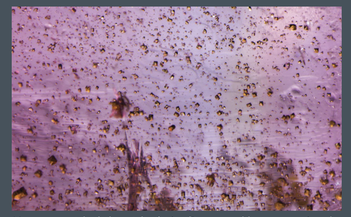

Numerous octahedral crystals of microlite, a pyrochlore-group mineral, are scattered throughout this pink elbaite tourmaline from Mozambique. Field of view 4.10 mm.

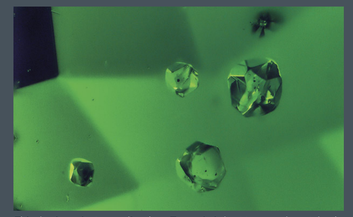

This dravite-uvite tourmaline from Tanzania is host to several crystals of apatite, pyrite, and graphite. Field of view 2.30 mm.

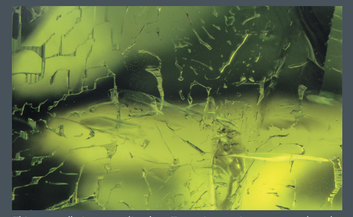

This green elbaite tourmaline from Tanzania contains numerous thread-like fluid inclusions known as "trichites." Field of view 2.87 mm.

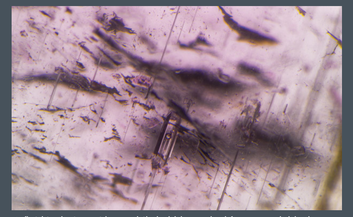

A fluid inclusion with a mobile bubble resulted from growth blockage caused by a nearly invisible tourmaline inclusion in this Brazilian tourmaline host. Field of view 2.08 mm.

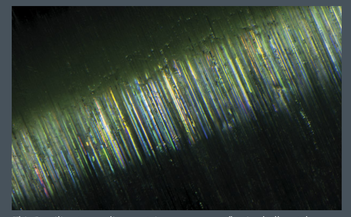

This Brazilian tourmaline contains numerous reflective hollow tubes that are responsible for a cat's-eye phenomenon in this chatoyant gem. Field of view 2.04 mm.

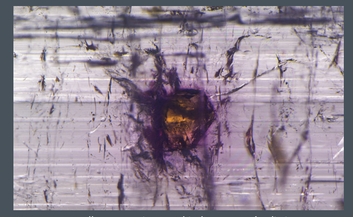

A transparent yellow monazite crystal is the source of radiation responsible for the localized pink color zoning in this tourmaline from California. Field of view 3.55 mm.

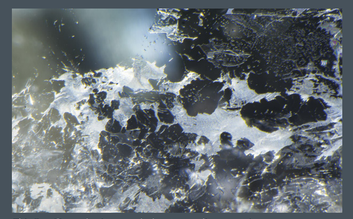

This Brazilian achroite, or colorless tourmaline, contains numerous etched fluid inclusions with a whitish appearance. Field of view 2.30 mm.

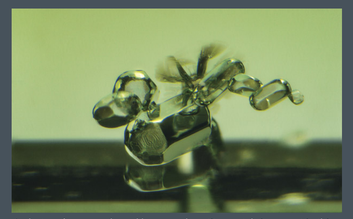

A cluster of sausage-shaped hexagonal apatite crystals is present in this elbaite tourmaline from Merelani, Tanzania. Field of view 1.86 mm.

Large spike-shaped growth blockage tubes are capped by small crystals in this uvite tourmaline from Magadi, Kenya. Large graphite crystals are also present. Field of view 4.67 mm.

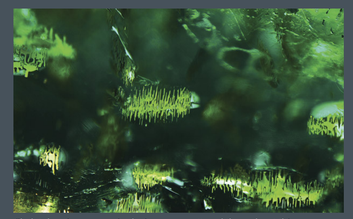

Skeletal native copper inclusions are scattered throughout this copper-bearing elbaite tourmaline from Brazil. Field of view 3.57 mm.

A slice of elbaite tourmaline from Brazil shows complex color zoning when viewed perpendicular to the *c*-axis of the crystal. Field of view 13.43 mm.

This pink tourmaline from California contains a blocky lepidolite inclusion as well as several colorless crystals. Field of view 1.80 mm.

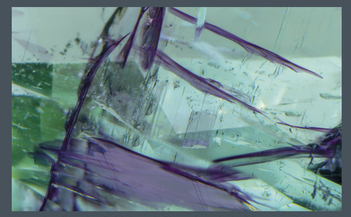

Natural radioactive fluids have infiltrated cracks in this Mozambican elbaite tourmaline, creating localized radiation-induced natural pink color zones along the walls of the fractures. Field of view 4.27 mm.

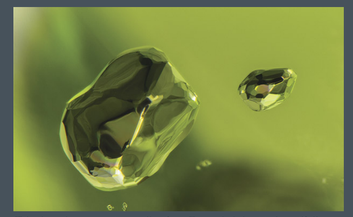

This chromium green tourmaline from Tanzania is host to beautifully rounded protogenetic pyrite crystals. Field of view 2.52 mm.

Tourmaline as an Inclusion

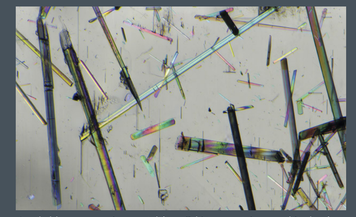

A pale blue aquamarine crystal from Pakistan contains a multitude of tourmaline inclusions that show vibrant interference colors using polarized light. Field of view 2.61 mm.

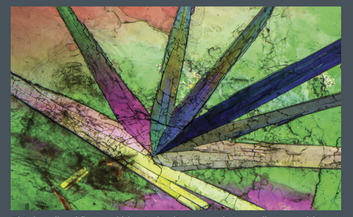

This bundle of flattened blue indicolite tourmaline needles resembling a palm frond is trapped in a mica host from Brazil. Vibrant interference colors are revealed using polarized light. Field of view 14.84 mm.

This kunzite spodumene from Afghanistan contains a dark blue tourmaline crystal indicative of its pegmatitic origin. Field of view 5.62 mm.

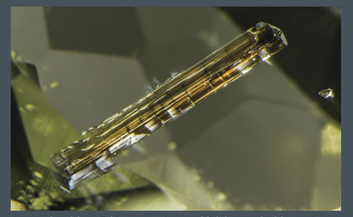

A green beryl from Pakistan contains a reddish brown doubly terminated crystal of tourmaline. Field of view 3.64 mm.

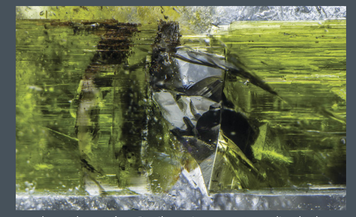

A rock crystal quartz from Brazil contains a green tourmaline that has separated, with a pyrite crystal interestingly perched between the tourmaline segments. Field of view 8.05 mm.

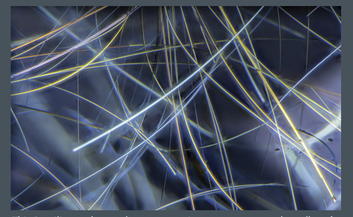

This Brazilian rock crystal quartz contains numerous curved needles of very fine tourmaline inclusions that show birefringence using polarized light. Field of view 4.27 mm.

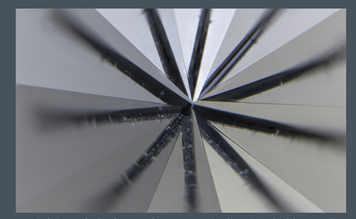

An inclusion of schorl tourmaline was creatively oriented table-to-cutlet in this round brilliant rock crystal quartz. The pavilion facets reflect the single tourmaline inclusion in a radial pattern. Field of view 5.74 mm.

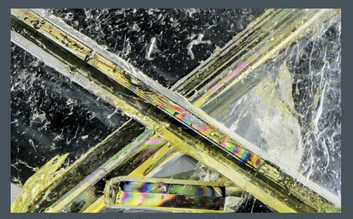

A Brazilian goshenite beryl is host to crossed green tourmaline inclusions. Vibrant thin-film interference colors are seen along the interface of the beryl and the tourmaline. Field of view 11.28 mm.

A yellow manganese-colored elbaite tourmaline from Sri Lanka is host to a dark needle-like inclusion of what is probably schorl tourmaline. Field of view 3.94 mm.

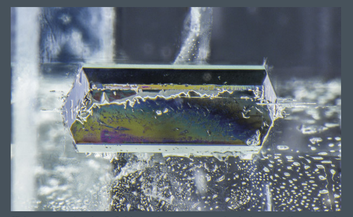

This aquamarine from Pakistan showcases a euhedral tourmaline crystal. Faint thin-film interference colors are also seen between the beryl host and tourmaline guest. Field of view 3.52 mm.

This chart contains a selection of photomicrographs of natural tourmaline and tourmaline inclusions in other natural gemstones. It is by no means comprehensive. The images show the appearance of numerous features a gemologist might observe with a microscope.

Published in conjunction with Nathan Renfro, Tyler Smith, John I. Koivula, Shane F. McClure, and James E. Shigley (2024), "Micro-Features of Tourmaline," *Gems & Gemology*, Vol. 60, No. 2, pp. 208–210. Photomicrographs by Nathan Renfro and Tyler Smith. Stones courtesy of GIA, the John I. Koivula inclusion collection, and the collection of Nathan Renfro.

GIA®